RADIO EMISSION FROM MASSIVE YOUNG STELLAR OBJECTS AND THEIR SURROUNDINGS: CHARACTERIZATION AND FEEDBACK

Dissertation
zur
Erlangung des Doktorgrades (Dr. rer. nat.)
der
Mathematisch-Naturwissenschaftlichen Fakultät
der
Rheinischen Friedrich-Wilhelms-Universität Bonn

vorgelegt von

Sac Nicté Xiomara Serrano Medina
aus
Morelos, Mexiko

Bonn 2019

Angefertigt mit Genehmigung der Mathematisch-Naturwissenschaftlichen Fakultät der Rheinischen Friedrich-Wilhelms-Universität Bonn

1. Gutachter:	Prof. Dr. Karl Menten
2. Gutachter:	Prof. Dr. Pavel Kroupa

Tag der Promotion: 02.12.2019
Erscheinungsjahr: 2020

Contents

Acknowledgements

I would like to thank Prof. Dr. Karl Menten to gave me the chance to performed my doctoral project at the Max Planck Institute for Radio Astronomy, for being my thesis supervisor, and for all his thoughtful support during my doctoral studies. To Prof. Dr. Pavel Kroupa to accepted to be my second thesis supervisor, and to Dr. Friedrich Wyrowski and Dr. Andreas Brunthaler to be my thesis advisors.

Thank you to Prof. Dr. Simon Stellmer and Prof. Dr. Hubert Schorle for kindly accept to be part of my evaluating committee.

Special thanks to my principal mentors: Dr. James Urquhart and Dr. Sergio Dzib for all their advice and help related to my work in the GLOSTAR survey. The results would have been impossible without you. To Dr. Jane Arthur to share her knowledge and also teach me about turbulence analysis. Thank you all for your advice and guidance during my research process. I do not find enough words to thank you, but I carry always with me your teachings. Also, thank you to Dr. Dario Colombo for performing the cloud extraction used in my on-going work and for all the productive discussions.

Thank you to Dr. Rainer Mauersberger and Dr. Simone Pott from the International Max Planck Research School (IMPRS), and Tuyet-Le Tran, Barbara Menten, Eva-Ingeborg Schmelmer, Edith Fingas, and Sylvia Mertens from the Max Planck Institute for Radio Astronomy administration, for all their support and help in my administrative formalities.

Also, I want to thank Joana Buerger-John from the Bonner Graduiertenzentrum and Sandra Papel from the International Office of the University of Bonn for their extraordinary work to incorporate the international students to the University activities.

Kaxan Eek'oobo' – The Hunter of Stars

At her seven years old, Zazil-Há only spoke the Mayan language. The economic difficulties of her family could not guarantee for her a good future, but her innocence let her dream about it without limits.

Her major passion was to observe the night sky. Her grandfather called her Kaxan Eek'oobo' (the hunter of stars). He did not know how to read, but he filled Zazil-Há's imagination with marvelous stories from their Mayan people about the stars. Zazil-Há wondered how did look like the night sky that the Itza, the ancient Mayans, used to study and how was possible for them to understand the stars.

Those nostalgic moments from her childhood exploded like a supernova into her head one night while she was typing commands of observation in a computer. She smiled and thought: The future is not written in the stars, but follow them let us find a great one.

1st prize of the IAU100-Short story written competition "Under One Sky" by Sac Nicté Medina.

A mi mejor amigo y el amor de mi vida,
Meine Liebe Sergio.
Thank you for so much cosmic love.

The list of publications related to the work of this thesis:

5. **GLOSTAR — Radio Source Catalogue I: $28^\circ < \ell < 36^\circ$ and $|b| < 1^\circ$.**
   Medina S.-N. X.; Urquhart J. S.; GLOSTAR team; et al., 2019.
   Astronomy & Astrophysics Vol. 627.

4. **The richness of compact radio sources in NGC 6334D to F.**
   Medina, S.-N. X.; Dzib, S. A.; Tapia, M.; et al., 2018.
   Astronomy & Astrophysics Vol. 610.

3. **SEDIGISM: Structure, Excitation, and Dynamics of the Inner Galactic Interstellar Medium.**
   Schuller, F.; Csengeri, T.; Urquhart, J. S.; Duarte-Cabral, A.; Barnes, P. J.; Giannetti, A.; Hernandez, A. K.; Leurini, S.; Mattern, M.; **Medina, S.-N. X.**; Agurto, C.; et al., 2017.
   Astronomy & Astrophysics Vol. 601.

2. **Turbulence in the ionized gas of the Orion nebula.**
   Arthur, S. J.; **Medina, S.-N. X.**; and Henney, W. J., 2016.
   Monthly Notices of the Royal Astronomical Society Vol. 463.

1. **Turbulence study of the W43 region**.
   Medina S.-N. X.; et al.; In progress.

A complete list of all the publications with contribution of Sac Nicté Xiomara S. Medina is in section 6.2.

Abstract

Massive stars or high-mass stars dominate their galactic environments. They play a major role in the energy budget of galaxies and are essential in their evolution. However, high-mass star formation is not fully understood, in particular, the physical characteristics of massive Young Stellar Objects (YSOs) are still unclear because they are deeply embedded in their natal molecular clouds obstructing the view at optical and sometimes even infrared wavelengths. Currently, competing models of high-mass stars formation have to be confronted with observations and by providing more observational data, we increase the statistical sample that constrains the characteristics of YSOs. The open issues include the following: In which conditions do the YSOs form? How are the YSOs linked to the turbulence of their parental molecular clouds? Do these properties vary across the Milky Way? To provide answers to these questions, high angular resolution observations throughout the galaxy, multi-frequency studies, and systemic emission characterization are required to detail the properties that constrain their physical characteristics. This work aims to provide more observational evidence of the YSOs physical properties, as well as, the processes occurring within them, and their effects on their surrounding material.

An important part of the thesis was to carefully analyze radio sources embedded in massive star-forming regions to report their physical properties. We observed a small sample of radio sources in the star-forming region NGC 6334. We report 86 radio compact sources from which 69 are new detections and 6 are massive stars. These results reveal important physical properties about this region and the processes occurring within it. We provide observational support of coexistence of YSOs at different evolutionary stages, for example, we reported two UCHII regions are within more evolved HII regions. Then, we characterized the radio emission of around 1500 sources in the Milky Way galactic plane and produced the first catalog of the GLOSTAR survey. Our work supports the emission nature for hundreds of sources previously detected. We provide the flux and physical characteristics of a statistically significant sample of YSOs. One of the most interesting results is that we detected 96 new possible HII regions.

We also studied the effects of the YSOs on their surrounding material with a turbulence analysis of optical and submillimeter observation of ionized and molecular lines, respectively. We used three statistical techniques to characterize the turbulence motion: Structure Function, Velocity Channel Analysis (VCA), and the Pricipal Component Analysis (PCA). We started with ionized gas from the HII region of the Orion nebula. We applied to it the Structure Function and the VCA techniques. These first results show that injection of energy that triggers the turbulent motion of the ionized gas may be related to the photoevaporation flows from the dense cores molecular gas. Furthermore, the Structure Function method is less reliable in characterizing the turbulent motion of the ionized gas than the VCA. In addition, the same analysis was applied to a sub-sample of molecular clouds in the SEDIGISM survey. Their VCA profiles suggest that molecular clouds

show similar scales of turbulence dynamics. Finally, we studied the relationship between the feedback effects of YSOs on their parental molecular clouds. We selected the W43 region due to its high stellar activity and, therefore, strong stellar feedback. Our preliminary results show that the turbulence profiles of gas motion could have a direct relationship with the stellar feedback, which is supported by the fact that the Principal Component Analysis (PCA) profile show very steep values. The results from our turbulent work provide evidence of interaction between YSOs and their molecular surroundings, as well as similar scales of turbulence dynamics, through the calculated turbulence profiles, energy transfer scales, and the molecular clumps sizes. All the turbulence profiles are calculated for the first time with these data sets.

Preface

The work presented here has been prepared under my own authorship. The contributions from co-authors are mentioned as they appear. It provides new observational studies of early stages in the formation of high-mass stars, also known as massive Young Stellar Objects (YSOs), and their stellar feedback effects leading to turbulent motions in their surrounding material. The proposed methodology provides successful results and suggests an innovative structure to apply well-known tools. The content of Chapters 3, 4, and 5 has been or is to be, published as independent peer-reviewed publications.

- Chapter 1. Here the motivation and the scientific question of this thesis are defined. It covers the theoretical background related to massive YSOs and their surroundings, such as their mass, density and lifetime, their emission at different frequencies, and their feedback effects.

- Chapter 2. It explains the innovative methodology implemented and used to extract and characterize the radio emission from YSOs as well as the statistical tools to characterize the turbulence in their surrounding material. The fundamental observations used in this thesis are at radio wavelengths, and they are also described in this chapter. These methods provide strong constraints related to the nature of the radio emission and the physical properties of YSOs that will be discussed in the next chapters.

- Chapter 3 contains our first approach to characterize radio emission from sources related to a star-forming region with high activity and diversity of evolutionary phases. The selected target is the NGC 6334 region. The source extraction method was used for the first time in this region and produced a first systematic census the compact radio sources embedded in the NGC 6334D to F region. We confirmed the nature of some sources and reported a large number of new detections. We analyzed the radio compact objects to associated them with YSO. The data, analysis, and conclusions presented in this chapter are in the peer-reviewed publication *The richness of compact radio sources in NGC 6334D to F.* **Medina, S.-N. X.**; Dzib, S. A.; Tapia, M.; et al., 2018. Astronomy & Astrophysics Vol. 610A.

- Chapter 4. Here, we extended the methodology to a large set of sources from the Global View of Star Formation in the Milky Way (GLOSTAR) survey. The analyzed map contains radio emission from highly active star-forming regions at different evolutionary phases. We discuss the results, the structure, physical properties, and nature of the identified sources in the first peer-reviewed publication *GLOSTAR — Radio Source Catalogue I:* $28^\circ < \ell < 36^\circ$ *and* $|b| < 1^\circ$. **Medina S.-N. X.**; Urquhart J. S.; GLOSTAR team; et al., 2019. Astronomy & Astrophysics Vol. 627.

- Chapter 5 contains our analysis of turbulence in ionized and molecular gas. We present the use of several analysis techniques for the first time with data sets that range from diffuse ionized gas to dense molecular gas. The ionized gas data are from the Orion nebula while the molecular gas data are from the Structure Excitation and Dynamics of the Galactic Interstellar Medium (SEDIGISM) survey and the W43-HERO large program. These results are part of the peer-refereed publications: *SEDIGISM: Structure, Excitation, and Dynamics of the Inner Galactic Interstellar Medium.* Schuller, F.; Csengeri, T.; Urquhart, J. S.; Duarte-Cabral, A.; Barnes, P. J.; Giannetti, A.; Hernandez, A. K.; Leurini, S.; Mattern, M.; **Medina, S.-N. X.**; Agurto, C.; et al., 2017. Astronomy & Astrophysics Vol. 601., *Turbulence in the ionized gas of the Orion nebula.* Arthur, S. J.; **Medina, S.-N. X.**; and Henney, W. J., 2016. Monthly Notices of the Royal Astronomical Society, Vol. 463., and the publication in progress *Turbulence study in the W43 region*. **Medina S.-N. X.**; et al.

- Chapter 6. Here the results from the present work are summarized and the future applications and follow up studies are discussed.

CHAPTER 1

Introduction

1.1 Problem statement

Massive stars or high-mass stars (also called OB stars), are stars with masses $> 8\,M_{\odot}$. They have a profound impact on their galactic environments and play a major role in the energy budget of galaxies as a whole via their radiation, winds, and supernova events. They also regulate future star formation and drive their evolution (Kennicutt 2005), they provide an important source of turbulence in the interstellar medium (ISM) and are the principal source of heavy elements and UV radiation (Motte et al., 2018). All of these processes make massive stars essential for the evolution of galaxies, including that of the Milky Way. Still, high-mass star formation remains as an enigma and it is far less understood than the low-mass, solar-type, star formation process. There are many reasons for this: During the formation of high-mass stars, they are still deeply embedded in their parental molecular clouds and the corresponding high dust extinction makes it difficult to observe them during critical early formation phases. They evolve very quickly, they are less common than low-mass stars (Liu et al. 2019; Reed 2003), and most importantly, their evolutionary phases are short-lived. Their formation is also extremely complex. Massive stars are seldom (if at all) formed in isolation, therefore, the proximity of other high-mass stars influences the formation of a new star and its local environment via gravitational interactions, powerful outflows and winds, ionizing radiation, and supernovae explosions.

One of the great challenges in modern astronomy is to understand the circumstances of high-mass star formation, in particular its early stages. The objects in these first stages of evolution are know as massive Young Stellar Objects (YSOs). Some results from numerical simulations suggest that stellar feedback from massive YSOs may play an important role in generating turbulence within their parental molecular clouds (e.g., Zhang and Chevalier 2019; Krumholz et al. 2018; Ali et al. 2018; Kim et al. 2018; Shima et al. 2018). Therefore, the study of high-mass star formation includes the analysis of the feedback effects from YSOs.

The work in this thesis aims to provide observational evidence of YSOs and their feedback effects through the characterization of their radio emission and the turbulence motion of their surrounding molecular clouds. The specific questions that we want to address are: What are the initial conditions in which YSOs form? How are YSOs linked to the turbulence of their parental molecular clouds, and do these properties vary across the Milky Way? To address these

questions, high angular resolution observations, from far-infrared to millimeter and centimeter wavelengths and Galaxy-wide surveys are required to provide a rich statistics for the analysis of the different stages in the evolution of YSOs. Also, statistical tools are mandatory to characterize the turbulence motions of the molecular gas that surrounds them.

1.2 Massive young stellar objects

There is no solid observational evolutionary sequence for the formation of high-mass young stellar objects as there is for low-mass young stellar objects. For example, what are the initial conditions in which YSOs form and how do they evolve and during their evolutionary sequence, how do they interact with their parental molecular clouds?

The objects associated with the first phase of high-mass star formation are massive dense clumps (e.g., Urquhart et al. 2014a) within giant molecular clouds that collapse gravitationally into high-mass protostellar cores (e.g., Tigé et al. 2017). In the following phases, they heat and eventually ionize the gas of its surrounding envelope, creating an HII region that develops by expanding within the molecular cloud (Spitzer 1978). Motte et al. (2018) summarize a scheme of high-mass star formation (Figure 1.1) that follows an empirical scenario within the framework of the global hierarchical collapse and clump-fed accretion models (e.g., Vázquez-Semadeni et al. 2009; Smith et al. 2009). The scheme starts with the formation of massive clumps (sizes$\sim$ 1 pc) in molecular cloud complexes (sizes $\sim$ 100 pc). According to their velocity and density structure, they are in a global but controlled collapse. Then, a starless phase ($\sim 10^4$ years.) starts: Low-mass prestellar cores are formed in massive cloud fragments (sizes $\sim$ 0.1 pc) which are called molecular dense cores (MDCs). The prestellar cores (sizes $\sim$ 0.02 pc) become protostars. This happens because the prestellar cores increase their mass through the gas flow streams originating from the global collapse of clumps. These protostars have still relative low masses (<8 $M_\odot$). In the following phases, YSOs are formed:

- In the next phase, the high-mass protostellar phase ($\sim 3 \times 10^5$ years), the protostars are fed by the inflowing gas streams and evolve into stellar embryos (<8 $M_\odot$). The stellar embryos power hot cores, and their strong accretion rates drive outflows. They are IR-quiet, which means that they cannot be observed at infrared wavelengths.

- Finally, when the stellar embryos reach more than 8 $M_\odot$ they become high-mass stellar embryos that are IR-bright. Their luminosity increases, hot cores grow in size, and they soon develop ionized regions that could be Hypercompact, Ultracompact or Compact HII regions (HCHII UCHII and CHII respectively) quenched by infalling gas or associated with photoevaporating disks.

- During the HII region phase ($\sim 10^5 - 10^6$ years), the gas accreation is stopped by UV radiation, outflows, and winds. The newly formed massive stars increase their UV fields and classic, or diffuse, HII regions develope (sizes $\sim$ 0.01 – 10 pc). This last phase is highly important for the interaction between stellar activity and the surrounding material because the HII region evolves and expands, which introduces dynamical feedback through radiation pressure and a stellar wind (Lequeux 2005).

These massive YSOs are very luminous and can be observed at several wavelengths, e.g., IR, millimeter, centimeter, and, in special cases, visible. Such observations allow to characterize and provide estimations of their physical properties. Some of the YSOs physical characteristics are listed in Table 1.1 and their emission properties will be described in more detail in the following section.

Table 1.1: Characteristics of Young Stellar Objects. Adapted from Motte et al. (2018).

	Median FWHM (pc)	Envelope mass ($M_\odot$)	Density $<n_{H_2}>$ (cm^{-3})	Statistical lifetime (years)	References
IR-bright high-mass protostars	~0.02[a]			$\sim 1.2 \times 10^5$	3
IR-quiet high-mass protostars	~0.02	10-100	10^6-10^8	$\sim 2 \times 10^5$	3, 4,5
All high-mass protostars	~0.02	>10	$\sim 10^7$	$\sim 3 \times 10^5$	3, 6
UCHII regions	~0.1	1-10^3	10^3-10^5	$\sim 3 \times 10^5$	1, 2

(a) Characteristics, which are postulated and thus not (yet) measured.
References: (1) Wood and Churchwell (1989), (2) Mottram et al. (2011), (3) Tigé et al. (2017), (4) Bontemps et al. (2010), (5) Louvet et al. (2014), and (6) Duarte-Cabral et al. (2013).

1.3 Emission from young stellar objects

Massive young stellar objects that have developed an HII region are strong free–free emitters at centimeter wavelengths (see, e.g., Churchwell 2002). At later stages, HII regions can be observed even at visible wavelengths when they have dispersed part of their molecular clouds; see, e.g., the archetypical Orion HII region Messier 42 (O'Dell and Wong 1996). Since the HII regions show different sizes in the distribution of their ionized material, Churchwell (2002) proposed an empirical evolutionary scenario based on the expansion of the ionized gas. In this scenario, the ultra-compact HII (UCHII) regions evolve into compact HII regions (CHII), and finally classical, or diffuse, HII regions. Later on, Kurtz (2005) using the first systematic survey for compact HII regions, introduced a new class of more compact objects named hypercompact HII regions (HCHII).

The smallest HII regions, UCHIIs and HCHIIs, have sizes of $\sim$ 0.1 pc and $<$ 0.05 pc, respectively, and $\sim 10^4$ cm^{-3} and $\sim 10^6$ cm^{-3} densities, respectively. They can shed light on the process of high-mass star formation itself, e.g., the mechanisms that would confine the ionized gas and delay its expansion (Kurtz et al., 2000; Hoare et al., 2007). Alternatively, HCHII regions could correspond to a very early phase of HII regions, their size quenched by infalling gas, or to high-mass protostars, whose photoevaporating disks and ionized accretion flow or jets are detected at centimeter wavelengths (e.g., Keto 2003, Hoare et al. 2007). Some physical properties of HII regions in this evolutionary scenario are summarized in Table 1.2 and examples are show in Figure 1.2.

The sources in the pre-HII region phase, the high-mass stellar embryos, have high IR luminosities. Wood and Churchwell (1989) were the first to systematically search for the youngest HII regions. They used the Galaxy-wide survey of high-luminosity mid- and far-IR sources provided

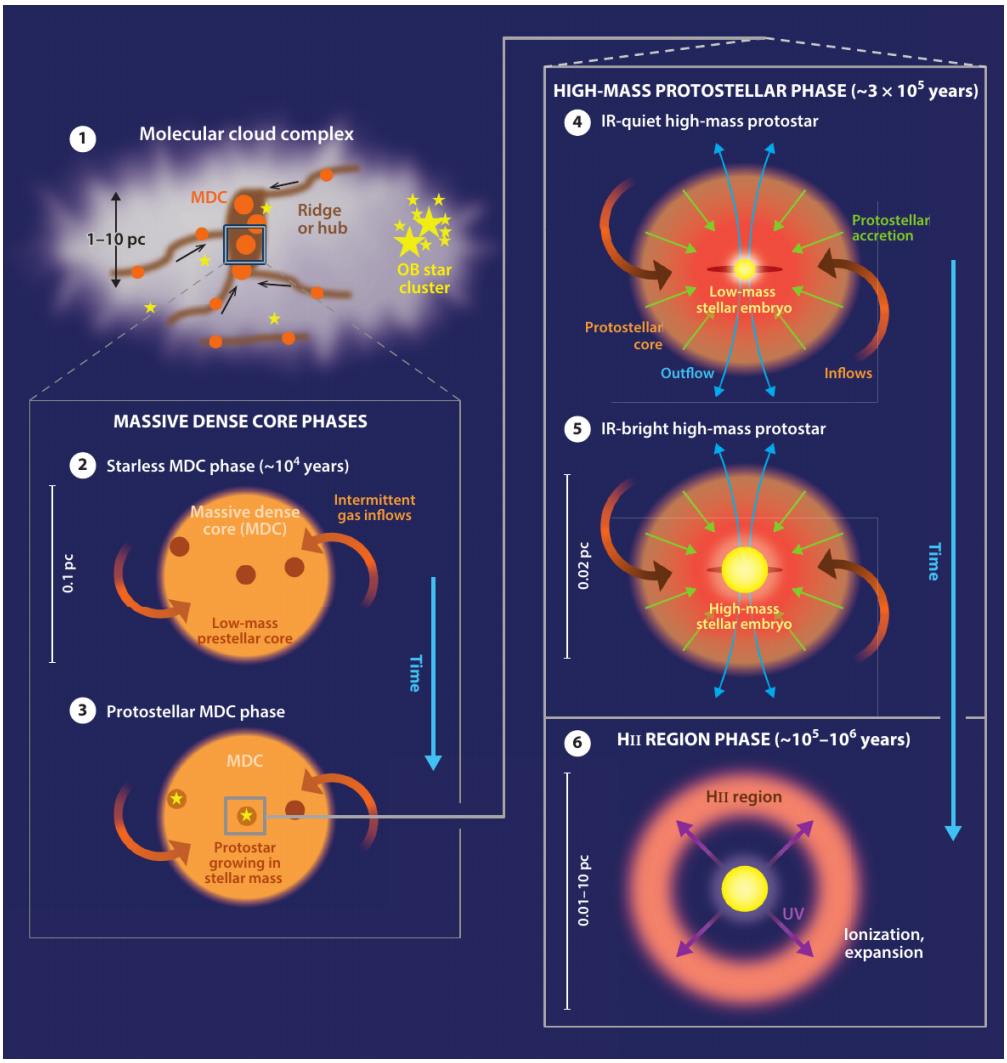

Figure 1.1: Schematic evolutionary diagram proposed for the formation of high-mass stars. (1) Massive filaments and spherical clumps, called ridges and hubs, host massive dense core (MDCs; 0.1 pc) forming high-mass stars. (2) During their starless phase, MDCs only harbor low-mass prestellar cores. (3) IR-quiet MDCs become protostellar when hosting a stellar embryo of low mass. The local, 0.02 pc, protostellar collapse is accompanied by the global, 0.1–1 pc, collapse of MDCs and ridges/hubs. (4) Protostellar envelopes feed on these gravitationally driven inflows, leading to the formation of high-mass protostars. The latter are IR-quiet as long as their stellar embryos remain low in mass. (5) High-mass protostars become IR-bright for stellar embryos with a mass larger than 8 $M_{\odot}$. (6) The main accretion phase terminates when the stellar UV field ionizes the protostellar envelope and an HII region develops. Image credits: Motte et al. (2018), Tigé et al. (2017).

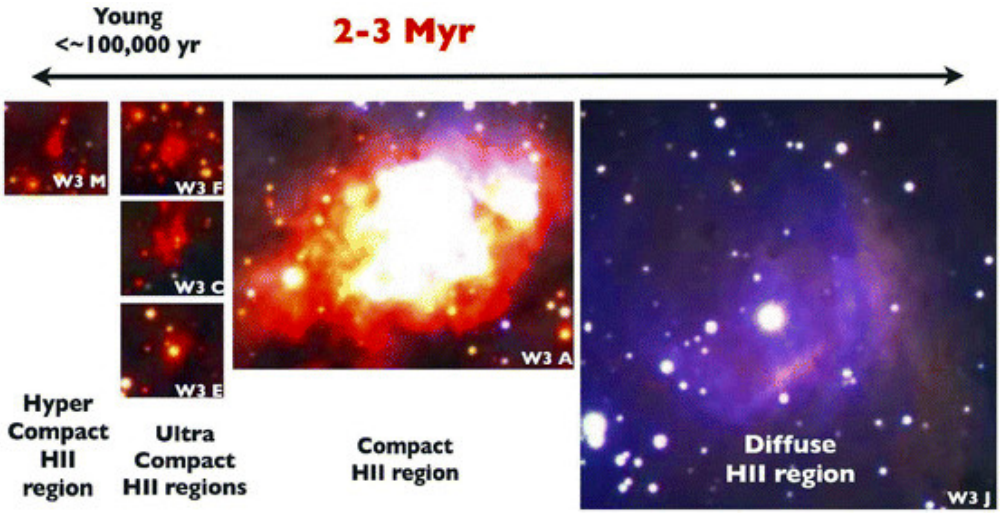

Figure 1.2: Near-infrared images of the different kinds of HII regions in W3 Main ordered from young to the more evolved regions. Image credits: Bik et al. (2014).

by the Infrared Astronomical Satellite (IRAS) point source catalogue and found UCHII regions, but also some sources in the earlier protostellar phase. These sources have been associated with dense gas detected through molecular lines or millimeter continuum wavelengths and, in the case of stellar embryos, absence or weak emission at centimeter wavelengths (e.g., Molinari et al. 2000; Sridharan et al. 2002; Faúndez et al. 2004).

In summary, sources in the last stages of high-mass stars formation can be observed over a large range of wavelengths: Radio continuum (millimeter and centimeter), IR, and visible. The framework of this thesis is a combination of very high-resolution observations at all these wavelengths that allows us to provide new evidence for these evolutionary stages.

1.4 Feedback and triggering from young stellar objects

There are several studies on the relation between high-mass star formation and their feedback effects at local and galactic scales (e.g., Mac Low and Klessen 2004; Ballesteros-Paredes et al.

Table 1.2: Physical parameters for different types of HII regions. Adapted from Kurtz (2005).

Class	Size pc	Density cm^{-3}	Emission Measure cm^{-6} pc	Ionized Mass $M_\odot$
Hypercompact	$\leqslant 0.05$	$\geqslant 10^6$	$\geqslant 10^{10}$	$\sim 10^{-3}$
Ultracompact	$\leqslant 0.1$	$\geqslant 10^4$	$\geqslant 10^7$	$\sim 10^{-2}$
Compact	$\leqslant 0.5$	$\geqslant 5 \times 10^3$	$\geqslant 10^7$	~ 1
Classical/diffuse	~ 10	~ 100	$\sim 10^2$	$\sim 10^5$

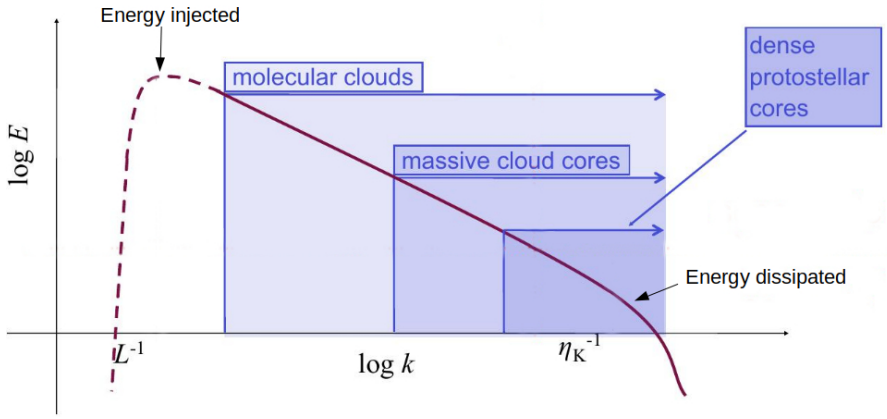

Figure 1.3: A cartoon picture of the turbulent energy spectrum. It shows how the kinetic energy, injected by supernovae or stellar winds, is carried by different wave numbers related to different cloud structures (sizes). Turbulence is driven on large scales size L and is dissipated on very small scales ν_k. Image credits: Adapted from Klessen (2011).

2007; Hennebelle and Falgarone 2012). Results from numerical simulations suggest that stellar feedback from massive stars may play an important role in generating turbulence within their parental molecular clouds (e.g., Zhang and Chevalier 2019; Krumholz et al. 2018; Ali et al. 2018; Kim et al. 2018; Shima et al. 2018). The ionizing radiation from high-mass stars feed the turbulent motion of the molecular gas and stimulate the collapse or the dissociation of them (e.g., Figure 1.3). In fact, the molecular clouds exhibit supersonic broad linewidths, which are interpreted as evidence for supersonic turbulence (e.g., Zuckerman and Evans 1974; Ballesteros-Paredes et al. 2007). Also, outflows and winds play an important role in producing turbulent motion in their surrounding material (e.g., Goicoechea et al. 2019; Offner and Chaban 2017; Tanaka et al. 2017; Dale 2015). Finally, there is evidence that radiation from massive stars can also trigger the formation of other stars (e.g., Elmegreen and Lada 1977; Kessel-Deynet and Burkert 2003).

Beside the interesting results that point to stellar feedback from massive stars as a generator of turbulent motion of their surrounding material, strong observational evidence is still needed. This thesis aims to provide such evidence through the characterization of the turbulent motions within molecular clouds that surround high-mass stars.

1.5 Motivation and outline

While there has been progress in the last years to identify individual stages of massive YSOs, a solid statistical basis is still missing. Here the following questions are addressed: (1) Under which conditions do YSOs form?, (2) Which characteristics do they have?, (3) How are YSOs linked to the turbulence of their parental molecular clouds, and (4) do these properties vary across the Milky Way? To answer them is essential to characterize the radio emission from YSOs. This information provides clues about the nature of them and their emission. However, how

to characterize the radio emission from YSOs and distinguish them from other radio sources?, moreover, once we know how to deal with this problem, how could we measure the interaction of YSOs and their surrounding molecular gas? Some of these issues can be addressed by statistical approaches.

To make progress on these questions with statistically significant samples, we used high angular resolution observations from far-infrared to (cm)millimeter wavelengths from Galaxy-wide surveys. We also used statistical tools to characterize the turbulence of the ionized and molecular gas that provide clues related to the energy injection scales, which can be compared with the scales of the main dynamical feedback from YSOs.

This thesis is organized as follows:

- Chapter 2 describes the methodology used to characterize the physical properties of radio emission from YSOs and the statistical tools to characterize the turbulent motion of their surrounding material.
- Chapter 3 presents a radio-wavelength study of the prominent NGC 6334 complex of star forming regions that contains sources in a variety of evolutionary phases.
- In Chapter 4 we apply the methodology to a large set of sources from the GLOSTAR survey. The analyzed emission is from highly active star-forming regions. We characterized the radio emission of hundreds of YSOs and we provide the physical properties of their radio emission.
- The Chapter 5 contains our study of turbulence due to stellar feedback effects. Here we are used a new statistical tools package mainly to analyze molecular gas from galactic surveys (SEDIGISM and W43 HERO-Program), but also optical lines from ionized gas (Orion nebula).
- The main findings and future applications of this thesis are summarized in Chapter 6. We provide a significant amount of new detections of YSOs, strong support for previous detections, and a new approach to relate the stellar radiation with dynamical properties like turbulent motion.

CHAPTER 2

Methodology

2.1 Observation at radio wavelengths

This thesis uses data mainly from radio wavelengths observations in the centimeter and millimeter regime. These kind of Radio Astronomy observations started in the early 1930s with the detection of an extraterrestrial signal reported by Karl Jansky[1], an engineer of Bell Telephone Laboratories. That discovery opened a new window for astronomical observations. The fundamental text books for radio astronomers includes *Tools of Radio Astronomy* by Wilson et al. (2012, sixth edition) and *Synthetic Imaging in Radio Astronomy* by Taylor et al. (1999). The following subsections are based on them.

2.1.1 The radio window

The atmosphere of the earth is transparent at some wavelength intervals. One such range is called the radio and (sub)millimeter window, and it extends from lower frequency $\sim$ 15 MHz ($\lambda \cong$ 20 m) to high frequency $\sim$ 600 GHz ($\lambda \cong$ 0.5 mm). The transparency varies with the weather, geographical location, altitude, and time (Figure 2.1). For example, radiation is partially absorbed by the atmosphere, due to rotational transitions of water (H_2O), at 22 GHz ($\lambda \cong$ 1.35 cm) and 183 GHz ($\lambda \cong$ 1.63 mm), and oxygen (O_2), at 60 GHz ($\lambda \cong$ 5 mm). Actually, water vapor is a determining factor for this opacity, but it is possible to extend the accessible frequency range by making radio observation from very high and/or dry sites. For example, the Atacama Pathfinder Experiment (APEX) submillimeter telescope is 5,100 meters above sea level in the Atacama Desert in Chile (Figure 2.2). The low frequency at about 30 MHz ($\lambda \cong$ 10 m), is limited by the ionosphere that reflects the radio waves and its transmission depends on the season and solar activity. Unfortunately, there are also other disturbances in the radio window produced by civil and military radio signals, so-called Radio Frequency Interference (RFI) that have been treated with international agreements to reserve small portions of the radio frequency range to radio astronomy studies exclusively.

[1] In radio astronomy it is common to see fluxes quoted in Jansky, where:1 Jy = 10^{-26} W m^{-2} Hz^{-1}

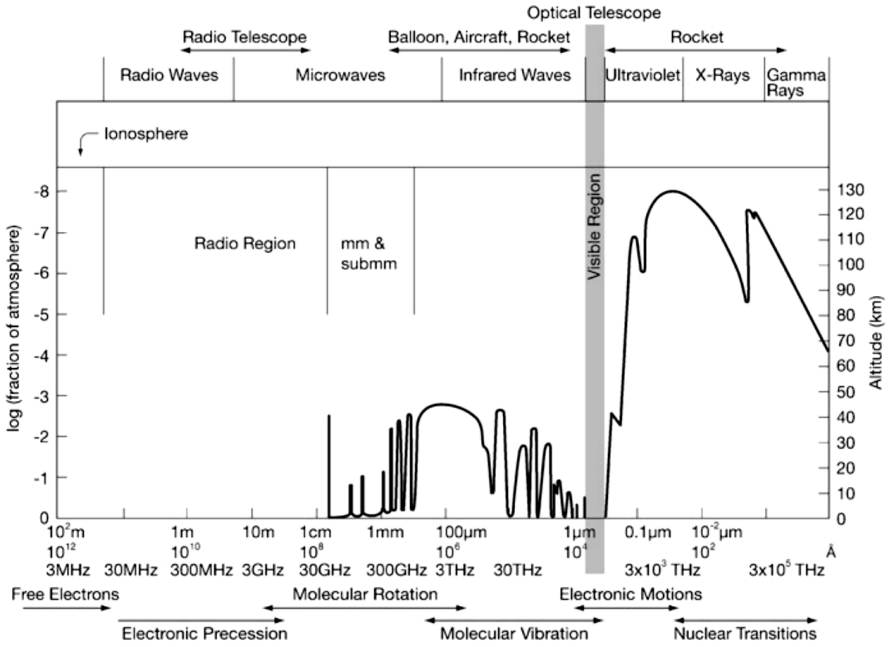

Figure 2.1: The transmission of the earth's atmosphere for electromagnetic radiation. The right hand vertical axis of this diagram gives the height in the atmosphere at which the radiation is attenuated by a factor 1/2. Image credits: Wilson et al. (2012).

Figure 2.2: *Letf*- The APEX (Atacama Pathfinder EXperiment) telescope. *Right* - The 30 m IRAM (Institut de RAdioastronomie Millimétrique) telescope. Credits: Sac Nicté Medina.

2.1.2 Single dish observations

The basic observations at radio wavelengths are performed with a parabolic dish (antenna), which is called a *single-dish telescope*. Radio telescopes measure the electromagnetic field of incoming radiation from a source. The electromagnetic waves are received, focused in a receiver or detector (feed), and converted in an amplified electric signal to be recorded and analyzed.

The *angular resolution* (Θ), the capacity to distinguish small details of an object or distinguish

also between two very close sources, of a single-dish telescope is dependent on the antenna diameter D and the observed wavelength λ as

$$\Theta \propto \frac{\lambda}{D} \tag{2.1}$$

When a radio antenna points to a position on the sky, it measures the power of the incoming signal. The *power pattern* (P) of the antenna describes the response of the antenna to a sources as a function of an angular distance (θ, ϕ) from the antenna axis. A classic example is in the left side of the Figure 2.3. The main beam, Ω_M, in polar coordinates of this pattern is given by:

$$\Omega_M = \int \int P(\theta, \phi) d\theta d\phi \tag{2.2}$$

where $P(\theta, \phi)$ is the power pattern as a function of the angular distances. The angular extent of the main beam is described by the *half power beam width* (HPBW), also knows a *full width of the half maximum* (FWHM). It is the angle between points of the main beam where the normalized power pattern falls to 1/2 of the maximum as is illustrated in the left side of the Figure 2.3. After detecting the arriving radiation, the antenna will measure a quantity called the *antenna temperature* T_A, which is a convolution of the brightness temperature (T_b) from a source with the beam pattern. It is defined as:

$$T_A = \frac{1}{2} A_e \int \int T_b(\theta, \phi) P(\theta, \phi) d\theta d\phi \tag{2.3}$$

where A_e is the effective collecting area of the antenna and $T_b(\theta, \phi)$ is the brightness temperature as a function of the angular distances. After that, the antenna temperature, assuming the Rayleigh-Jeans approximation, can be transformed to flux density, S_ν, as

$$S_\nu = \frac{2k}{A_e} T_A \tag{2.4}$$

where k is the Boltzmann constant. Finally, The raw observed data are calibrated with astronomical software that produce the final radio images to study. For single-dish radio astronomy, GILDAS is one of the most commonly used packages. It has been developed since 1983 and is being constantly updated by the Institute for Radio Astronomy at Millimeter wavelengths (IRAM) in Grenoble. Equation 2.1 implies that the larger the size of an antenna, the better the angular resolution. However, for technological reasons it is is difficult (and becomes very expensive) to built radio telescopes with arbitrarily large diameters. The next subsection will describe a solution to this problem implemented in 1960's and widely used by the radio astronomical community.

2.1.3 Radio interferometric observations

The method of *radio interferometry* is a brilliant solution to the problem of the modest angular resolution that is inherent to the long radio wavelengths (Eq. 2.1). A radio interferometer combines several antennas to work together as one big telescope. The resolution of an interferometer is equivalent to that of a single gigantic telescope with a diameter equal to the maximum separation of the antennas, therefore, interferometers can reach much higher resolution than a single-dish

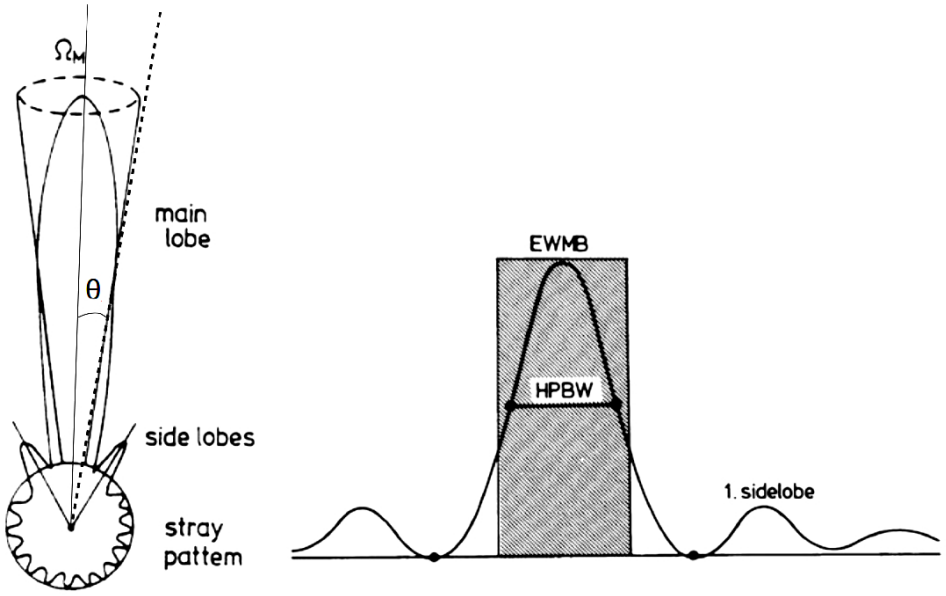

Figure 2.3: *Letf-* A polar power pattern showing the main beam, and near and far side lobes. The weaker far side lobes have been combined to form the stray pattern. *Right* - A sketch of the telescope beam-width, together with commonly used measurements of beam size for a one-dimensional power pattern. The EWMB is the equivalent width of the (full) half power beam width, while The HPBW is half power beam width. Image credits: Adopted from Wilson et al. (2012).

telescope. The most basic interferometer consists of two telescopes separated by a distance called *baseline* (b). The baseline can be considered as the diameter of a bigger telescope and replaces equation 2.1 to:

$$\Theta \propto \frac{\lambda}{b} \tag{2.5}$$

The pair of telescopes observers simultaneously the same astronomical source, in a direction defined by a vector ($\vec{s}$). The radiation, with frequency ν, is received in each telescope with a time delay called the *geometric delay* and defined as $\tau_g = \vec{b} \cdot \vec{s}/c$ with c as the light speed, because both signals follow different path lengths to arrive at each telescope (see Fig. 2.4). The signals $x(t)$ and $y(t)$ received at telescope 1 and 2, respectively, are of the form

$$x(t) = V_1 cos(2\pi\nu t) \tag{2.6}$$

$$y(t) = V_2 cos(2\pi\nu t + \tau_g) \tag{2.7}$$

where V_1, V_2 are the voltages. Both signals are send into a computer known as a *correlator* where the signals are coherently combined through a convolution :

$$R_{x,y}(\tau_g) = x(t) \circledast y(t) \tag{2.8}$$

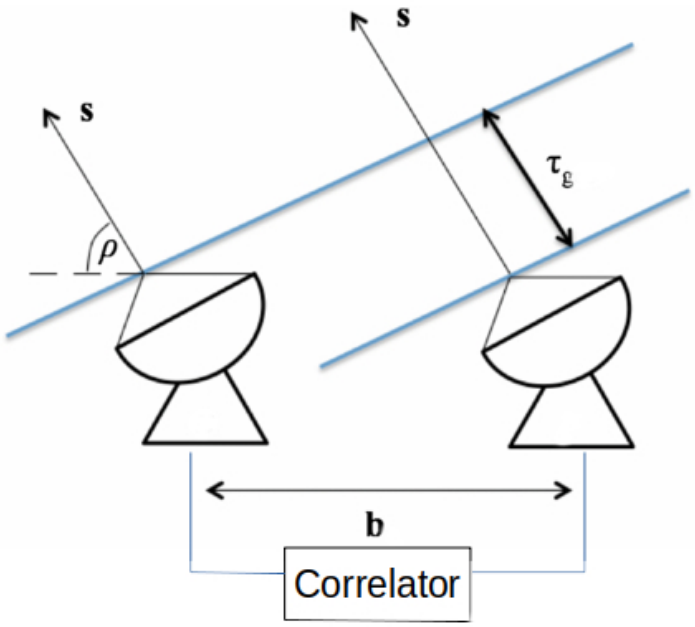

Figure 2.4: Diagram of a basic two element interferometer. Blue lines represent the incoming wave front of photons at times t and $t + \tau$. Image credits: Adopted from (Avison and George, 2012).

$$R_{x,y}(\tau_g) = \frac{V^2}{2}\Big[cos(4\pi\nu t - 2\pi\nu\tau_g) + cos(2\pi\nu\tau_g)\Big] \tag{2.9}$$

The correlator takes a time average long enough ($\Delta t \gg (2\pi\nu)^{-1}$) to remove the high-frequency term from the correlator response, $R_{x,y}$, and keep only the cosinusoidal form, R_{cos}, as:

$$R_{cos} = \frac{V^2}{2} sin(2\pi\nu\tau_g) \tag{2.10}$$

but the cosinusoidal response is not sufficient for recovering the total source function, the sinusoidal pattern, R_{sin}, is needed. It can be generated by introducing a 90°phase shift in one of the signals and the response is

$$R_{sin} = \frac{V^2}{2} cos(2\pi\nu\tau_g) \tag{2.11}$$

When R_{cos} and R_{sin} are combined, they produce the *complex visibilities*, V. This function is defined as:

$$V = R_{cos} - iR_{sin} = \mathscr{A}(s)\exp^{i\Phi} \tag{2.12}$$

where $\mathscr{A}(s) = \sqrt{R_{cos}^2 + R_{sin}^2}$ is the complex visibility amplitude and $\Phi = tan^{-1}(R_{sin}/R_{cos})$ is the visibility phase. If the radio brightness distribution of a source is given by $I_\nu(s)$ (in a solid angle

$d\Omega$), the power received by the interferometer is the visibility function ($V(s)$)

$$V(s) = \iint \mathscr{A}(s) I_\nu(s) \exp\left(-2\pi i \nu \vec{b} \cdot \vec{s}/c\right) d\Omega \tag{2.13}$$

The signal components of a source emanate from different points and the antennas need to integrate them over an angle $\vec{\sigma}$. Therefore, the visibility function is

$$V(\sigma) = \iint \mathscr{A}(\sigma) I_\nu(\sigma) \exp\left(-2\pi i \nu \vec{b} \cdot \vec{\sigma}/c\right) d\Omega \tag{2.14}$$

In 3D, this function is normally defined by the direction cosines (l, m, n) as in Figure 2.5. In this system, u points in the local east direction while v points north. The lm-plane represents a projection of the celestial sphere into a tangent plane while the uv-plane is always perpendicular to the direction of the source Therefore, the equation 2.14 becomes:

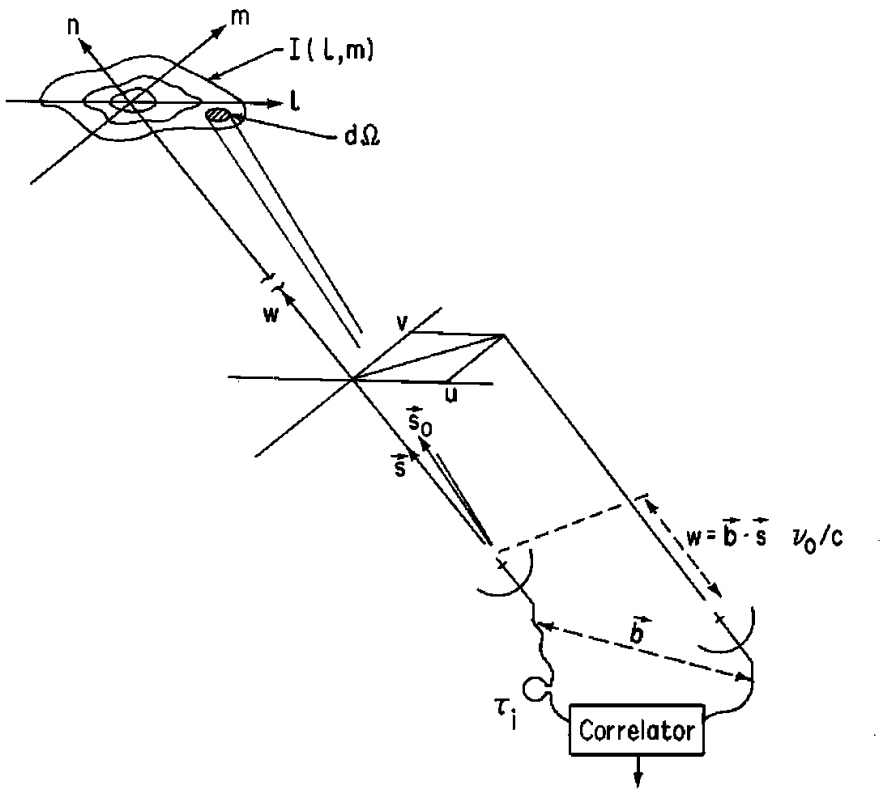

Figure 2.5: Geometry and coordinates for a detailed discussion of interferometry, leading to aperture synthesis. Image credits: Taylor et al. (1999).

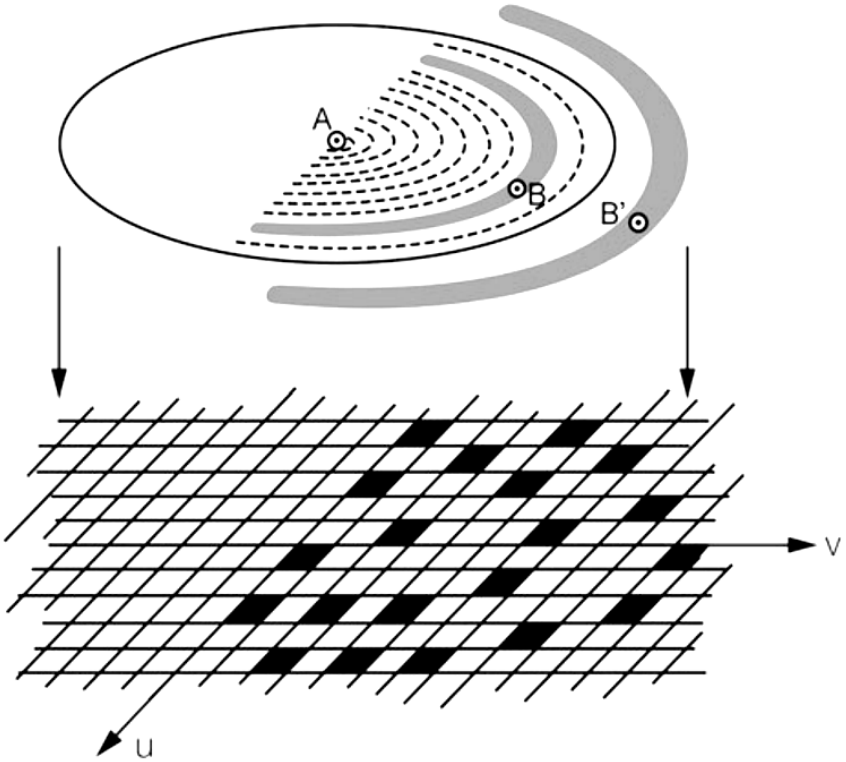

Figure 2.6: A sketch showing the locations in the uv-plane which are filled with correlated data from the outputs of three antennas located along an east-west baseline. The data are taken at discrete time intervals while tracking a source. The regions filled in black represent those where data was taken; there is no data for those no filled. The data are the correlation of antenna A with B and A with B'. The filled squares form parts of elliptical rings. The correlation of antenna B with B' produces the region close to the origin since the spacing between B and B' is small. The gaps between regions are exaggerated. These are meant to show that not all positions in the uv-plane have data. This missing data gives rise to a worse estimate of the equation 2.13. Image credits: Wilson et al. (2012).

Figure 2.7: *Letf*- Karl G. Jansky Very Large Array (VLA) in New Mexico, USA. *Right* - Atacama Large Millimiter Array (ALMA) in Atacama desert, Chile. Image credits: NRAO/ESO.

$$V(u,v,w) = \iint \mathscr{A}(l,m) I_\nu(l,m) \exp\left[-2\pi i \left(ul + vm + w\left(\sqrt{1-l^2-m^2} - 1 \right) \right) \right] \frac{dldm}{\sqrt{1-l^2-m^2}} \tag{2.15}$$

this equation express the intensity distribution of a source in specific point of the *uv*-plane, therefore, to have a better reconstruction of it, more samples in this plane are needed. This is achieved by increasing the number of antennas. The filling of the *uv*-plane is called *uv*-coverage and it is incomplete and limited by the positions and number of antennas. Figure 2.6 shows this phenomenon, not all positions in the *uv*-plane have data. It is clear from equations 2.15 that to increase the angular resolution and the sensitivity of an interferometer, several telescopes are needed. The first large antenna array was the Karl G. Jansky Very Large Array (VLA) in New Mexico, constructed in the USA around 1980. The VLA revolutionized radio astronomy increasing the sensitivity without precedents and was the base of the new generation of radio telescopes as the Atacama Large Millimiter Array (ALMA) (see Fig. 2.7).

The previous paragraphs explained the basic steps to produce a raw radio image, but they need a post-process analysis to obtain the final calibrate data. For interferometers this is commonly performed with the *Common Astronomy Software Applications* (CASA) package, which is capable to process both interferometric and single dish data and consists of a set of C++ tools bundled together under an iPython interface. CASA is developed by an international consortium of scientists based at the National Radio Astronomical Observatory (NRAO).

2.2 Source extraction and radio emission characterization

At its most basic, image analysis with the goal to identify, extract and validate discrete sources in large radio maps requires "manual" inspection. To address this task on an objective, unbiased basis sophisticate source extraction methods have been developed (e.g., Condon 1997; MIRIAD by Sault et al. 1995) but they are unsuited for large survey data. Recently, the `BLOBCAT` Gaussian fitting routine (Hales et al. 2012a) has demonstrated that is suitable to the general analysis of large survey data (Bihr et al. 2016; Wang et al. 2018), which makes it highly relevant to the work in the thesis due the large amount of data that will be used.

The `BLOBCAT` software package is a Python script that utilizes a flood fill algorithm to detect and identify blobs, or islands of pixels that represent sources, in two-dimensional astronomical radio-wavelength images. An overview of `BLOBCAT` is presented in Figure 2.8.

`BLOBCAT` produces an output catalogue containing 41 entries for each detected blob and other optional program outputs like the first blobs image in which all flooded pixels have been highlighted. To extract the blobs it used the algorithm from Murphy et al. (2007), which operates as follows:
(i) Locate all pixels in the signal-to-noise map that have values larger than threshold for detecting blobs (T_f), including those pixels that would meet this detection threshold if it were not for pixellation attenuation.
(ii) Form blobs about each of these pixels by 'flooding' adjacent pixels that have values larger than T_f.

(iii) For each isolated blob, perform bias corrections.
The area, $f(r, s)$, of the extracted blobs are described by a 2D elliptical Gaussian that satisfied the equation

$$f(r,s) = A \exp\left[-4ln(2)\left(\frac{r^2}{\psi_r^2} + \frac{s^2}{\psi_s^2}\right)\right] \tag{2.16}$$

where A is the peak signal-to-noise and ψ_r and ψ_s are major and minor FWHMs, respectively. The bias correction is applied on the integrated surface brightness, S_{int}^{OBS}, of each detected blob to have the unbiased brightness, S_{int}, by

$$S_{int} = \frac{S_{int}^{OBS}}{\left(erf\sqrt{-ln\frac{T_f}{A}}\right)^2}. \tag{2.17}$$

The inputs required to run `BLOBCAT` are a surface brightness radio-wavelength image, and optionally, a background rms noise map and a bandwidth smearing (Image that details the degree of chromatic aberration at any location within the surface brightness image). It should be also specifying three parameters: a background rms noise value, in case of no noise map was provided, a blob detection signal-to-noise threshold (T_d) and a cut-off signal-to-noise threshold for flooding (T_f). If position-dependent rather than spatially invariant blob detection thresholds are required, then the background rms noise map must be specified. The `SExtractor` package has been found to be reliable to generate noise maps from radio data (Bondi et al. 2003; Huynh et al. 2005). It determines the rms noise at each spatial pixel in an image by extracting the distribution of pixel values within a local mesh, iteratively clipping the most deviant values until convergence is reached at $\pm 3\sigma$ about the median. The local mesh size (in pixel^2), H_{mesh}, is calculated by

$$H_{mesh} = \frac{N_b}{\sqrt{12}} \frac{\Theta_{maj}\Theta_{min}}{4ln(2)}, \tag{2.18}$$

where Θ_{maj} and Θ_{min} are the major and minor axes, respectively, of the observational beam size and N_b is the independent resolution elements (beams) per mesh area that are required in order to reduce the uncertainty in estimates of local rms noise. It should be at least $N_b = 80$.

2.3 Spectral index calculation

Astrophysical sources mainly emit two types of radio emission, thermal and non-thermal. Example of the first is the bremsstrahlung radiation and for the latter is the synchrotron radiation (e.g., Wilson et al. 2012). While the intensity (energy) of thermal radiation increases with frequency, the intensity of non-thermal radiation usually decreases with it. This behaviour can be seen in Figure 2.9. Thermal bremsstrahlung radiation is produced by the electromagnetic energy of hot, ionized gases, e.g., from an HII region or planetary nebulae. This radiation is composed of photons that are emitted by free electrons when they are accelerated by nearby protons and change direction from their original paths. It is commonly referred as free-free emission because

the electron is unbound at the beginning and at the end of the interaction. On the other side, non-thermal synchrotron radiation is produced by charged particles spiralling around magnetic field lines at relativistic speeds and it is commonly detected in supernova remnants and the general diffuse ISM.

The most common tool to have clues about the emission nature, e.g. if the emission is thermal or non-thermal, from a source is the spectral index. For example, the bremsstrahlung radiation usually has spectral indices (α) between -0.1 and $+2$, while synchrotron radiation has negative spectral indices, typically between -1 and -0.5 (Condon 1984; Dzib et al. 2013b; Rodriguez et al. 2012). Therefore, the spectral index value is a fundamental tool in this thesis to analyze the emission nature of the high-mass stars at early stages. It is defined as:

$$S_\nu \propto \nu^\alpha, \tag{2.19}$$

where S_ν is the flux density and ν is the frequency. It is a linear fit (in logarithmic scale) of the measured flux density from the detected sources at different frequencies. In Table 2.1 we summarize the characteristic radiation of some type of sources.

2.4 Statistical tools for turbulence

2.4.1 Turbulence in Astronomy

Turbulence is developed in a fluid when its Reynolds number is larger than 1000, i.e., the velocity is dominant over dissipation. The Reynolds number depends upon the linear dimension, L, of the system, the coefficient of viscosity μ, the density ρ, and the velocity ν is the following manner:

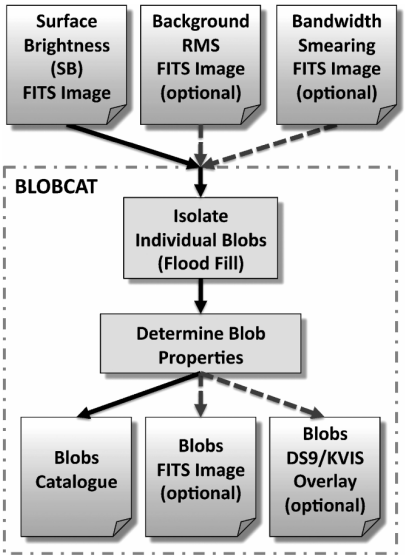

Figure 2.8: Overview of BLOBCAT from Hales et al. (2012a).

Table 2.1: Characteristics of some radio continuum sources. Adapted from Rodriguez et al. (2012).

Class of source	Emission Mechanism	Spectral Index
HII region	Free−free	~ 1
Proplyds	Free−free	~ -0.1
Jet	Free−free	~ 0.6
Spherical wind	Free−free	~ 0.6
Low-mass protostars	Gyrosynchrotron	-2 to $+2$

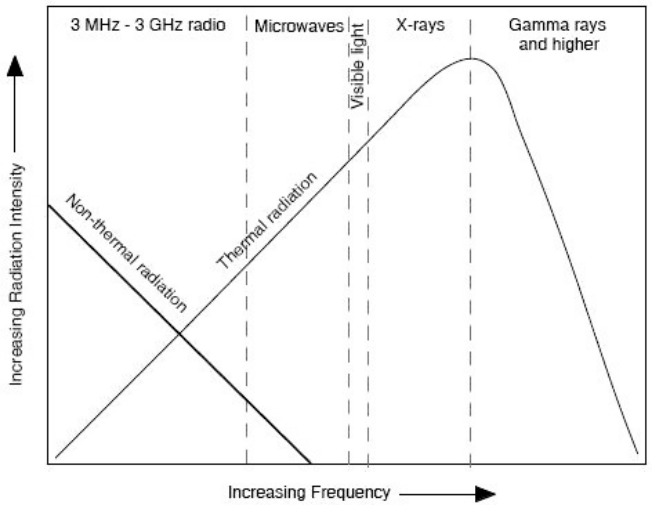

Figure 2.9: Behavior of thermal versus non-thermal radiation. At radio frequencies, the intensity (energy) of thermal radiation increases with frequency, while the intensity of non-thermal radiation usually decreases with frequency. Image credits: NRAO.

$$R = \frac{\rho v L}{\mu} \tag{2.20}$$

It was Chandrasekhar (1949) who first suggested that turbulence is ubiquitous in astrophysics and that it could be analyzed statistically via the spectrum of the velocity field, which expresses the correlations between instantaneous velocity components at all possible pairs of points in the medium. Turbulence is often described in terms of an energy spectrum $E(v)$ and an inertial range, i. e., the range between which the injection and the dissipation of energy is transferred at a constant rate. They are represented by a power-law relationship

$$E(v) \propto k^{\beta} \tag{2.21}$$

where k is the wavenumber related with the physical scales. For incompressible, homogeneous, isotropic, 3D turbulence (Kolmogorov 1941a), we have $\beta = -5/3$, while in the limit of high Mach number, shock-dominated turbulence in one dimension (Burgers 2013), the power law is $\beta = -2$.

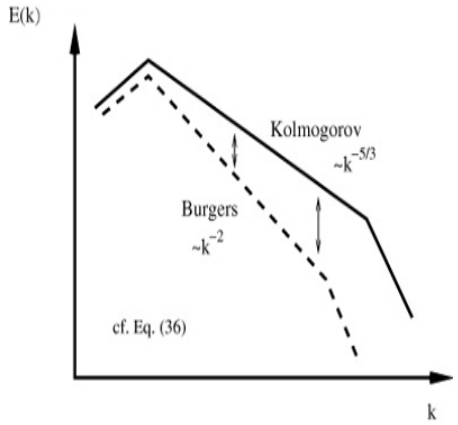

Figure 2.10: A sketch of the power spectrum from Kolmogorov versus Burgers turbulence model. The x-axes is wavenumber k, which is inversely proportional to the length scales, while the y-axes is the power spectrum $E(K)$. Image credits: Schleicher et al. (2013).

In Figure 2.10 both cases are shown.

The dynamical evolution of the Interstellar Medium (ISM) and many of its observational parameters cannot be understood without the turbulence. Several authors had studied the relation between turbulence and star formation at local and galactic scales (e.g., Mac Low and Klessen 2004; Ballesteros-Paredes et al. 2007; and Hennebelle and Falgarone 2012). One of the most discussed results from numerical simulations suggest that stellar feedback from stars may play a important role in generating turbulence within their parental molecular clouds (e.g., Zhang and Chevalier 2019; Krumholz et al. 2018; Ali et al. 2018; Kim et al. 2018; Shima et al. 2018), however, observational evidence is needed. Work in this thesis aims to provide such evidence through the characterization of turbulence motion within molecular clouds that surround high-mass stars that are known to provide strong stellar feedback, e.g., through strong stellar winds.

2.4.2 Statistical tools

The best approach to study the turbulent motion of the clouds surrounding high-mass stars is through the analysis of spectral line emission (or sometimes absorption) from atomic or molecular species in order to obtain information about the velocity distribution of gas along the line of sight (LOS). Mapping the velocity resolved intensity of the line emission towards all LOS of a cloud results in a position-position-velocity (PPV) data cube, which is essential for kinematic studies of ISM dynamics.

Modern turbulence analysis of the ISM consists in mathematical characterization of the PPV data cubes. For instance, the power spectrum, or turbulent energy spectrum, of the spectral line emission can be calculated and with this information it is possible to derive the scales on which the studied gas is turbulent. These scales give clues about the origin of the turbulence, and also the kind of turbulence through the β index as in the equation 2.21. Several techniques have proven to be useful for the analysis of emission line data (Medina et al., 2014) and are the main tools used in this thesis. One is using Second-order Structure Functions, second the Velocity Channel

Analysis technique, and the third is the Principal Component Analysis.

Second-order Structure Functions

The second-order structure function of the velocity centroids, line-of-sight velocity projected into the plane-of-the-sky, is defined as

$$S_2(\boldsymbol{l}) = \frac{\sum_{\rm pairs}[V_c(\mathbf{r}) - V_c(\mathbf{r}+\boldsymbol{l})]^2}{\sigma^2_{\rm vc} N(\boldsymbol{l})} \,. \tag{2.22}$$

In this definition, $\mathbf{r}$ is the two-dimensional position vector in the plane of the sky, while $\boldsymbol{l}$ is the lag, or separation vector. The normalization is by the number of pairs of points at each separation, $N(\boldsymbol{l})$, and the variance of centroid velocity fluctuations, $\sigma^2_{\rm vc}$, defined by

$$\sigma^2_{\rm vc} \equiv \frac{\sum_{\rm pixels}[V_c(\mathbf{r}) - \langle V_c\rangle]^2}{N} \,. \tag{2.23}$$

Here, $\langle V_c\rangle$ is the mean centroid velocity

$$\langle V_c\rangle \equiv \frac{\sum_{\rm pixels} V_c(\mathbf{r})}{N} \,. \tag{2.24}$$

Velocity Channel Analysis technique

The Velocity Channel Analysis (VCA) (Lazarian and Pogosyan 2000a) technique was developed to extract the individual contributions of density and velocity fluctiations from spectral line PPV data cubes. The cubes are analysed in terms of velocity channels, or slices, as a function of the velocity resolution used (δv).

When the velocity channel width of a PPV cube increases, the relative contribution from velocity fluctuations to the total intensity fluctuations decreases. This happens because the contributions from velocity fluctuations will be averaged out in broader velocity channels. VCA consists of obtaining the 2D power spectrum for each velocity channel and then averaging over all velocity channels for each PPV cube. As the width of the velocity channel increases, density fluctuations begin to dominate the emissivity over velocity fluctuations.

A channel is described as thick when the dispersion of turbulent velocities is less than the velocity channel width on the turbulence scale studied, otherwise the channel is thin. In the thickest velocity channels, we obtain only information about the density fluctuations, since the velocity information is averaged out. Conversely, the velocity fluctuations dominate in thin channels. Esquivel et al. (2003) stress that whether a channel in velocity space is considered thin or thick depends not only on the channel width $\delta v = (v_{max} - v_{min})/N$, where N is the number of channels, but also on the scale of the turbulence. Therefore, a velocity channel will remain thin up to wavenumber:

$$\kappa \leqslant 2\pi\left[\frac{1}{\sigma_L^2}(\delta v^2 + 2v_T^2)\right]^{-1/m} \tag{2.25}$$

where σ_L is the velocity dispersion over the scale L, V_T is the thermal width, and m is the velocity structure function index. The thermal width smears velocity fluctuations on smaller scales.

The Principal Component Analysis

PCA is mathematically defined as an orthogonal linear transformation that transforms the data to a new coordinate system such that the greatest variance by some projection of the data comes to lie on the first coordinate, the first principal component, the second greatest variance on the second coordinate, and so on (Jolliffe 1986). In spectroscopic imaging observations, this technique identifies differences in line profiles as they contribute to the variance of the data cube. Heyer and Schloerb (1997) used PCA to decompose spectral line imaging observations of molecular clouds. From their analysis, they calculated a relationship that describes the magnitude of velocity differences of line profiles and the spatial scale at which these differences occur within the image, proving that it is a method to identify kinematic variability within a target cloud.

A general description of the Principal Component Analysis (PCA) can be found in Brunt and Heyer (2002a) as follows; A spectroscopic image from an observation is composed by an ensemble of $n = N_x \times N_y$ spectra and p spectroscopic channels. The data cube can be written as $T(x_i, y_i, \upsilon_j) = T(r_i, \upsilon_j) = T_{ij}$, where $r_i = (x_i, y_i)$. The covariance matrix S_{ij} is

$$S_{jk} = \frac{1}{n} \sum_{i=1}^{n} T_{ij} T_{ik} \tag{2.26}$$

a set of eigenvectors, u_{lj}, and eigenvalues, are calculated from the equation

$$S\,u = \lambda u \tag{2.27}$$

where the eigenvalue, λ_l, corresponds to the amount of variance projected onto its corresponding eigenvector, u_l, in a l^{th} principal component. To spatially isolate the sources of variance contained in the l^{th} component, an eigenimage, $I^l(r_i)$, is constructed from the projected values of the data, T_{ij}, onto the eigenvector, u_{lj},

$$I^l(r_i) = \sum_{j=1}^{p} T_{ij} u_{lj}. \tag{2.28}$$

The characteristic velocity and the spatial scales over which these differences occur are calculated from the autocorrelation functions of the eigenvectors, $C^l{}_v(d\upsilon)$, and eigenimages, $C^l{}_I(\tau)$, respectively

$$C^l{}_v(d\upsilon) =< u^l(\upsilon) u^l(\upsilon + d\upsilon) > \tag{2.29}$$

$$C^l{}_I(\tau) =< I^l(r) I^l(r + d\tau) > \tag{2.30}$$

The characteristic velocity scale, $\delta\upsilon_l$, is therefore determined from the velocity lag at which $C^l{}_v(\delta\upsilon_l)/C^l{}_v(0) = e^{-1}$. The spatial correlation lengths along the cardinal directions, δx_1, δy_1, are derived from

$$\frac{C^{l}_{I0}(\delta x_1)}{C^{l}_{I0}(0)} = e^{-1} \tag{2.31}$$

$$\frac{C^{l}_{I0}(\delta y_1)}{C^{l}_{I0}(0)} = e^{-1} \tag{2.32}$$

where the characteristic spatial scale is defined as

$$L = \sqrt{\delta y_1^2 + \delta y_1^2} \tag{2.33}$$

The known PCA velocity statistics, α_{PCA}, is then obtained from the set of $\delta\upsilon$ and L pairs, which are larger than the respective spectral and pixel resolution limits and form a power-law relationship as

$$\delta\upsilon \propto L^{\alpha_{PCA}}. \tag{2.34}$$

CHAPTER 3

Characterization of compact radio sources in the NGC 6334 region

This chapter contains our first approach to characterize radio emission from a star forming region with high activity and diversity of evolutionary phases: The NGC 6334 complex. It is important to highlight that the performed data analysis (Sec. 3.3) makes use of an innovative methodology used for the first time in this region and produced the first systematic census of the compact radio sources in the NGC 6334D to F region.
This chapter is published in Vol. 610 of the Astronomy & Astrophysics journal as "The richness of compact radio sources in NGC 6334D to F" (Medina et al., 2018). Some changes in the format have been made to fit to the present publication. The Sects. 3.2, 3.5, and 3.8 are mainly contributions from the co-authors, who took charge of the corresponding research.

3.1 Background of the NGC 6334 region

The giant molecular cloud NGC 6334 is a complex with very active spots of massive star formation at different evolutionary stages (Persi and Tapia 2008). Located at the relative nearby distance of $1.34^{+0.15}_{-0.12}$ kpc ((Reid et al., 2014)) it is an ideal target for the study of the different phases of massive star formation and detailed analysis of its content of compact radio sources may provide strong clues on the phases to which they belong (see Figure 3.1).

Early radio maps with high resolution ($\sim 1''$) of NGC 6334 showed the existence of six strong radio sources which were named as sources NGC 6334A to F (Rodriguez et al., 1982, from now on they will be refer only with the alphabetic name). Source B is extragalactic (Moran et al. 1990, Bassani et al. 2005), while the others are compact and UCHII regions. This section focuses on the study of compact radio sources, including radio emission from YSOs, around regions D, E and F and their surroundings, including the region called NGC 6334I(N) (hereafter I(N)). These sources are located in the north-east portion of the cloud.

Briefly described, source D is an evolved HII region with a nearly circular shape of approximate radius of $75''$ (0.5 pc), centered on what appears to be one of its main ionizing early B type stars, 2MASS J17204800-3549191, reddened by about $A_V = 10$ (Straw et al. 1989). At its western edge, the expansion of the HII region seems to be halted by a dense dark cloud, on CXOU

172031.76-355111.4 (also known as 2MASSJ17204466-3549168 or NGC6334II-23), a luminous late O-type ionizing star, lies (Feigelson et al., 2009; Straw et al., 1989). This interaction appears to have triggered a second star formation stage in the region inside the dense dark cloud (Persi and Tapia, 2008). Regions E and F, widely studied at several wavelengths, are HII regions that contain many signs of star formation (Persi and Tapia, 2008 and references therein). The CHII region E shows an extended shell-like structure with a compact radio source at its center (Carral et al., 2002). Source F is a younger and complex UCHII region with a cometary shape and a radio flux of $\sim$ 3 Jy. This source and its surroundings are collectively known as NGC 6334I. Finally, the region I(N) is the youngest of all, as it has just started to form massive stars (Rodriguez et al., 2007; Hunter et al., 2006).

Figure 3.1: NGC 6334: The Cat's Paw Nebula. At $\sim$ 1.34 kpc (5,500 light years) distant, Cat's Paw is an emission nebula with an abundant red color that originates from the high amount of ionized hydrogen atoms. Image credits: George Varouhakis.

3.2 Observations and data reduction

We will use an archival observation of NGC 6334 obtained with the Karl G. Jansky Very Large Array (VLA) telescope of the NRAO[1] in the C-band (4 to 8 GHz) obtained as part of the project 10C-186. The data were taken on 7 July 2011, while the array was in A-configuration, its most

[1] The National Radio Astronomy Observatory is operated by Associated Universities Inc. under cooperative agreement with the National Science Foundation.

extended. Two sub-bands, each 1 GHz wide and centered at 5.0 and 7.1 GHz, respectively, were recorded simultaneously. The average frequency of the whole observation is 6.0 GHz. The quasars J1717−3342, J1924−2914 and J1331+3030, were used as the gain, bandpass, and flux calibrators, respectively. The total time spent on source was 84 minutes. First results of this observation were reported by Hunter et al. (2014) and Brogan et al. (2016), we point the reader to these papers for further details of the observation.

The data were edited, calibrated and imaged using the software CASA with the help of the VLA Calibration Pipeline. The image at 6.0 GHz was produced by combining the two sub-bands using a multi-frequency deconvolution software (e.g., Rau and Cornwell, 2011) and with a pixel size of $0\farcs06$. The resulting beamsize is $0\farcs67\times0\farcs19$; P.A. = $-2\fdg7$. The used weighting scheme was intermediate between natural and uniform (robust = 0, Briggs, 1995). Similar images were also produced for both sub-bands separately, with pixel sizes of $0\farcs06$ and $0\farcs04$ for 5.0 GHz and 7.1 GHz, respectively. The restoring beamsize for the 5.0 GHz image is $0\farcs91\times0\farcs25$; P.A. = $-2\fdg3$, and $0\farcs66\times0\farcs17$; P.A. = $-2\fdg8$ for the image at 7.1 GHz. All the images are corrected for the primary beam response.

3.3 Data analysis

3.3.1 Source extraction: BLOBCAT software

A source extraction was performed on the final image using the BLOBCAT software (Hales et al., 2012b). The BLOBCAT software was explained in section 2.2, to summarize, this software is a flood fill algorithm that extracts islands of agglomerated pixels (blobs) within locally varying noise. It is designed for two-dimensional input FITS images of surface brightness (SB). BLOBCAT makes improvements in the morphological assumptions and applies bias corrections to extract blob properties (Hales et al., 2012b). To run BLOBCAT it is also necessary to use the rms estimator algorithm implemented within the SExtractor package (Bertin and Arnouts, 1996, Holwerda, 2005a) to make a suitable noise map of the SB image. The used mesh size was of 60×60 pixels, calculated using equation 2.18, and Signal to Noise Ratio (SNR) = 5 as threshold for detecting blobs for the 6.0 GHz image. For the 5.0 and 7.1 GHz images the mesh size was 80×80 pixels and SNR = 3 as threshold, but in this case only sources that were also founded in the 6.0 GHz map were considered as real. The previous calculations were made following the derivations of Hales et al. (2012b).

3.3.2 False and background detections

The expected number of false detections in the final image is calculated using the complementary cumulative distribution function $\Phi(x) = 1 - \phi(x)$ where $\phi(x)$ is the cumulative distribution function. Assuming that the noise in our radio maps follows a Gaussian distribution

$$\phi(x) = \frac{1}{2}\left[1 + erf\left(\frac{x}{\sqrt{2}}\right)\right] \tag{3.1}$$

where erf is the error function given by

$$erf(x) = \frac{1}{\sqrt{\pi}} \int_{-x}^{x} e^{-t^2} dt. \tag{3.2}$$

$\Phi(x)$ is the probability that a value of a standard normal random variable X will exceed an x level. So, the probability that any independent pixel (synthesized beam) will have a value up to 5σ is $\Phi(5) \approx 3 \times 10^{-7}$. In consequence, it is expected a total of 1 source above 5σ in our 6 GHz maps, and conclude that essentially all our sources catalogued in the region are real. In consequence, the sources above 5σ at 6.0 GHz are trustworthy. Even so, a visual inspection is also done of all these sources to confirm their detection. The artifacts located close to the edge of the image are excluded.

Using equation A11 from Anglada et al. (1998) the expected number of background extragalactic sources in the imaged area with flux densities above 50 μJy is 7±3. This previously computed number only reflects an upper limit because the emission of the extended sources affects the noise distribution and this changes the value of the expected background sources. Most of the detected compact radio sources are Galactic objects and most probably related to the NGC 6334 complex.

3.3.3 Spectral index calculations

In order to compute the spectral index (α; $S_\nu \propto \nu^\alpha$) and have clues about the emission nature of the radio sources (see section 2.3), we measured the flux density of the detected sources in the 5.0 GHz and 7.1 GHz maps to calculated the slope between both points. The error was calculated by using the standard error propagation theory. As the field of view of the map at 7.1 GHz is smaller than at 5.0 GHz, we could not calculate the spectral index for some sources that lie outside the edges of the 7.1 GHz image. Additionally, some sources were detected in one band but not in the other, in those cases we just calculate a limit for α. The spectral index for each individual source is shown in Appendix A.

3.3.4 Literature search

Using the SIMBAD database we searched for counterparts of detected radio sources. Inside a radius of $0\farcs5$ from the VLA position, we found 17 radio sources with counterparts at different wavelengths and are shown in Appendix A. Additionally, the source SSTU J172053.96-3545.6 is at an angular distance of $0\farcs9$ from VLA J172054.06-354548.4. This shift is larger than the combined position errors of both telescopes (pointing accuracy for IRAC is $\sim 0\farcs5$) and indicates that these sources are not the same object, but we cannot discard that they may be related (e.g., a binary system). Finally, source [S2000e] SM6 is at an angular distance from source VLA J172053.26-354305.7 of $\sim 1\farcs2$, this agrees within the position error of $2''$ for the millimeter source (Sandell, 2000). To look for more infrared counterparts we perform a more detailed search, that is described in the next section.

3.4 Results

3.4.1 Radio sources

We obtain an image of $10' \times 10'$, which is displayed in Figure 3.2, combining the two observed sub-bands. The noise level is position dependent and produces the following two effects. The first is that the noise increases at the edges of the image, which is expected from the Gaussian primary beam pattern. The second is due to the imperfect sampling of the UV-space and it mainly affects areas around the extended strong emission. Thus, the noise level is close to 50 μJy near the HII regions, but only about 8 μJy in areas free of extended emission and not far from the center of the image. A similar effect is present in the Orion observations of Forbrich et al. (2016).

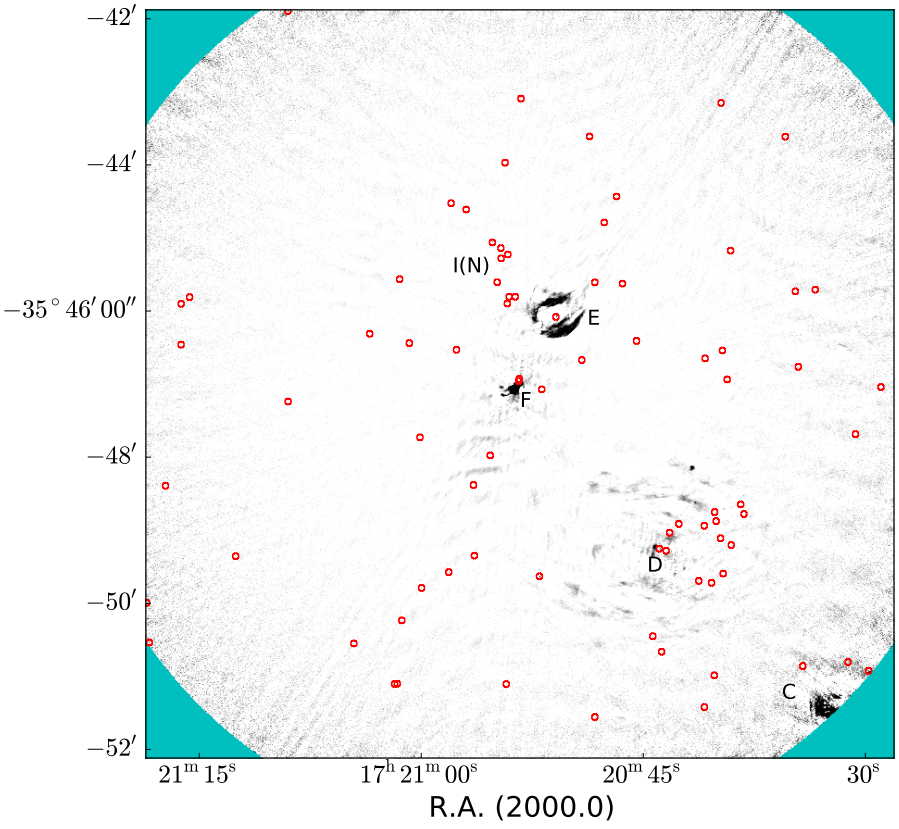

Figure 3.2: VLA image of NGC 6334E to F and I(N). Small circles indicate the position of the detected compact sources.

In Figure 3.2, the UCHII region F and CHII region E are immediately appreciated, while only a fraction of the extended emission of source D is recovered. Only a small portion of region C falls inside the primary beam of this observation. Additional to the extended emission of the HII

regions, a total of 83 compact[2] radio sources were also detected (the complete list is in Appendix A), including those previously reported in the E, I, and I(N) regions. The compact sources cannot be easily appreciated in this large field figure and they are represented by small red circles. The astrometric accuracy for the positions is better than $0''.1$, and we have used the positions of the sources to name them according to the IAU nomenclature.

Region D, presented in Figure 3.3, contains a significant fraction of all of the detected compact radio sources. Also, at the north side of this region there are two cometary shaped radio sources and at its center a double source. All of them, the compact radio sources, the cometary radio sources and the double radio sources, are reported here for the first time.

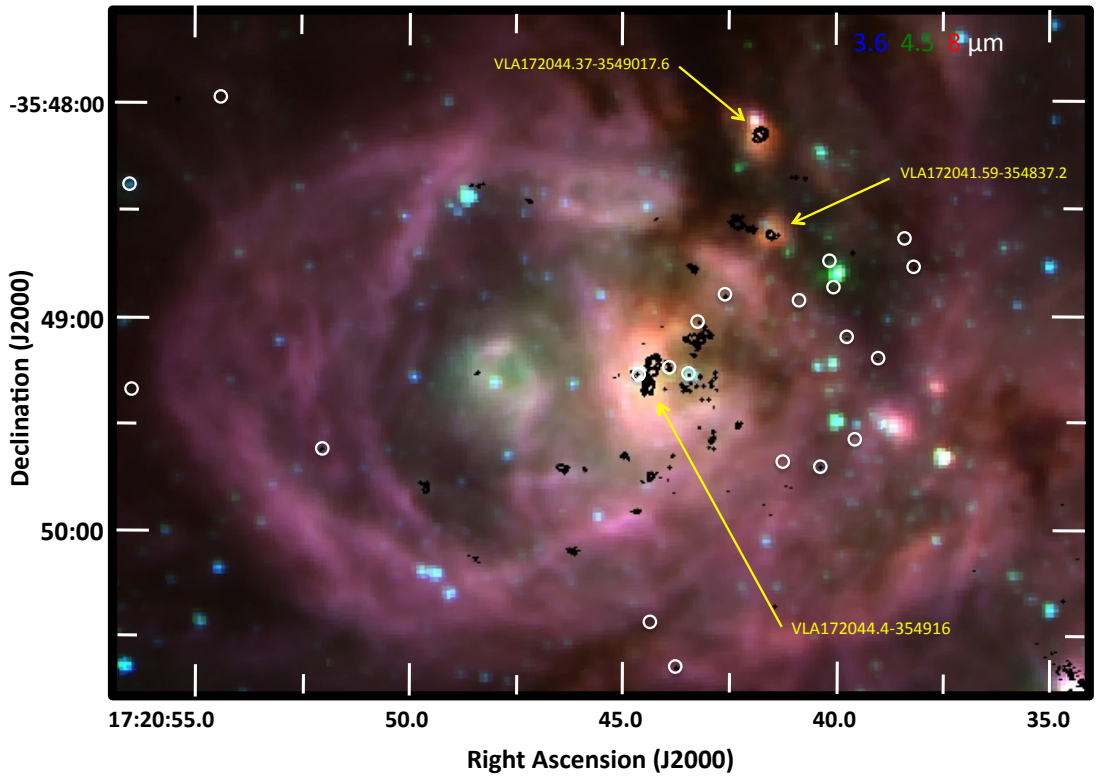

Figure 3.3: Composite SPITZER/GLIMPSE infrared image of NGC 6334D. Small circles indicate the position of the detected compact radio sources. Contours trace the radio continuum image at 6.0 GHz, and the contour levels are at 90, 180, 300, 450, 750, and 1500 μJy/beam. Slightly extended radio sources are indicated.

[2] Compact sources are defined here as source whose deconvolved sizes are similar to, or smaller than the synthesized beam.

3.5 Infrared counterparts

We use the source catalog from the *Spitzer* space mission as well as published near- and mid-IR photometry data by Willis et al. (2013) and Tapia et al. (1996) to search for infrared counterparts of our compact radio sources. We complemented the search with unpublished JHK_s photometric data from M. Tapia (in preparation). Defining reliable criteria for assigning a positive infrared counterpart to a compact radio source is not straightforward, as we are dealing with several infrared sets of infrared photometric measurements, namely from *Spitzer* images in the mid-IR and from ground-based observations with three different telescopes (and set-ups) in the near-IR. For the present work, we cross-checked the coordinates of the VLA compact sources with those from *Spitzer* and also from ground-based images. We selected those with coordinates coinciding (in all wavelength ranges) within $0\farcs9$ or less to obtain a list of candidate counterparts. We then examined by eye each source on all available individual images (i.e., each wavelength) and checked for the consistency of the corresponding flux measurements. The mean differences in the radio, mid- and near-IR source positions for the 27 counterparts were -$0\farcs07$ in right ascension and +$0\farcs07$ in declination, with standard deviations of $0\farcs44$ and $0\farcs30$, respectively. In all, no systematic coordinate offsets were found in the (small) area covered by this survey.

From the 83 VLA sources in Appendix A, only 27 IR counterparts were found. Interestingly, 10 of these infrared sources are inside the dark cloud in region D. The ground-based near-IR and *Spitzer*/IRAC mid-IR photometry of all these sources are listed in Table 3.1. The diagnostic two-color and color-magnitude diagrams are presented in Figs. 3.4, 3.5, 3.6, and 3.7. The $J-H$ versus $H-K_s$ and the $H-K_s$ versus K_s-[3.6] diagrams are accurate tools for discriminating reddened photospheres (those lying along the reddening vectors) from stars with disks (i.e. near-IR excesses). The latter stars would lie shifted towards redder colors in these diagrams. The amount of dust extinction (i.e., the value of A_V along the line of sight) for the former set of stars, is determined by the color-excess indices, under a "standard" reddening law, represented by the reddening vectors. References for the intrinsic colors and reddening law assumed for determining these parameters are given in the figure captions.

The color-magnitude plot K_s versus $H-K_s$, on the other hand, is the best tool for estimating approximate spectral types and intra-cloud extinction values for embedded stellar sources located at the distance of the star formation complex (d = 1.34 kpc and foreground value of A_V = 1.0 in this case). Finally, the IRAC two-colour magnitude [3.6]-[4.5] versus [4.5]-[5.8] diagram provides a simple diagnostics for classifying the evolutionary status of YSOs and of emission-line-dominated regions (mainly Polycyclic Aromatic Hydrocarbons, PAHs, or shocked molecular hydrogen). This is described in detail by Ybarra et al. (2014) and references therein. The combined results for these analyses in terms of the derived properties of a number of individual sources are listed in the last column of Table 2, where we also indicate whether it was detected as an X-ray source (within $0\farcs6$) by Feigelson et al. (2009).

3.6 Discussion

To define the nature of the radio emission of the compact sources, we need information on the different characteristics (α, polarization, time variability). However we are only able to do a rough

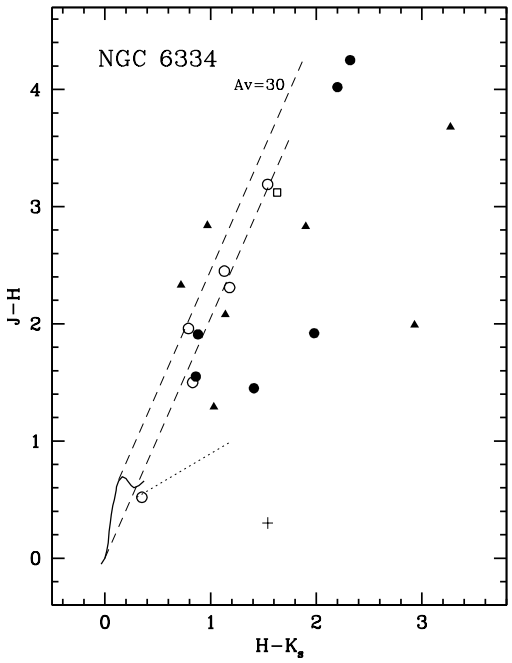

Figure 3.4: $J-H$ versus $H-K_s$ diagram of the near-IR counterparts with measurements in the three bands. Solid circles are sources in the dark cloud west of the HII region D. Solid triangles correspond to sources within the limits of CNN. Open squares are in region I(N). Open circles are for sources in the rest of the observed field. The solid line marks the locus of the main sequence (Koornneef 1983), the dashed lines delineate the reddening band for all main sequence star and giant stars (Rieke and Lebofsky, 1985). The small plus sign near the bottom of the plot illustrates the maximum photometric errors.

measure of the spectral index, which only gives clues on the emission mechanism. While thermal free-free radio emission has spectral indices with values $-0.1 \leq \alpha \leq +2.0$, gyrosynchrotron emission has values in the range $-2.0 \leq \alpha \leq +2.0$, and optically-thin synchrotron emission from wind collision regions has values $\alpha \sim -0.7$ (Rodriguez et al., 2012).

3.6.1 Region D

Compact sources

Although the reported compact radio sources are spread over the entire observed area, there is a group of 15 objects, reported here for the first time, that is well concentrated (within a radius of 0.3 pc) in the dark cloud on the western edge of region D. Of these, 73% (11 sources) have unresolved infrared counterparts (see Fig. 3.3) and all but 3 are X-ray emitters (Feigelson et al. 2009). In the first parts of Appendix A and Table 3.1 we list the observational data of the compact sources in region D that we now focus on.

The clustering of compact radio sources clearly coincides with the densest part of the dark cloud, where one would suspect to have the latest stage of star formation in the region. From the near-IR colors, we can distinguish only four stars that have a late-O or early-B spectral

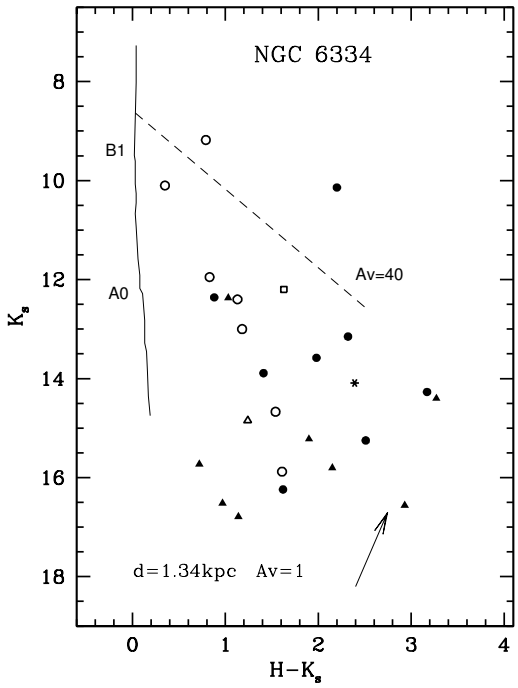

Figure 3.5: K_s versus $H-K_s$ diagram of the near-IR counterparts with measurements in the H and K_s bands. The open triangle refers to Mir-4 in DNS and the rest of the symbols are as in Fig. 3.4. For reference, the almost vertical solid line delineates the zero-age main sequence (ZAMS; Drilling and Landolt, 2000) for d = 1.34 kpc and A_V = 1.0. The dashed lines are the reddening vectors of length A_V = 40 for B0 ZAMS stars. The arrow represents the average slope of the near-IR emission excess caused by discs around YSOs, as determined by López-Chico and Salas (2007).

types, while the rest are less massive. Two of these three massive stars have a negative spectral index, and thus their radio emission may originate in wind collision regions. The majority of the remaining sources (eight sources) have negative spectral indices (non-thermal) values and only three are positive. The association of these sources with X-ray emission is compatible with a non-thermal origin for the radio emission, but there are a few cases where the spectral index is positive in spite of the presence of an X-ray source (Dzib et al., 2013a). As the sources are compact and likely associated with the star forming region, an attractive interpretation is that they are magnetically active low mass YSOs with gyrosynchrotron radio emission. However, the errors are large and this will have to be confirmed with multi-epoch monitoring to measure their flux variability, as nonthermal low mass stars tend to be very variable on scales of days (Andre, 1996). These future observations will also help to obtain a better estimate of their spectral indices.

It is worth highlighting that in the HII region associated with the Orion core (at d≃400 pc; Menten et al. 2007; Kounkel et al. 2017), there is a significant population of YSOs that produce radio emission (e.g. Forbrich et al. 2016, Zapata et al. 2004). In order to compare with region D, if the Orion core were located at 1.34 kpc, the distance of the NGC 6334 complex, the flux density of the 556 compact sources detected in Forbrich et al. (2016) would be 11.2 times lower. Considering 50 μJy as the detection threshold, only 47 compact sources from Forbrich et al.

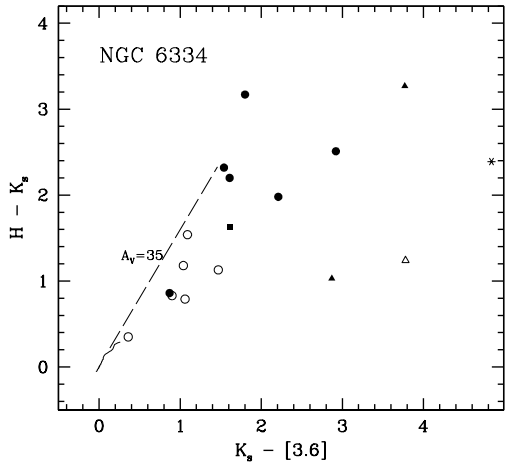

Figure 3.6: $H - K_s$ versus $K_s - [3.6]$ of the IR-counterparts with measurements in the H, K and IRAC channel bands. the solid square corresponds to the central C-HII region E, the asterisk to source #43 in region F. The rest of the symbols are as in Fig. 3.4 and 3.5. The solid line close to the origin represents the locus of the main sequence (Koornneef, 1983) and the dashed line represents the reddening vector of length $A_V = 35$ (Tapia, 1981).

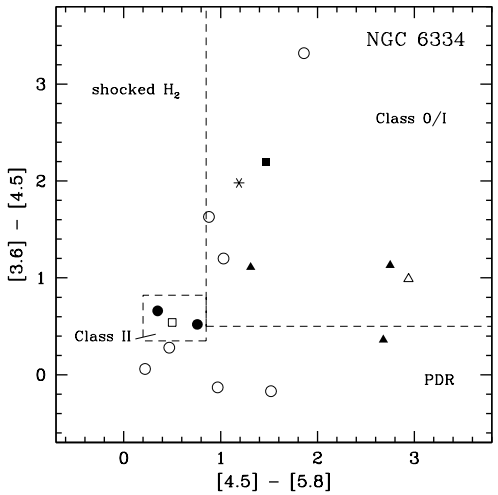

Figure 3.7: [3.6] - [4.5] versus [4.5] - [5.8] diagram of the IR counterparts measured in the three IRAC bands. Symbols are as in Figs. 3.4 and 3.6. The dashed rectangles mark the locii of the Class II and Class 0/I sources and the labels "shocked H_2" and "PDR" mark, respectively, the areas occupied by shocked regions emitting molecular hydrogen lines and PAH-emission-dominated photodissociation regions (Ybarra et al. 2014).

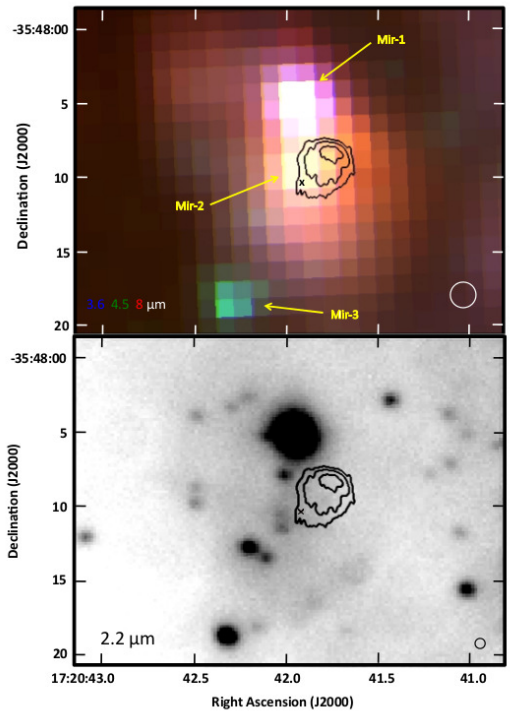

Figure 3.8: Top: Composite color image of the infrared nebula coincident with VLA172041.75-3548082 (CNN) in the IRAC bands centered at 3.6 (blue), 4.5 (green) and 8 μm (red). Superposed in black are the 6.0 GHz contours (levels are the same as Fig. 3.3) with the small cross marking the position of the compact source. The three brightest mid-IR unresolved sources are labeled (Table 3.2). The white circle represents the mean resolution of the IRAC images. Bottom: Same as 7–Top, showing a higher-resolution (0.7″) 2.2 um image taken with the DuPont telescope at Las Campanas Observatory (Tapia et al., in preparation).

(2016) could be detected. We are only detecting 14 compact sources, or about one third of the expectation based on the Orion population. This is consistent with other similar comparisons (e.g., Masqué et al. 2017), which may indicate that the Orion core may be richer in radio sources than other similar regions. Also, our images are highly contaminated by the extended emission making it difficult to identify all compact sources. Finally, there may be more sources below our detection threshold but we need deeper radio observations to clarify this point.

Cometary Nebula North (CNN) = VLA J172041.75-354808.2

Close to the north-western edge of the expanding HII region D, we discovered an extended radio source with a cometary structure. From now on, we will refer to this source as CNN (for Cometary Nebula North). Its flux density at 6.0 GHz is 18.4±0.1 mJy with a peak flux of 385±12 μJy bm^{-1}. The position of its peak flux is R.A.=$17^{\rm h}20^{\rm m}41\overset{\rm s}{.}75$; Dec.= $-35^\circ48'08\overset{''}{.}2$.

This peak of the extended radio emission reported here is at the center of a mid-IR nebulosity with an ovoid shape of size around 15″. It is relatively bright in the 4.5, 5.8 and 8 μm *Spitzer*/IRAC

images, as shown in Fig. 3.8–Top. Although their spatial resolution (1″.5 to 2″.0) is much worse than that obtained with the VLA, a similar morphology of the diffuse emission is evident. The mid-IR structure is complicated by the presence of at least three bright, unresolved mid-IR sources (Mir-1, Mir-2 and Mir-3), most likely of protostellar nature embedded in the nebulosity. Fig. 3.8–Bottom shows the same field at 2.2 μm as observed in excellent seeing conditions ($\sim$ 0″.55) with the 2.5-m DuPont telescope at Las Campanas Observatory (Tapia, Persi & Roth, in preparation). In addition to the mid-IR sources, there are a dozen near-IR stars detected within the nebula. Comparison with the surrounding field shows that at least 60% of them must be embedded in it. IRAC and *JHK* photometry of these sources are reported in Table 3.2 and their colors are plotted in Figs. 3, 4, 5 and 6.

The nature of the IR sources in CNN can be deduced from the multi-wavelength photometry. From the nebula-subtracted fluxes of sources Mir-1, Mir-2 and Mir-3, we conclude that they are Class I young stellar objects with spectral types earlier than A and each with quite different characteristics. The notes in column 9 of Table 3.2 summarize the results. Interestingly, in the cometary nebulae there is another emission peak evident in the radio maps at the three frequencies (see Fig. 3.9) at the position R.A.=$17^{\rm h}20^{\rm m}41.^{\rm s}93$; Dec.= $-35°48'10''.5$. This position is consistent, within errors, with the position of source Mir-2 and we suggest that it may be its radio counterpart.

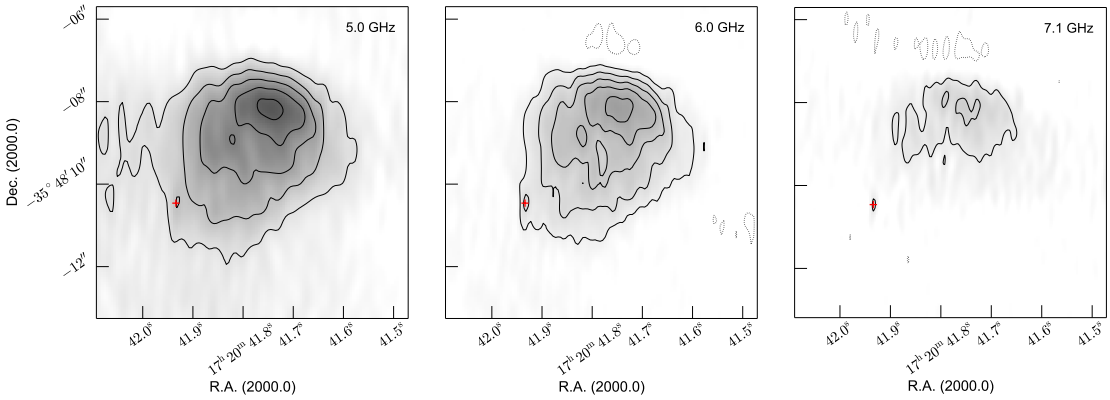

Figure 3.9: Radio emission at the different frequencies from the cometary source close to region D. The noise levels around the source at each frequency are 25 μJy, 15 μJy and 19 μJy for the 5.0 GHz, 6.0 GHz and 7.1 GHz maps, respectively. The contour levels are -3, 5,10, 15, 20 and 25 times the noise level on each map. The red cross indicates the position of a source that is present in the three maps and may be related to Mir-2.

Concerning the diffuse, nebular emission, from the present images, we attempted to measure nebular fluxes at several IR wavelengths. Because of many limitations (poor and very variable resolutions, presence of point-like sources, etc.) we found it impossible to deduce total fluxes reliably. Nevertheless, by integrating the near- and mid-IR flux densities that are well-derived from the ground-based and *Spitzer* observations and extrapolate them into the far-IR, we can estimate a lower limit to the total IR luminosity of the nebulosity to be $\sim 10^3 L_\odot$. Undoubtedly, this arises from thermal emission of warm dust.

Thus we will assume that the CNN source is an HII region, surrounded by a dusty envelope,

and derive its properties under that assumption. At a frequency of 6.0 GHz, we derive[3] a brightness temperature of 44 K, an electron density of $4.8{\times}10^{3}$ cm^{-3}, an emission measure of 0.6×10^{6} cm^{-6} pc, an ionized mass of $8{\times}10^{-3}$ M$_{\odot}$, and a flux of ionizing photons of $1.4{\times}10^{46}$ s^{-1} assuming a circular shape with a radius of $2'' = 0.013$ pc, and an electron temperature of $T_e = 10^4$ K. These values are consistent with an UCHII region being photoionized by a B0.5 ZAMS star (Kurtz et al. 1994, Panagia 1973). This is consistent with the approximated spectral types of sources Mir-1, Mir-2 and Mir-3.

Cometary Nebula South (CNS) = VLA J172041.59-354837.2

As can be seen in Fig. 3.3, a second small mid-IR nebula was found about 27″ south of CNN (hereafter, we will refer to this source as CNS for Cometary Nebula South). Both nebulosities have similar mid- and far-IR colors implying matching dust temperatures, though the integrated Herschel flux at 70 μm for CNS is four times fainter than that from CNN. Unfortunately, no photometry could be obtained at longer wavelengths and, thus, no reliable dust temperature can be derived. CNS has at its center a compact near- and mid-IR source (Mir-4 in Fig. 9 and Table 3). The IR photometry of this source suggests that this is an intermediate luminosity Class I YSO with $A_V \simeq 13-16$. This object was also detected in X-rays by Feigelson et al. (2009). At the same position, our 6.0 GHz image shows the presence of a small, roundish radio source with a diameter of around 2″. Its total flux density at 6.0 GHz is 4.5±0.4 mJy. As for CNN, the presence of warm dust also indicates that the radio emission of CNS also traces ionized gas. The derived parameter in this case are a brightness temperature of 39 K, an electron density of $6.2{\times}10^{3}$ cm^{-3}, an emission measure of 0.5×10^{6} cm^{-6} pc, an ionized mass of $1{\times}10^{-3}$ M$_{\odot}$, and a flux of ionizing photons of $3.0{\times}10^{45}$ s^{-1}, which suggests that CNS is being photoionized by a B1 star (Panagia 1973).

It should be noted that the neighboring bright star that appears "blue" in the mid-IR IRAC image (Fig. 3.10) is, given its IR colors, a foreground star unrelated to CNS.

Double Nebula Source (DNS) = VLA J172044.4-354917

Most intriguing is the extended double radio source VLA J172044.47-3549017 (hereafter DNS for Double Nebula Source), located almost at the center of the radio HII region D (e.g. the 1.6 GHz map by Brooks and Whiteoak 2001). This source is surrounded by three radio compact sources (VLA 13, VLA 14 and VLA 15) with IR counterparts, see Fig. 3.11. Their IR counterparts indicate that they are massive stars with spectral types from late to early-B.

The nature of the double radio source is unknown. As can be seen in Fig. 3.2 and Fig. 3.11, there is a lot of diffuse emission in region D. Thus, we speculate that DNS is gas ionized by the above mentioned three massive stars.

To test this hypothesis we analyze additional VLA archive data. The observations were made on 2013 July 25 in L (1 to 2 GHz) band under project 13A-448. The array was in the C configuration. The data were calibrated following the standard CASA procedures. To obtain the best angular resolution possible an image was made using the spectral window with the highest frequency,

[3] We have used the basic equations of brightness temperature, emission measure, electron density, and ionizing photon rate (e.g., Masqué et al. 2017).

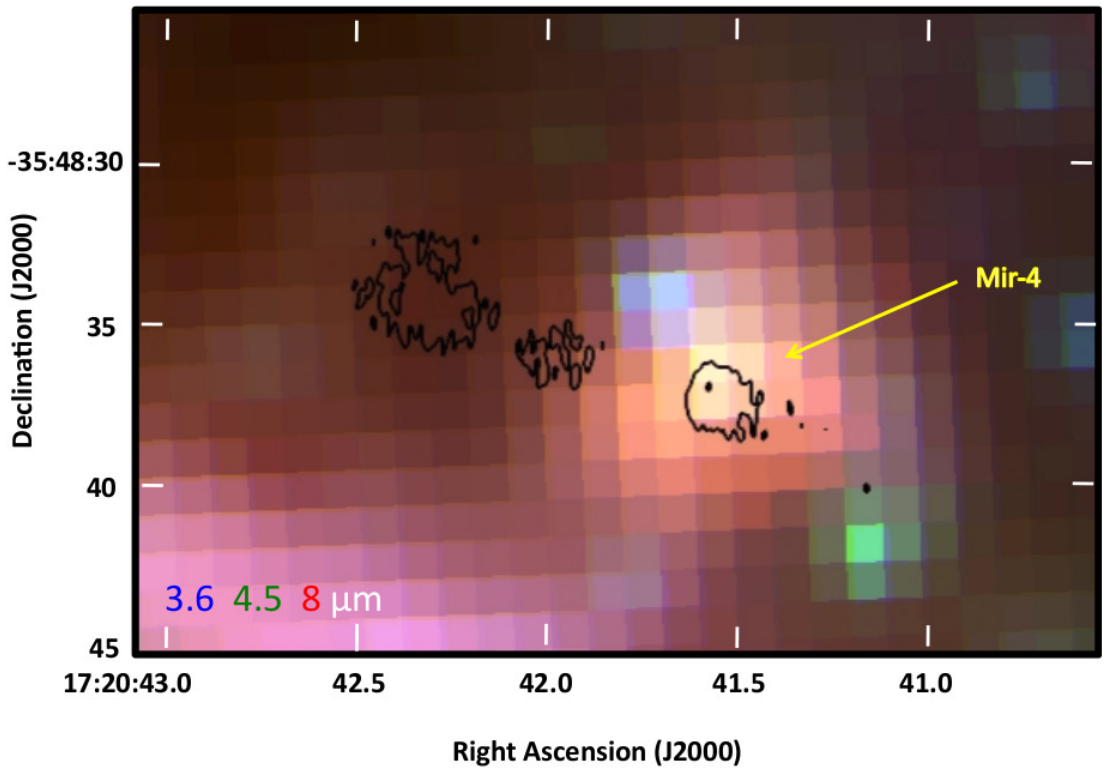

Figure 3.10: Composite infrared image around VLA J172041.59−354837.3 (CNS). Contours correspond to the radio image at 6.0 GHz, and contour levels are the same as Fig. 3.3. The yellow arrow indicate the positions of Mir-4 source.

centered at 1.92 GHz and with a bandwidth of 128 MHz. We additionally used superuniform weighting in the CLEAN task of CASA. The image was also corrected for the response of the primary beam and is shown in blue contours in Fig. 3.11 . This image indicates that source D has a shell-like morphology and that the double radio source coincides with the brightest, eastern edge of the shell. Then, the double source may not be a true independent source but simply the brightest part of a larger structure.

3.7 The central source in the CHII region E

This compact radio source was discovered by Carral et al. (2002) close to the center of the CHII region E (see Fig. 3.12) and it is our source No. 42 (Appendix A and Table 3.1). It is coincident with IR source 161 of Tapia et al. (1996), and was undetected in Feigelson et al. (2009) X-ray survey. Carral et al. (2002) measured a spectral index of $\alpha = 1.0 \pm 0.7$ which is compatible with an ionized stellar envelope and, thus, they interpreted this source as the ionizing star of source E. The IR photometry here reported confirms that this is a Class I YSO, with $A_V > 55$ and $L_{\rm IR} > 10$ $L_\odot$. Lacking mid- and far-IR fluxes, we cannot rule out, nor confirm that this star is the ionizing star of the CHII region, though the spatial coincidence makes it very probable.

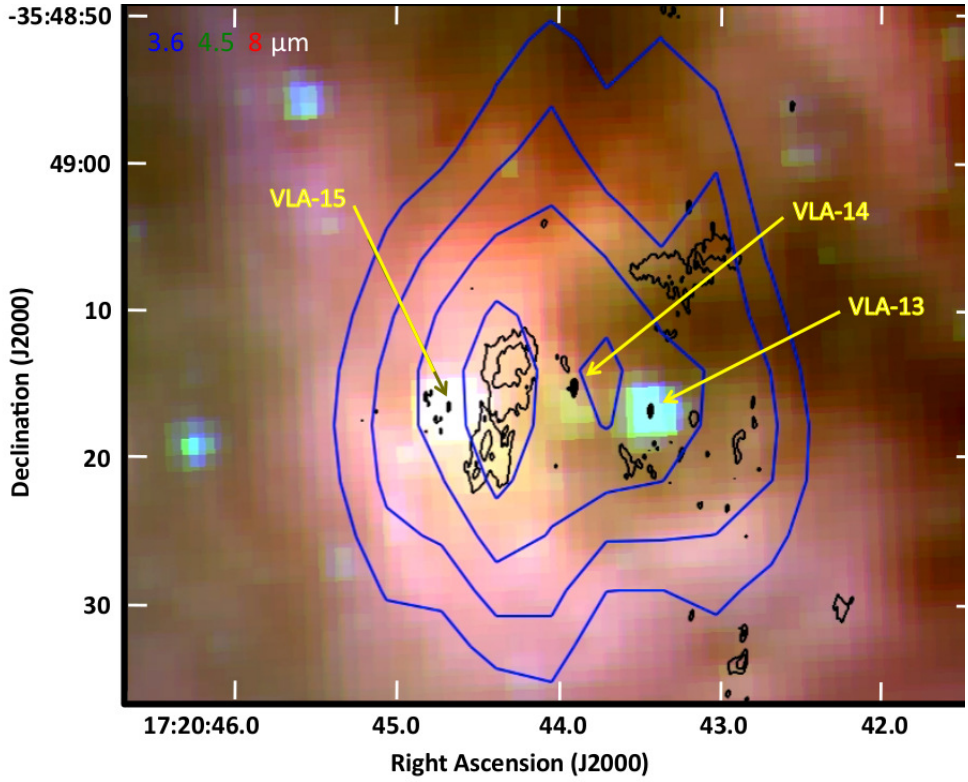

Figure 3.11: Composite infrared image around VLA J1720444.4−354917 (DNS). Black contours correspond to the radio image at 6.0 GHz, and contour levels are the same as Fig. 3.3. Blue contours correspond to the image 1.92 GHz, and the contour levels are 0.32, 0.37, 0.41 and 0.46 Jy/beam. The beamsize of this image is $26\overset{''}{.}3\times6\overset{''}{.}4$; PA=$-179^{\circ}$.

The measured spectral index in our maps is $\alpha = 1.1 \pm 0.3$ which is consistent with the previous results and the thermal nature of this source is corroborated. Using the estimated spectral index to extrapolate our measured flux to 8.4 GHz, we obtain a flux density of 1.2±0.3 mJy, which is in good agreement with the flux density measured by Carral et al. (2002). This non-variability also supports the thermal nature of the radio source.

3.8 Long term variability

Most of the previous radio observations on NGC 6334 were focused on regions E, F, and I(N), as they have shown the most recent star formation on this molecular cloud. Furthermore, they reached noise levels that were much poorer than those of the final images reported on this paper. Still, we may use these observations to roughly measure variability on some sources. In the VLA archive we found a VLA observation, in A configuration, obtained on 11 August 1995 at 8.4 GHz, that is part of project AM495. These observations were reported in Carral et al. (2002). The pointing center was RA=$17^{h}20^{m}53\overset{s}{.}40$; Dec.=$-35^{\circ}46'25\overset{''}{.}0$ (i.e. roughly equidistant from regions E, F, and I(N)). The data were edited and calibrated in a standard way. Images were produced with

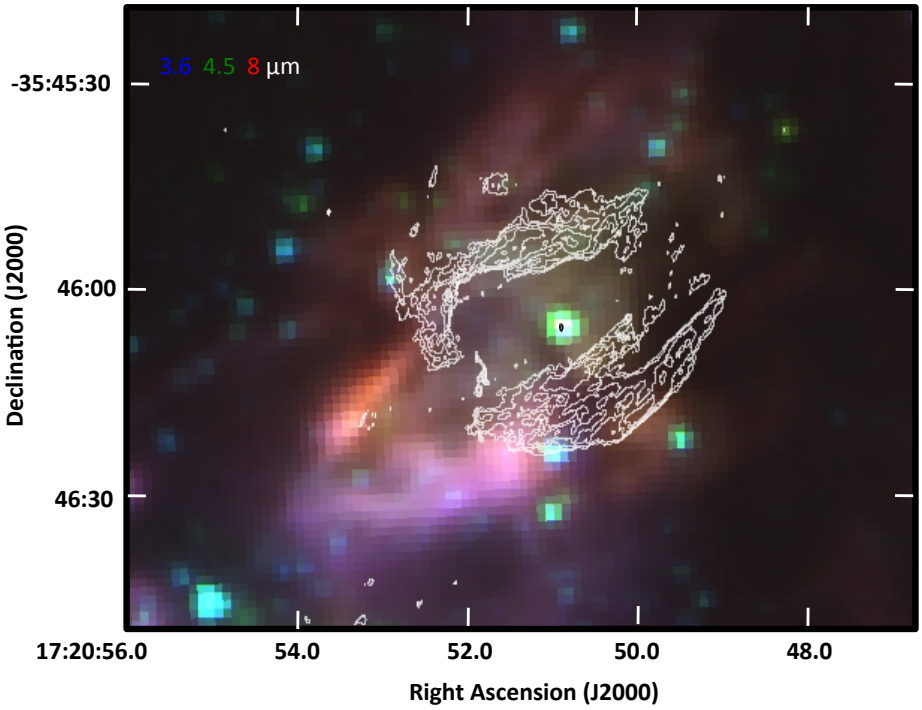

Figure 3.12: Composite infrared image around VLA J172050.91−354605.0 (the source near the center of region E). Contours correspond to the radio image at 6.0 GHz, and contour levels are the same as Fig. 3.3.

a pixel size of 0.″06 and, as it was done by Carral et al. (2002), removing the short spacings below 100 kλ (to filter out structures larger than 2″). The final beamsize of this image was 0.″48×0.″19; PA=0.°7. We look at the position of sources in Appendix A and that are inside the imaged area. In this case, we used a threshold of three times the noise level to consider a detection. Five sources were detected using this restriction and their fluxes from this image are reported in Table 3.3. Additionally, using the calculated spectral index, we extrapolate our measured fluxes at 6.0 GHz and determine their fluxes at 8.4 GHz, these are also listed on Table 3.3. Most of the sources are in good agreement with their expected flux in 2011, which suggests that these sources are not strongly variables. The only exception is source VLA J172058.14−354934.6 which shows a decrease in its flux from 1995 to 2011 by a factor of 2.4 ± 0.3.

On the other hand, we notice that due to the smaller imaged area and larger noise, most of the sources are not expected to be detected because they fall outside the primary beam or their flux will be below three times the noise level. However, using the extrapolated flux in epoch 2011 and assuming non-variability, three sources should be detected above this threshold in the 1995 image. Interestingly, they are not. In Table 3.3 we list these sources, an upper limit of three times the noise level (with the noise level of the area as the flux error) and its predicted flux at 8.4 GHz for the epoch 2011. Clearly sources VLA J172052.02−354938.0 and VLA J172053.65-354548.4 are strong variables ($\gtrsim$100%) on scales of years. We could not support a variability for source

VLA J172057.98−354431.6, since its non-detection may be due only to fluctuation in the flux caused by the noise of the observations.

We also searched for possible additional new sources by using BLOBCAT and with the parameters used for the 6.0 GHz map. We did not find any additional new source.

The three strongly variable sources reported here may be good examples of magnetically active YSOs. With future deep observations we could study variability from the weakest radio sources.

3.9 Other sources

We could not determine the spectral classification for most of the remaining radio sources. However, the infrared emission of two sources, 24 and 50 in Appendix A, indicate that they are early B stars. Their spectral index has large uncertainty but suggest a flat spectrum, so they are most probably thermal emitters. The radio emission in these cases may originate in the winds of the massive stars.

It is hard to speculate on the radio emission of the remaining sources, because of the scarce information. Future multi-wavelength and multi-epoch observations with better sensitivity may help to reveal their nature.

3.10 Summary and conclusions

We have presented a deep radio observation ($\sigma \sim 50\,\mu$Jy bm^{-1}) with high angular resolution ($0''.2$) of the NE of the NGC 6334 complex (covering the regions D, E, F, I(N), and part of the region C) searching for compact radio sources. We also searched for infrared counterparts of detected compact radio sources and characterized them. Now we list the results and conclusions from our analysis.

- A total of 83 radio compact sources in the NE of NGC 6334 are detected, 15 of them are located inside the region D. Most of these sources are new detections and only around 10 of them were previously reported and are located in regions E, I, and I(N).
- The stellar nature of 27 of the 83 compact radio sources is confirmed by the properties of their infrared emission.
- We computed the spectral index of the sources in order to speculate about the nature of their radio emission. In region D the values tend to be negative, suggesting non-thermal emission. Most of these sources are likely magnetically active low mass YSOs as in the Orion core. However, the IR emission of three of them suggest that they are early B stars and their radio emission may originate in strong shocks of wind collision regions.
- Two interesting cometary radio sources, CNN and CNS, were detected close to region D and are here reported for the first time. They are spatially coincident with more extended mid-IR nebulosities of similar shape. We suggest that they are HII regions (traced by the radio emission) surrounded by dusty envelopes (traced by the mid-IR). Interestingly we found three stars (Mir-1, Mir-2 and Mir-3) with spectral types earlier than A, which could

be the sources of the ionizing photons of CNN. On the other hand, the possible ionizing source of CNS is Mir-4.

- Through the inspection of an additional 1.92 GHz image, we suggest that the double source VLA J1720444.4-354917 (DNS) is part of the diffuse ionized gas from the region D.
- Our observations support the thermal nature of source VLA J172050.91−354605.0, which is located near the center of the radio HII region E.
- By comparing with an observation obtained in 1995, we analyzed the variability in flux of eight sources. Three of them show strong variability suggesting that they are magnetically active low mass stars.

Our analysis has provided clues on the nature of several of the detected compact radio sources. However, future observations are necessary to better establish the nature of most of them. Ideally, these observation should be multi-wavelength and multi-epoch.

Table 3.1: Infrared photometry for stellar counterparts of compact radio sources. Units of the IR values are magnitudes.

ID	J	H	K	[3.6]	[4.5]	[5.8]	[8]	Notes
Sources inside region D								
3	–	17.76 ± 0.04	15.25 ± 0.02	12.33 ± 0.18	12.41 ± 0.19	–	–	2,4,9,X
4	16.75 ± 0.02	15.30 ± 0.08	13.89 ± 0.07	–	–	–	–	2,4,8,X
5	...	–	15.98 0.10	12.65 ± 0.10	11.98 ± 0.11	–	–	
8	19.72 ± 0.11	15.47 ± 0.02	13.15 ± 0.02	11.61 ± 0.16	11.32 ± 0.15	–	–	1,8,X
9	–	–	15.55 ± 0.05	–	–	9.78 ± 0.12	7.25 ± 0.13	X
10	–	17.86 ± 0.12	16.24 ± 0.08	–	–	–	–	
11	15.15 ± 0.02	13.24 ± 0.02	12.36 ± 0.03	–	–	–	–	2,4,8,X
12	–	17.44 ± 0.12	14.27 ± 0.05	12.47 ± 0.18	–	–	–	1,9,X
13	16.36 ± 0.10	12.34 ± 0.08	10.14 ± 0.09	8.53 ± 0.04	7.87 ± 0.05	7.52 ± 0.04	6.85 ± 0.16	1,9,6,X
14	17.48 ± 0.08	15.56 ± 0.04	13.58 ± 0.03	11.37 ± 0.10	10.21 ± 0.10	–	–	2,9,4,5
15	11.34 ± 0.03	9.79 ± 0.03	8.93 ± 0.03	8.06 ± 0.12	7.54 ± 0.11	6.78 ± 0.07	99.99 ± 9.99	1,4,5,6,X
Remaining sources								
25	11.93 ± 0.02	9.97 ± 0.03	9.18 ± 0.02	8.12 ± 0.03	7.84 ± 0.01	7.37 ± 0.03	6.77 ± 0.06	1,8,4
27	16.49 ± 0.01	14.18 ± 0.02	13.00 ± 0.01	11.96 ± 0.05	12.13 ± 0.05	10.61 ± 0.09	8.73 ± 0.13	2,4,X
35	–	–	16.60 ± 9.15	13.14 ± 0.03	12.00 ± 0.03	–	–	5
38	14.28 ± 0.02	12.78 ± 0.01	11.95 ± 0.01	11.05 ± 0.07	10.50 ± 0.10	–	–	2,8
39	–	–	–	14.07 ± 0.03	10.75 ± 0.03	8.89 ± 0.02	7.68 ± 0.03	5,7
42	–	–	14.40 ± 0.02	9.49 ± 0.03	7.29 ± 0.07	5.82 ± 0.06	4.46 ± 0.07	5,7,9, CHIIE
43	–	16.48 ± 0.04	14.09 ± 0.04	9.25 0.08	7.27 ± 0.06	6.08 ± 0.04	5.08 ± 0.05	4,5,7
44	15.98 ± 0.01	13.53 ± 0.01	12.40 ± 0.02	10.93 ± 0.07	11.06 ± 0.05	10.09 ± 0.08	–	2,8,5,X
45	–	–	–	13.22 ± 0.08	12.02 ± 0.03	10.99 ± 0.08	–	5,7,X
49	–	–	–	13.28 ± 0.03	12.28 ± 0.09	–	–	X
51	16.95 ± 0.02	13.83 ± 0.03	12.20 ± 0.03	10.59 ± 0.03	10.05 ± 0.04	10.88 ± 0.19	8.65 ± 0.04	1,4,5,6,8,X
52	–	17.49 ± 0.04	15.88 ± 0.05	–	–	–	–	
53	–	–	16.09 0.05	11.80 ± 0.02	10.17 ± 0.02	9.29 ± 0.02	8.67 ± 0.02	5,7,X
60	10.97 ± 0.03	10.45 ± 0.03	10.10 ± 0.02	9.74 ± 0.07	9.68 ± 0.06	9.46 ± 0.07	–	3
65	–	–	–	15.59 ± 0.03	12.17 ± 0.07	12.01 ± 0.02	9.12 ± 0.15	5
75	19.40 ± 0.07	16.21 ± 0.02	14.67 ± 0.02	13.58 ± 0.02	13.44 ± 0.02	–	–	3,8

1 = early B spectral type, 2 = late B to early A spectral type, 3 = late-type, 4 = near-IR excess, 5 = mid-IR excess, 6 = Class II, 7 = Class I, 8 = 10 < A_V < 28, 9 = A_V > 28, and X = X-ray source (Feigelson et al. 2009).

Table 3.2: Infrared photometry around the region of cometary nebulae. Units of the IR values are magnitudes.

R.A. (J2000)	Dec. (J2000)	J	H	K	[3.6]	[4.5]	[5.8]	[8]	Notes*	Other
Around VLA J172041.75−354808.2										
17:20:41.92	−35:48:04.7	14.69±0.01	13.40±0.01	12.37±0.02	9.50±0.15	9.14±0.12	6.46±0.12	5.33±0.12	2,8,4,5,7	Mir-1
17:20:41.93	−35:48:09.7	-	-	-	10.52±0.18	9.39±0.13	6.64±0.13	5.35±0.12	5,7,X	Mir-2
17:20:42.31	−35:48:18.3	21.35±0.13	17.67±0.01	14.40±0.02	10.63±0.17	9.52±0.12	8.21±0.20	-	1,9,4,5,7	Mir-3
17:20:42.19	−35:48:12.5	19.95±0.09	17.12±0.03	15.22±0.01	-	-	-	-	2,9,4	-
17:20:42.00	−35:48:07.7	18.78±0.12	16.45±0.04	15.73±0.03	-	-	-	-	3	-
17:20:42.02	−35:48:11.0	-	17.95±0.05	15.80±0.09	-	-	-	-	2,9	-
17:20:42.49	−35:48:09.5	21.48±0.12	19.49±0.24	16.56±0.04	-	-	-	-	2,4	-
17:20:42.49	−35:48:08.5	-	-	17.2±0.2	-	-	-	-	-	
17:20:42.48	−35:48:03.8	-	-	16.9±0.2	-	-	-	-	-	-
17:20:42.29	−35:48:03.2	20.01±0.10	17.93±0.11	16.79±0.04	-	-	-	-	3	-
17:20:42.20	−35:48:02.6	20.33±0.17	17.49±0.11	16.52±0.06	-	-	-	-	3	-
17:20:42.02	−35:49:10.1	-	17.42±0.03	16.70±0.07	-	-	-	-	-	-
17:20:42.15	−35:48:17.8	-	-	17.0±0.2	-	-	-	-	-	-
17:20:42.11	−35:48:13.2	-	-	16.05±0.10	-	-	-	-	-	-
17:20:42.10	−35:48:05.2	-	-	15.8±0.2	-	-	-	-	-	-
Around VLA J172041.59−354837.3										
17:20:41.58	−35:48:36.9	-	16.09±0.15	14.85±0.05	11.07±0.09	10.08±0.13	7.14±0.10	5.51±0.15	7,X	Mir-4

* Same as Table 3.1.

Table 3.3: Comparison from radio sources of epoch 1995 and 2011.

VLA name	S_ν (1995) (μJy)	S_ν (2011) (μJy)
J172103.47−354618.8	406±59	453±52
J172052.02−354938.0	< 408±136	1038±93
J172053.65−354548.4	< 171±57	338±62
J172057.98−354431.6	< 216±72	220±24
J172050.91−354605.0	1380±110	1188±290
J172055.19−354503.8	401±107	365±23
J172058.14−354934.6	1240±110	510±52
J172054.62−354508.5	290±60	192±25

Upper-limits to fluxes are obtained as three times the noise level, that are at the same time used as the error for these upper-limits.

CHAPTER 4

Characterization of radio emission from the galactic plane with the GLOSTAR survey data

This chapter contains the extraction and characterization of the radio emission from the pilot region of the GLOSTAR-VLA survey. This study produced the first catalogue of the survey and is the first in a series of publications about the survey. The 16 square degrees of the analyzed map contains radio emission from highly active star forming regions at different evolutionary phases. This chapter is published in Vol. 601 of the Astronomy & Astrophysics journal as "GLOSTAR - Radio Source Catalogue I: $28^\circ < \ell < 36^\circ$ and $|b| < 1^\circ$" (Medina et al. 2019). Some changes in the format have been made to fit to the present publication. The Sects. 4.2, 4.4.2, and 4.4.3 are mainly a contribution from the co-authors on charge of the corresponding research.

4.1 Introduction

One of the great challenges in modern astronomy is understanding the circumstances of the formation of high-mass stars ($> 8\,M_\odot$). Massive stars dominate the energy budget of galaxies, regulate future star formation, and drive their evolution (Kennicutt 2005). Over the past 10-15 years there has been a huge effort to map the Galactic mid-plane at infrared (e.g., GLIMPSE; Churchwell et al. 2009, MIPSGAL; Carey et al. 2009), (sub)millimeter (e.g., HiGAL; Molinari et al. 2010, ATLASGAL; Schuller et al. 2009, BGPS; Aguirre et al. 2011, & SEDIGISM; Schuller et al. 2017), and radio wavelengths (e.g., CORNISH; Hoare et al. 2012, MAGPIS; Helfand et al. 2006, THOR; Beuther et al. 2016; Bihr et al. 2015; Wang et al. 2018). These surveys have provided Galaxy-wide and unbiased samples of high-mass star-forming regions (Urquhart et al. 2014a; Urquhart et al. 2018; Elia et al. 2017) that include all evolutionary stages and, for the first time, allow star formation to be studied in a global context. The recent upgrade of the *Karl G. Jansky* Very Large Array (VLA) telescope of the NRAO[1] has resulted in a significant increase in frequency coverage and sensitivity (Perley et al., 2011). This provides an excellent opportunity

[1] The National Radio Astronomy Observatory is operated by Associated Universities Inc. under cooperative agreement with the National Science Foundation.

to conduct powerful and comprehensive radio-wavelength surveys of both the ionized and the molecular tracers of star formation in the Galactic plane that will complement previous surveys. The GLOSTAR (Global View of Star Formation in the Milky Way) survey[2] is one of these new radio-wavelength surveys. Combined with accurate distances determined by the BeSSeL trigonometric parallax survey (the Bar and Spiral Structure Legacy Survey; Reid et al. 2016), it will provide a more complete view of star formation in the Milky Way. The GLOSTAR-VLA survey (Brunthaler et al. in prep.) uses the wideband (4-8 GHz) C-band receivers of the VLA to conduct an unbiased survey to characterize star-forming regions in the Milky Way. This survey of the Galactic mid-plane allows us to detect tell-tale tracers of early phases of high-mass star formation: compact, ultra-, and hyper-compact HII regions, and 6.7 GHz methanol (CH_3OH) masers, which trace some of the earliest evolutionary stages in the formation of high-mass stars (Minier et al. 2003) and can be used to pinpoint the positions of very young stellar objects, many of them still deeply embedded in their natal material. The observations also cover emission from the 4.8 GHz formaldehyde (H_2CO) and multiple radio recombination lines (RRLs) all of which will be presented in future publications. GLOSTAR observations were made with the VLA B- and D-configurations.

In this work, we present the first source catalog covering the 16 square degrees of the Galactic mid-plane observed with the VLA in its most compact (D) configuration ($28^\circ < \ell < 36^\circ$ and $|b| < 1^\circ$). We provide a description of the observational and data reduction strategies used in Sect. 4.2. In Sect. 4.3 we describe the source extraction and steps used to identify reliable sources and dubious sources that were removed from the final catalog. In the Sect. 4.4 we compare the detected sources with other Galactic surveys to look for counterparts at other wavelengths, and therefore to verify our catalog. We discuss the physical properties and the resulting statistics of the sources in Sects. 4.5 and in 4.6 we use the multiwavelength data available to determine their nature (e.g., HII regions, planetary nebulae, extragalactic). In Sect. 4.7 we focus on the properties and distribution of a sample of HII regions identified from our source classification. Finally, in Sect. 4.8 we give a summary of our results and highlight our main findings.

4.2 GLOSTAR-VLA survey observations

4.2.1 Observation strategy

The *Karl G. Jansky* VLA of the national radio astronomy observatory (NRAO) was used in D-configuration to observe the C-band (4−8 GHz) continuum emission. The correlator setup consisted of two 1 GHz wide sub-bands, centered at 4.7 and 6.9 GHz. The primary beam at the full with of the half maximum (FWHMs) are $\sim 9'$ and $\sim 6'$ at 4.7 and 6.9 GHz, respectively. Each sub-band was divided into eight spectral windows of 128 MHz, and each spectral window observed 64 channels of 2 MHz. Higher spectral resolution windows were used to cover the most prominent methanol maser emission line at 6.7 GHz, formaldehyde absorption at 4.8 GHz, and seven radio recombination lines. The results of these line observations will be reported in forthcoming works. The chosen setup avoids strong and persistent radio frequency interference

[2] This VLA survey was part of the proposal for ERC Advanced Investigator Grant (247078) GLOSTAR that partially funded early stages of the research described here.

Table 4.1: Observation epochs.

Region (ℓ)	Observation date (yyyy.mm.dd)
28°- 29°	2013.04.09
29°- 30°	2013.04.06
30°- 31°	2013.04.11
31°- 32°	2013.04.15
32°- 33°	2013.04.16
33°- 34°	2013.04.20
34°- 35°	2013.04.29
35°- 36°	2013.05.02

(RFI) seen at 4.1 and 6.3 GHz, and allows a rough estimation of spectral indices.

The region of the GLOSTAR-VLA survey presented in this work was observed over a total of eight epochs and a total of 40 hours of telescope time (project ID 13A-334). The observations were taken during the spring of 2013 (see Table 4.1 for details). Each epoch consisted of observations of five hours. The phase calibrator was J1804+0101 and the amplitude calibrators 3C 286 and 3C 48 were observed periodically during each observing block. During each epoch, an area of $2^\circ \times 1^\circ$ was covered by about 630 pointings. The pointings were on a hexagonal grid with a spacing of $\theta_{hex} = 3.''25$. This corresponds to $\theta_B/2$, where $\theta_B = 6.''5$ is the FWHM width of the primary beam at the central frequency of the higher frequency continuum band (6.9 GHz). Each grid position was observed twice for 11 seconds which, after considering the slewing time, resulted in a total integration time of 15 seconds per position. The theoretical noise level from these observations is $\sim 90\,\mu$Jy beam^{-1} per position and per sub-band. This noise is improved by a factor of two by combining the two observations of each position and both 1 GHz sub-bands (theoretical noise $\sim 45\,\mu$Jy beam^{-1}).

4.2.2 Calibration, data reduction, and imaging of continuum data

The data were calibrated using the *Obit* software packages (Cotton, 2008), which was designed for handling radio astronomy data. *Obit* applications can be accessed through a Python interface (ObitTalk). *Obit* also inter-operates with classic astronomical image processing system (AIPS) software (Greisen, 2003) and has access to its tasks.

Observations made with the VLA are well standardized, as is the data calibration, and as such calibration pipelines are now available. These implement the data reduction and calibration using amplitude, phase, and bandpass calibrators (for an example consult the common astronomy software applications (CASA) package pipeline webpage: https://science.nrao.edu/facilities/vla/data-processing/pipeline). Following the methodology of these pipelines, we have developed a pipeline in *Obit* to calibrate the GLOSTAR-VLA data with some differences. The details of these differences are described in what follows:

1. One of the first steps that most pipelines apply is to flag[3] the first record of every scan to consider the slew of the antennas. As our target scans last only ~11 s this flagging covers an important fraction of our science data. Furthermore, the distance between the target pointings is only a few arcminutes so that the slewing time is minimized. Thus, our pipeline only performs the flagging of the first record on scans that observe calibrators.

2. The GLOSTAR observations use a mixed setup of continuum and spectral lines, which are not handled well by pipelines. Thus, the next step of our pipeline is to distinguish between the different observational sets, that is, for continuum, radio recombination line, formaldehyde, and methanol data, and then load solely the continuum data.

3. A standard VLA calibration was applied in the *Obit* package, which alternates editing of data affected by instrumental problems or interfering signals with various calibration steps. External calibration includes VLA system temperature (T_{sys}) calibration, group delay, bandpass, amplitude and phase, and polarization calibration. After a Hanning smoothing of the data, an automated search for outliers in the data is performed by a comparison against running medians in time and frequency for each data product. Calibrator data is checked for adequate signal to noise ratio by an RMS/mean test. After the initial pass at data editing, the various parallel hand calibration steps are performed applying further editing based on outliers in the calibration solutions. Following the first pass at calibration, a second set of automated editing steps is done on the calibrated data. The calibration tables are then reset, the flagging table kept, and the calibration is repeated. This assures that the calibration is based on fully edited data. After flagging cross hand outliers, the polarization calibration is performed. Per pointing flagging is also included as part of the imaging. An initial, shallow *clean* is done to determine the approximate flux density in the field. Data for that pointing are then clipped at five times the estimated pointing integrated flux density.

4. The *Obit* task MFImage was used for the continuum imaging (Cotton et al. 2018). First, we imaged the data after a shallow cleaning to identify strong sources that needed to be imaged in outlier fields in the final imaging. This program uses wideband multifrequency synthesis by dividing the observed bandwidth into frequency bins, that is, sections of the sub-band, with a fractional bandwidth of less than 5%. The number of frequency bins for our observation is eight. These are narrow enough such that the effects of variable spectral index and antenna pattern variations are minor when performing a joint spectral deconvolution.

5. The *cleaning* is driven by a weighted average of the residual images from these frequency bins. Each pointing is imaged separately with a 0.28×0.28 square-degrees-sized area, centered on the phase center, using a Briggs' weighting with robustness parameter 0 and using its native restoring beam and with a pixel size of $2.''5$. Outlier fields are used if a

[3] "Flagging" is a colloquial term used for marking faulty data to exclude them from further use.

source with an integrated flux density of more than 10 mJy is known from the NRAO VLA Sky Survey (NVSS) or a previous imaging run from our own data out to a distance of 0.4 degrees. Multiscale clean was used with three different sizes: a delta function, and tapers of 20 and 40 pixels (50″ and 100″), respectively. Cleaning stopped when 5000 iterations were reached or the maximum in the residual image was below a level 0.25 mJy. Phase only, and amplitude plus phase self-calibration were applied for images with sufficiently bright peaks (> 10 mJy for phase only and > 100 mJy for amplitude plus phase self-calibrations). The shortest baselines of 30 meters allowed imaging of scales up to 4′.

6. After imaging the data from each pointing, the images were merged together in *Obit*. Since all pointings had a slightly different native beam size and orientation due to different *uv*-coverage, all pointings were smoothed in a first step to a circular synthesized beam of 18″ in diameter. This beam size corresponds roughly to the major axis of the largest beam size of all the pointings. Primary beam corrections were applied during the merging of the images. After combining all the pointings at each frequency bin, a combined image at the reference frequency was generated.

7. The maximum sensitivity can be obtained by a weighted combination of the overlapping observed pointing images onto a set of images covering the surveyed region. All else being equal, weighting by the square of the antenna power pattern in a given direction gives the optimum sensitivity. The mosaic formation process for each image plane is given by the summation over overlapping pointing images:

$$M(x,y) \;=\; \frac{\sum_{i=1}^{n} A_i(x,y)\, I_i(x,y)}{\sum_{i=1}^{n} A_i^2(x,y)} \tag{4.1}$$

where $A_i(x,y)$ is the antenna gain of pointing i in the direction (x,y) and $I_i(x,y)$ is the pointing i pixel value interpolated to the direction (x,y) and M is the mosaic image. After combination, the spectrum in each pixel is redetermined. The pointing images have already been corrected by the antenna gain pattern. A more detailed discussion of these image considerations is given by Cotton et al. (2018).

4.3 Analysis of the continuum map

4.3.1 Radio continuum map

A mosaic of the 16 square degrees that results from the eight sub-images integrated and discussed in this work is presented in the upper panel of Fig. 4.1. The effective frequency of the integrated image is 5.8 GHz. Although the observed region extends slightly beyond $|b| = 1$, the noise increases significantly in these regions due to poorer *uv*-coverage and differences in the beam sizes of the different sub-maps, and therefore these edges have been removed. The final map

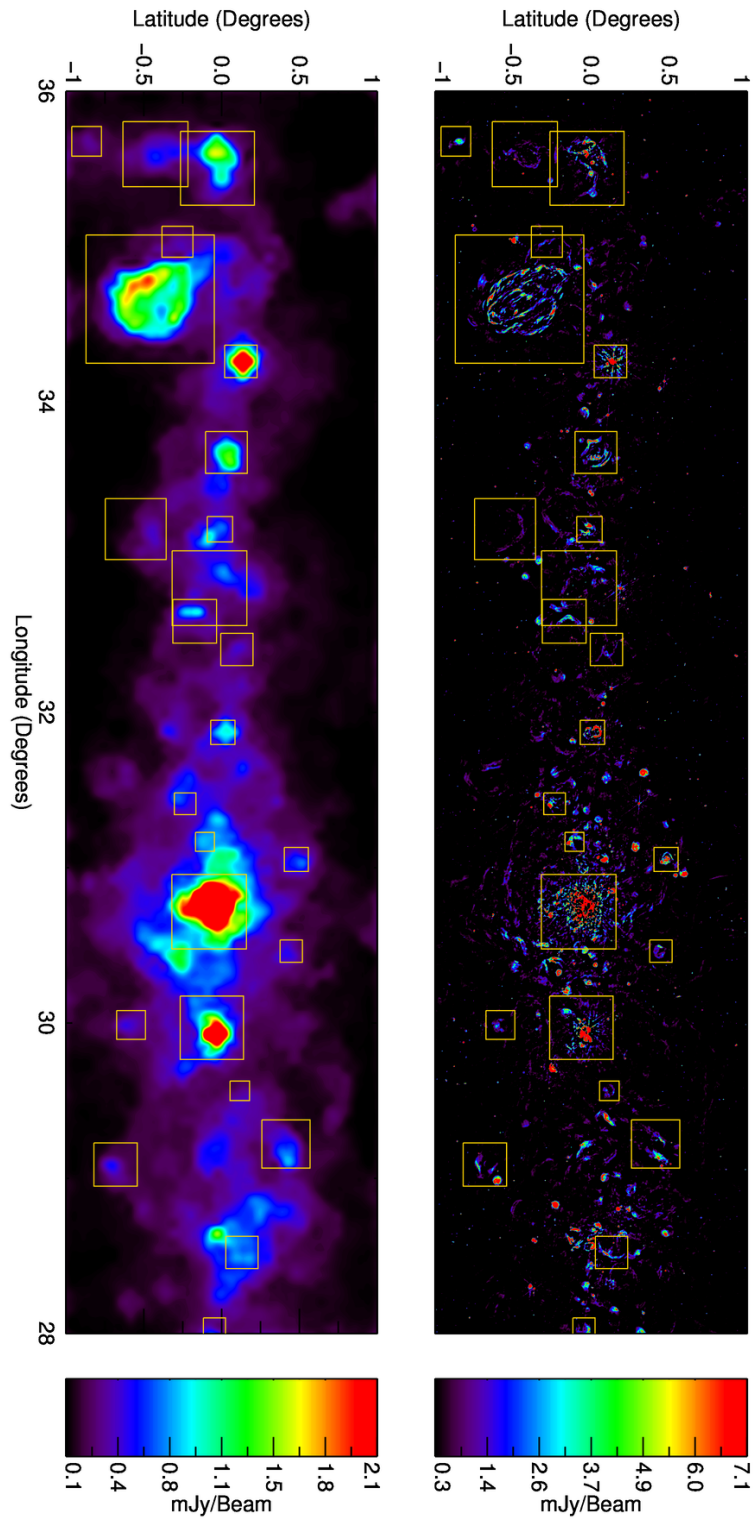

Figure 4.1: GLOSTAR mosaics and noise map of the present catalog. Upper panel: GLOSTAR radio continuum map at 5.8 GHz of 16 sq degrees of the Galactic plane ($28^\circ < \ell < 36^\circ$ and $|b| < 1^\circ$). Lower panel: Full resolution noise background map determined by SExtractor using a mesh size of 80×80 pixels and threshold of 5σ. The yellow boxes correspond to the complexes that have been identified (see Sect. 4.3.2 and Table 4.2 for more detailed and positions, respectively).

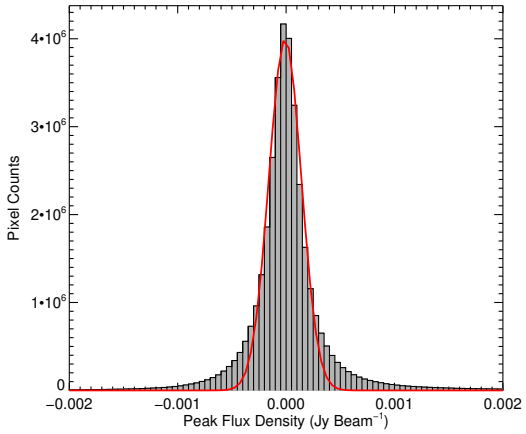

Figure 4.2: Noise distribution of the map presented in Fig. 4.1. We have restricted the range of pixel values to between −2 and 2 mJy in order to estimate the noise in the map and determine its sensitivity. The red line shows the results of a Gaussian fit to the distribution, which gives the standard deviation of the noise as 150 μJy. The bin size is 50 μJy.

has a spatial resolution of 18″. In the lower panel of this figure, we present a map of the noise distribution created using `SExtractor` (Bertin and Arnouts, 1996; Holwerda, 2005b). A full description of the maps can be found in Sect. 4.3.2. In Fig. 4.2 we present a histogram of the pixel values from which we estimate the sensitivity of the survey by fitting a Gaussian profile to the pixels clustered around zero. The standard deviation of the distribution of the pixel values is $\sigma_{\rm rms}$ = 150 μJy beam^{-1}. However, as can be seen from the lower panel of Fig. 4.1 there are strongly localized variations in the noise across the map particularly towards prominent complexes (e.g., W43, W44, G34.26+0.15), most of which are concentrated towards the mid-plane. This is a consequence of the poor *uv*-coverage of the observations themselves. These large variations of the noise across the GLOSTAR map produce the non-Gaussian profile of the pixel values in Fig. 4.2. In regions free of extended emission the noise level is around 60 μJy beam^{-1}. In Fig. 4.3 we show the noise as a function of Galactic latitude, which reveals a steep increase in noise closer to the Galactic mid-plane from ∼100 μJy beam^{-1} to ∼450 μJy beam^{-1}.

To measure the accuracy of the astrometry of the GLOSTAR map, we have matched the GLOSTAR unresolved sources (Y-factor < 1.2; this factor is the ratio of the integrated and peak flux densities, and will be fully described in Sect. 4.5) with more compact radio sources detected by the 5 GHz CORNISH radio continuum survey (Purcell et al. 2013) and measured the positional offsets between them. The offsets in ℓ and b are plotted in Fig. 4.4, which are clearly clustered around the center; the mean values are 0.″2 ± 0.″9 and -0.″4 ± 0.″9, respectively, where the uncertainties are the standard deviations in the measurements. We therefore conclude that the GLOSTAR astrometry is reliable. We estimate the combined uncertainty on position, by adding the standard deviations in quadrature, to be 1.″2, which is an order of magnitude lower than our angular resolution (18″).

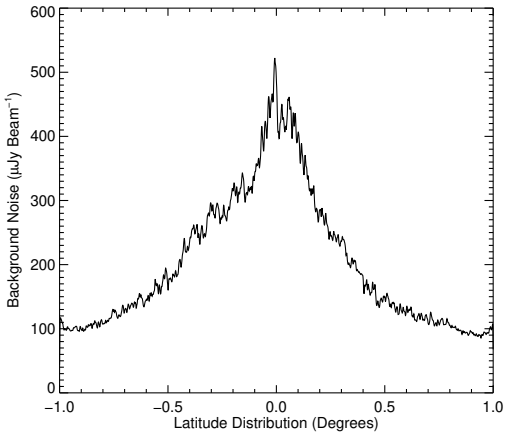

Figure 4.3: Noise distribution of the map presented in Fig. 4.1 as a function of Galactic latitude. This has been produced in the same way as Fig. 4.2 but for each increment in latitude.

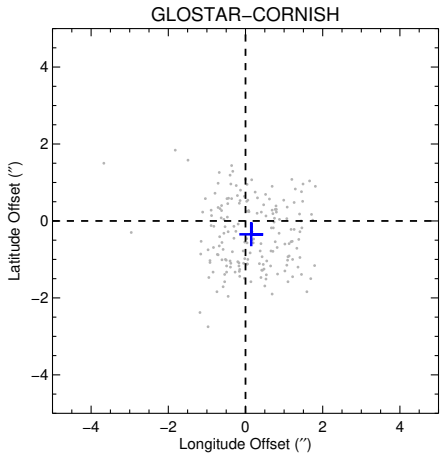

Figure 4.4: Position offsets between GLOSTAR compact sources (Y-factor < 1.2) with their CORNISH counterparts. The blue cross indicates the mean value of the offsets and the dashed lines indicate where the longitude and latitude offsets are equal to zero.

4.3.2 Source extraction

The source extraction has been performed using the BLOBCAT software package as in Sect. 3.3.1. The package has been successfully used to create the source catalogue for The HI/OH/Recombination line survey of the inner Milky Way (THOR; Beuther et al. 2016) survey, and has been adopted by us to facilitate the comparison with this complementary VLA continuum and line survey. We have followed the same method used by the THOR team at 1.4 GHz, which is outlined in Bihr et al. (2016).

The GLOSTAR radio continuum image has position-dependent noise and so we need to produce an independent noise map of the region to perform the automatic source extraction. We use the *rms* estimation algorithm within the SExtractor package that has been proven to be trustworthy in creating noise maps from radio data (Bondi et al., 2003; Huynh et al., 2005). This algorithm defines the *rms* value for each pixel in an image by determining the distribution of pixel values within a local mesh until all values are around a chosen σ value. Most real emission is removed from the noise image and the determined noise map contains the correct noise level. We use a detection and analysis threshold of 5σ, a minimum size of five pixels, and a mesh size of $80 \times 80\,\mathrm{pixels}^2$ (following the calculation of Hales et al. 2012a). The resulting noise map is shown in the lower panel of Fig. 4.1, its large scale emission is consistent with the large scale emission previously reported by Bihr et al. (2016) at 1.4 GHz.

To perform the automatic source extraction, we use the noise map as an input into BLOBCAT along with the FITS[4] image of the region under study. We applied a detection threshold (parameter dSNR in BLOBCAT) of four and a minimum source size of five pixels in diameter ($\sim 13''$). This resulted in the extraction of all sources that have flux above four times the local noise (i.e., the ratio between the input image and the *rms* map) and have a size comparable to or larger than the beam; these criteria reduce the number of false detections, particularly in complex regions.

These input parameters resulted in the detection of 1975 sources within the 16-square-degrees map. However, this sample is likely to contain a significant number of artifacts and emissions from large scale structures that have been over-resolved, resulting in the emission being separated into multiple components (e.g., the W44 supernova remnant at $\ell = 34.6^\circ$, $b = 0.5^\circ$), and from the blending of discrete sources towards star formation regions found towards the Galactic mid-plane. In the following subsections, we will describe how we have dealt with some of these issues, while in Sect. 4.4 we will describe the steps taken to identify and remove artifacts, and check the consistency of our catalog.

Superposition of distinct radio sources

In the visual inspection process, we flagged any sources that appeared to consist of two or more distinct emission peaks. We have grouped these into three categories: 1) elongated 'double lobed' sources; these look like extended emission regions powered by twin jets from active galactic nuclei (AGN; Treichel et al. 2001; Malarecki et al. 2015; Neff et al. 2015); 2) superposition of a compact, bright radio source and a larger, more diffuse radio source; 3) superposition of spherical radio sources; these are likely to be HII regions in the same star-forming complexes. An example of each of these three types is shown in the upper, middle, and lower panels of Fig. 4.5.

[4] Flexible image transport system.

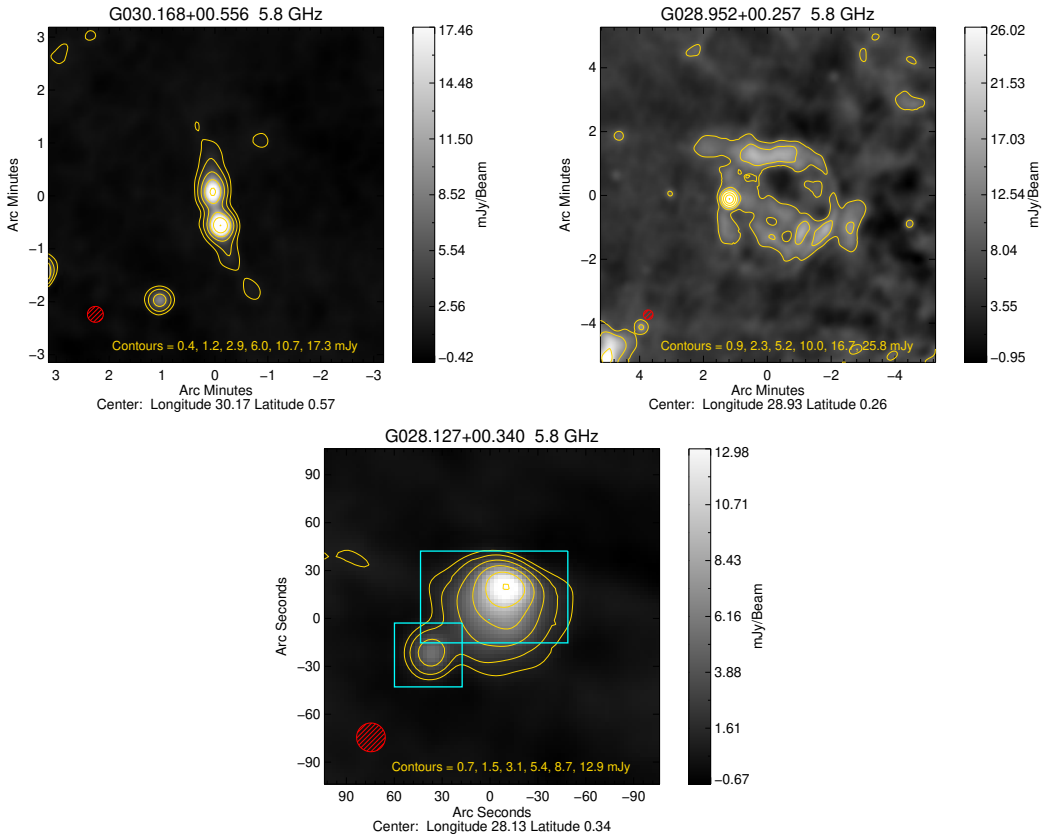

Figure 4.5: Examples of various types of radio sources (see text). The contour levels start at 3σ and increase in steps determined using the dynamic range power-law fitting scheme where $D = N^i + 3$, where D is the dynamic range, S_{peak}/σ, N is the number of contours, in this case six, and i is the power law that determines the separation between consecutive contours; this is a modified version of a scheme developed by Thompson et al. (2006). The red hatched circle shown in the lower left corner of the map indicates the GLOSTAR beam size. The cyan boxes indicate the two sources identified and the region from which the flux has been estimated.

We have made no attempt to separate the emission for the double lobed sources as it is likely to be associated with the same object. We have also made no attempt to separate the emission in cases in which a bright compact source is coincident with larger scale structures as there is not enough information to split them into reliable components as any measurement will be highly uncertain. There are a total of 51 such cases. We have, however, separated the emission into two or more sources where the overlap is small and the integrated flux density can be reliably determined (see lower panel of Fig. 4.5 as an example).

Inspection of the GLIMPSE 4.5, 8.0, and 24 μm mid-infrared images of these blended sources identified 20 cases for which the emission peaks appear to be associated with distinct sources and could be separated. We split them into two or three sources according to the number of infrared counterparts. We use the `CASA` software to select and split the regions in which emission is above 4σ and then calculate their parameters such as flux and size from their emission area. For some sources, for example, uniform and compact radio emission, we make a Gaussian fit using the task `imfit` also from the `CASA` software suite. An example of these type of sources is shown in the lower panel of Fig. 4.5. This process resulted in 44 sources being identified from the 20 blended sources examined. These split sources are treated in the source catalog (see Table 4.7) as individual sources but we also include a flag to the entry so these can be easily identified. The peak and centroid position values are considered the same for these cases.

Compact sources in noisy regions

Visual inspection of the extracted sources and comparison with other catalogs (some of which are discussed in Sect. 4.4.1) revealed a small number of compact (15), low surface brightness sources (with peak flux $\sim$1 mJy beam^{-1}) that are located near regions of bright extended sources. An example is the source in Fig. 4.6. `BLOBCAT` does not extract these objects due to the higher localized noise surrounding them and poor dynamic range of snapshot interferometric observations. We have calculated their physical properties again using the `CASA` task `imfit`. This performs an elliptical Gaussian fit to the region identified around the source. The source parameters for these objects are included in the final catalog presented in Table 4.7 but, as with the split sources, we also include a flag to the entry so these can be easily identified.

Large scale structures

We have identified 27 regions with large scale emission, by comparing the distribution of radio emission to that of the 8 μm maps extracted from the GLIMPSE archive. We have drawn a box around the coherent infrared structures that are morphologically correlated with the radio emission, but for which the radio emission has been broken up into two or more components. These 27 regions are indicated by squares in the upper and lower panels of Fig. 4.1. It is clear that these regions are also correlated with the noisiest regions of the map where much of the large angular scale emission is poorly recovered by the observations. In Table 4.2 we give the name of each structure, the extent of the boxed region in ℓ and b, and the integrated flux of the total emission in the box minus the emission from any compact sources that are considered distinct sources. The name of each structure has been constructed from the central coordinate of the enclosing box.

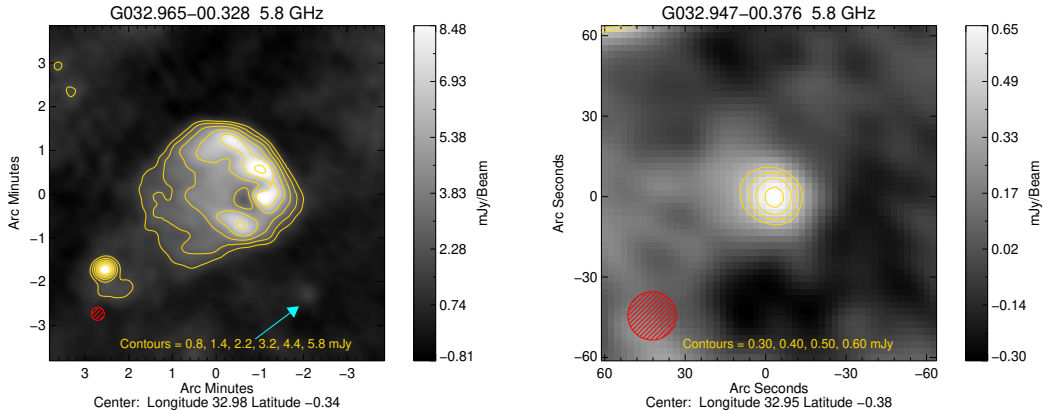

Figure 4.6: Example of compact source in noisy region. In the upper panel we show an example of an instance where a bright extended source has increased the local noise such that a nearby compact 7σ source located to the southwest has been missed. The position of this source is indicated by the cyan arrow. In the lower panel we show a smaller region centered on the missed compact source.

In Fig. 4.7 we show some examples of these large scale structures. All extended radio sources in these boxed regions are considered to be part of the large scale structure and have been excluded from the final catalog of radio sources. However, compact radio sources that are considered likely to be associated with discrete objects and not part of the larger scale structure have been retained in the final catalog as distinct sources.

In total, 195 sources are associated with the 27 large scale structures identified. Of the 27 large scale regions identified, two stand out as being particularly significant; these are the W43 star-forming complex ($29^\circ \leq \ell \leq 32^\circ$ and $|b| \leq 1^\circ$; Blum et al. 1999) and the well-known supernova remnant W44 (Clark and Parkinson 1975). Between them they contain 92 of the 195 individual fragments that have been associated with large scale emission regions. We note that radio recombination lines have been detected towards a radio source (G034.793−00.711) seen towards the southeastern edge of W44 (Lockman 1989; G34.758-0.681). In the lower right panel of Fig. 4.7 we present a map of the radio emission seen towards W44 and indicate the position of this nearby HII region with an arrow. The association of RRL emission with this radio source provides strong evidence that this source is a HII region that is coincident with the edge of this supernova remnant (G034.8−00.7; Ortega et al. 2010) rather than part of W44 itself. Therefore, we treat this as a separate source, which we classify as a HII region.

The W43 region has two prominent components: W43-main and W43-south. W43-main hosts a giant HII region (Blum et al., 1999) and has been classified as a mini star-burst region (Motte et al. 2003). Due to the complexity of the region and our limited *uv*-coverage, the central parts of both regions are not well reconstructed in the radio emission map. That could also be a reason for the different integrated flux density measurement of the central part of W43-main between the THOR team, 55.55 Jy at 2 GHz (Bihr et al. 2016), and our value, 13.43 Jy at 6.0 GHz. However, our observations have been able to recover very well much of the emission from the shell structure of W44 (see lower-right panel of Fig. 4.7). This extended object is ~30 pc across

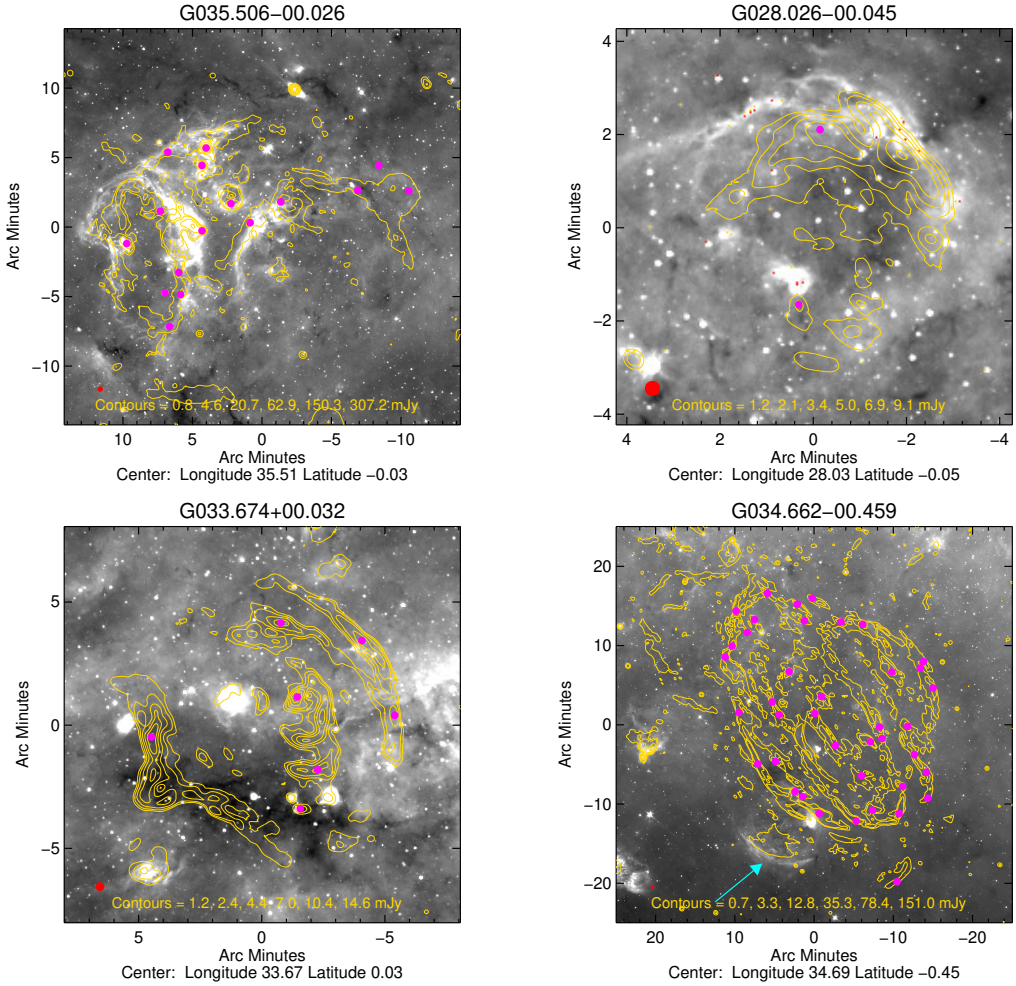

Figure 4.7: Example of radio emission associated with large scale structures. The background images are GLIMPSE 8 μm while the yellow contours are the GLOSTAR 5.8 GHz radio continuum emission. These regions often show coherent infrared structures that are morphologically correlated with most of the radio emission (see examples presented in the upper panels), however, the correlation is not always present but the radio emission is clearly correlated (see examples presented in the lower panels). These large scale structures have been excluded from the final catalog of radio sources. The contours are determined as described in Fig. 4.5 and the red filled circle shown in the lower left corners shows the GLOSTAR beam. The magenta circles indicate the peak positions of radio sources associated with these regions. In the lower-right panel the W44 SNR is shown; the cyan arrow points to the HII region (G034.793−00.711) located close to the edge of this complex (see text for details).

Table 4.2: Large scale structures. The source name is constructed from the central position of the box used to encapsulate the regions. The sources with * are associate with supernova remnants from the catalog of Green, 2014.

Name	ℓ_{min} (°)	ℓ_{max} (°)	b_{min} (°)	b_{max} (°)	Int flux (Jy)
G028.026−00.045	27.970	28.082	−0.100	0.010	0.32
G028.520+00.132	28.470	28.570	0.049	0.215	0.30
G028.6−00.1 (SNR)*	28.544	28.694	−0.188	−0.038	0.95
G029.087−00.682	28.976	29.199	−0.756	−0.608	0.22
G029.219+00.415	29.095	29.343	0.344	0.486	0.50
G029.6+00.1 (SNR)*	29.512	29.612	0.071	0.165	0.13
W43−south center	29.805	30.131	−0.195	0.071	9.08
G029.986−00.582	29.913	30.060	−0.650	−0.513	0.11
G030.462+00.449	30.405	30.519	0.393	0.506	0.16
W43 center	30.525	30.908	−0.238	0.080	13.43
G031.053+00.482	30.992	31.115	0.435	0.529	0.59
G031.166−00.106	31.117	31.214	−0.050	−0.162	0.42
G031.411−00.234	31.355	31.467	−0.286	−0.183	0.60
G031.5−00.6 (SNR)*	31.400	31.700	−0.790	−0.490	0.14
G031.9+00.0 (SNR)*	31.821	31.920	−0.053	0.071	1.01
G032.4+00.1 (SNR)*	32.322	32.488	0.027	0.172	0.10
G032.586−00.172	32.534	32.637	−0.284	−0.059	0.26
G032.8−00.1 (SNR)*	32.649	32.950	−0.269	0.115	0.67
G033.179−00.010	33.118	33.240	−0.075	0.055	0.66
G033.2−00.6 (SNR)*	33.033	33.327	−0.708	−0.395	0.09
G033.6+00.1 (SNR)*	33.567	33.781	−0.067	0.132	0.93
G034.260+00.125	34.177	34.343	0.043	0.207	10.17
W44 − G034.6−00.5 (SNR)*	34.390	34.930	−0.760	−0.093	2.96
G035.032−00.283	34.994	35.070	−0.363	−0.204	0.04
G035.506−00.026	35.316	35.696	−0.157	0.106	2.36
G035.6−00.4 (SNR)*	35.502	35.692	−0.593	−0.258	2.36
G035.680−00.868	35.610	35.750	−0.943	−0.792	0.19

with thermal x-ray emission seen towards its center (Clark and Parkinson, 1975). We measure an integrated flux density of 2.96 Jy, which is significantly larger than the value of 1.2 Jy determined by Wynn-Williams et al. (1981) from 5 GHz VLA observations; this new integrated flux density estimation is due to our higher sensitivity to more extended emission.

Our sample of large scale emission structures also includes three other well-known regions. The first of these is the very bright ultra-compact HII region G34.3+0.2 (G034.260+00.125 in Table 4.2). Garay et al. (1986) estimated the integrated flux density at 5 and 8 GHz, to be ∼1.5 Jy and ∼2 Jy respectively. We calculate the flux to be significantly higher at ∼10 Jy, but we are unable to fully resolve the structure of this object with the resolution of the current GLOSTAR data. Our higher integrated flux density determination is likely to be caused by our sensitivity to larger scale emission that its resolved out in the higher angular resolution data of Garay et al. (1986). The other two regions worth mentioning are G035.506−00.026 and G030.462+00.449, both of which have counterparts in the catalog of star-forming regions reported by Rahman and Murray (2010) (complexes 17 and 23 respectively). The W44 and W43 regions also have

counterparts in this catalog. Therefore, we have recovered four of the most luminous free-free sources in the Galaxy.

Searching the literature we find that ten of these large scale structures, including W44, have been previously identified as supernova remnant (SNR) (Green 2014); this corresponds to over a third of this sample. Where a match has been made we have adopted the catalog name from Green (2014) in Table 4.2.

Table 4.3: Summary of detection categories.

Description	Number of sources
Total number of sources extracted	1975
Number of sources assoc. with large structures	195
Number of split sources	20 (44)
Number of sources recovered near bright sources	15
Number of sources rejected	237
Number of source in final catalogue	1575

4.3.3 Catalog completeness and reliability

The BLOBCAT source extraction method was verified by the THOR team (Bihr et al. 2015; Wang et al. 2018). They performed a detailed set of completeness tests. They chose a region of 0.5×0.5 degrees with a constant noise level and added artificial 2D Gaussian sources with the size of the beam and different peak intensities. They measured the fraction of sources recovered as a function of intensity and found that at a threshold of 7σ the extraction algorithm was 95% complete. Given that our data are similar to the THOR data (both are VLA continuum surveys and have similar resolutions) we have simply adopted their results.

The CORNISH team used a similar flux threshold ($7.2\,\sigma$; Purcell et al. 2013) as the minimum required for inclusion in their catalog. This was determined by calculating the number of spurious detections expected as a function of σ and set at a level above which no spurious detections would be expected (e.g., Medina et al. 2018). The CORNISH survey consisted of 5.6×10^8 beams and so a high threshold was required to avoid any false detections. The region presented here consists of approximately 1000 times fewer beams ($\sim 5.65 \times 10^5$ beams) and so we can set our threshold for reliable sources at a lower level. Based on Gaussian statistics, the number of spurious sources we would expect in our catalog using 5σ flux threshold is < 1 and so this is the level above which sources in the catalog are considered to be highly reliable. We find another ~250 radio sources between 4 and 5σ of which we estimate 7% are likely to be spurious (~17 sources); we include these in the final catalog as the vast majority are likely to be real sources and have counterparts in other surveys, but these are considered to be less reliable.

4.4 Verification of the source catalog

As discussed in the previous section, only a small number of spurious sources are expected in our final catalog. However, due to the nature of these interferometric snapshot observations,

the *uv*-plane is relatively sparsely sampled, which can result in a significant number of imaging artifacts in the restored maps. As a consequence the number of spurious sources expected from Gaussian statistics is, therefore, a lower limit to the actual number of spurious sources detected.

To improve the reliability of the catalog produced by `BLOBCAT` we need to identify any spurious noise peaks and imaging artifacts (side lobes and emission from over-resolved structures). We have already taken emission from over-resolved structures into account by identifying the large scale structures as described in Sect. 4.3.2; this reduces the number of sources in the catalog to 1819. Next we assume that any radio source that has a counterpart in a published radio or mid-infrared catalog is real; this is because it is extremely unlikely that a false detection would randomly appear in the same position in other independent surveys.

4.4.1 Complementary surveys

A number of complementary multiwavelength surveys have produced catalogs of sources located in the Galactic plane, which we have used to verify whether the sources recovered from the GLOSTAR map are real and to help determine their nature. Below we provide a brief summary of the surveys used in this work. In all cases we have used a $10''$ radius to identify matches with the exception of the ATLASGAL dust emission; this is because the dust emission tends to be more extended. The surveys selected are either well matched in resolution (e.g., WISE, ATLASGAL, MAGPIS, and THOR, with angular resolutions of 6-19$''$) or in wavelength (e.g., CORNISH at 5 GHz).

Table 4.4: Statistics of the matches between GLOSTAR and other published surveys. A match radius of $10''$ has been used centered on the peak of the GLOSTAR emission, except for the ATLASGAL dust emission, which is more extended than the radio and mid-infrared catalogs.

Survey	Wavelength	Resolution ($''$)	*rms* level mJy beam^{-1}	Num. of sources in region	Num. of matches
CORNISH	6 cm	1.5	0.33	353	327
MAGPIS	6 cm	6-9	0.3	218	128
THOR	20 cm	10-25	0.3-1	1036	772
ATLASGAL	870 μm	19.2	50-70	747	132
WISE	3.4-22 μm	6-12	...	...	988

CORNISH

The Co-Ordinated Radio 'N' Infrared Survey for High-mass star formation (CORNISH; Hoare et al. 2012) is a sensitive and high-resolution 5 GHz radio continuum survey that focuses on the northern GLIMPSE region ($10^\circ < \ell < 65^\circ$ and $|b| < 1^\circ$). The survey was conducted using the Very Large Array before its upgrade in B-configuration, which provides an angular resolution of $1.''5$ and has a 7.2σ sensitivity of $\sim$2.7 mJy beam^{-1}.

The CORNISH catalog consists of $\sim$2600 sources above 7σ (Purcell et al. 2013), 353 of which are located in the GLOSTAR region presented in this work. We find a GLOSTAR counterpart for

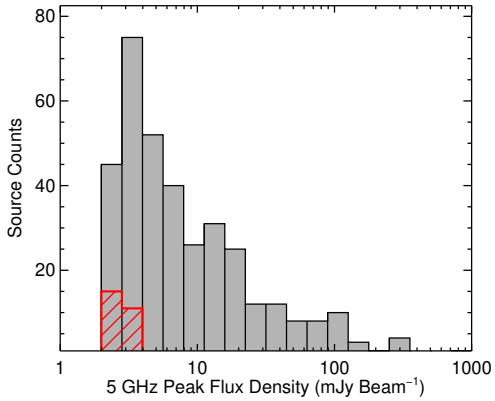

Figure 4.8: Peak flux distribution of CORNISH sources located in the GLOSTAR field. The gray and red hatched histograms show the distribution of all CORNISH sources and those without a GLOSTAR counterpart, respectively. The bin width is 0.15 dex.

327 of these (~80%). Inspection of the emission maps for the brighter CORNISH sources reveals that 20 more are associated with extended or multipeak emission sources found in GLOSTAR where the positions are less well constrained and consequently these sources were not matched. In Fig. 4.8 we show the peak flux distribution of all 353 CORNISH sources and the 26 sources where we have failed to find a GLOSTAR counterpart using either 10″ search radius or through inspection of the emission maps. It is clear from this plot that all of the radio sources that are not picked up by GLOSTAR correspond to the weakest CORNISH sources. We have estimated the noise values from the GLOSTAR maps towards these 26 CORNISH position and find a mean noise value of 166 μJy beam^{-1} and a standard deviation of 154 μJy beam^{-1} (minimum and maximum noise values are 47 and 768 μJy beam^{-1}, respectively), which is significantly lower than the typical CORNISH 1σ (0.33 mJy beam^{-1}) noise values (see Fig. 4.9).

There are two possible explanations for these missing sources: 1) the flux density is variable and has decreased between the time the CORNISH observations were completed and the GLOSTAR observations were made; and 2) these are spurious CORNISH detections. The variability of radio sources has been investigated by Kalcheva et al. (2018) from an analysis of the CORNISH and MAGPIS integrated flux densities (we will discuss the MAGPIS survey in the next subsection). Kalcheva et al. (2018) estimate that ~5% of the CORNISH UCHII region sample are potentially variable sources (flux increases of over 50 % over a 15 year time period), which is consistent with the number of CORNISH detections that do not have a matching GLOSTAR counterpart (~ 7%). In Table 4.5 we provide the source name and integrated and peak flux densities of the unmatched CORNISH sources (taken from Purcell et al. 2013) along the local *rms* noise determined from the GLOSTAR maps.

In the case of variable sources, we should expect to find approximately as many sources with significantly larger fluxes in CORNISH than measured in GLOSTAR, and comparing the fluxes we find seven matches for which this is the case (following Kalcheva et al. 2018 we set this criterion to be > 50% more flux). The radio names of these sources and the flux ratio are given in Table 4.6. The discrepancy between this number and that of the number of CORNISH sources not

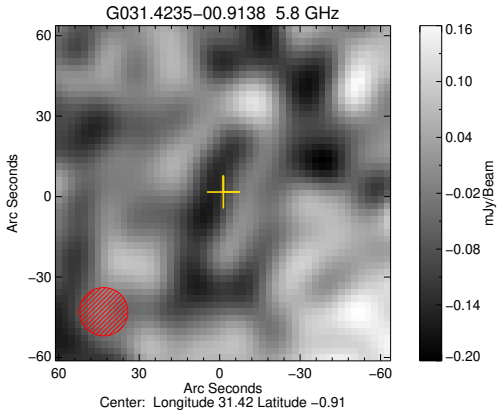

Figure 4.9: Example of a CORNISH source not detected in GLOSTAR. The grayscale is the GLOSTAR map of a $2' \times 2'$ region centered on the position of the CORNISH source G031.4235−00.9138 (as indicated by the yellow cross). The noise towards this source is 63 μJy beam^{-1} and given that the integrated CORNISH flux is 3.47 mJy, it should have been easily detected in the GLOSTAR map. The red hatched circle shown in the lower left corner indicated the size of the GLOSTAR beam.

detected in GLOSTAR (Table 4.5) suggests that variability alone cannot fully account for the 26 CORNISH source not detected in GLOSTAR. The highest flux ratio is 3 and so the differences are relatively modest compared to those reported by Kalcheva et al. (2018) (range between 2.4 and 73.9). All of the sources are either marginally detected or unresolved, have integrated fluxes below 10 mJy, and all but one have negative spectral indices, and so the variability appears to be restricted to weak and unresolved extragalactic sources. We note that these radio properties are similar to those reported for T Tauri stars (e.g., Dzib et al. 2013b), however, given these radio sources appear to be mid-infrared dark this possibility is considered less likely.

Kalcheva et al. (2018) considered only HII regions in their analysis, whereas none of the variable candidates we have identified have been classified as being HII regions, planetary nebulae (PNe), or radio stars. However, Kalcheva et al. (2018) only found one variable HII region in the region being considered here and, given the shorter temporal baseline (~7 yrs), the lack of variable HII regions and the lower levels of variation are not surprising.

MAGPIS

One of the first VLA surveys of a large fraction of the Galactic plane at 5 GHz was conducted in the early 1990s ($350^\circ < \ell < 40^\circ$ and $|b| < 0.4^\circ$; Becker et al. 1994). This survey is now part of a larger collection of re-reduced radio surveys known as the Multi-Array Galactic Plane Imaging Survey (MAGPIS; Helfand et al. 2006).[5] This part of the MAGPIS survey has a resolution of 6-9″ and a 5σ sensitivity of ~2.5 mJy beam^{-1}. This reprocessing has resulted in the identification of 1272 discrete sources including 218 that are located within the GLOSTAR region presented in this work. Of these, we have found that 128 are coincident with 125 GLOSTAR sources (the lower resolution of GLOSTAR results in three cases where a GLOSTAR source is associated with

[5] https://third.ucllnl.org/gps/.

Table 4.5: Catalog names and fluxes for CORNISH sources not detected in GLOSTAR. The last column gives the measured *rms* towards the position of the CORNISH source in the GLOSTAR map. The flux errors are comparable to the CORNISH noise level, 0.33 mJy beam^{-1}.

CORNISH name	$S_{\rm peak}$ (mJy beam^{-1})	$S_{\rm int}$ (mJy)	GLOSTAR rms (mJy beam^{-1})
G028.1875+00.5047	2.61	2.61	0.083
G028.3660−00.9640	2.92	2.92	0.073
G028.5690+00.0813	2.99	5.34	0.359
G028.9064+00.2548	3.47	3.47	0.768
G029.2555−00.8653	2.37	3.16	0.084
G029.2620+00.2916	2.76	2.76	0.120
G029.2648+00.9527	2.59	2.97	0.060
G029.3096+00.5124	2.84	2.84	0.072
G029.4302−00.9967	2.83	2.83	0.103
G029.4404−00.3199	2.81	2.81	0.160
G029.5184+00.9478	2.43	2.43	0.065
G029.7805−00.2661	3.35	7.53	0.451
G030.1884+00.1110	3.00	4.45	0.223
G030.2193+00.6501	2.80	2.80	0.122
G030.4543+00.3223	2.69	3.74	0.195
G030.6328−00.7232	2.57	2.57	0.163
G031.2859−00.2095	2.43	3.76	0.286
G031.4235−00.9138	2.66	3.47	0.063
G032.2408+00.1667	3.06	3.66	0.218
G032.2783−00.1705	2.84	4.80	0.152
G033.9622−00.4966	2.81	2.81	0.062
G034.1382+00.3805	2.61	3.23	0.139
G034.2171−00.6886	2.16	2.37	0.077
G034.3555−00.0876	2.98	4.61	0.087
G034.3852+00.3526	3.89	4.66	0.105
G035.0605+00.6208	2.76	2.76	0.047

Table 4.6: Variable source candidates where the integrated CORNISH flux is more than 50% higher than the peak GLOSTAR flux.

GLOSTAR name	CORNISH name	$S_{\rm peak,GLOSTAR}/S_{\rm int,CORNISH}$
G029.589+00.579	G029.5893+00.5789	2.17
G030.104+00.399*	G030.1039+00.3983	1.53
G031.585−00.063	G031.5854−00.0635	1.94
G032.453+00.368	G032.4535+00.3679	2.02
G032.599+00.826	G032.5996+00.8265	1.86
G034.178+00.257	G034.1782+00.2564	1.51
G034.265+00.719	G034.2655+00.7195	3.05

* The source was previously reported as a variable radio source by Becker et al. (2010).

two MAGPIS sources). A further 22 MAGPIS sources are coincident with sources associated with large scale structures discussed in Sect. 4.3.2. In total, 150 MAGPIS sources are matched in GLOSTAR, which corresponds to approximately 70% of the MAGPIS 5 GHz sample. We

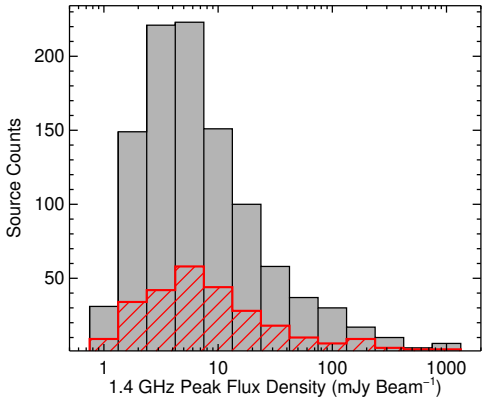

Figure 4.10: Peak flux distribution of THOR sources located in the GLOSTAR field. The gray and red-hatched histograms show the distribution of all THOR sources and those without a GLOSTAR counterpart, respectively. The bin width is 0.25 dex.

have investigated a few of the MAGPIS sources not matched in GLOSTAR and find many of these to be associated with sources that are over-resolved in MAGPIS. The offsets between the partially recovered fragments and the GLOSTAR source are larger than the $10''$ used to identify counterparts.

THOR

The HI, OH, Recombination line survey (THOR; Beuther et al. 2016; Bihr et al. 2015; Wang et al. 2018) is a 1.4 GHz radio continuum and line survey of ~100 deg^2 of the Galactic plane in the first quadrant of the Milky Way. This survey covers the 21 cm HI line, four OH transitions, 19 radio recombination lines, and continuum emission between 1 to 2 GHz. The survey was conducted using the Karl G. Jansky Very Large Array (VLA) in C-array and has a spatial resolution of 10-25$''$. The data reduction strategy and source catalog for the first half of the survey (ℓ = 14° -37.9°, ℓ = 47.1° - 51.2°, and $|b| \leq 1.1°$) are described in Bihr et al. (2016). The catalog contains a total of ~4,400 sources, of which ~1200 are spatially resolved and ~1,000 are possible artifacts.[6]

A total of 1036 THOR sources are located in the region of the GLOSTAR survey described here; we are able to find a GLOSTAR counterpart for 711 of these. We have matched a further 61 THOR sources with GLOSTAR sources that have been identified as being part of large scale structures. In Fig. 4.10 we show the 1.4 GHz peak flux distribution of all THOR sources located in the GLOSTAR region and the flux distribution of those without a counterpart in GLOSTAR (gray and red-hatched histograms, respectively). It is clear from this plot that a higher proportion of the weaker THOR sources have not been matched. Spectral index measurements are only available in the THOR catalog for the brightest of these unmatched sources (203 of the 264 unmatched) and the majority of these have negative values (71% have $\alpha < 0$, with a mean value = −0.85), which means they are weaker at 5 GHz than at 1.4 GHz and are hence less likely to be

[6] These sources have been incorporated into the complete THOR source catalog that consists of ~10,000 sources (Wang et al. 2018).

detected in the GLOSTAR map. The smaller proportion of unmatched sources that do have a positive spectral index (29% have $\alpha > 0$, with a mean value = 0.28) are a little harder to explain. However, we note that the THOR team acknowledge that ~23% of their catalog are possibly artifacts, which corresponds well with the fraction of unmatched sources we have found here.

ATLASGAL

The APEX Telescope Large Area Survey of the Galaxy (ATLASGAL; Schuller et al. 2009; Beuther et al. 2012) is the first high-resolution ($\approx 20''$ FWHM) ground-based submillimetre (870 μm) survey of the thermal dust emission in the inner Galactic plane. It has produced an unbiased catalog of ~10000 massive pre- and proto-stellar clumps (ATLASGAL Compact Source Catalog (CSC); Contreras et al. 2013; Urquhart et al. 2014a). Correlating the GLOSTAR and ATLASGAL catalogs is an excellent way to identify embedded or dust-enshrouded objects such as UCHII regions and planetary nebulae (e.g., Irabor et al. 2018, Urquhart et al. 2007; Urquhart et al. 2009; Purcell et al. 2013; Urquhart et al. 2013).

As previously mentioned, the dust emission is more extended than the radio sources, the majority of which are unresolved and so rather than using a $10''$ matching radius we identify matches where the radio source falls within the 4σ boundary of the ATLASGAL dust emission. There are 747 ATLASGAL sources located in the GLOSTAR region, of which 132 are positionally coincident with a radio source. Of these, 92 have been previously identified as HII regions (Kalcheva et al. 2018; Anderson et al. 2014; Giveon et al. 2005a), one has been identified as a PN, and one as a radio star by the CORNISH team (Purcell et al. 2013). The relatively low fraction of ATLASGAL matches is to be expected as only clumps hosting HII regions will have a radio counterpart and HII regions are only present in the most massive and evolved clumps.

WISE

The Wide-field Infrared Survey Explorer (WISE) is a NASA infrared-wavelength astronomical space telescope mission that mapped the entire sky in four infrared bands, W1, W2, W3, and W4, centered at 3.4, 4.6, 12, and 22 μm using a 40 cm telescope, which fed arrays with a total of four million pixels; these wavelengths correspond to angular resolutions of 6.1, 6.4, 6.5, and $12''$. A full description of the mission can be found in Wright et al. (2010).

The WISE ALL-sky Release Source Catalog contains astrometry and photometry for over half a billion objects. We have searched this data repository to identify and extract the mid-infrared fluxes towards 988 GLOSTAR sources; where two or more WISE sources are found within the search radius, we have picked the infrared counterpart to be the source with the smallest angular offset to the peak radio emission.

The WISE catalog is optimized for compact sources and so may overlook more extended mid-infrared emission associated with more evolved HII regions. We have therefore also cross-matched the GLOSTAR sample with a catalog of HII region candidates identified from a combination of a visual and automatic search of WISE data based on their mid-infrared emission morphology (Anderson et al., 2014). This catalog contains ~8000 HII region candidates, of which 667 are located in the GLOSTAR field. We find 130 of these mid-infrared sources to be coincident with a radio source, including 26 not found in the search made of the WISE catalog. Although we have

only found a radio counterpart for ~20% of the HII region candidates, Anderson et al. (2014) estimate that they are sensitive to HII regions with radio fluxes greater than 0.2 mJy, which is lower than our 4σ sensitivity; this sensitivity can be as poor as 1.6 mJy towards the Galactic mid-plane (i.e., see Fig. 4.3) where most of the HII regions are likely to be located. Also, objects being resolved out ($> 4'$) could only explain a small proportion (10%) of unmatched WISE HII regions and so the rest are weak HII regions. In total, we have matched 988 radio sources with a WISE counterpart.

4.4.2 Correlation with other surveys

We have searched for counterparts in the THOR, CORNISH, and MAGPIS radio continuum surveys and the ATLASGAL dust and WISE mid-infrared surveys. The correlation process with other catalogs allows us to find any large scale structures and all compact sources that have a counterpart. This analysis has identified counterparts for 1315 radio sources and these are therefore considered to be reliable detections.

The remaining 465 radio sources are a mix of compact, moderately extended sources, imaging artifacts and spurious detections. The extended sources are also likely to be associated with extended HII regions or supernova remnants. This can be confirmed by comparing the morphology of the radio emission with that at mid-infrared wavelengths. This can also identify weak mid-infrared counterparts to the compact radio sources that were not picked up in the mid-infrared catalogs. The next step is, therefore, to compare the radio and mid-infrared emission maps for these 465 sources; sources for which mid-infrared counterparts can be identified can be considered real. This visual inspection is also useful in identifying and removing imaging artifacts.

We have compared the radio emission with mid-infrared maps extracted from the GLIMPSE 4.5 and 8.0 μm bands, and MIPSGAL 24 μm band archives. We have discarded any compact radio sources that appear to be localized peaks in high-noise regions, sources that are smaller than the beam (these tended to be clustered towards the detection threshold), and extended emission that appears to be associated with large scale structures which, due to poor uv-coverage, have not been reliably imaged (these have a wider range of fluxes). This process resulted in 237 sources being excluded from the 465 without a counterpart in one of the other surveys.

Combined with the split sources and recovery (by hand) of compact sources in noisy regions, previously discussed in Sect. 4.3.2, the final radio catalog therefore consists of 1575 sources. In Table 4.3 we present a summary of the various steps taken in the source verification process and in Table 4.4 the summary of the search for counterparts with continuum, dust, and mid-infrared surveys.

4.4.3 Comparison of fluxes with other 5 GHz surveys

As mentioned earlier, we have identified matched counterparts of GLOSTAR sources in the CORNISH and MAGPIS catalogs. Although these surveys were conducted at a higher resolution than the part of the GLOSTAR survey reported here, they were conducted at a similar frequency and can hence provide a useful consistency check on the measured fluxes. Due to the different resolutions, we have compared the GLOSTAR peak fluxes with the integrated fluxes from CORNISH and MAGPIS, except when the sources in those surveys are larger than the GLOSTAR

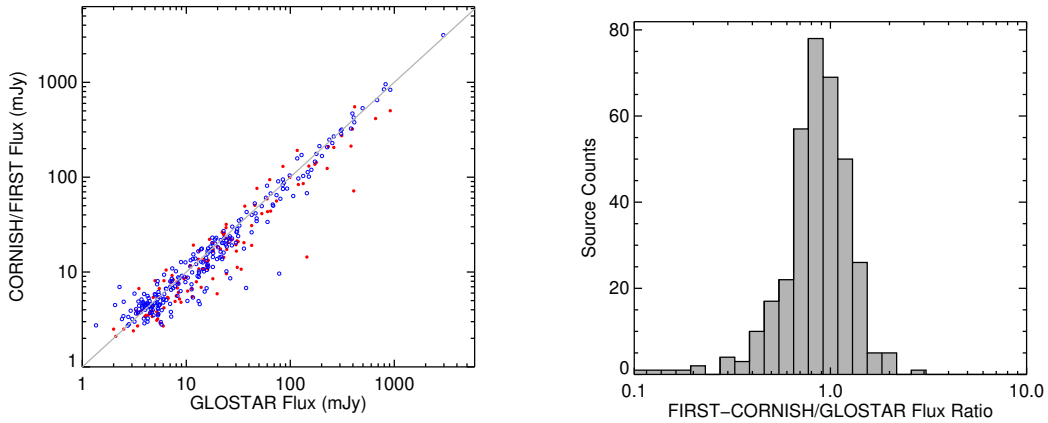

Figure 4.11: Comparison of GLOSTAR fluxes with other 5 GHz surveys. Upper panel: Comparison of the GLOSTAR flux measurements with the Becker et al. (1994) survey (MAGPIS) and CORNISH; data from these are represented as red (filled) and blue (open) circles, respectively. Due to the difference in resolution between the surveys, we compare the integrated CORNISH flux densities with the peak GLOSTAR flux densities, while for the Becker et al. (1994) survey we compare the integrated flux densities with the peak GLOSTAR flux densities, when the Becker et al. (1994) source size is less than 20″ and the integrated flux from both surveys if the source is larger than 20″. The gray line is the line of equality. Lower panel: Flux ratio distribution (as described above), which has a mean of 0.9 and standard deviation of 0.34.

beam in which case we compare the integrated fluxes from both surveys; CORNISH filters out any structures larger than ∼15″ and so this is only a consideration for some of the MAGPIS sources.

In Fig. 4.11 we show the results of this flux comparison. It is clear that the fluxes from all three surveys are in very good agreement, however, it is noticeable that there is bias towards higher fluxes measured by GLOSTAR. This is to be expected given the lower resolution resulting in more flux being present in the beam and a result of some of the flux being filtered out by the high-resolution surveys due to their poorer sensitivity to larger angular scales. We also note that a handful of CORNISH sources have a significantly higher flux than measured in the GLOSTAR data; these appear as a small cluster of sources above the line of equality towards the lower left corner of the plot and have been previously discussed in Sect. 4.4.1.

4.5 Catalog properties

The final catalog consists of 1575 distinct sources with flux densities above 4σ, where σ corresponds to the local noise. We give the names of the sources and the observed parameters in Table 4.7. The source names are constructed from the peak flux density positions. The position given in Columns 2 and 3 are the barycentric coordinates determined from the first order moments of the longitude and latitude profiles. The barycentric position generally defines the centroid position of a source. However, if the emission profile of a source is extended and consists of multiple peaks, then this can be offset from the peak position. The mean uncertainties on the peak flux density positions is 1.″22 with a standard deviation of 0.″81; the positional uncertainties

Table 4.7: GLOSTAR source catalogue. The source names are appended with a ‡ to indicate if a source has been split (as described in Sect. 4.3.2) and a † if the source has been recovered (as described in Sect. 4.3.2).

GLOSTAR name	ℓ	b	SNR	$S_{\rm peak}$	$\Delta S_{\rm peak}$	$S_{\rm int}$	$\Delta S_{\rm int}$	Y-factor	Radius	Spectral index				Classification	
	(°)	(°)		(mJy beam^{-1})		(mJy)			(″)	α	$\Delta\alpha$	α*	$\Delta\alpha$*	Type	Ref.
(1)	(2)	(3)	(4)	(5)	(6)	(7)	(8)	(9)	(10)	(11)	(12)	(13)	(14)	(15)	(16)
G028.091−00.092	28.091	-0.093	11.4	3.12	0.32	4.26	0.35	1.1	16	···	···	−0.07	0.25	···	···
G028.097−00.951	28.097	-0.951	6.1	0.54	0.09	0.45	0.09	0.6	10	···	···	−0.36	0.69	···	···
G028.098−00.781	28.098	-0.781	186.9	17.80	0.96	22.06	1.11	1.2	25	-0.91	0.01	−1.08	0.03	Radio star	8
G028.100+00.644	28.099	0.644	6.5	0.87	0.14	0.76	0.14	0.6	10	···	···	−0.57	0.28	···	···
G028.107−00.301	28.109	-0.300	5.6	0.81	0.15	1.89	0.17	1.3	16	···	···	−0.57	0.62	···	···
G028.109−00.490	28.108	-0.490	20.0	2.84	0.21	2.70	0.20	0.9	15	0.06	0.09	−0.18	0.1	···	···
G028.116−00.368	28.116	-0.368	44.0	5.77	0.34	5.82	0.32	1.0	18	-0.1	0.04	−0.12	0.05	···	···
G028.120+00.419	28.120	0.419	4.9	0.87	0.19	0.64	0.18	0.4	8	···	···	0.15	0.43	···	···
G028.126+00.742	28.126	0.742	33.6	4.26	0.26	3.86	0.23	0.9	17	-0.28	0.04	−0.81	0.1	···	···
G028.127+00.341‡	28.127	0.341	58.2	12.98	0.22	51.78	0.45	4.0	···	···	···	···	···	···	···
G028.137−00.194	28.138	-0.194	4.2	0.77	0.19	0.68	0.19	0.4	8	···	···	0.53	0.37	···	···
G028.137−00.567	28.137	-0.566	5.7	1.15	0.21	1.29	0.21	0.7	11	-0.58	0.15	−1.14	0.48	···	···
G028.140+00.329‡	28.140	0.329	11.0	4.50	0.43	7.30	1.00	1.6	···	0.23	0.12	-0.52	0.19	HII region	3
G028.144−00.378	28.144	-0.379	8.0	1.08	0.15	1.11	0.15	0.8	12	···	···	−0.46	0.55	···	···
G028.146+00.517	28.145	0.517	8.7	1.21	0.15	1.86	0.17	1.2	16	···	···	-0.66	0.27	···	···
G028.149−00.998	28.149	-0.997	76.9	11.93	0.66	19.71	1.00	1.6	25	···	···	−1.05	0.05	···	···
G028.151+00.164	28.148	0.149	38.6	10.38	0.62	194.53	9.73	18.0	95	···	···	···	···	HII region	1
G028.151−00.958	28.151	-0.957	16.0	2.00	0.16	2.25	0.17	1.0	17	-0.37	0.09	−0.4	0.28	···	···
G028.159−00.024	28.157	-0.020	8.0	2.91	0.40	28.85	1.49	6.6	38	···	···	···	···	Extended/Diffuse	1
G028.159−00.798	28.159	-0.798	29.1	2.97	0.19	2.67	0.17	0.9	16	-0.35	0.05	−0.36	0.23	···	···
G028.160−00.046	28.160	-0.046	4.8	1.68	0.36	1.59	0.36	0.5	9	···	···	−0.15	0.52	HII region	3
G028.163−00.163†	28.163	-0.163	7.0	0.50	0.07	2.00	0.34	4.0	···	···	···	···	···	HII region	3
G028.172−00.605	28.173	-0.606	4.9	1.13	0.24	14.55	0.76	5.5	32	···	···	···	···	Ionization Front	1
G028.178+00.074	28.178	0.072	4.3	1.49	0.35	9.56	0.59	2.5	21	···	···	···	···	···	···
G028.187+00.583	28.187	0.583	22.3	3.02	0.21	2.75	0.19	0.9	15	-0.01	0.06	−0.71	0.11	···	···
G028.189−00.744	28.189	-0.744	17.0	1.74	0.14	1.36	0.12	0.7	13	-0.33	0.08	−1.09	0.2	···	···
G028.193−00.785	28.193	-0.785	8.6	0.87	0.11	1.29	0.12	1.1	16	-0.68	0.12	−0.22	0.26	Pulsar	5
G028.197−00.891	28.198	-0.892	4.6	0.48	0.11	0.96	0.11	1.0	13	···	···	−0.94	0.47	···	···
G028.200−00.050	28.191	-0.050	771.1	332.67	17.92	396.10	19.81	1.2	48	···	···	···	···	HII region	3
G028.209+00.226	28.209	0.226	5.8	1.07	0.19	0.95	0.19	0.6	10	···	···	0.22	0.4	···	···

References: (1) this work, (2) Kalcheva et al. (2018), (3) Anderson et al. (2014), (4) Giveon et al. (2005a), (5) SIMBAD, (6) Irabor et al. (2018), (7) Ortega et al. (2010), (8) Purcell et al. (2013)

* Values calculated using the 8 sub images are described in Sect. 4.2.

Notes: Only a small portion of the data is provided here, the full table is available in Appendix B.

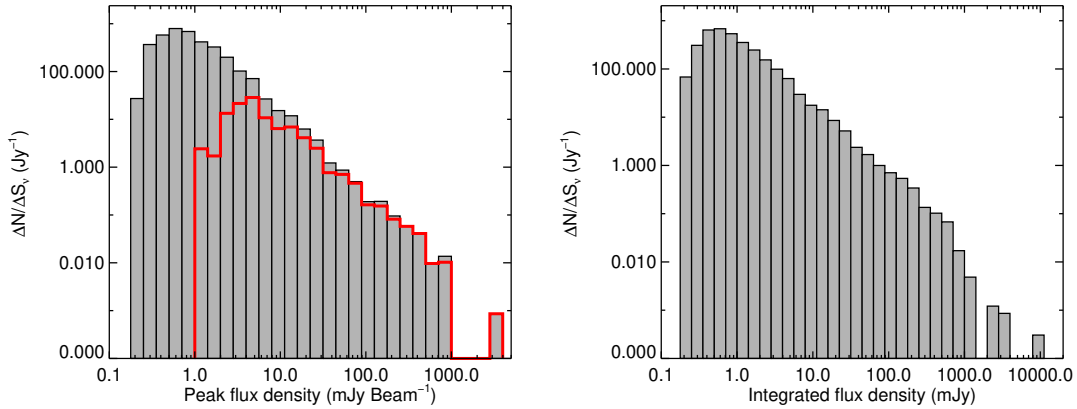

Figure 4.12: Peak and integrated flux distribution of GLOSTAR sources are shown in the upper and lower panels, respectively. The thick red histogram on the upper panel shows the flux distribution of sources previously identified by CORNISH and/or MAGPIS. The bin width is 0.15 dex.

associated with individual sources are provided in the electronic version of Table 4.7. Combined with the uncertainty in the map astrometry the mean uncertainty in the catalog positions is $\sim 2''$. The signal to noise values are given in Column 4; these are estimated by dividing the peak flux by the *rms* at the same position. The flux density values given in Columns 5-8 have been corrected for clean bias and bandwidth smearing (Hales et al., 2012a) and in Column 9 we give the Y-factor, which is the ratio of the integrated and peak flux densities (i.e., $S_{\rm int}/S_{\rm peak}$); this gives an indication of how compact a source is, with unresolved sources having a value of one and very extended sources having values of several 10s. The radius in Column 10 is determined from the number of pixels associated with the source and is therefore a rather crude estimate of the size of a source particularly for extended structures and should be used with caution. In Columns 11 and 12 we give the spectral index for compact sources (i.e., Y-factor < 2) that have a 20 cm counterpart detected by the THOR survey, while in Columns 13 and 14 are the values calculated from the eight sub-images discussed in Sect. 4.3.1; this will be described in Sect. 4.5.2. In Columns 15 and 16 we give the classification assigned to the source and a reference when available.

4.5.1 Fluxes and angular sizes

In Fig. 4.12 we show the peak and integrated flux densities distribution of the detected sources. Together with the peak flux density distribution, we also show the integrated flux density distribution of all GLOSTAR sources that are matched to sources previously identified by CORNISH and/or MAGPIS (red histogram overlaid on the upper panel); this shows clearly that the vast majority of 5 GHz sources detected in the GLOSTAR map with a peak flux density above a few mJy beam^{-1} have been detected before. The sources not picked up by the previous surveys are all extended and would have been filtered out by CORNISH or in regions not covered by MAGPIS. What is also clear from this plot is that the improved sensitivity of GLOSTAR has resulted in the detections of many previously unknown integrated low-flux density sources.

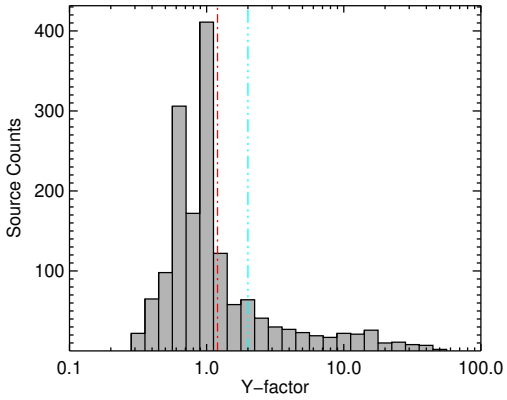

Figure 4.13: Distribution of the Y-factor ($S_{\rm int}/S_{\rm peak}$). The red dashed-dotted (Y-factor = 1.2) and cyan dashed-dotted lines (Y-factor = 2) indicate the criterion used to distinguish between unresolved, compact, and extended sources, respectively. The bin size used is 0.1 dex.

In Fig. 4.13 we show the distribution of Y-factor for the sample; this parameter is the ratio between integrated and peak flux density (i.e., $S_{\rm int}/S_{\rm peak}$) and gives an indication of the source size. While for unresolved sources the Y-factor should be equal to 1, allowing for measurement uncertainties we classify all sources with a Y-factor < 1.2 as unresolved (cf. Bihr et al. 2016). We make a further distinction between compact (which includes all of the unresolved sources) and extended sources using a Y-factor = 2 as dividing line. We note that a significant number of sources have Y-factors smaller than 1 and this has been discussed in detail by Bihr et al. (2016) who identified three possible explanations for this unexpected result: 1) `BLOBCAT` does not fit enough pixels for weak sources, which leads to lower integrated flux densities; 2) unresolved sources are located in slightly negative side lobes from nearby strong sources; 3) weak sources are not cleaned properly. Bihr et al. suggest using the peak flux densities for unresolved sources in any analysis and we have also adopted this recommendation.

`BLOBCAT` gives source size in terms of the number of pixels (parameter *npix*) that are flood-filled in the source extraction process. We convert this into a radial size using

$$R_{\rm source} = \sqrt{\frac{A}{\pi}} \tag{4.2}$$

where $R_{\rm source}$ is the effective radius, and A is the area covered by the source calculated by *npix* times the pixel size squared, which in this case is $2.''5 \times 2.''5$. Figure 4.14 shows the distribution of the angular radius of the sources.

4.5.2 Spectral index

As was mention in section 2.3, the astrophysical sources mainly emit two types of radio emission, thermal and non-thermal. The first refers to bremsstrahlung radiation and the latter is also known as synchrotron radiation (e.g., Wilson et al. 2012). Thermal bremsstrahlung radiation is produced in HII regions and planetary nebulae and usually has spectral indices between −0.1

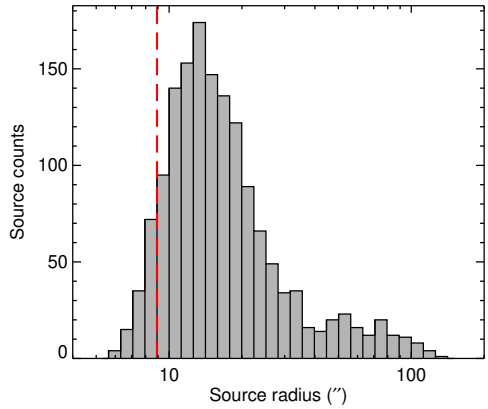

Figure 4.14: Distribution of the source radii. The dashed-dotted red line indicates the resolution of the observations (radio beam). The bin size used is 0.1 dex.

and 2 depending on whether the emission region is optically thin or thick, respectively. Active galactic nuclei (AGN) galaxies and supernova remnants give rise to synchrotron radiation, which has negative spectral indices, typically between −1 and −0.5 (Condon 1984; Dzib et al. 2013b; Rodriguez et al. 2012 and references therein). The spectral index can, therefore, help to broadly distinguish between different types of radio sources.

As mentioned in Sect. 4.2.2, the calibration process produced eight sub-images in the frequency range between 4 and 8 GHz, which we used to estimate the spectral index only of the compact sources (i.e., Y-factor < 2). We used the peak flux density from each sub-image, derived with the `CASA` task `imfit`, and a χ^2 linear fit to calculate the spectral index value.

We also estimate the spectral index of the compact sources by combining their peak flux densities with the peak lower frequency flux densities determined by THOR. As previously mentioned, we have matched 711 sources with a THOR source, of which 640 have Y-factors smaller than 2 and so can be assumed to be relatively compact. The mid-frequencies for THOR and GLOSTAR are 1.5 GHz and 5.8 GHz, respectively. Following Kalcheva et al. (2018) we estimate the spectral index using

$$\alpha = \frac{\ln\left(S_{\mathrm{GLOSTAR}}/S_{\mathrm{THOR}}\right)}{\ln(5.8/1.5)}, \tag{4.3}$$

where S_{THOR} and S_{GLOSTAR} are the peak flux densities at 6 cm and 20 cm, respectively. The uncertainty is calculated using

$$\Delta\alpha = \frac{\sqrt{\left(\sigma_{\mathrm{THOR}}/S_{\mathrm{THOR}}\right)^2 + \left(\sigma_{\mathrm{GLOSTAR}}/S_{\mathrm{GLOSTAR}}\right)^2}}{\ln\left(5.8/1.5\right)} \tag{4.4}$$

where $\sigma_{\mathrm{GLOSTAR}}$ and σ_{THOR} are the uncertainties in the peak flux densities.

For a comparison of both methods discussed above, we selected sources with reliable GLOSTAR internal spectral indices, $\sigma_\alpha < 0.2$, and compared them with their GLOSTAR-THOR spectral indices (see Fig. 4.15). A linear fit to these values yields that the slope is $m = 0.94 \pm 0.03$, close

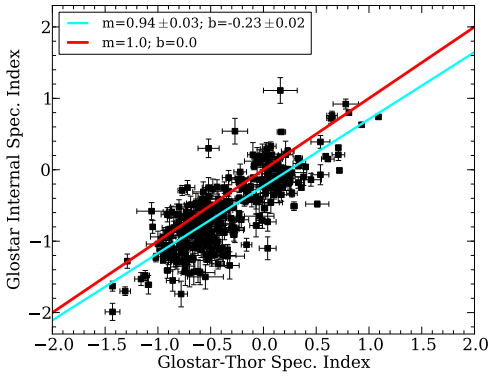

Figure 4.15: Comparison of spectral index values between only GLOSTAR data with uncertainties less than 0.2, and GLOSTAR combined with THOR data. The m and b are the slope and intersection of the linear fit, respectively, and are represented with the blue line. The red line is the line of equality.

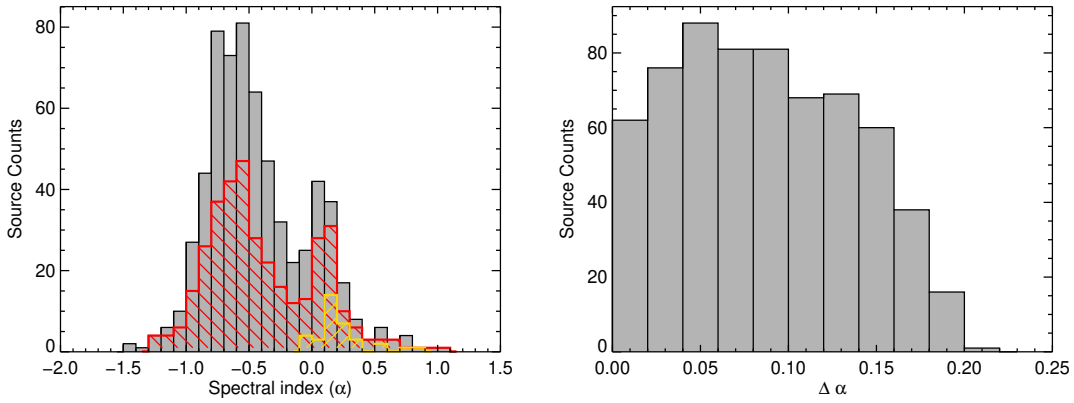

Figure 4.16: Histograms of the spectral index distribution. The upper panel we show the spectral index distribution of all compact GLOSTAR sources with Y-factor < 2 and a counterpart detected at 1.5 GHz in the THOR survey. The red and yellow hatched histograms show the distribution of compact radio sources that are associated with mid-infrared sources and dust emission, respectively. In the lower panel we show the distribution of the associated uncertainties to the spectral index measurements. The bin sizes used in the upper and lower panels are 0.1 and 0.02, respectively.

to the slope of the equality line. In conclusion, the spectral index values derived with the two methods are statistically similar.

The spectral index derived from the combination of GLOSTAR and THOR data and their associated uncertainties are given in Columns 11 and 12 of Table 4.7. In the upper panel of Fig. 4.16 we show the distribution of spectral indices; these cover a range of values between −1.5 and 1 and have a bimodal distribution with peaks at approximately −0.7 and 0.1. The dip between these two peaks occurs at approximately −0.2, which we consider the transition from thermal and non-thermal emission. We also show the spectral indices of radio sources that are associated with mid-infrared emission (i.e., have a WISE counterpart) and associated with dust emission (i.e., have an ATLASGAL counterpart); these are shown in red and yellow hatched histograms, respectively. It is clear from a comparison of these distributions that the sources with mid-infrared counterparts span the whole range of spectral indices, while the sources associated with dust are almost exclusively thermal sources. So while sources associated with dust are likely to be a mix of HII regions and PNe, the association of a particular source with mid-infrared emission does not provide any constraints on its nature. We will explore this issue of source types in the next section. In the lower panel of Fig. 4.16 we show the distribution of the uncertainties associated with the spectral index measurements; these have typical values of ±0.1 but can be as large as ±0.2.

We have calculated the spectral indices for 671 GLOSTAR sources without a THOR counterpart. The values and their associated uncertainties are given in Columns 13 and 14 of Table 4.7. We note that the limited frequency range or poor signal to noise results in large uncertainties for the majority (74% have $\Delta\alpha > 0.2$). The spectral indices range between −1 and 1 for the sources for which they are considered to be reliable. Given that the sample of GLOSTAR-internal spectral index is relatively modest, we decided not to perform a detailed statistical analysis of the spectral index.

4.6 Classification of radio sources

4.6.1 Literature search

A number of studies have investigated the nature of radio and mid-infrared sources. By correlating our catalog with these we can adopt their classifications. Cross-matching our radio sources with HII region catalogs compiled by Purcell et al. (2013) and Kalcheva et al. (2018) using CORNISH data, Giveon et al. (2005b) using MAGPIS data, and Ortega et al. (2010), we have identified a total of 46 previously known HII regions. As described in Sect. 4.4.1 we also cross-matched our radio sources with a catalog of HII region candidates identified by Anderson et al. (2014) from their analysis of WISE colors. This revealed a match for 130 radio sources including 90 not previously matched to a CORNISH or MAGPIS source. Of these, 43 have spectral indices determined from the THOR and GLOSTAR data; 42 of these have spectral indices between −0.17 to 0.88, which supports their classification as HII regions (Anderson et al. 2014). Combined with the 46 sources identified from the literature, this brings the sample of reliable HII regions in the GLOSTAR region to 136.

A further 28 sources have been identified as PNe by the CORNISH team (Purcell et al. 2013 and Irabor et al. 2018), and another 15 as radio stars (12 identified by Purcell et al. 2013 and three

found in SIMBAD[7] database. We found, with a cross-match radius of 10″, that three of these candidates have a counterpart in the HASH (Hong Kong/AAO/Strasbourg Hα) planetary nebula database (Parker et al. 2016). Our literature search has also identified another three interesting compact radio sources that are consistent in position with pulsars: G032.763+00.092 with PSR J1850-0006 (Keith et al. 2009), G028.880−00.938 with PSR B1844-04, and G028.193−00.785 with PSR B1842-04 (Hobbs et al. 2004). Radio continuum emission from energetic pulsars is usually associated to the integrated emission of their pulses, but other mechanisms such as a pulsar wind and magnetic activity have been recently discussed by Dzib et al. (2018). For the GLOSTAR data discussed here, the angular resolution is insufficient to decide whether or not the radio emission comes from the pulsar, from the surrounding medium, or from an unassociated object. This will be better constrained with the GLOSTAR VLA B-configuration data when it becomes available.

The importance of pulsars with radio continuum emission is that they may targeted by very long baseline interferometry (VLBI) observations to determine their astrometric parameters, such as proper motions and trigonometric parallaxes (Brisken et al., 2000). This information may be used to associate them with supernova remnants (SNRs) to better constrain their luminosity, and Galactic electron distribution models (Brisken, 2005; Deller, 2009).

We also identified two SNRs from a cross-matching with a radius of 10″ between the GLOSTAR sources and the THOR ~20 SNR candidates identified by Anderson et al. (2017) located in the GLOSTAR field; these are G028.642+00.187 and G028.218−00.080. The low number of matches may be due the negative spectral index of the SNRs, which are better recovered at lower frequencies, or may be due to the fact that SNRs tend to be extended and so many are likely to be either filtered out by the interferometer entirely or only partially detected and classified as extended emission. To investigate this further we also searched for SNRs using the Green (2014) catalog. This identifies 12 SNRs within the GLOSTAR region, ten of which are matched with the large scale emission regions identified in Table 4.2 and mentioned in Sect. 4.3.2. Of the remaining two SNRs in the field, one is not detected at all (G032.1−00.9), and one is detected as a compact radio source (G029.7−00.3; see Fig. 4.17 for an image of this compact SNR). The one SNR not recovered in our map happens to be the largest identified by Green (2014) in the GLOSTAR field, with a size of $40' \times 40'$ and so its surface brightness may have fallen below the GLOSTAR detection threshold.

4.6.2 Analysis of mid-infrared images

The correlation of compact radio emission with dust and mid-infrared emission is an indicator of the presence of HII regions and there have been a number of studies that have used this correlation to identify samples of HII regions (e.g., Urquhart et al. 2013; Urquhart et al. 2009; Urquhart et al. 2007; Thompson et al. 2006). In addition to identifying and removing spurious sources (as discussed in Sect. 4.4.2) we have, therefore, also used the mid-infrared images to distinguish between the nature of different kinds of radio emission. In the following two subsections we will give a brief description of the rationale used to define these different kinds of sources. To do this, we split the remaining unclassified radio sources into extended sources (Y-factor > 2) and

[7] Set of Indications, Measurements, and Bibliography for Astronomical Data.

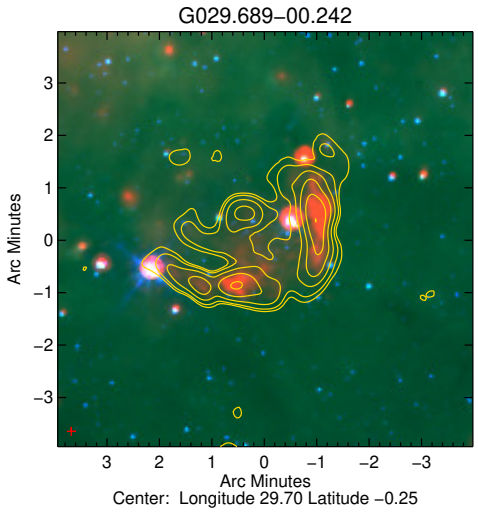

Figure 4.17: Compact SNR G029.689−00.242 identified from the Green (2014) catalog (G029.7−00.3 in their catalog). The background image is a false color composite image produced by combining the GLIMPSE 5.8 and 8.0 μm bands and the MIPSGAL 24 μm band; these are shown in blue, green, and red, respectively. The yellow contours show the distribution of the 5.8 GHz radio emission associated with the GLOSTAR source.

Table 4.8: Summary of emission types. The number in parentheses in the SNR column indicates the number of SNRs identified as large scale structures in Sect. 4.3.2.

Description	Number
Ionization fronts	37
Extended emission sources	62
Planetary nebulae	46
HII regions	231
Radio stars	15
Pulsars	3
SNR	3 (10)

compact sources (Y-factors < 2) because the size and structure of the radio emission itself can provide some useful clues to their nature.

We indicate the emission type attributed to each source and a reference if the identification has come from the literature in the last column of Table 4.7. In Table 4.8 we provide a summary of the number of each type identified.

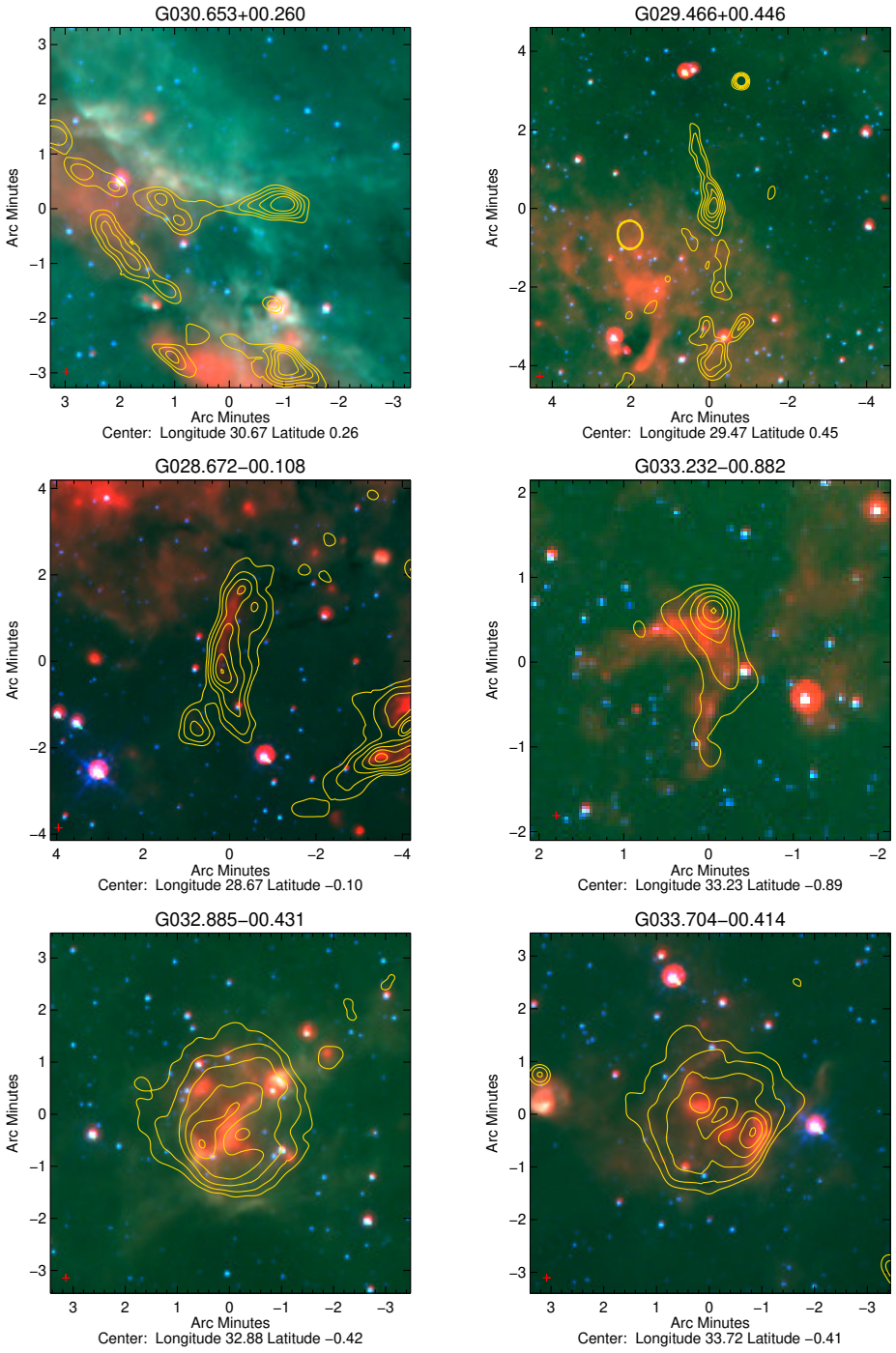

Figure 4.18: Examples of radio sources classified according to their morphology. The upper, middle, and lower panels we show examples of sources classified as extended radio sources, ionization fronts, and evolved HII regions, respectively. In all cases the background image is a false color composite image produced by combining the GLIMPSE 5.8 and 8.0 μm bands and the MIPSGAL 24 μm band; these are shown in blue, green, and red, respectively. The yellow contours show the distribution of the GLOSTAR 5.8 GHz radio emission.

Classification of extended radio sources (Y-factor > 2)

There are 225 radio sources in the catalog that have Y-factors greater than 2 that have not been previously classified (see Sect. 4.6.1 for details). We can assume that any extended radio source is also likely to have thermal bremsstrahlung emission associated with evolved HII regions. In some cases, although the extended radio emission is positionally coincident with the mid-infrared emission, the morphological correlation is poor, and in these cases we classify the emission more loosely as being associated with larger scale extended structures, the nature of which is unclear. In other cases, the radio emission appears to be associated with a section of an ionized rim of an evolved HII region and these are classified as ionization fronts. Although in these cases the radio emission is likely to be associated with an HII region, we are only capturing part of the emission and want to make the distinction between compact HII regions, where we can be confident we are capturing all of the emission, and more extended sources where we are only capturing a less well determined fraction of the total integrated flux density.

We have classified 57 radio sources as being associated with large scale emission and a further 31 sources have been associated with ionization fronts. We have classified 71 of the extended radio sources as HII regions. In Fig. 4.18 we present three-color composite images of two examples of each of these three morphological types of structures. We classify another two sources as potential PNe due to the compact nature of the mid-infrared emission and relative isolation and lack of any nebulosity typically observed towards star-forming regions. The nature of the remaining 68 extended radio sources that are not classified as either extended emission, ionization front, or HII region is still unclear.

Classification of compact radio sources (Y-factor < 2)

There are 1284 compact radio source in the catalog, of which 133 have been previously classified. In the previous section, we have seen that the spectral index is useful for separating the compact radio sources into thermal and non-thermal bremsstrahlung emission. However, PNe and some extragalactic radio sources, known as high frequency peakers (Dallacasa et al. 2000), can have positive spectral indices and so this alone does not definitively identify HII regions. From an inspection of the mid-infrared and submillimeter dust emission towards all of the remaining compact sources (1151), we have identified another 20 HII region candidates. The mid-infrared emission towards these sources generally reveals a bubble-like or complex morphology and is associated with compact dust emission.

We have identified a further 16 sources as PNe candidates due to the correlation between the compact radio and mid-infrared emission and the lack of any evidence of dust emission from the ATLASGAL maps. This will be further explored via the information provided by the GLOSTAR RRL data. We have also classified six more sources as being associated with an ionization front and four others as being extended emission; although in these cases the radio emission is compact, it is coincident with a strong and/or extended 8 μm emission. The nature of the remaining 1105 that are not classified is uncertain. The mean value of the spectral index, for those 523 with this parameter, is ~ -0.5 with a standard deviation of 0.3. This suggests that the vast majority of these unclassified sources are likely to be extragalactic background objects.

To calculate the number of extragalactic background objects expected in the surveyed area

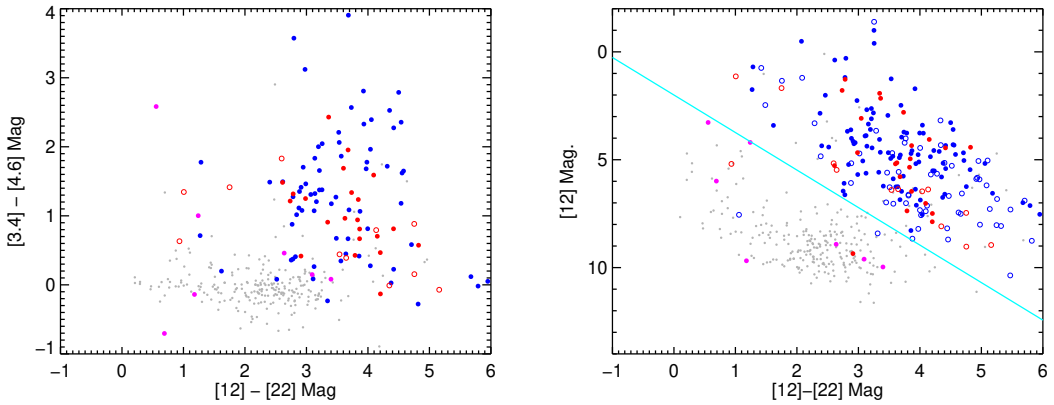

Figure 4.19: Mid-infrared colors of compact GLOSTAR sources associated with a WISE counterpart. Sources classified as HII regions from the literature are shown as filled blue circles, while the HII classified in this study are shown as open blue circles. Similarly, PNe identified by Purcell et al. (2013) are shown as red filled circles, while PNe identified in this work are shown as open circles. Radio stars identified by Purcell et al. (2013) are indicated by filled magenta circles. The smaller gray circles show the distribution of compact sources with a WISE counterpart that we have been unable to classify.

(57600 arcmin^2), we have followed Fomalont et al. (1991). These authors observed an area free of stars, and showed that the number of background objects at 5 GHz above a flux S, is described by

$$\left(\frac{N}{\text{arcmin}^2}\right) = (0.42 \pm 0.05)\left(\frac{S}{30\,\mu\text{Jy}}\right)^{-1.18\pm0.19} . \tag{4.5}$$

Even though our observed frequency is slightly different, this study is the nearest in frequency of this kind to ours. Thus we may use their results for an approximation. Using $S = 450\,\mu$Jy, that is, three times the mean noise level, the number of expected background sources in our map is 990 ± 640. These numbers also suggest that most of the 1151 unclassified sources are extragalactic radio sources.

4.6.3 Mid-infrared colors of radio sources

We have identified WISE counterparts for 988 radio sources from the WISE all sky point source catalog and will use these to investigate their mid-infrared color. Of these only 470 have reliable fluxes in all four bands. This increases to 475 when considering the three longest wavelength bands. We will use these to examine the colors of previously identified HII regions in an effort to confirm the classifications made and to look for possible trends that can be used to define a set of criteria to identify new HII region candidates. In Fig. 4.19 we present color-color and color-magnitude diagrams showing the distribution of all HII regions and PNe identified in the literature (filled blue and red circles, respectively) and from our visual inspection of the mid-infrared images (open blue and red circles, respectively). We also show the distributions of the radio stars (filled magenta circles).

Inspection of these plots shows that the locations in color-color and color-magnitude diagrams of HII regions and PNe identified in our work agree very well with those published in the literature, providing confidence that our classifications are robust. The unclassified radio sources (shown as gray filled circles) and radio stars almost exclusively occupy the same region of the parameter space as field stars and background objects (cf. Figs. B2 and B3 in Csengeri et al. 2014) while the embedded and dust enshrouded objects (HII regions and PNe) have redder colors and are clearly separated from the field stars. This is particularly clear in the color-magnitude plot shown in the lower panel of Fig. 4.19, where all of the HII regions and the vast majority of the PNe are located in an area of parameter space defined by

$$[12]\,\mathrm{Mag.} < 1.74 \times ([12] - [22]) + 2. \tag{4.6}$$

This is also indicated on the lower panel of Fig. 4.19 with a cyan line. Only two PNe (G029.493+00.931 and G033.120-00.894) and two HII regions (G030.246-00.91 and G033.704-00.414) are found to the left of this color criterion. One of the PNe was identified by the CORNISH team, while the other PN and both HII regions have been classified by us. We note that the latter of the two HII regions is very evolved, with a number of WISE sources being located within its boundary. For the other three sources it is possible that these are the result of chance alignments between radio and mid-infrared sources, but it is also possible that the colors of these objects cover a larger range or that the classifications themselves are wrong. The sample is too small to test any of these possibilities statistically, but we note that the one of the PNe identified by the CORNISH team that falls on the wrong side of this criterion (G033.120−00.894) is positionally coincident with the WISE source J185457.96-001424.3. The positional offset is $\sim 3''$ and the photometric flux qualities are classified as AABB, and so the correlation and data are reliable.[8]

4.6.4 New compact HII regions

Our analysis has identified a total of 231 HII regions, of which 46 were previously known (Kalcheva et al. 2018; Ortega et al. 2010; Giveon et al. 2005b) and 90 were proposed as candidates from analysis of the WISE data by Anderson et al. (2014). We have therefore identified 96 new HII regions and confirmed the nature of those proposed by Anderson et al. (2014). The majority of the new HII regions (84) have Y-factors > 1.2 and are therefore resolved in GLOSTAR, and are unlikely to have been picked up in earlier high-resolution surveys where the extended emission is filtered out (CORNISH and MAGPIS). The remaining 12 HII region candidates are unresolved in GLOSTAR and so could have been picked up in earlier surveys. However, their peak fluxes are lower than the sensitivity limit of CORNISH ($7\sigma \sim 2.7\,\mathrm{mJy\,beam^{-1}}$) except in the case of two sources. We checked the CORNISH maps of these two sources but did not find any emission present coincident with the GLOSTAR position (the noise values are 0.34 mJy and 0.32 mJy for G030.371+00.483 and G030.678+00.767, respectively). Both of these sources have mid-infrared

[8] The quality of the profile-fit photometry measurement is indicated by a four letter code (one for each band [W1/W2/W3/W4]; see Sect. 4.4.1). The letters 'A' and 'B' correspond to the sources detected in a particular band with a flux signal-to-noise ratio > 10 and between 3 and 10, respectively. Detections with a quality flag of 'A' and 'B' are considered to be reliable.

Table 4.9: Catalog of new compact HII region candidates. Sources that are bright enough to have been detected by CORNISH are indicated by appending a † to the source name. The fluxes and spectral indices are drawn from the GLOSTAR catalog (i.e., Table 4.7). In the last two columns we indicate the presence of compact (✓), extended (✓✓), or absence (✗) of any corresponding ATLASGAL or WISE emission. In the last column we indicate which are still UCHII region candidates after analysis (see text for details).

GLOSTAR name	S_ν (mJy beam^{-1})	ΔS_ν	α	$\Delta\alpha$	Sub-mm emission	Mid-IR emission	UCHII candidate
G029.367−00.317	2.26	0.24	···	···	✓✓	✓✓	✗
G030.154+00.583	0.55	0.13	···	···	✓	✓	✓
G030.241−00.592	1.73	0.18	−0.12	0.16	✗	✓	✗
G030.371+00.483†	3.47	0.33	···	···	✓	✓	✓
G030.678+00.767†	3.95	0.26	0.07	0.08	✗	✓	✓
G032.051−00.091	2.12	0.24	−0.34	0.15	✓✓	✓	✗
G032.460+00.386	0.67	0.16	···	···	✓✓	✓✓	✗
G033.714+00.256	1.50	0.22	···	···	✓	✓	✓
G034.274−00.151	1.01	0.16	···	···	✓	✓	✓
G034.338−00.694	0.49	0.12	···	···	✓	✓	✓
G034.440+00.060	1.53	0.35	···	···	✓✓	✓	✓
G035.344+00.348	0.46	0.11	···	···	✓✓	✓	✓

counterparts and are hence real. These sources are therefore either both extended and completely filtered out in the CORNISH data or are variable radio sources.

In Table 4.9 we give the peak flux densities and spectral indices of the new unresolved HII regions; only three sources have a detection in THOR and consequently we only have a measurement for the spectral index for three of these HII regions, all of which are consistent with what is expected for optically thin HII regions (i.e., $\alpha = -0.1$). This suggests that these are more evolved than the UCHII region stage, which are usually characterized by optically thick emission ($\alpha \sim$ 1-2; Kurtz and Hofner 2005). We note that no dust emission is detected towards two of these HII regions (G030.241−00.592 and G030.678+00.767), which is also consistent with them being more evolved having already dissipated their natal clump. We further note that the latter of these is also one of the bright sources we would have expected to have been detected by CORNISH, and so the spectral index and absence of dense envelope are consistent with this source being quite evolved and perhaps explains its non-detection in CORNISH.

In Table 4.9 we also list the new HII regions association with mid-infrared and submillimeter emission. As can be seen from this table, all of these sources are associated with mid-infrared emission and the majority are associated with dust emission. The mid-infrared emission looks to be extended in two cases indicating these are likely to be quite evolved HII regions ($> 12''$ in diameter).[9] We have searched in SIMBAD database towards all of these sources. This revealed that G035.344+00.348 had been previously identified as an HII region (Urquhart et al. 2011; MSX6C G035.3449+00.3474). In the last column of Table 4.9 we identify the HII regions that

[9] We have made these associations with dust and mid-infrared emission from inspection of the ATLASGAL and WISE maps as not all emission is captured in the catalogs. All but one of these HII regions has a counterpart in WISE and five have a counterpart in the ATLASGAL CSC.

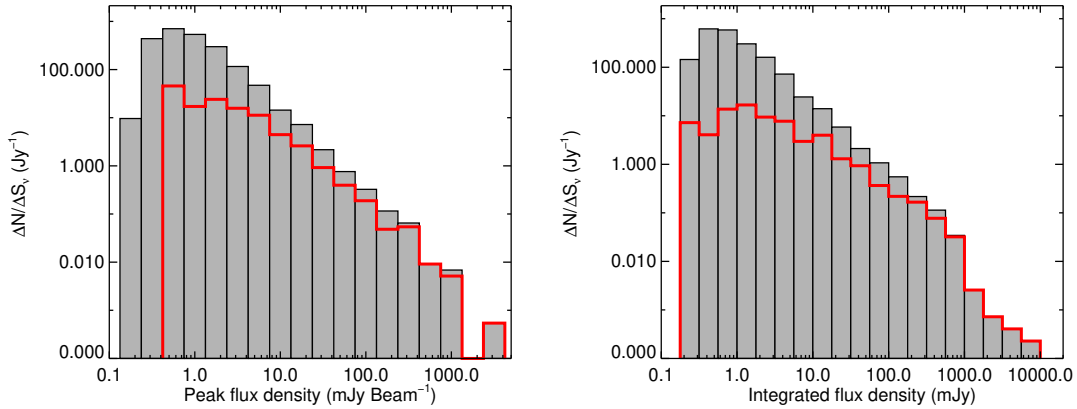

Figure 4.20: Distribution of HII region properties. In the upper and lower panels we show the peak and integrated flux density for the whole GLOSTAR catalog (gray) and those classified as HII regions (red). The bin sizes in both plots is 0.25 dex.

are likely to be good UCHII region candidates; this is done by eliminating sources that are not associated with dust, have spectral indices indicting optically thin emission, or are extended in the mid-infrared, all of which point to sources that are more evolved than the UCHII phase.

4.7 Properties and galactic distribution of the HII regions

From a combination of visual inspection of mid-infrared images and cross-matching with other studies, we have identified a total of 231 HII regions in our catalog. This is the most complete sample of HII regions identified in this part of the sky to date, incorporating HII regions with sizes of a few arcseconds to a few arcminutes. In this section we will provide an analysis of their properties and distributions.

4.7.1 Observed and measured properties

In Fig. 4.20 we present plots of the peak and integrated flux density for the whole GLOSTAR catalog and of the HII regions identified. By comparing these two samples we see that nearly all of the very bright radio sources are associated with HII regions, but that the fraction of the population decreases as the flux decreases and turns over between 0.5 and 2 mJy beam^{-1} and between 1-2 mJy for the peak and integrated flux densities, respectively. This indicates that there are relatively fewer weak HII regions in comparison to the total number of radio sources detected at low surface brightnesses. The fact that we find no HII region with fluxes below the turnover in the peak flux density may indicate a minimum flux density threshold for HII regions. However, this corresponds to a flux density of $\sim$ 0.4 mJy beam^{-1}, which is close to the 3-4σ noise found towards the Galactic mid-plane where the vast majority of HII regions are to be found. Radio sources detected below this threshold are primarily extragalactic background sources located away from the mid-plane where the noise level drops off significantly (see lower panel of Fig. 4.3).

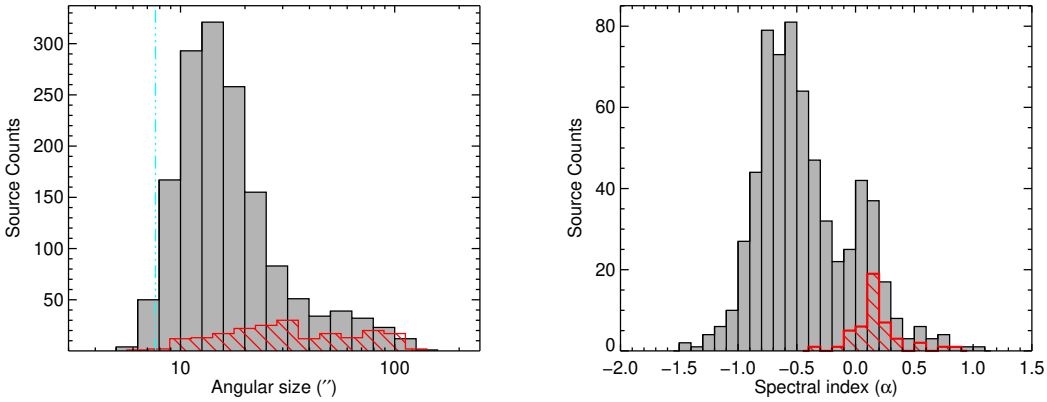

Figure 4.21: Distribution of HII region properties. In the upper and lower panels we show the angular radius and spectral index for the whole GLOSTAR catalog (gray) and those classified as HII regions (red). The dashed-dotted vertical line drawn on the upper panel shows the radius of the beam. The bin sizes used in the upper and lower panels are 0.1 dex and 0.1, respectively.

In Fig. 4.21 we compare the source sizes and spectral indices for the whole GLOSTAR sample and those identified as HII regions. It is clear from the upper panel in this figure that the vast majority of the radio sources are unresolved, with the numbers dropping off steeply for sizes larger than $\sim 15''$. The distribution of the HII region sizes appears to be roughly uniform over the whole range of sizes, which is consistent with other studies (e.g., Kurtz et al. 1999; Masqué et al. 2017), and is to be expected given that the sample is likely to cover a larger range of distances and ages. We also note that the HII regions contribute a significant fraction of the radio sources with sizes above $\sim 30''$, with the others being classified as ionization fronts or extended emission sources. We find very few radio sources with sizes larger than $\sim 100''$, but this is a consequence of the interferometric snapshot observations themselves as the poor *uv*-coverage puts limits on the angular size of structures that can be reliably imaged.

The spectral index distribution of the whole sample is bimodal and peaks at $\alpha = -0.6$ and 0.1; the former is likely to be associated with synchrotron emission from the extragalactic background population, while the latter is likely to be associated with thermal emission from Galactic sources such as HII regions and PNe. It is therefore reassuring to see the distribution of HII regions correlating with the thermal emission peak. This is comparable with the spectral index calculation of the THOR team (Wang et al. 2018), but our sources show a higher density of positive index.

4.7.2 Galactic distribution

The majority of the detected radio sources are likely to be extragalactic, and are expected to be smoothly distributed across the whole sky. However, the HII region population should show significant variations in Galactic longitude and latitude, with peaks that correlate with the most active star-forming complexes and the distribution of molecular material, both of which are concentrated in the Galactic mid-plane.

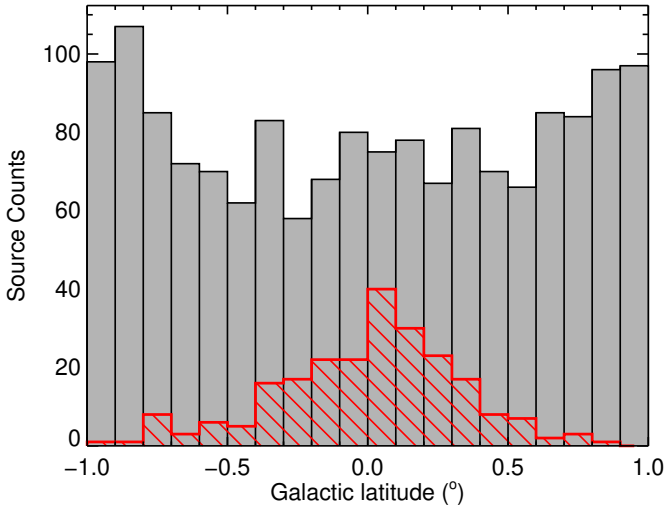

Figure 4.22: Distribution of GLOSTAR radio sources as a function of Galactic latitude. The whole catalog is shown as the gray histogram, while the sources identified as HII regions are shown as the hatched red histogram. The bin size used for both distributions is 0.1°.

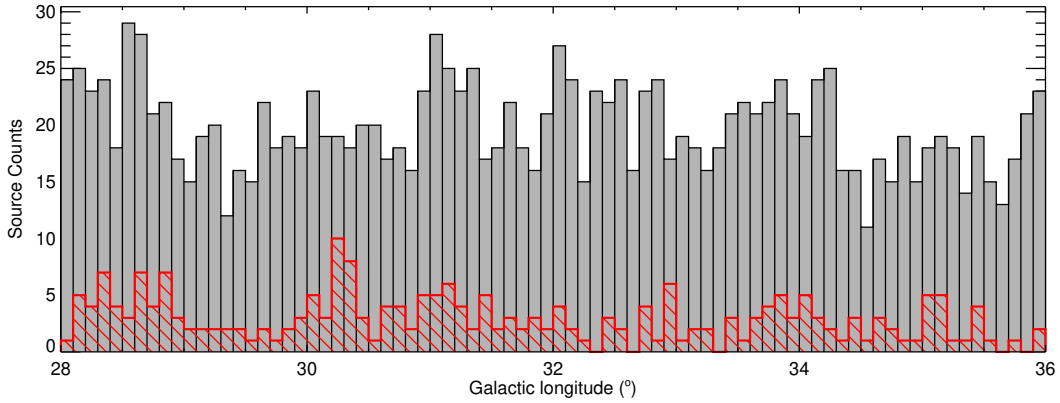

Figure 4.23: Distribution of GLOSTAR radio sources as a function of Galactic longitude. The whole catalog is shown as the gray histogram while the sources identified as HII regions are shown as the hatched red histogram. The bin size used for both distributions is 0.1°.

In Fig. 4.22 we show the Galactic latitude distribution of all the radio sources and the HII region subsample. It is clear from this plot that the HII regions are indeed tightly concentrated around the Galactic mid-plane with a peak at $b \sim 0^{\circ}$, which is consistent with previous studies of HII regions (Urquhart et al. 2013; Kalcheva et al. 2018) and dense, massive star-forming clumps (Urquhart et al. 2014b). The distribution of the full sample is relatively flat for the inner part of the mid-plane but rises close to the edges of the surveyed region ($|b| \sim 1^{\circ}$), which is probably related to the reduction in the local noise value as one moves away from the Galactic mid-plane where much of the extended emission from extended HII regions and supernova remnants is located (see Figs. 4.1 and 4.3).

In Fig. 4.23 we show the distribution of all GLOSTAR sources and the HII regions as a function of the Galactic longitude. Before we discuss the longitude distribution we should bear in mind that since we have excluded emission associated with the 27 large scale structures, many of which are associated with active HII regions, the peaks seen in the HII region distribution are likely to be somewhat suppressed. All of these large scale structures are Galactic in origin and are unlikely to affect the distribution of the extragalactic population, which is rarely resolved.

The distribution of the whole catalog can be described as being broadly flat. As expected, the distribution of HII regions reveals some significant peaks. We note the strong peak near $\ell \sim 30^{\circ}$, which is related to emission from the massive star-forming regions W43-main and W43-south. This region is located where the Scutum-Centaurus arm interacts with the end of the Galactic long bar (Rodriguez-Fernandez and Combes 2008; Nguyen Luong et al. 2011), which is expected to lead to a rise in star formation activity in this area. The latitude and longitude distributions are consistent with the distribution of the high-reliability ($\sigma \geq 7$) CORNISH catalog (Purcell et al. 2013) and the lower frequency THOR catalog (Bihr et al. 2016; Wang et al. 2018), which provides confidence that the catalog we have produced is reliable.

4.8 Summary and conclusions

The GLOSTAR survey is a VLA survey of the Galactic mid-plane 1st quadrant ($-10^{\circ} < \ell < 80^{\circ}$ and $|b| < 1^{\circ}$). In this work we present the radio continuum data for a 16 square degree part of the survey covering 8 degrees in longitude and 2 degrees in latitude and centered on $\ell = 32^{\circ}$, $b = 0^{\circ}$ (i.e., $28^{\circ} < \ell < 36^{\circ}$ and $|b| < 1^{\circ}$). We provide a systematic and effective methodology to characterized the radio emission from tracers of early phases of high-mass star formation: compact, ultra- and hyper-compact HII regions. Our results provide support to previous studies, and produce a list of new HII and UCHII regions candidates previously unknown. The main conclusions are summarized below:

- We have also identified 27 large scale structures that are over-resolved at the GLOSTAR resolution ($\sim 18''$) and where the emission has been broken up into multiple radio sources. In these cases we have regrouped the various fragments and give the parameters for these objects separately. The individual fragments are removed from the final catalogue, which consists of 1582 distinct radio sources. The initial catalog has been cross-matched with other radio and mid-infrared catalogs to verify that the extracted sources are real. We have visually examined mid-infrared and submillimetre images for radio sources without

a counterpart to identify and remove artifacts. We discuss the observed properties of this new catalogue of sources and compare them to previous studies.

- We have used the multi-wavelength analysis and searched the literature to identify the nature of the radio sources. This has resulted in the identification of 231 HII regions. Of these, only 46 had been previously identified with high resolution radio surveys, and a further 90 HII region candidates identified in the mid-infrared by Anderson et al. (2014) have now been confirmed. We have identified a further 96 HII regions not previously known. The majority of the new HII regions are well-resolved (71 with Y-factor > 2) and have been missed by previous high-resolution interferometric surveys due to their lack of short baseline data and consequent poor sensitivity to large angular scales. Twelve of the new HII regions identified are considered to be unresolved (i.e., Y-factor < 1.2), of these we identify 8 UCHII region candidates.

- We have investigated the properties of the full sample of HII regions and compared them to the previously identified samples. The improved flux sensitivity (~100-400 $\mu Jy\,\mathrm{beam}^{-1}$) and sensitivity to larger angular scales (~20-200″) of GLOSTAR compare with other surveys, has increased the number of HII regions in this part of the Galaxy by a factor of 4, which means that we provide new detection of HII regions.

- We have also identified 12 radio stars, 46 PNe, 3 pulsars, 3 compact SNR-candidates and 99 radio sources associated with more extended structures such as the ionization fronts of much more extended HII regions. We are unable to classify 1186 radio sources; these can be broadly categorized as being weak and unresolved, the majority of which are likely to be extragalactic background sources.

CHAPTER 5

The impact of stellar feedback on turbulent motions in ionized and molecular gas

This chapter describes our work related to a turbulence analysis of ionized and molecular gas in order to provide evidence of the stellar feedback role in the turbulent motions of both ionized and molecular gas. In section 5.1 we present the use of the Structure function and Velocity Channel Analysis (VCA) techniques on ionized gas data from the Orion nebula. Section 5.2 contains the analysis performed with SEDIGISM survey data on the ^{13}CO(2-1) molecular emission. Finally, the section 5.3 has the results of the Principal Component Analysis (PCA) on ^{13}CO(2-1) molecular emission from the W43 region.
This chapter includes results from two peer reviewed publications. The first is "Turbulence in the Ionized Gas of the Orion Nebula" (Arthur et al. 2016) published in the Monthly Notices of the Royal Astronomical Society journal Vol. 463, for which I performed two statistical techniques: VCA and computation of the Structure Function were applied to the ionized gas from the Orion Nebula. My main contributions are described from Sects. 5.1.3 to 5.1.6. The second one is "SEDIGISM: Structure, excitation, and dynamics of the inner Galactic interstellar medium" (Schuller et al. 2017) published in the Astronomy & Astrophysics journal Vol. 601, where my main contribution was a calculation of the turbulent profiles using VCA and it is described in Sect. 5.2.2. Finally, results of "Turbulence study of the W43 region" (Medina et al. in preparation) are presented, where stellar feedback effects on turbulence profiles are presented and discussed.

5.1 Turbulence in the Orion Nebula

5.1.1 The Orion Nebula

The Orion Nebula or M42 (see Figure 5.1) is the closest and brightest HII region (~ 440 pc, e.g., O′Dell and Henney 2008) and its geometry, main kinematic features and stellar population are well known (O′Dell 2001). The inner part of the nebula measures some 0.38 × 0.63 pc at the quoted distance and is bright in optical emission lines such as [SII] λ6716 and [SII] λ6731, [NII] λ6583, Hα and [OIII] λ5007. The principal ionizing star is Θ^1 Ori C (a massive star type ~O7), which also possesses a fast stellar wind (O′Dell et al. 2009), and there are also 3 B-type

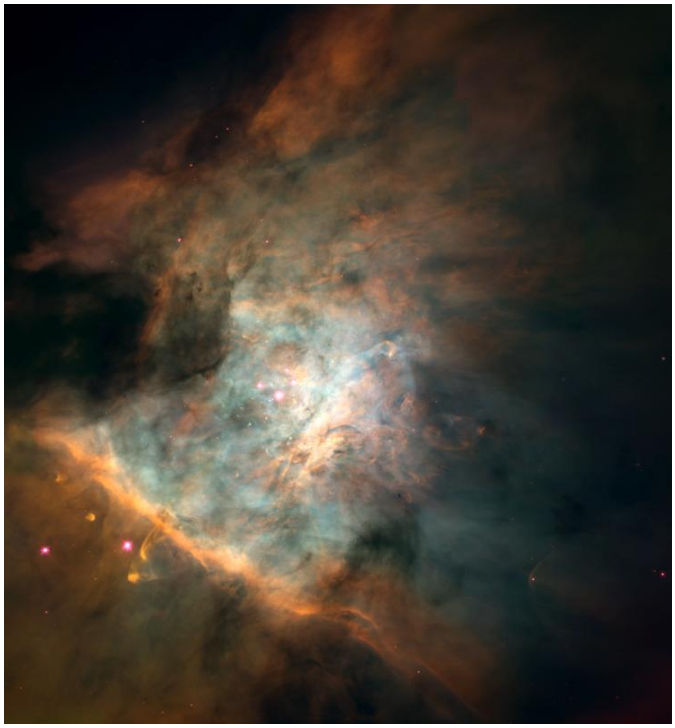

Figure 5.1: Panorama of the center the Orion nebula with the Hubble Space Telescope. Image credits: NASA, C.R. O'Dell and S.K. Wong (Rice University).

stars. These 4 early type stars are the Trapezium cluster. M42 is a site of ongoing star formation on the nearside of the Orion Molecular Cloud (OMC-1) and there is a large population of young stars, some of which are the sources of stellar jets and Herbig-Haro objects and some have associated protoplanetary discs (proplyds, O'dell et al. 1993). M42 is an example of a blister HII region (Zuckerman and Evans 1974; Balick et al. 1974; Tenorio-Tagle 1979; O′Dell et al. 2009) and the photoionized gas is streaming away from the background molecular cloud with blueshifted velocities of order 10 km s^{-1} .

All the previous characteristics make M42 an ideal target to study and understand the relation between a YSO and its surroundings, in particular the turbulence of the ionized gas. Early attempts at characterizing the turbulence in M42 using the [OIII] λ5007 emission line were inconclusive and suffered from poor spatial coverage (von Hoerner 1951; Munch 1958). Detailed kinematic studies of the [OIII] λ5007 emission line (Castaneda, 1988) and the [SIII] λ6312 emission line (Wen and O′Dell, 1993) in the inner region of the Orion Nebula, which decomposed the line profiles into individual components, found evidence for the presence of turbulence. They obtained statistical correlations in the structure functions of the principal line component at spatial scales $< 15''$. However, the power-law indices do not agree with those expected from the standard Kolmogorov theory for isothermal, homogeneous turbulence nor with those predicted by von Hoerner (1951), taking into account projection smoothing. O′Dell and Wen (1992) carried out a similar study for [OI] λ6300. Although their structure functions appear to agree with Kolmogorov theory for a wide range of spatial scales, there is a problem with the line widths, which are much

larger than they should be for the calculated structure function. O'Dell and Wen (1992) conclude that the [OI] emission comes from the vicinity of the highly irregular ionization front, and that the large line widths are due to the acceleration of the gas away from the corrugated surface. These results are still insufficient to characterize the turbulent motion of the ionized gas in M42, and even less to give the physical scales to which the energy that produces the turbulent movement is injected. This problems will be addressed in this section.

5.1.2 Observational ionized gas data

We used high spatial and velocity resolution observations of low- and high-ionization emission lines of the central region of the Orion Nebula. These observations were presented in the form of an atlas of emission lines by Garcia-Diaz and Henney (2007) and Garcia-Diaz et al. (2008). We made use of the Hα, [SII] 6716, 6731 Å, [NII] 6583 Å and [OIII] 5005 Å lines. They were obtained with the echelle spectrograph mounted on to the 4 m telescope at Kitt Peak National Observatory (KPNO; Doi et al., 2004), with supplementary [SII] data observed with the Manchester Echelle Spectrometer attached to the 2.1 m telescope at the Observatorio Astronómico Nacional at San Pedro Mártir (OAN-SPM), Mexico. The data covers the $3' \times 5'$ central (Huygens) region of the Orion Nebula[1] and the Hα, [NII] and [OIII] data consists of 96 approximately $300''$ North-South orientated slits at $2''$ intervals, where the slit width corresponds to $0.8''$. The velocity resolution of these observations is 8 km s^{-1}. The [SII] 6716, 6731 Å dataset has a total of 92 North-South pointings covering the same region, consisting of 37 positions observed at KPNO and 55 positions observed at OAN-SPM. The KPNO [SII] data consists of two disjoint regions, one in the east and one in the west of the nebula, while the OAN-SPM data consists of 35 pointings with a slit width corresponding to $2''$ and 12 km s^{-1} velocity resolution, and 20 pointings with a $0.9''$ slit width and 6 km s^{-1} velocity resolution. The slit length at OAN-SPM is $312''$. We used the calibrated position-velocity (PV) arrays obtained by Garcia-Diaz et al. (2008) from each individual longslit spectrum of each emission line and their velocity moment maps.

5.1.3 Statistical methods

To analyze the velocity fluctuations due to turbulence in the ionized gas, we will use the statitical methods described in section 2.4.2: Velocity Channel Analysis (VCA) of the PV data arrays and second-order structure functions of the velocity centroid maps.

Velocity Channel Analysis

The VCA (see secction 2.4.2) consists of taking the spatial power spectrum of the emission intensity (or brightness) in velocity channels of spectroscopic PV data. First, the PV data is binned into velocity channels of width δv. The relative contribution of velocity fluctuations to fluctuations in the total intensity decreases as the width of the velocity slices increases, because thicker velocity slices average out the contributions of many velocity fluctuations. The thickest velocity slice gives information only on the density spectral index. A velocity slice has width

[1] The total observed area is from $5^h35^m10.4^s$ to $5^h35^m23.2^s$ in right ascension and from $-5°21'36''$ to $-5°26'10''$ in declination. The position of θ^1Ori C is R.A. $5^h35^m16.5^s$ Dec. $-5°23'23''$ (J2000).

$\delta v = (v_{\rm max} - v_{\rm min})/N$, where N is the number of channels and for the spectra used in this work $v_{\rm max} = 70$ km s^{-1} and $v_{\rm min} = -40$ km s^{-1}.

The thickest velocity channel ($N = 1$) corresponds to the total velocity integrated emission-line surface brightness at each pixel along the slit. The thinnest velocity slices for the present work are chosen to have $\delta v = 4$ km s^{-1}, to give a good sampling of the spectrograph velocity resolution (FWHM) of 6–8 km s^{-1} for all the emission lines. To use velocity slices thinner than 4 km s^{-1} would amplify the noise (Medina et al., 2014). The power spectra for each velocity slice of each PV array for a given emission line are summed and normalized by the total power.

Second-order Structure Functions

Returning to the equations of section 2.4.2, the second-order structure function of the velocity centroids, line-of-sight velocity projected into the plane-of-the-sky, is

$$S_2(\boldsymbol{l}) = \frac{\sum_{\rm pairs}[V_c(\mathbf{r}) - V_c(\mathbf{r}+\boldsymbol{l})]^2}{\sigma^2_{\rm vc} N(\boldsymbol{l})} \,. \tag{5.1}$$

In this definition, $\mathbf{r}$ is the two-dimensional position vector in the plane of the sky, while $\boldsymbol{l}$ is the separation vector. The normalization is by the number of pairs of points at each separation, $N(\boldsymbol{l})$, and the variance of centroid velocity fluctuations, $\sigma^2_{\rm vc}$, defined by

$$\sigma^2_{\rm vc} \equiv \frac{\sum_{\rm pixels}[V_c(\mathbf{r}) - \langle V_c\rangle]^2}{N} \,. \tag{5.2}$$

Here, $\langle V_c\rangle$ is the mean centroid velocity

$$\langle V_c\rangle \equiv \frac{\sum_{\rm pixels} V_c(\mathbf{r})}{N} \,. \tag{5.3}$$

The summation in Equation 5.1 is over all data pairs for each separation, $N(\boldsymbol{l})$, while the summations in the centroid variation and mean (Eqs. 5.2 and 5.3) are over the total number of array elements, i.e., valid pixels in the (x, y)-plane.

The intensity weighted structure function is defined by

$$S_2(\boldsymbol{l}) = \frac{\sum_{\rm pairs}[V_c(\mathbf{r}) - V_c(\mathbf{r}+\boldsymbol{l})]^2 I(\mathbf{r}) I(\mathbf{r}+\boldsymbol{l})}{\sigma^2_{\rm vc} W(\boldsymbol{l})} \,, \tag{5.4}$$

where $W(\boldsymbol{l}) = \sum_{\rm pairs} I(\mathbf{r}) I(\mathbf{r}+\boldsymbol{l})$ is the sum of the weights for each separation and $I(\mathbf{r})$, $I(\mathbf{r}+\boldsymbol{l})$ are the weights (i.e., intensities) of each pair of pixels. This form of the structure function obviously favours bright structures and reduces the contribution of fainter regions. This is one way to reduce the contribution of noise to the structure function.

The structure function is affected by small-scale, high velocity features such as jets and Herbig-Haro objects and we aim to eliminate these pixels since they are not associated with the underlying turbulence. The first step is to examine the probability density function (PDF) of the velocity centroid maps and the corresponding velocity dispersion maps of the Hα λ6583, [NII] λ6853,

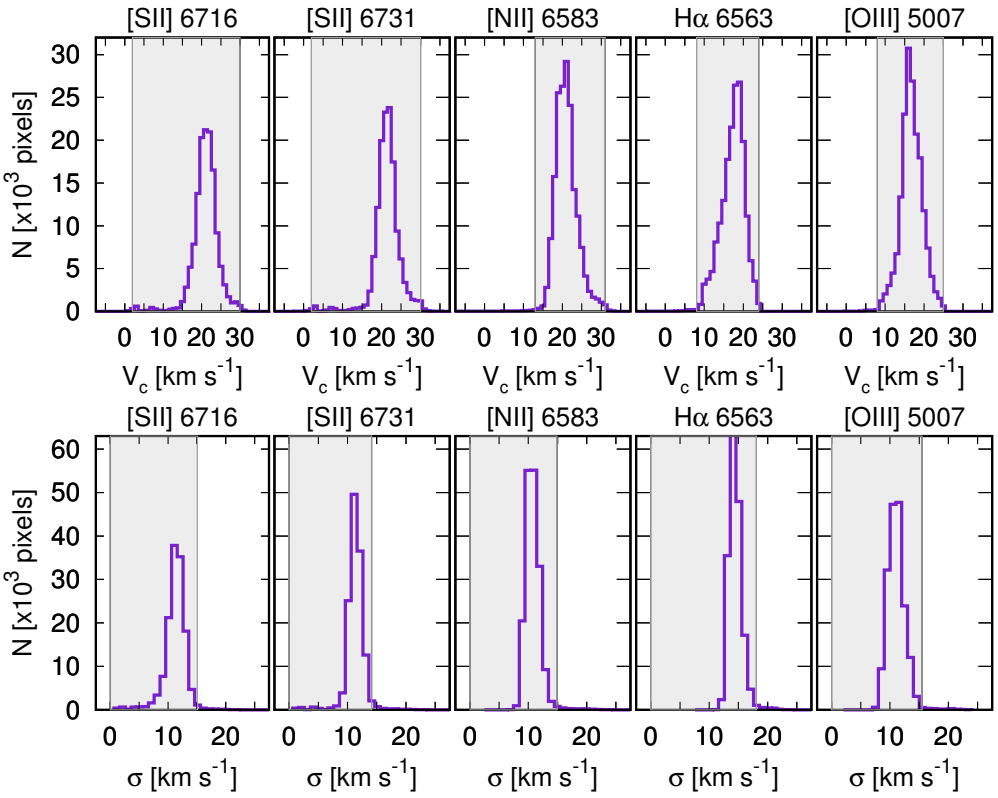

Figure 5.2: Probability density functions (PDF) of the [SII] λ6716 Å and [SII] λ6731 Å [NII] λ6584 Å, Hα and [OIII] λ5007 Å, emission line velocity centroids (top panel) and velocity dispersions (bottom panel). The shaded grey areas indicate the selected ranges of the centroid velocities and velocity dispersions used to create masks. The velocity dispersions have not been corrected for thermal broadening nor for the instrumental width.

[OIII] λ5007, [SII] λ6716 and [SII] λ6731 lines from the emission line atlas published by Garcia-Diaz et al. (2008). In practice, a 2% threshold was uniformly applied to the velocity centroid pdf binned at 1 km s^{-1} resolution. The same threshold was also applied to one side of the velocity dispersion PDF binned at 1 km s^{-1} resolution to eliminate the small number of pixels with anomolously high values. Figure 5.2 shows the initial PDFs of the centroid velocities and the velocity dispersions of the 5 emission lines studied in this paper. Note that the velocity dispersions have not been corrected for the instrumental width (around 3 km s^{-1}) nor thermal broadening. Thermal broadening most affects the Hα line, and is responsible for the peak of the velocity dispersion distribution occurring at σ = 15 km s^{-1}, instead of the lower value of σ = 11 km s^{-1} seen for the other emission lines. Figure 5.2 also highlights in grey the range of values used to create masks of "good" pixels for the subsequent structure function calculations. Pixels having V_c or σ values outside these ranges are excluded from the structure function analysis.

Figures 5.3 and 5.4 show the 2D interpolated velocity centroid maps together with the masks constructed from pixels with extreme values of the centroid velocity or velocity dispersion identified through consideration of the pdfs.

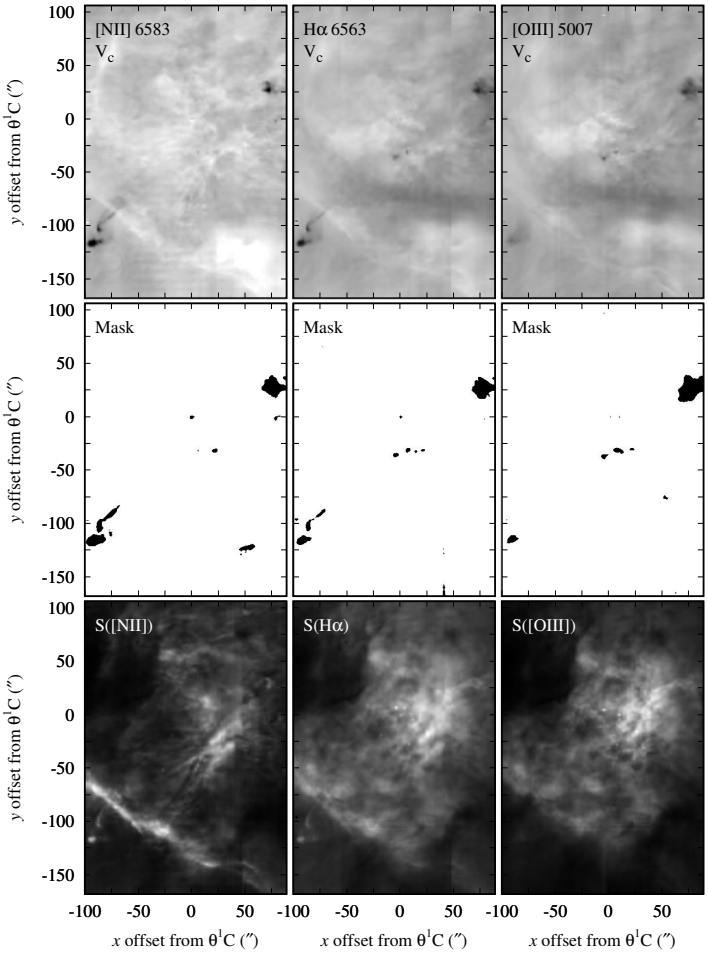

Figure 5.3: Two-dimensional interpolated maps of velocity centroids of the (left to right) [NII] λ6584 Å, Hα and [OIII] λ5007 Å emission lines. The upper panels show the initial 2D interpolated velocity centroid maps with a linear greyscale between −40 and 70 km s^{-1}. The centre panels show the masks obtained by eliminating pixels with extreme values (dark regions) of the centroid velocity (V_c) or velocity dispersion (σ), as indicated in Fig. 5.2. The lower panels show the integrated intensity (surface brightness) with a linear greyscale. In these images, North is up and East is to the left and the x and y scales give the offset in arcsec with respect to the position of the main ionizing star of the Orion Nebula, Θ^1Ori C.

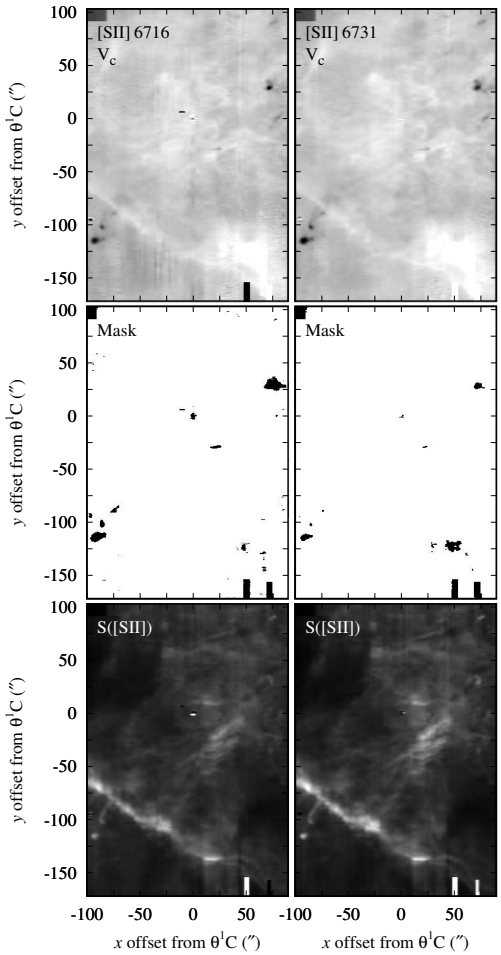

Figure 5.4: Same as Fig. 5.3 but for the [SII] λ6716 Å and [SII] λ6731 Å emission lines.

5.1.4 Application to the Orion Nebula

The Orion Nebula is a complex, inhomogeneous object with ill-defined boundaries. We expect variation in the power-law indices obtained from both the velocity channel analysis and the second-order structure functions depending on position in the nebula due to large-scale inhomogeneities. We estimated the confidence bounds on the power-law indices by resampling.

For the velocity channel analysis, this takes the form of a bootstrap Monte Carlo method, that is, resampling with replacement of the set of PV arrays. The power-law indices of the power spectra resulting from 10 different resamplings of the set of PV arrays (96 arrays in the case of the [NII], Hα and [OIII] emission lines and 20 arrays for [SII]. The variation of these sample power-law indices provides an estimate of the confidence bounds for the power-law index across the Orion Nebula. Furthermore, our longslit spectra are all oriented North-South and so in order to check whether this has any effect on the power-law index, we analyze a supplementary PV dataset of [OIII] λ5007 observations from 18 slit positions perpendicular to the main data set (i.e., oriented East-West).

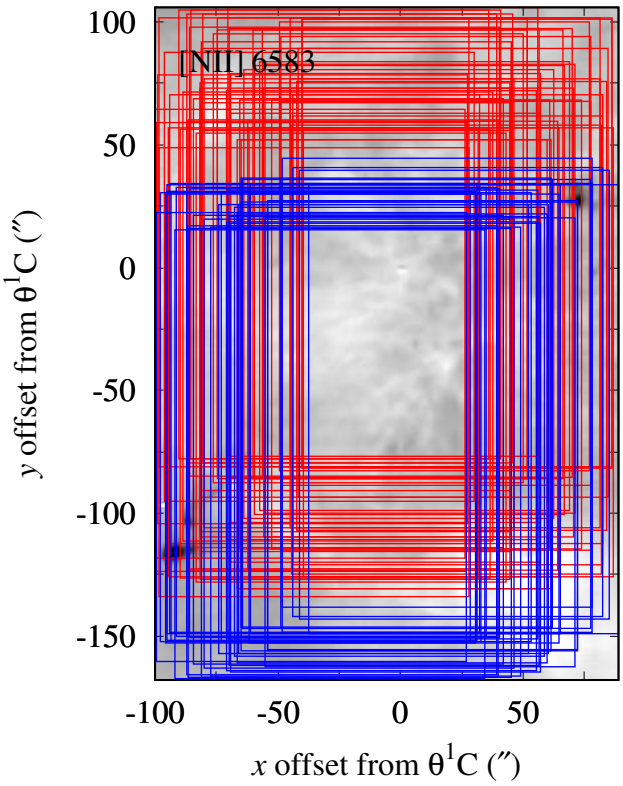

Figure 5.5: Distribution of randomly selected rectangular frames for the structure function calculations for [NII]. The [NII] frames show the spatial separation of the two distinct structure function populations (depicted with red and blue rectangles).

We estimate the effects of large-scale spatial inhomogeneity on the second-order structure function by evaluating $S_2(\boldsymbol{l})$ (see Eqs. 5.1 and 5.4) for 100 distinct, randomly selected rectangular frames within each 2D map. Each frame has two-thirds the x and y dimension of the initial map (see Fig. 5.5). The variation in power-law indices of the smaller maps give us an estimate of the spread of power-law behaviour due to location.

5.1.5 Results

We present the results of the velocity channel analysis in the form of power spectra plotted against wavenumber k in units of number of waves per arcsecond and also number of waves per parsec. The conversion to parsec assumes a distance of 440 pc to the Orion Nebula (O′Dell and Henney, 2008). The second-order structure functions are plotted against separation scale in both arcseconds and parsec.

Velocity Channel Analysis

The 1D, normalised, compensated power spectra $k^3P(k)$ for thin (4 km s^{-1}) and thick velocity channels are shown for all emission lines in Figures 5.6 and 5.7 and for the [OIII] horizontal slits

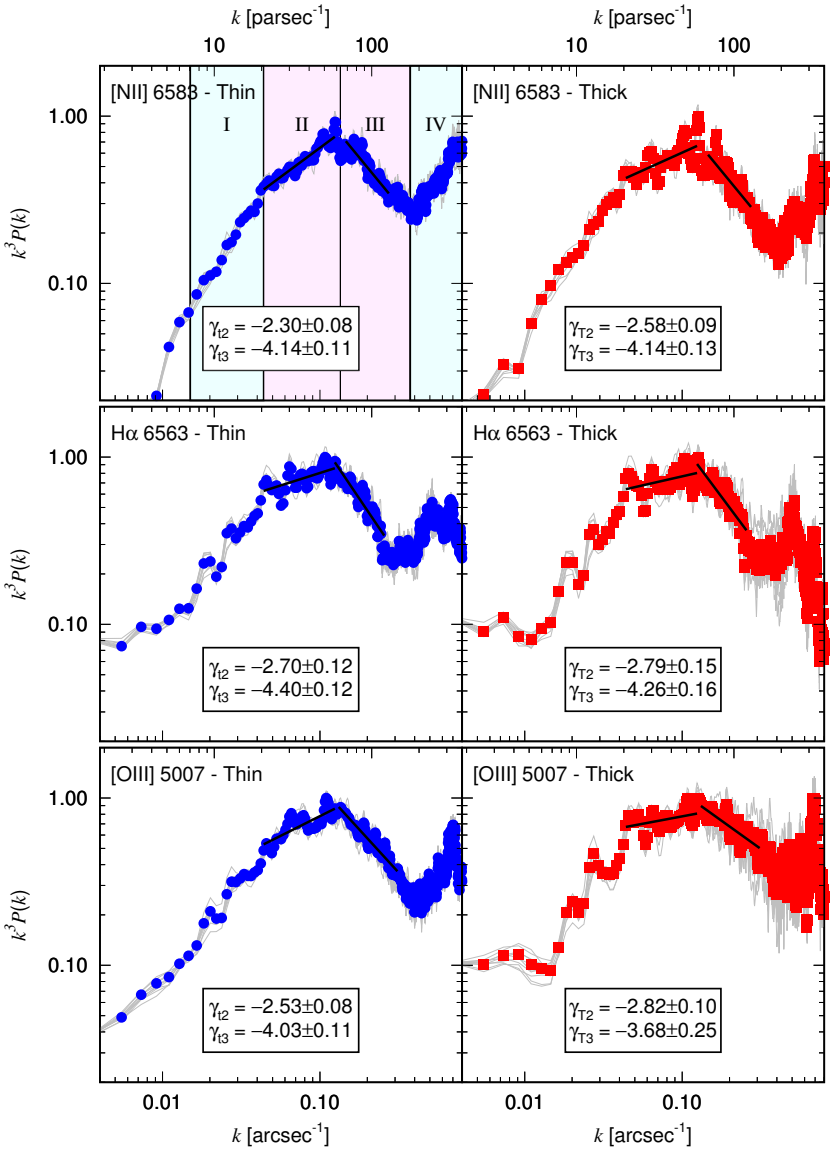

Figure 5.6: Compensated power spectra $k^3P(k)$ of the velocity channels for the [NII], Hα and [OIII] emission lines for thin (32 velocity slices) velocity slices and thick (one velocity slice) in the velocity range −40 to 70 km s^{-1}. Four different slope regimes and their approximate wavenumber ranges can be identified for each emission line and are indicated approximately in the first panel only as regimes I, II, III and IV. The blue symbols and red symbols show the combined compensated power spectra for the set of 96 different observed longslit data. The grey lines show the combined compensated power spectra for a random selection (with replacement) of 96 observed longslit data. Also shown are the least-squares fits to the data points for wavenumber ranges corresponding to power-law indices steeper than −3 and power-law indices shallower than −3 in regimes II and III. The errors on the power-law indices come from the variation of slope among the set of grey lines.

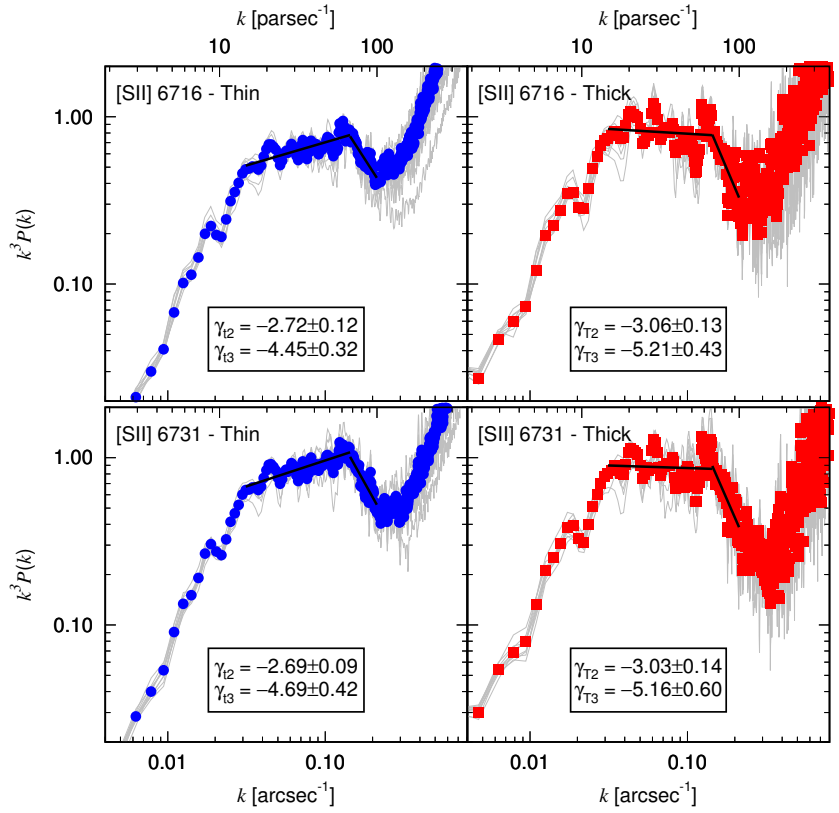

Figure 5.7: Same as Fig. 5.6 but for the [SII] 6716 and [SII] 6731 emission lines.

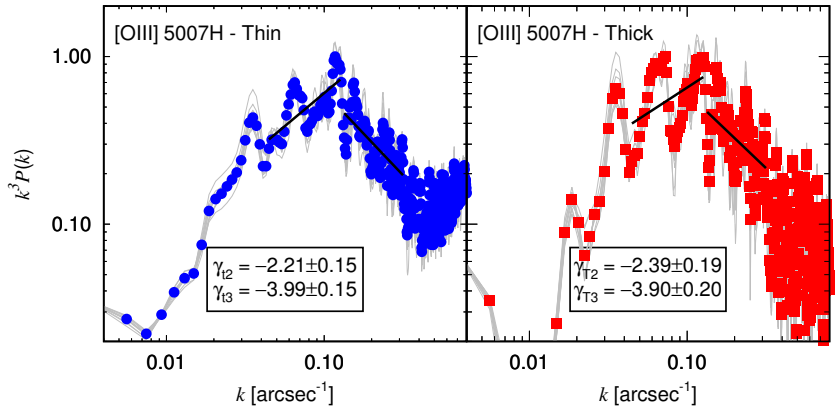

Figure 5.8: Same as Fig. 5.6 but for the [OIII] 5007 horizontal slits.

in Figure 5.8. The coloured points represent the average power spectrum of 96 distinct slits, in the case of the [NII] λ6583, Hα, and [OIII] λ5007 emission lines, where the slits cover uniformly the region shown in the velocity centroid maps. In the case of the two [SII] emission lines, only the 20 highest resolution slits are used, since the other slits are too affected by noise at high wavenumber.

By plotting $k^3P(k)$ it becomes very apparent that there is a break in the power-law behaviour around wavenumber $k = 0.124$ arcsec^{-1} ($k = 0.144$ arcsec^{-1} for the [SII] lines). This corresponds to a size scale of $l \sim 7'' - 8''$ (~0.02 pc). Indeed, the behaviour of the power spectrum for all the emission lines can be divided into four wavenumber ranges, which we have indicated by I, II, III and IV in the first panel of Figure 5.6 and are the same for all emission lines. Regimes I and II correspond to wavenumbers smaller than the break point, while regimes III and IV correspond to wavenumbers larger than the break point.

For wavenumbers in regime II, the power-law indices of all the power spectra for all the emission lines are all $\gamma > -3$ for both the thin velocity channels and the thick channels, with the exception of the [SII] emission lines, where the power law index is ~ -3. In all cases the power laws for the thin channels are less steep than those of the thick channels. For wavenumbers in regime III, the power-law indices are all steeper than the critical value $\gamma = -3$, indicating that there is very little power at small spatial scales. Noise dominates the spectra in regime IV. The spectral indices in regimes I and IV are similar and are both shallow indicating that the velocity fluctuations at the largest and smallest scales are uncorrelated.

The overall shape of the compensated power spectra are qualitatively similar for all lines and for both thin and thick slices. In particular, the regime II, occurring between 7–8$''$ (~0.02 pc) and 22$''$ (~0.05 pc), indicating that it must be a feature of the emissivity fluctuations in the nebula. The power spectrum of the thin slices is generally shallower (less negative) than that of the thick slices, which is indicative of the additional effect of velocity fluctuations. One possible driver of the turbulent motions in the nebula could be the fractal nature of its molecular density that accelerates it on multiple scales, from the global outward radial expansion of the HII region (which in Orion is a highly one-sided champagne flow) down to photoevaporation flows from individual globules. One piece of evidence to the connection between molecular density fluctuations and ionized velocity fluctuations is that Kainulainen et al. (2017) find correlation lengths of order 0.08 pc for the separations of molecular cores along the ridge that lies behind the Orion Nebula, which is similar to the correlation lengths in this regime.

The power spectra resulting from 10 different slit resamplings are shown in grey in Figures 5.6 and 5.7. The spread in power-law indices we obtain from these resamplings gives an estimate of the confidence bounds on the spectral index of the average power spectrum. This spread is not primarily due to observational uncertainties, which are negligible for all but the very smallest size scales (largest wavenumbers) but rather to large-scale inhomogeneity of the power spectrum depending on the position of the observations.

Second-order Structure Functions

We use Equation 5.1 to calculate the second-order structure functions of the velocity centroid maps for the [NII] λ6583, Hα, [OIII] λ5007, [SII] λ6716 and [SII] λ6731 emission lines. Figures 5.9 and 5.10 (top panels) show the complete structure function of the pdf-selected pixels, together

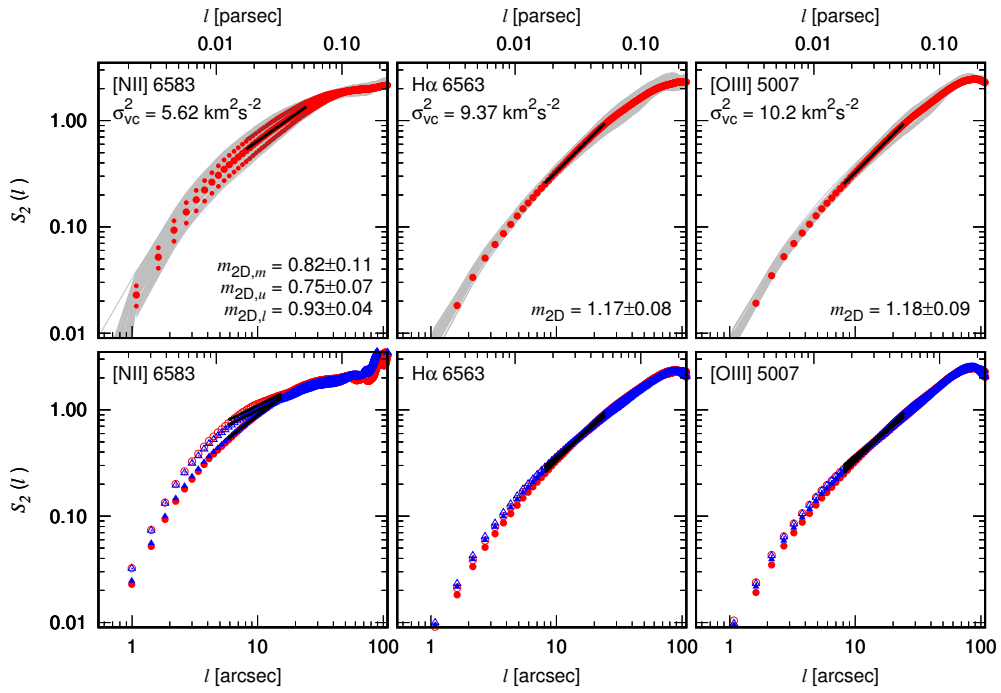

Figure 5.9: Second-order structure functions for the velocity centroid images of the [NII] λ6583, Hα and [OIII] λ5007 emission lines considered in this work. Top panel (pdf-selected pixels): the structure functions of a random sample of 100 rectangles are shown with grey lines, the combined structure function is shown with red circles and the power-law fit to the combined structure function is shown with a thick black line. The power-law index of the fit and the standard deviation obtained by considering fits to the individual rectangle structure functions is indicated in each panel. The [NII] emission line shows a clear bimodal distribution and so fits to the upper and lower parts (60 and 40 rectangles, respectively) were also obtained separately (small red circles). Lower panel: number-of-points weighted structure functions (solid symbols) and intensity weighted structure functions (open symbols). Red circles are for the pdf-selected pixels from the velocity centroid maps whereas blue triangles are for the full velocity centroid map with no pixel selection. A pixel width is equivalent to 0.54″ in the corresponding velocity centroid maps from which these structure functions were obtained.

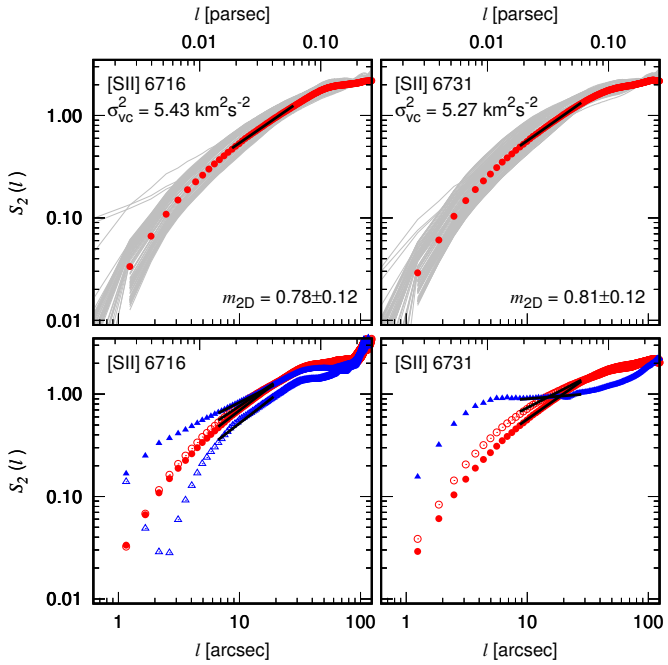

Figure 5.10: Same as Fig. 5.9 but for the [SII] λ6716 and [SII] λ6731 emission lines. A pixel width is equivalent to 0.62″ in the corresponding velocity centroid maps from which these structure functions were obtained.

with the structure functions obtained from 100 smaller rectangular frames within the velocity centroid map (see Fig. 5.5). The fit to the power-law index of the structure function is performed over the spatial separations corresponding to regime II of the velocity channel analysis (roughly $8'' < l < 22''$ for the [NII], Hα and [OIII] emission lines, and $7'' < l < 32''$ for [SII] emission lines; see Fig 5.6). The noise, estimated to be equal to the one-pixel separation value $S_2(1)$, has been subtracted from the structure function. In the figures, we only plot the structure function up to spatial separations $l = 120''$. Above this value, the structure function falls away steeply.

Unlike in the case of the power spectra, the structure functions show no clear break at a scale of $\sim 8''$. The power-law fit to scales $\sim 8''$ is not too bad a fit to smaller scales also. The structure function has a slight negative curvature, giving gradually steeper slopes at smaller scales. The more pronounced steepening below $2''$ is due to the spatial resolution of the observations and corresponds to the region where the seeing and inter-slit separation become important.

The steepest power-law indices over the fit range are for the Hα and [OIII] emission lines. The form of the structure function curves is the same for both emission lines and the value of the power-law index is $m_{2D} \sim 1.2 \pm 0.1$ in both cases. The two [SII] emission lines have very similar structure functions to each other. Their slopes are shallower than those of the Hα and [OIII] structure functions, having $m_{2D} \sim 0.8 \pm 0.1$. There is considerable variation at the smallest scales in the structure function among the different randomly selected frames. Finally, the structure functions for the [NII] line can be divided into two distinct populations: one set corresponds to frames selected from the upper part of the velocity centroid map, the other to frames from the

lower half (see Figure 5.5). One set has a power-law index similar to that of the [SII] lines, while the other is intermediate between the [SII] and Hα cases.

In the lower panels of Figures 5.9 and 5.10 we show the alternative structure functions, intensity weighted structure functions from Equation 5.4, for the same emission-line velocity centroid maps. The solid red circles show the same pdf-selected structure functions as in the upper panels, while the solid blue triangles show the structure functions obtained when all the pixels are used. There is little difference between the two structure functions for the [NII], Hα and [OIII] emission lines but the [SII] structure functions show considerable differences. This is because more pixels are eliminated from the velocity centroid maps on the basis of the pdf analysis for the [SII] lines: some of these pixels correspond to high-velocity features, such as HH objects, while others correspond to numerical noise. Evidently, these pixels influence the structure function.

Also in the lower panels of Figures 5.9 and 5.10, we plot the intensity weighted structure functions of the corresponding cases. The figures show that once again, for the Hα and [OIII] emission lines, there is little difference between these new structure functions (open symbols) and the number-of-points-weighted structure functions (solid symbols). However, this time the [NII] structure functions are different, with the intensity weighting producing structure functions with shallower slopes (smaller power-law indices). For the shorter wavelength [SII] λ6716 case, the intensity weighting makes little difference to the PDF-selected structure function (red circles) but does reduce the noise contribution to the full structure function (blue triangles) and leads to a similar power-law index to the PDF-selected cases over the fitted range. For the longer wavelength [SII] λ6731 case, the intensity weighting produces a shallower power law, even for the PDF-selected case (red circles). It is not possible to plot the intensity weighted structure function for the full set of pixels on the same scale because the contributions of regions of bad pixels both in the velocity centroid map and the intensity map dominate at all scales.

5.1.6 Comparison with previous results

Previous studies of the velocity structure function in Orion have been carried out based on slit spectra (Castaneda, 1988; O′Dell and Wen, 1992; Wen and O′Dell, 1993). Table 5.2 compares these results with our own for different emission lines, ordered from lower to higher ionization. In spite of the differences in methodology, a broad agreement is seen, with both the magnitude of the velocity dispersion and the steepness of the structure function slope increasing with ionization. The most directly comparable methodology to our own is that of O′Dell and Wen (1992) who used the flux-weighted mean velocity of the OI λ6300 line. The fitted range of $6''$ to $85''$ extends to larger scales than in studies of other lines, and this biases the slope determination towards lower values due to the slight curvature of the structure function.

The other studies are harder to compare with our own since they are based on multi-component Gaussian fits to the line profiles. In order to check the effects of this methodological difference, we have calculated the OIII structure function for the strongest component of the three-Gaussian decomposition of our line profiles, with results that are also included in Table 5.2. We find a slightly larger plane-of-sky velocity dispersion and shallower structure function than we found using the mean velocity of the entire profile, which is consistent with the results of Castaneda (1988) for the same line. Experimentation shows that this is partly due to under-determination of the Gaussian fits, particularly for components A and B, which are severely blended at most

positions. This results in a fitting degeneracy between the velocity separation $v_A - v_B$ and the flux ratio F_A/F_B of the two components, which spuriously contributes to the variation in v_A.

By the other side, the spectral index of the 3D power spectrum of the underlying velocity fluctuations from simulations by Medina et al. (2014) was $n \sim -3.1$, which is shallower than that predicted by Kolmogorov theory. The velocity channel analysis of the emission lines of the heavier ions, [OIII], [NII] and [SII], the measured values of the thin velocity slice spectral index γ_t agree to within 0.1 with the values derived using the formulae highlighted in Table 5.1 using the simulation value of n. On the other hand, the second-order structure functions proved less capable of reliably recovering the 3D velocity power spectrum. In the results from this work, the VCA spectral indices show some similarities but also some differences with respect to those obtained from the simulations. We will discuss only the heavier ions, since Hα is seriously affected by thermal broadening. To begin with, for the simulations, we found that the [NII] and [SII] values of γ_T (thick velocity slice spectral index) could be considered "shallow" ($\gamma_T > -3$), while the [OIII] had a "steep" spectral index ($\gamma_T < -3$). For the compensated power spectra $k^3P(k)$, a power-law index equal to the critical value $\gamma_T = -3$ would appear horizontal. We remark that the 2D power spectra of the simulations are not at all noisy, unlike the 1D power spectra presented here and, moreover, a single power law is sufficient to cover most of the wavenumber range. In contrast, our observationally derived power spectra can be split into different regimes where different power laws apply with sharp breaks between them (see Figs. 5.6 and 5.7). In the principal wavenumber range the spectral index of the thick velocity slices, γ_T, is "shallow" for [NII] and [OIII] but apparently steep for [SII]. Thus, while there is agreement in the [NII] spectral index between observational and simulation results, the [OIII] spectral index is shallower in real life. The spectral index of [SII] is misleading, since this emission line is affected by collisional deexcitation for electron density greater than about 10^3 cm^{-3}, which will suppress power at higher k (smaller length scales). This was not an issue in the numerical simulations because the electron densities were lower than in the Orion Nebula.

The simulation show a clear sequence like $1 > m_{2D}(\mathrm{OIII}) > m_{2D}(\mathrm{H}\alpha) > m_{2D}(\mathrm{NII}) > m_{2D}(\mathrm{SII})$, while the observational results, summarized in Table 5.3, show a similar sequence but the absolute values are slightly different. We note that the offset of approximately 0.3 in m_{2D} values between simulation and observational results is no larger than the spread in observationally derived results obtained with different methodologies. The simulation structure function follows a clear power law over a wide range of spatial separations (straight line in log-log space) whereas the observational structure function has a slowly varying power law as a function of separation scale.

Both the structure function power-law indices and the VCA $\gamma_t - \gamma_T$ values are potential diagnostics of the underlying velocity power spectrum. The differences we find in these quantities between the simulations and the observations are consistent with a steeper velocity spectrum for the real nebula. On the other hand, the thick slice VCA spectral index γ_T, which is simply the spectral index of the surface brightness power spectrum, is a diagnostic of the underlying emissivity power spectrum. The simulation results give very different values for the [NII] and [OIII] thick-slice spectral indices, suggesting a very different spatial distribution for these two emission regions. The observational values are more similar for [NII] and [OIII]. It is important to highlight the simulations are not a model for the Orion Nebula. The simulations omitted several physical processes, the real Orion Nebula contains a large population of low-mass stars, some of which are sources of jets and Herbig-Haro objects. Although the effect of such structures

Table 5.1: Description and Relationships between Power-Law Indices

Description	Power-law Index	Relationship		Kolmogorov Value
3D emissivity fluctuations	$n_{\rm E}$			
3D velocity fluctuations	n	$n = -3 - m_{\rm 3D}$	*(a)*	$-11/3$
3D second-order structure function	$m_{\rm 3D}$	$m_{\rm 3D} = -3 - n$	*(a)*	$2/3$
2D second-order structure function	$m_{\rm 2D}$			
Projection Smoothing		$m_{\rm 2D} = m_{\rm 3D} + 1$	*(b)*	$5/3$
Sheetlike Emission		$m_{\rm 2D} \sim m_{\rm 3D}$	*(c)*	$2/3$
Intensity fluctuations	γ			
Very Thick Velocity Slice	$\gamma_{\rm T}$	$\gamma_{\rm T} \sim n_{\rm E}$	*(d)*	
Thin Velocity Slice	$\gamma_{\rm t}$			
Shallow density $n_{\rm E} > -3$		$\gamma_{\rm t} = \gamma_{\rm T} + m_{\rm 3D}/2$	*(d)*	
Steep density $n_{\rm E} < -3$		$\gamma_{\rm t} = -3 + m_{\rm 3D}/2$	*(d)*	$-8/3$

(a) Kolmogorov (1941b)
(b) von Hoerner (1951)
(c) Castaneda and O'Dell (1987)
(d) Lazarian and Pogosyan (2000b)

Table 5.2: Comparison of structure function slopes

Reference	Ion	Method	σ^2 (km^2 s^{-2})	Range ($''$)	Slope
O'Dell and Wen (1992)	OI	Mean	3.0	6–85	0.68
This work	SII	Mean	5.4	7–32	0.80 ± 0.12
This work	NII	Mean	5.6	8–22	0.82 ± 0.11
Wen and O'Dell (1993)	SIII	Comp A	13.8	5–20	0.92
This work	Hα	Mean	9.4	8–22	1.17 ± 0.08
This work	OIII	Mean	10.2	8–22	1.18 ± 0.09
Castaneda (1988)	OIII	Comp A	13.7	3–15	0.86 ± 0.05
This work	OIII	Comp A	15.3	3–15	0.73 ± 0.05

is spatially limited and we have excised extreme velocity features from our sample used to calculate the structure function, there still could be a small contribution from bright features that lie more-or-less in the plane of the sky.

5.1.7 Conclusions

We have used statistical analysis of high-resolution spectroscopic observations of optical emission lines in the central 0.4×0.6 pc ($3' \times 5'$) of the Orion Nebula. In order to characterize the turbulence in the ionized gas, we have applied the second-order structure function of velocity centroids, which gives the variation as a function of plane-of-sky separation of the differences in

Table 5.3: Structure function power-law indices and relationships

Emission Line	m_{2D}	m^*_{3D}	
		$m_{2D} - 1$	m_{2D}
[SII] λ6716	0.78 ± 0.12	...	0.78 ± 0.12
[SII] λ6731	0.81 ± 0.12	...	0.81 ± 0.12
[NII] λ6583	0.82 ± 0.11	...	0.82 ± 0.11
Hα λ6563	1.17 ± 0.08	0.17 ± 0.08	...
[OIII] λ5007	1.18 ± 0.09	0.18 ± 0.09	...

average line-of-sight velocity, and the VCA, which compares the spatial power spectrum slope of velocity-resolved and velocity-integrated emission profiles of the same line. We provide good evidence of the scales for the turbulence energy injection and that the VCA is a more reliable technique to characterize the velocity fluctuation in a turbulent gas. Our principal empirical findings are as follows:

- Our results show that the VCA technique is more reliable means to determine the spectrum of velocity fluctuations in the ionized gas, and we find consistent evidence from both low and high ionization lines for a Kolmogorov-type spectrum ($\delta u \sim l^{1/3}$) for length scales, l, between 0.05 pc ($\approx 22''$) and 0.02 pc ($\approx 8''$). This regime could be related with the correlation lengths of the order of 0.08 pc for the separations of molecular cores along the ridge that lies behind the Orion Nebula (Kainulainen et al. 2017). Unfortunately, VCA can not be applied if the thermal or instrumental line width is larger than the velocity differences of interest, which rules out its application to the Hα line and to scales smaller than 0.02 pc.

- The structure functions show that the changes in slopes are difficult to interpret because of the influence of projection smearing and sensitivity to details of the observational methodology.

- The characteristic length of 0.05 pc is special in at least two ways, corresponding to both the autocorrelation scale of velocity differences for low-ionization lines (Figs. 5.9 and 5.10) and also a break in the power spectrum of surface brightness fluctuations in all lines (Figs. 5.6–5.8). We suggest that this is the dominant scale for density fluctuations in the nebula and is also the main driving scale of the turbulence. A further break in the surface brightness power spectra occurs at the smaller scale of 0.02 pc, but there is no obvious feature in the structure functions at this scale.

- Comparison of the application of turbulent diagnostics to numerical simulations (Medina et al., 2014) with application of the same diagnostics to Orion leads us to conclude that even the high-ionization line emission (e.g., [OIII]) is confined to a thick shell and does not fill the interior of the nebula. Furthermore, the underlying power spectrum is shallower in the simulations, implying that small-scale turbulent driving is less important in the nebula than it is in the simulations.

- The velocity fluctuations are not homogeneous on the largest scales, but rather that the turbulent conditions themselves vary, both across the sky and along the line of sight, on scales larger than the velocity autocorrelation length of 0.05–0.15 pc.

5.2 Turbulence within molecular clouds in the SEDIGISM survey

5.2.1 Observational molecular gas data

Many large-scale surveys of the Galactic plane have been conducted recently, allowing for rapid progress in the study of the origin and life-cycle of molecular clouds due to their importance related with the evolution of the interstellar medium. Nevertheless, a sub-arcminute resolution global view of the large-scale distribution of molecular gas, from the diffuse medium to dense clouds and clumps, and of their relationship to the spiral structure, has been missing.

The SEDIGISM (Structure, excitation, and dynamics of the inner Galactic interstellar medium; Schuller et al. 2017) survey complements galactic surveys available such as the GRS (Galactic Ring Survey; Jackson et al. 2006) in order to expand the view of the large-scale distribution of the molecular gas in the Milky Way. It covers 78 deg^2 of the inner Galaxy ($-60^\circ \leqslant l \leqslant 18^\circ$,$|b| \leqslant 0.5^\circ$; see Fig 5.11). The observational setup covers the ^{13}CO(2–1), which has low to moderate optical depths and higher critical density that makes it an ideal tracer of the cold and dense interstellar medium, and C^{18}O(2–1) lines, plus several transitions from other molecules. The spectroscopy data of the SEDIGISM survey are crucial to obtain information about distances and gas dynamics. The data were collected between 2013 and 2015 with the 12 m diameter Atacama Pathfinder EXperiment telescope (APEX, Güsten et al. 2006), located at 5100 m altitude on Llano de Chajnantor, in Chile. They were calibrated using the CLASS software from the GILDAS package[2]. The final angular resolution of the ^{13}CO(2–1) data is $30''$, for C^{18}O(2–1) and the other transitions is possibly higher. The average 1σ sensitivity is 0.8 K at 0.25 km s^{-1}.

This work focuses on the ^{13}CO(2–1) emission in a science demonstration field ($-20^\circ \leqslant l \leqslant -18.5^\circ$). This field contains a total of 182 molecular cloud structures extracted with the SCIMES algorithm (Spectral Clustering for Interstellar Molecular Emission Segmentation; Colombo et al. 2015). This algorithm applies the spectral clustering paradigm in order to find relevant structures (i.e. clouds) within dendrograms of emission (Rosolowsky et al. 2008), reproducing the work of the human eyes for the emission segmentation. It considers the dendrogram tree of the 3D structures in the data cube in the broader framework of graph theory, and groups different leaves (in this case, the emission peaks) together into clusters of leaves, based on some criteria (e.g. intensity, luminosity, or volume).

The properties, provided by the dendrogram algorithm for each cloud, are: centroid position in Galactic coordinates, velocity V_{LSR}, velocity dispersion σ_V, intensity-weighted semi-major and semi-minor axes, and respective position angle. Following Rosolowsky and Leroy (2006), the aspect ratio is then computed as the ratio of the major/minor axis. Combining these basic properties we can obtain derived properties such as CO luminosity, masses from the CO luminosity and from the virial parameter, molecular gas mass surface densities.The kinematic distances were derived using the Galactic rotation model of Brand and Blitz (1993). These properties are

[2] http://www.iram.fr/IRAMFR/GILDAS/

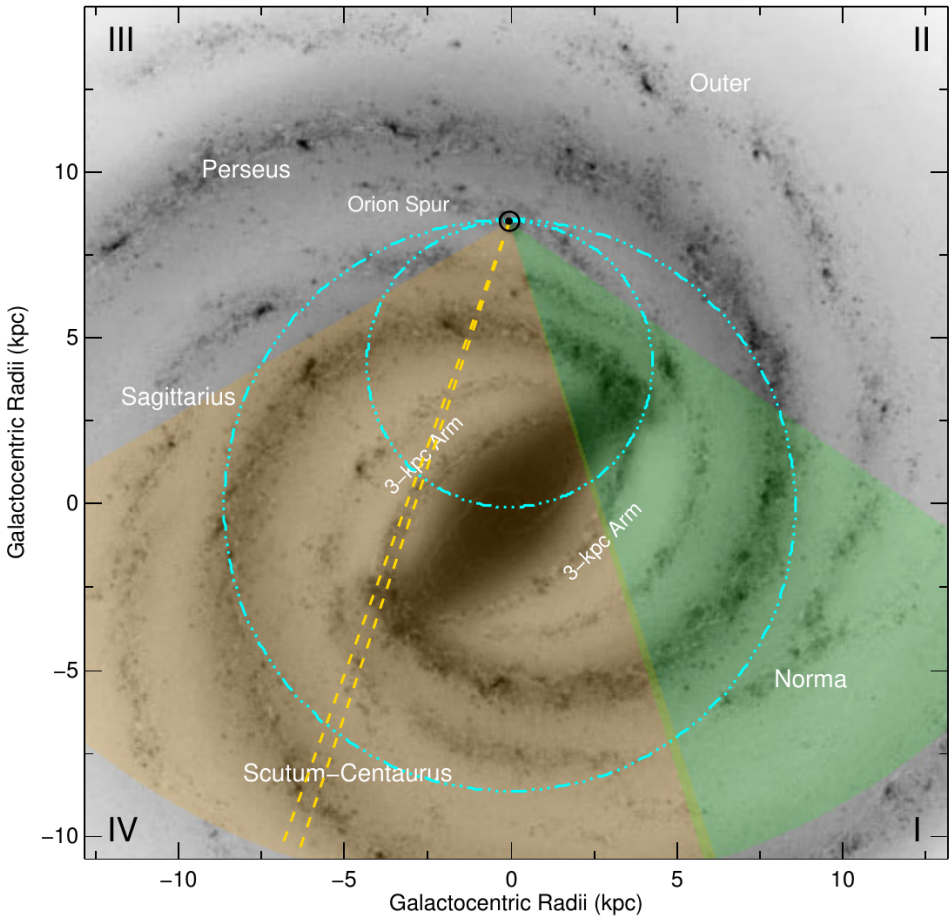

Figure 5.11: Coverage of the SEDIGISM and GRS surveys, shown respectively in orange and green shading, overlaid on the top down image of the Milky Way produced by Robert Hurt of the Spitzer Science Center in consultation with Robert Benjamin (Churchwell et al. 2009). The large and small cyan circles indicate the Solar Circle and the position of the tangent points (maximum radial velocity), respectively, while the dashed yellow lines demarcate the region selected as the science demonstration field (see Sect. 5.2.1). The position of the Sun is indicated by the ⊙ symbol.

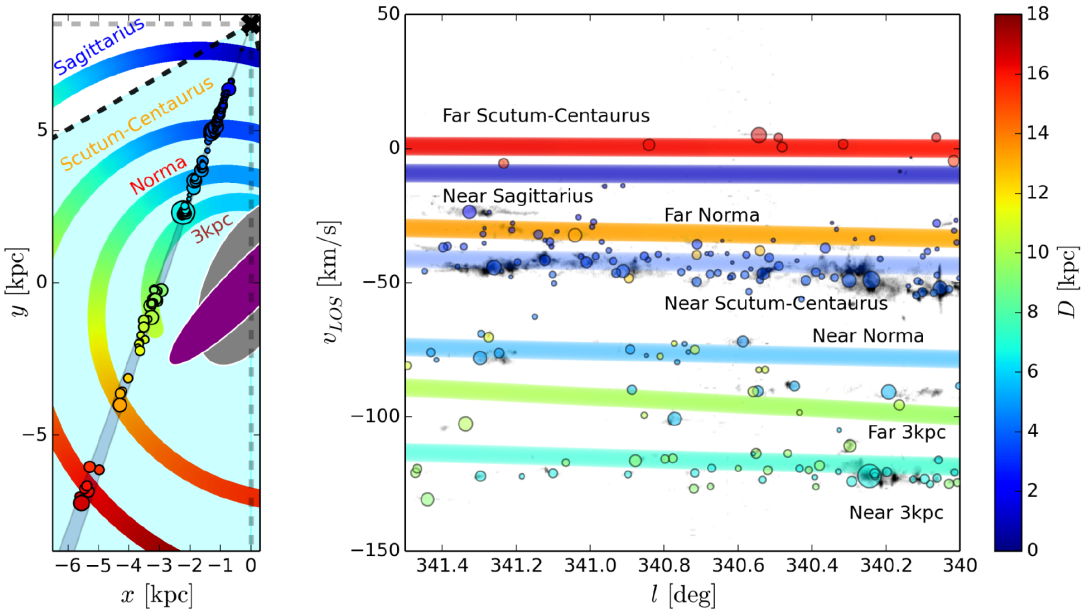

Figure 5.12: *Left*: top-down view of the Galaxy showing the SEDIGISM coverage (full survey in turquoise, and the science demonstration field as the small shaded line of sight). The different spiral arms from our model (see text for details) are shown and labelled with different colours. The positions of all the clouds in the science demonstration field are over plotted as coloured circles, whose colours indicate their assigned distances(see the colour bar to the right), and the size is proportional to the mass of the cloud. *Right*: lv plot of the peak intensity of ^{13}CO in the science demonstration field (grey scale) overlaid with the positions of all the molecular clouds with assigned velocities (colours and sizes as in the left panel). The positions of the spiral arms are over plotted and labelled, also colour-coded with their distance.

summarized in Table 5.4 for a sub-sample of the largest GMCs. The positions of all the molecular clouds extracted from the science demonstration field are shown in Fig 5.12 , overlaid on a model of the spiral arms.

5.2.2 Statistical method

Velocity Channel Analysis technique

To describe the turbulence, we have applied only the Velocity Channel Analysis (VCA) technique, as described in section 2.4.2, on different sections of the ^{13}CO(2–1) ℓbv data cube. As a reminder, this technique consists of computing the spatial power spectra of the two dimensional brightness distribution (I_{2D}) in velocity slices, and letting the thickness δv of the slices vary. As the thickness of velocity slices increases, density fluctuations begin to dominate the emissivity over velocity fluctuations. It is expected that the power spectrum keeps steepening with increasing thickness δv up to a characteristic thickness, above which there is no significant change in the index. When integrating over larger δv, most of the velocity fluctuations average out, so that the power spectrum

traces only static density fluctuations.

According to turbulence theory (e.g., Lazarian and Pogosyan 2000a), the power spectrum is related with spatial scales as $P_{I_{ND}}(k) \propto k^{\kappa_{ND}}$, where *ND* denotes the number of spatial dimensions, and k is the wave number. Values of k go from 1, the whole length of the longer axis in the data, to $N_{pix}/2$, i.e. half the total number of pixels. For incompressible, homogeneous, and isotropic turbulence, $\kappa_{3D} = -11/3$, and $\kappa_{2D} = -8/3$ (Kolmogorov 1941a). In the limit of shock-dominated, compressible turbulence, the spatial power index is $\kappa_{3D} = -4$, $\kappa_{2D} = -3$ (Burgers 1974). However, Lazarian and Pogosyan (2000a) predict that the spectral index should saturate to $\kappa_{2D} = -3$ for an optically thick medium, and many observations support their predictions (cf.Burkhart et al. 2013, who also provide a numerical confirmation for this value of κ_{2D}=–3).

5.2.3 Results

We have applied the VCA method on the six molecular structures extracted with SCIMES with the highest numbers of leaves (Table 5.4), corresponding to some of the most massive and highly complexes in this field. The masks generated by SCIMES were used to isolate the ^{13}CO(2–1) brightness distribution of each GMC from the data: new cubes were generated to cover each GMC, and the voxels outside of the masks were set to zero; the size of each cube along each axis was adjusted to the nearest power of two. For our analysis, we let the thickness of the velocity slices vary from twice the velocity resolution (0.5 km s^{-1}) up to the thickest slice case, corresponding to integrated maps that include the whole velocity range of the cloud in one channel.

We computed the power spectra as azimuthal median values of the 2D FFT of the data. To properly consider the measured noise, we also calculated the power spectra for emission-free channels. We corrected for the effects of measured noise and beam smearing following the method described in Brunt and Mac Low (2004). In summary, the final output power spectrum (P_{out}), corrected for noise (P_{obs}) and beam smearing spectra (P_B), is $P_{out} = (P_{obs} - P_{noise})/P_B$. The normalised power spectra for our sample of six GMCs are shown in Fig 5.13. We only show the results for angular scales larger than two times the spatial resolution because at smaller scales the effects of the beam size start to dominate. Figure 5.13 also shows the range over which the least square fitting of the spectral index was performed. Following Medina et al. (2014), the power spectrum fits are made between a minimum scale corresponding to 2.5 times the instrumental resolution, and a maximum scale corresponding to the semi-major axis of each cloud (blue range in Figure 5.13). Given the distances to the various GMCs, the range of scales over which we computed the spectral indices corresponds to linear scales between 1 and 10 pc. Therefore, this range is well suited to probe turbulence from the scale of a complete cloud, where it may be externally driven (e.g. by supernovae), down to scales where internal sources may contribute to turbulence (e.g. HII regions, stellar winds, proto-stellar outflows; Elmegreen and Scalo 2004; Dobbs et al. 2014).

In Fig 5.14, we show the variations of the spatial power indices κ_{2D} as a function of velocity slice thickness, δv. The spectra become steeper with increasing δv, as predicted. Following Lazarian and Pogosyan (2000a) and Esquivel et al. (2003), we computed the spectral index for thin slices (γ_t) as the mean value of all indices corresponding to a thickness $\delta v <$ velocity dispersion, σ_v. The thick index (γ_T) is taken as the average of the indices where $\delta v > \sigma_v$, but restricted to the regime where this index is almost constant. Finally, the index of the second order

structure function is computed as $m = 2(\gamma_t - \gamma_T)$ in the shallow cases (i.e. where $\gamma_t > -3$), or m = $2(\gamma_t + 3)$ in the steep cases (SDG 15 and SDG 298 clouds). We find values in the range 0.6–1.8, in rough agreement with the index of the first order structure function derived from principal component analysis (γ_{PCA}, where m = $2\times\gamma_{PCA}$) and published in other studies (e.g. $\gamma_{PCA} \simeq 0.4$–0.5, Brunt and Heyer 2002b; Roman-Duval et al. 2011). These results are based on a very limited sample of six GMCs, and should therefore be regarded with caution.

5.2.4 Conclusions

We cannot draw robust conclusions from these preliminary results due to the small number of analyzed clouds, but there are some interesting findings that can be studied in more detail in a future analysis. The main findings of those are:

- From the thin and thick indices (γ_t and γ_T) we found that the six GMCs have similar characteristic scales of turbulence, corresponding to velocity thickness typically between 4

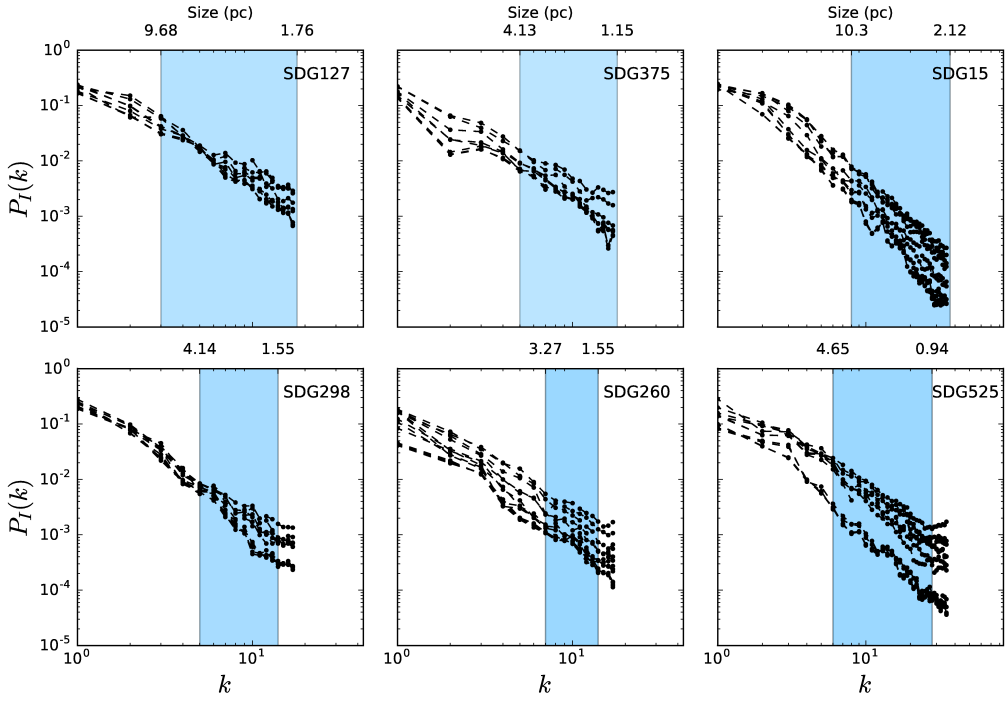

Figure 5.13: Normalised spatial power spectra for the six molecular clouds extracted with SCIMES with the highest numbers of leaves, for a range of velocity thickness δv: in each panel, the different curves correspond to increasing thickness from top to bottom, with δv values in the range 0.5 to 18 km s^{-1}. The blue area indicates the range of spatial scales over which a least square fitting of the spatial power index was performed. The scale on the lower X-axis gives the wave numbers (κ_{2D}), while that on the upper X-axis indicates the corresponding scale in pc, using the distance to each GMC, as listed in Table 5.4 . Each panel is labelled with the ID of each GMC (as per Col. 1 in Table 5.4).

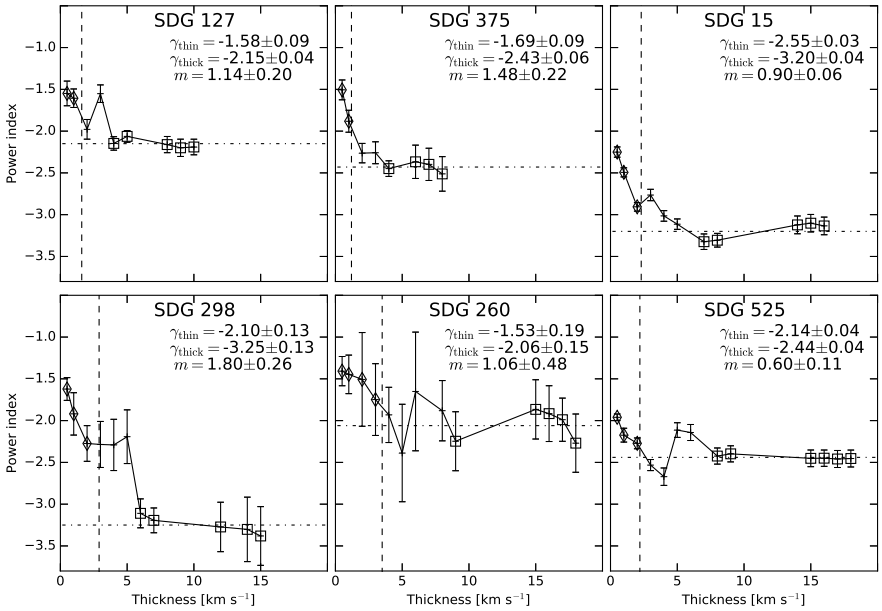

Figure 5.14: Variations in the power spectrum indices with velocity thickness for the different GMCs. The error bars correspond to the 1σ statistical uncertainties on the least square fit. The dotted horizontal lines indicate the saturation index for each GMC, corresponding to the thick regime where density fluctuations dominate. The dashed vertical lines show the respective velocity dispersion, σ_V, for each GMC. The data points used to compute the thin and thick indices (γ_t and γ_T), are indicated with diamonds and square symbols, respectively. These values, as well as the index of the second order structure function (m), are indicated in each panel (see text for details).

and 8 km s^{-1}, above which velocity fluctuations average out and the spectral indices do not vary much. This could indicate that similar processes are responsible for the turbulence in all clouds in our (small) sample.

- We find significant variations in the spatial spectral indices but giving the error bars, the results between clouds are statistically significant. The SDG 15 and SDG 298 clouds have steep spectra, with indices that saturate around –3.5, consistent with the picture of the Kolmogorov energy cascade for other clouds, and with results reported elsewhere (e.g. Dickey et al. 2001; Muller et al. 2004; Elmegreen and Scalo 2004). The other clouds show spectra that are significantly shallower, with κ_{2D} between –2.0 and –2.5 for the thick case. According to Lazarian and Pogosyan (2000a), this can be explained by a significant contribution to the turbulence on small scales. The particular behavior of the clouds seems not to be related with their reported physical properties (see Table 5.4), however a large SEDIGISM sample is needed to confirm this.

- Our results are consistent with Burkhart et al. (2013) results, that have shown that the spectral indices also depend on the line excitations. In particular, for a very optically thin, supersonic CO gas, with low density or low abundance, the spectral index is shallower than

the theoretical expectations for its column density.

Table 5.4: Properties of a sub-sample of clouds from the SCIMES extraction, restricted to GMCs with at least 5 leaves.

		Measured properties								Physical properties						
ID	Name	a ($''$)	b ($''$)	PA ($^\circ$)	AR	v_{lsr} (km s^{-1})	σ_v (km s^{-1})	$<W_{CO}>$ (K km s^{-1})	N_l	d (kpc)	Area (pc^2)	R (pc)	l_{max} (pc)	M (10^3) M$_\odot$)	Σ (M$_\odot$ pc^{-2}))	α_{vir}
SDG 15	SDG340.245–0.056	322	203	–161	1.6	–122.0	2.3	9.7	14	6.58±0.28	915	17.1	72.2	196.9	214	0.5
SDG 34	SDG340.096–0.252	76	69	110	1.1	–123.2	1.8	4.0	5	6.63±0.29	51	4.1	14.5	4.7	89	3.3
SDG 127	SDG340.193–0.369	364	146	153	2.5	–90.7	1.6	5.1	9	5.47±0.26	275	9.4	44.0	31.3	113	0.9
SDG 234	SDG340.054–0.214	151	105	70	1.4	–51.9	2.6	15.8	5	3.86±0.36	62	4.5	17.6	22.0	350	1.6
SDG 260	SDG340.240–0.213	180	147	148	1.2	–48.9	3.5	17.4	9	3.73±0.37	137	6.6	23.8	53.3	386	1.7
SDG 271	SDG340.582+0.069	114	88	–157	1.3	–47.1	3.6	3.3	6	3.66±0.38	38	3.5	13.5	2.8	73	18.4
SDG 298	SDG340.300–0.395	228	92	176	2.5	–49.1	2.9	14.3	7	3.74±0.37	76	4.9	20.1	24.1	317	2.0
SDG 375	SDG341.260–0.276	238	107	–153	2.2	–44.4	1.2	12.5	8	3.57±0.40	105	5.8	23.0	29.2	277	0.3
SDG 408	SDG341.010–0.151	229	110	89	2.1	–42.3	1.1	6.1	6	3.44±0.41	70	4.7	20.2	9.5	134	0.7
SDG 508	SDG341.212–0.345	146	42	–136	3.4	–30.4	1.6	5.5	5	2.00±0.49	7	1.5	7.7	0.9	121	5.2
SDG 525	SDG341.327+0.219	422	219	104	1.9	–23.6	2.2	6.2	13	2.27±0.56	147	6.9	26.7	20.4	138	1.9

Notes. The ID number shows the catalogue number associated with the cloud (same as the colour-scale in Fig 5.12). The GMC name is defined as SDG (for SEDIGISM) followed by the Galactic coordinates of the clouds' centroid. Columns 3 and 4 show the intensity-weighted semi-major and semi-minor axes, a and b, respectively; Column 5 shows the position angle (PA), and Column 6 shows the aspect ratio (AR) defined as a/b. In Columns 7–9 we show the centroid velocity, velocity dispersion, and average ^{13}CO(2–1) integrated intensity across the area of the cloud. Column 10 shows the number of dendrogram leaves, N_l, that make up each GMC. Column 11 shows the adopted kinematic distances (d) and their uncertainties. Columns 12–14 show the exact area defined by the clouds' masks, the equivalent radius (R, assuming circular geometry) and maximum length (l_{max}). Columns 15–17 show the total mass (M), the average surface density (Σ), and the virial parameter (α_{vir}).

5.3 Turbulence in the W43 region

In section 1.4 we discussed that the stellar feedback from massive stars may play an important role in generating turbulence within their parental molecular clouds (e.g., Zhang and Chevalier 2019; Krumholz et al. 2018; Ali et al. 2018; Kim et al. 2018; Shima et al. 2018). So far we have only characterized turbulent movements in ionized and molecular gas without special considerations about their relationship with stellar feedback from massive YSOs. However, these results will serve as benchmarks for the analysis presented in this last section, which explores the turbulence driven by stellar feedback.

5.3.1 The molecular emission from W43 region

To analyze turbulence in molecular clouds and its relation with stellar feedback, one needs to study regions with high stellar activity surrounded by molecular gas. The W43 region is an ideal target for this purpose because it is a very active star forming region with significant stellar feedback (Motte et al. 2003). It has two principal star formation structures: W43-main and the W43-south (see Figure 5.15). The core of W43-main contains a giant HII region powered by a particularly luminous cluster of Wolf-Rayet (WR) and OB stars contributing to a high infrared luminosity of ~3.5 x 10^6 $L_\odot$ (Blum et al. 1999). W43-main is a dense region equivalent to a mini-starburst (Motte et al. 2003). While W43-south represents a less extreme cloud which hosts an interesting compact HII region; G29.96-0.02 (Cesaroni et al., 1998). According to Nguyen Luong et al. (2011), the W43 region is located in the intersection of the galactic bar and the Scutum-Centaurus spiral arm (l=29°-32°, |b|<=1°). Its distance is around 5.5 ± 0.5 Kpc (Zhang et al., 2014). The complex contains a total gas mass, including atomic and molecular gas, of ~10^7 $M_\odot$ and shows a star formation rate of 0.1 $M_\odot$ yr^{-1} (Motte et al. 2003; Nguyen Luong et al. 2011; Carlhoff et al. 2013).

There is evidence for large turbulence motions in the molecular gas of the W43 region. In particular, Herpin et al. (2012) showed, through models, that the observed molecular emission in W43-MM1 is dominated by supersonic turbulent velocities (v_{tur} > 2.2 km s^{-1}). They also found that the turbulent velocity varies with the distance from the center to the dominant source W43-MM1. Therefore, the turbulent motions increase with radius. This conclusion is in good agreement with the turbulent core model of McKee and Tan (2003). The star formation activity in the core is also linked with high velocity shocks. The line width of the shock tracer transition SiO(2-1) suggests a combination of low and high shock velocities between 4 km s^{-1} to 14 km s^{-1} (Louvet et al., 2016).

To perform a turbulence analysis in the W43 region we need to study molecular gas emission that is sensitive to environmental conditions (Liszt and Pety, 2012), that traces the column density with moderate optical depth. The ^{13}CO emission is then an excellent candidate. Therefore, we used archival data from the W43-HERO large program, which is publicly available. These data were taken with the IRAM 30 m telescope and the observed molecular emission lines are ^{13}CO(2-1) and C^{18}O(2-1) at ~ 220.4 GHz and ~ 219.6 GHz, respectively. This survey includes the two main clouds, W43-Main and W43-South. It covers a rectangular map of 145 x 105 pc at ~ 6 Kpc distance (Zhang et al., 2014). The observations have a spectral resolution of 0.15 km s^{-1} and a spatial resolution of 12″ (0.3 pc). The bandwidth is 100 km s^{-1}, which covers a velocity

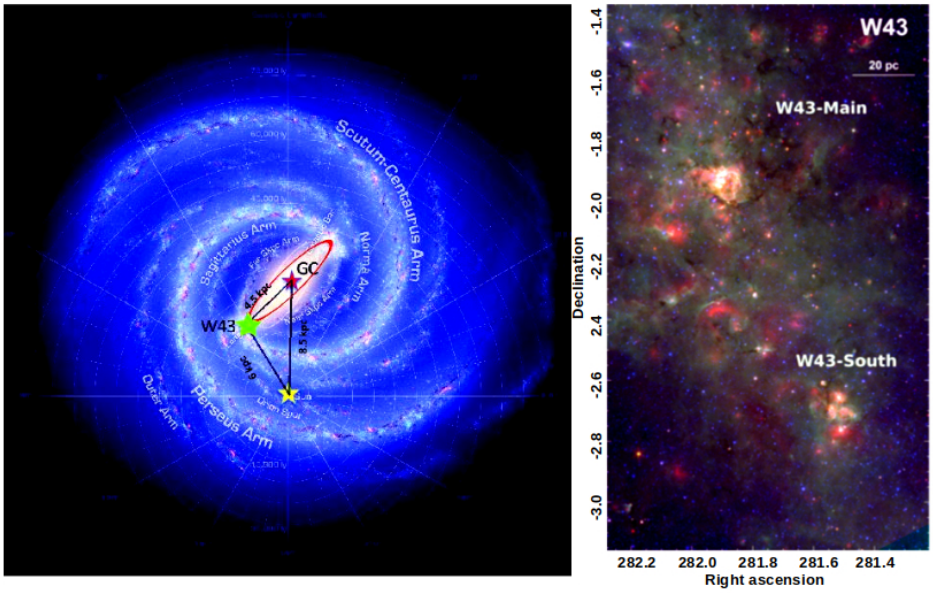

Figure 5.15: *Right*- Artist view of the Galaxy seen face-on with the 'long bar' outlined by a red ellipse (Churchwell et al., 2009). The W43 region (green star) is located at the expected transition zone between the bar-dominated region (R_{GC} < 5 Kpc) and the normal Galactic disk. Image credit: Nguyen Luong et al. (2011). *Left*- The entire W43 is shown in Spitzer IRAC bands 3.6. 8.0, 24 μm. Image credit: Saral et al. (2017).

range from 30 km s^{-1} to 130 km s^{-1} (Carlhoff et al., 2013).

Previous analysis from Carlhoff et al. (2013) shows that most of the emission is concentrated in the velocity range between 65 and 120 km s^{-1}. Due to the complexity of the spectra, for this work we only selected the principal position-position-velocity (PPV) cube of ^{13}CO(2-1) in the velocity range from 80 km s^{-1}to 110 km s^{-1}, which is part of the main velocity range of W43 (Nguyen Luong et al. 2011). The integrated intensity map in the selected velocity range is shown in Figure 5.16.

5.3.2 Turbulence analysis technique

In the previous sections, 5.1.3 and 5.2.2, we discussed the use of the VCA and Second Order Structure Function techniques to study the turbulent properties of the gas. However, to study the stellar feedback effect on the turbulent profiles we need tools sensitive to that. Boyden et al. (2016) made an analysis of the stellar feedback effect on the turbulent motion of simulated molecular gas. They tested 16 statistical tools of the *TurbuStat* package (Koch et al., 2019) that were developed to characterize turbulence. Their simulations include two cases, with stellar feedback and without it. The first case is a standard simulation of a turbulent molecular cloud, while the second begins with the same initial conditions, but it has evolved for 0.2 Myr with a wind launching model. Thus, in the last one the cloud is shaped by stellar feedback. The 16 tools were used on each of the two cases. The results show that some techniques are sensitive to stellar feedback, that means

a turbulence profile different in the two cases (e.g. with and without feedback). In particular, the VCA does not show sensitivity to the wind activity while the Principal Component Analysis (PCA) does.

Following the analysis of Boyden et al. (2016) to characterize the turbulence behavior of the molecular gas in W43 region, we decided to start a first test with the PCA technique from the *TurbuStat* package. As a reminder from section 2.4.2, the general description given by Brunt and Heyer (2002a) derived the power-law relationship (Eq. 2.34) known as PCA velocity statistics, α_{PCA}, as

$$\delta\upsilon \propto L^{\alpha_{PCA}}, \tag{5.5}$$

where $\delta\upsilon$ is the characteristic velocity and L is characteristic spatial scale. The PCA technique has been tested on several data sets of molecular clouds, both observed (e.g., ^{13}CO(1-0) emission) and simulated (e.g., Brownian motion of molecular gas), and the average velocity statistics α_{PCA} is $\sim$ 0.6 (e.g., Brunt and Heyer 2002a, Brunt and Heyer 2002c, Roman-Duval et al. 2011). To apply the PCA technique on our ^{13}CO HERO data, we arrange the data into independent clouds and independent sub-cubes. This division allows us to characterize the turbulence profiles of independent regions and measure the possible influence of the stellar feedback within them. Both arrangements are explained in the following section.

5.3.3 Molecular cloud extraction

We extracted independent cloud structures with the SCIMES algorithm (Sec. 5.2.1) in order to allow direct comparison with SEDIGISM results. The algorithm obtained from the principal PPV cube of the W43-HERO data contains $\sim$ 13400 cloud structures. However, we selected the top-ten of the biggest clouds, in terms of projected area, but we only analyzed nine of them, because one particular case has its velocity centroid in a different velocity range, suggesting it is not part of W43. This selection will provide us a highly sampled PCA spectrum (e.g. a size-linewidth relation with several data points). The masks of the top-nine clouds are illustrated in Figure 5.16, each cloud has an ID number.

To test any possible bias effects on the PCA statistics due to the identification algorithm, we also created a sample of sub-cubes extracted from the principal PPV cube of the W43-HERO data. The extracted sub-cubes are related with three regions that possibly have different physical conditions: the core of W43-main, W43-south and an isolated region. Their ID names are *Core*, *South*, and *Isolated*, respectively. The *Core* has a mini-starburst and a large amount of energy is expected to be injected from it to the molecular gas. Its physical size corresponds to $\sim 37 \times 29$ pc at a distance of 6 Kpc. The *South* injects energy on a less extreme energy scale. Its physical size $\sim 29 \times 24$ pc. Finally, the *Isolated* region does not inject energy due to stellar feedback. Its size is $\sim 29 \times 26$ pc. The three cubes cover the same velocity range, from 80 km s^{-1} to 110 km s^{-1}. There extents are illustrated in Figure 5.16 by magenta masks.

5.3.4 Preliminary results and discussion

We apply the PCA technique on the extracted structures from the ^{13}CO W43-HERO data. First we consider the nine of the top-ten extracted clouds. We calculated the resulting PCA profile from the

correlation between the spatial length and the linewidth. We used all the points to determine the linear fit. The slope of this linear fit is the α_{PCA} value, which according to theoretical expectations should be ~ 0.6. The PCA profiles of the top-nine clouds are shown in Figure 5.17 and their α_{PCA} values and correlation coefficients are listed on Table 5.5. The mean α_{PCA} value is ~ 1 and the correlation coefficients do not show significant differences. The clouds *6748* and *6561* are located in W43-main and W43-south respectively, which are regions with high stellar activity. These two clouds have more points to correlate, which should guarantee more robust results. However, their profiles are not statistically different from those of the other clouds. The contours of cloud *15971* are not closed, so its fit might not be accurate.

All clouds show similar α_{PCA} and correlation coefficients. A previous study (Boyden et al. 2016) shows that PCA profiles of molecular clouds with stellar feedback are different from the profiles of clouds without feedback. However, our results are not consistent with their result, although their data do only cover regions less complex that W43, which could be a significant reason for the differences.

The other independent structures to which we apply the PCA are the three sub-cubes. For each sub-cube we calculated the PCA profile and performed a linear fit to the data points. Some examples of these PCA profiles are shown in Figure 5.18, but all α_{PCA} values are listed in Table 5.5. The *Core* and the *South* sub-cubes are the main part of W43-main and W43-south respectively and the *Isolated* sub-cube corresponds to a region without associated molecular gas emission.

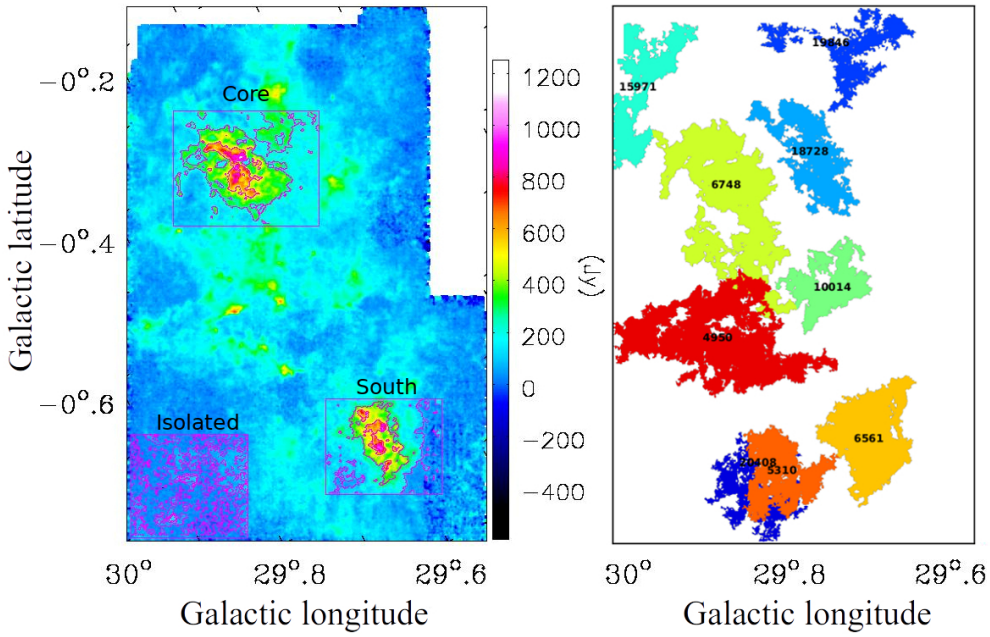

Figure 5.16: *Left*- The integrated intensity map of the W43 region ^{13}CO emission from the HERO program data. The velocity range goes from -80 to -110 km s^{-1}. The three selected regions of the cube are indicated in magenta. *Right*- The masks of the corresponding top-nine clouds extracted with SCIMES. The numbers are their ID names.

Table 5.5: The resulting α_{PCA} values for each of our W43 molecular structures.

W43 molecular structures								
Sub-cubes			Clouds					
ID name	α_{PCA}	Correlation coefficient*	ID name	α_{PCA}	Correlation coefficient*	ID name	α_{PCA}	Correlation coefficient*
Core	1.34 ±0.01	0.95	20408	1.19 ±0.05	0.94	18728	1.12 ±0.02	0.95
South	1.08 ±0.01	0.94	4950	1.03 ±0.02	0.95	15971	1.33 ±0.03	0.95
Isolated	0.92 ±0.03	0.88	6748	0.99 ±0.01	0.97	5310	1.09 ±0.02	0.94
			6561	1.00 ±0.01	0.95	10014	1.01 ±0.02	0.94
			19846	1.04 ±0.03	0.93			

* The correlation is quantify using the Pearson correlation coefficient *r*.

The *Isolated* cube shows a Pearson's r slightly lower with respect to the *Core* and the *South* sub-cubes, suggesting a marginally less correlated PCA spectrum, and possibly less organized emission. However, the mean α_{PCA} is still very high ~ 1.1, indicating that the cloud extraction method does not influence this value.

Results from 367 ^{13}CO spectral maps of molecular clouds in the Galactic Ring Survey(GRS; Jackson et al. 2006) analyzed by Roman-Duval et al. (2011), show that α_{PCA} could be > 0.6 fitting the PCA profile at values higher than their spatial resolution, for example, using 2×FWHM ($96''$), the mean α_{PCA} is 0.74. Even when we used a lower limit for our linear fit ($\sim 12''$), the spatial and velocity resolution of our data are different to Roman-Duval et al. (2011) and compare with their results is not straightforward. However, it will be interesting to reproduce their analysis with our data in order to check if we would get similar results.

Finally, the turbulence profiles from SEDIGISM (Sec. 5.2.4) do not show big differences with the theoretical expectation, but the high α_{PCA} from these W43-HERO data does. This could be a consequence of high amount of energy injected to the molecular clouds. The W43 region is a complex environment with several possible energy sources and it is also located at the galactic bar, which is a position in the Galaxy with complex dynamics. To clarify this, further analysis is needed.

5.3.5 Future work

A conclusion from these preliminary results is that the turbulence profiles of molecular cloud structures from W43 region are very steep compared with theoretical expectations. These results could reflect the influence of the stellar feedback or the large-scale motion related to the bar itself, since the α_{PCA} values of all cloud structures are similar. However, to confirm these preliminary results further tests are needed and we propose the following:

- Use a bootstrap Monte Carlo method to re-sample the sub-cubes and clouds, and calculate the turbulence profiles and confidence α_{PCA} values in order to provide a general sample of independent cubes and statistical significance of our results.

- Use other tracers of molecular gas to test the capacity of the PCA to reproduce the same

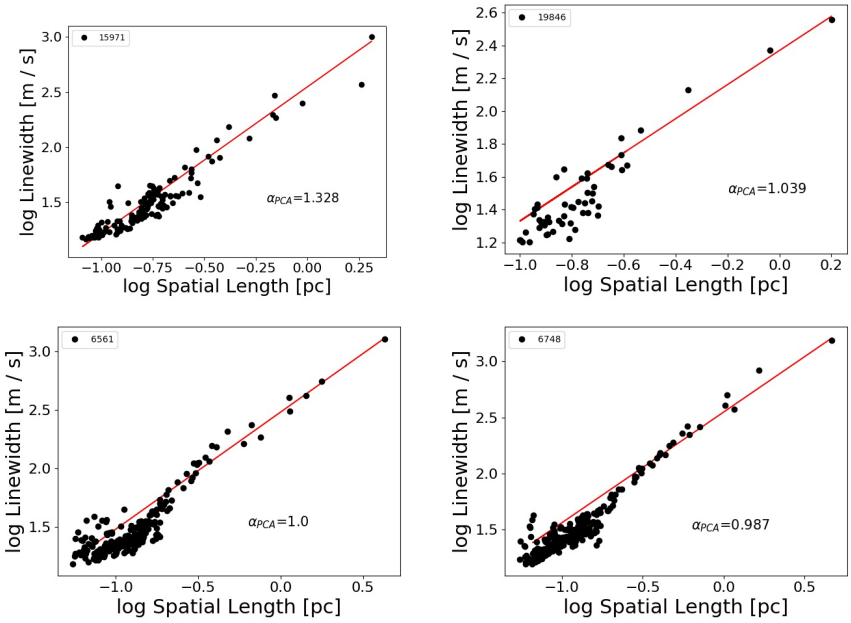

Figure 5.17: The individuals PCA profiles of the four of the biggest clouds. The number correspond the their associated mask number as is Figure 5.18. The red line represents the linear least squares fit from *TurbuStat* and α_{PCA} is the slope of the linear fit.

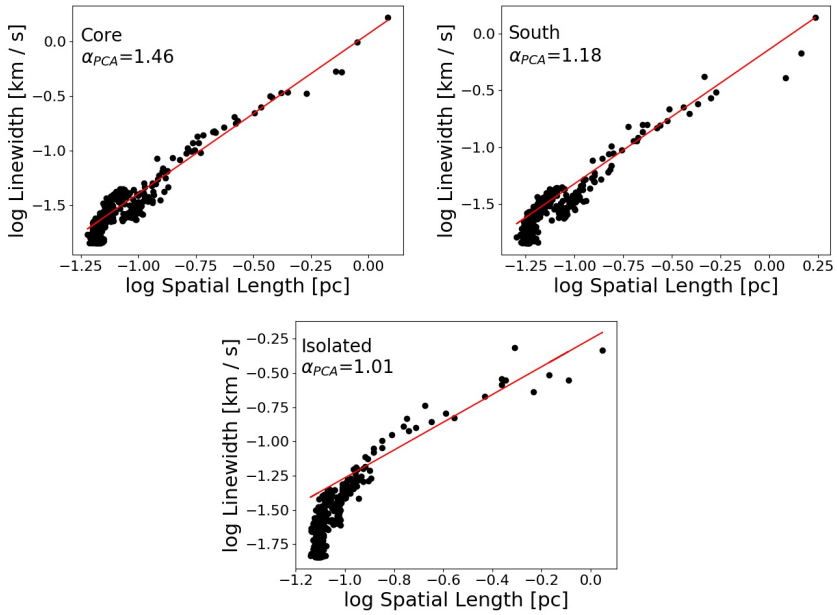

Figure 5.18: PCA profiles of the sub-cubes of the core of W43-main, the W43-south and an isolate region. The red line is the linear least squares fit from *TurbuStat* and α_{PCA} is the slope of the linear fit.

results and investigate whether stellar feedback plays mayor role in the turbulent motions measured with ^{13}CO in W43 region.

- Constrain the influence of the accelerated ionized gas that produces a pressure gradient in the molecular clouds. This can be performed through a correlation between the continuum emission, e.g., from the GLOSTAR (Medina et al. 2019) and THOR surveys (Bihr et al. 2015), with our ^{13}CO emission.
- According to section 5.3.2, there are other intensity statistics that are also sensitive to stellar feedback. However, the applicability of these tools needs to be confirmed and they need to be tested with the W43-HERO data.

CHAPTER 6

Summary and outlook

6.1 Summary

The goal of this thesis was to investigate the last evolutionary phases of high-mass star formation. These phases consist of high-mass stellar embryos with sizes from 0.01 to the several pc of young HII regions. They are the most luminous phases and can be observed at several wavelengths, e.g., IR, millimeter, centimeter, and visible. Their emission is strong enough to characterize and provide more reliable values of their physical properties than can be attained for early phases. Moreover, the newly formed high-mass stars have important influence on their local environment. They inject energy and momentum into their parental clouds, e.g., via gravitational interactions, powerful outflows and winds, and ionizing radiation. One of their feedback effects, turbulent motion of the parental molecular and ionized gas, was discussed in this thesis.

The framework of this thesis was a combination of very high resolution observations at several wavelengths (IR, millimeter, centimeter, and visible) and statistical tools that allow us to provide new evidence of these evolutionary stages and their dynamical effects on the turbulent motion of their surroundings. The main results from Chapters 3, 4, and 5 are summarized as follows:

6.1.1 Chapter 3

From the deep radio observation ($\sigma \sim 50\,\mu$Jy bm^{-1}) with high angular resolution (0$''$.2) of the NGC 6334 complex (covering the regions D, E, F, I(N), and part of the region C) we extracted 83 compact radio sources. We calculated their spectral indices and searched for their infrared counterparts to characterize them. Our analysis has provided clues on the nature of many of the detected compact radio sources.

- A total of 83 radio compact sources in the NE of NGC 6334 are detected and only around 10 of them were previously reported.
- The stellar nature of 27 of the 83 compact radio sources is confirmed by the properties of their infrared emission.
- Most of these sources in the HII region (region D) have negative spectral index, suggesting non-thermal emission and, therefore, are likely magnetically active low-mass YSOs as in

the Orion Nebular Cluster. However, the IR emission of three of them suggest that they are early B stars and their radio emission may originate in strong shocks of wind collision regions.

- Two interesting cometary radio sources were detected and are here reported for the first time. They are spatially coincident with more extended mid-IR nebulosities of similar shape. We suggest that they are HII regions (traced by the radio emission) surrounded by dusty envelopes (traced by the mid-IR). Interestingly we found three stars (early spectral type), which could be the sources of the ionizing photons for these possible HII regions.
- By comparison with an observation obtained in 1995, we analyzed the flux variability of eight sources. Three of them show strong variability suggesting that they are magnetically active low mass stars.

6.1.2 Chapter 4

The GLOSTAR survey is a VLA survey of the Galactic mid-plane 1st quadrant ($-10^\circ < \ell < 80^\circ$ and $|b| < 1^\circ$). In this work we present the radio continuum data for a 16 square degree part of the survey covering 8 degrees in longitude and 2 degrees in latitude and centered on $\ell = 32^\circ$, $b = 0^\circ$ (i.e., $28^\circ < \ell < 36^\circ$ and $|b| < 1^\circ$). We provide a systematic and effective methodology to characterize the radio emission from tracers of early phases of newly formed high-mass stars: compact, ultra- and hyper-compact HII regions. Our results provide support to previous studies, and produce a list of new HII and UCHII regions candidates previously unknown.

- We have identified 1575 radio sources and have investigated their nature and physical properties. The data presented here is only a small fraction of the total GLOSTAR coverage.
- We have used a multi-wavelength analysis and searched the literature to identify the nature of the radio sources. This has resulted in the identification of 231 HII regions. Of these, only 46 had been previously identified with high resolution radio surveys, and a further 90 HII region candidates identified in the mid-infrared by Anderson et al. (2014) have now been confirmed.
- We have identified a further 96 HII regions not previously known. The majority of the new HII regions are well-resolved and have been missed by previous high-resolution interferometric surveys due to their lack of short baseline data and consequent poor sensitivity to large angular scales. Twelve of the new HII regions identified are considered to be unresolved, of these we identify 8 UCHII region candidates.
- We have investigated the properties of the full sample of HII regions and compared them to the previously identified samples. The improved flux sensitivity ($\sim$100-400 $\mu Jy\,\mathrm{beam}^{-1}$) and sensitivity to larger angular scales ($\sim$20-200$''$) of GLOSTAR compared to other surveys, has increased the number of HII regions in this part of the Galaxy by a factor of 4, which means that we provide new detections of HII regions.
- We have also identified 12 radio stars, 46 PNe, 3 pulsars, 3 compact SNR-candidates and 99 radio sources associated with more extended structures such as the ionization fronts of

much more extended HII regions. We are unable to classify 1186 radio sources; these can be broadly categorized as being weak and unresolved, the majority of which are likely to be extragalactic background sources.

6.1.3 Chapter 5

We have used statistical analysis of high-resolution spectroscopic observations of submillimeter and optical emission lines. In order to characterize the turbulence in the ionized gas, we used optical emission lines from the Orion Nebula and we applied the second-order structure function of velocity centroids and the VCA techniques on the PPV cube. We constrain the scales for the turbulence energy injection. We also characterize the turbulence in the molecular gas through ^{13}CO emission lines from the SEDIGISM and W43-HERO data surveys. Here we also applied the second-order structure function and the VCA techniques, but in the case of W43-HERO data we incoorpate the PCA technique. From these data set we determine the characteristic scales of turbulence and the relation of the turbulent motion of molecular gas due the influence of stellar feedback.

- The analysis of the ionized gas in the Orion nebula shows that the VCA technique is more a reliable means to determine the spectrum of velocity fluctuations in the ionized gas than the structure function technique, and from both low and high ionization lines we find consistent evidence for a Kolmogorov-type spectrum ($\delta u \sim l^{1/3}$) for length scales, l, between 0.05 pc ($\approx 22''$) and 0.02 pc ($\approx 8''$). This regime could be related with the correlation lengths of the order of 0.08 pc for the separations of molecular cores along the ridge that lies behind the Orion Nebula (Kainulainen et al. 2017). Unfortunately, VCA cannot be applied if the thermal or instrumental line width is larger than the velocity differences of interest, which rules out its application to the Hα line and to scales smaller than 0.02 pc.

- For the ionized gas the changes in slope of the structure function index are difficult to interpret because of the influence of projection smearing and sensitivity to details of the observational methodology.

- The characteristic length of 0.05 pc is special in at least two ways, corresponding to both the autocorrelation scale of velocity differences for low-ionization lines and also to a break in the power spectrum of surface brightness fluctuations in all lines. We suggest that this is the dominant scale for density fluctuations in the Orion nebula and is also the main driving scale of the turbulence.

- The velocity fluctuations in the ionized gas of the Orion nebula are not homogeneous on the largest scales, but rather the turbulent conditions themselves vary, both across the sky and along the line of sight, on scales larger than the velocity autocorrelation length of 0.05–0.15 pc.

- From the thin and thick indices (γ_{thin} and γ_{thick}) we found that the six clouds from the SEDIGISM survey have similar characteristic scales of turbulence, corresponding to velocity thickness typically between 4 and 8 km s^{-1}, above which velocity fluctuations

average out and the spectral indices do not vary much. This could indicate that similar processes are responsible for the turbulence in all clouds in our (small) sample.

- We find significant variations in the spatial spectral indices but given the error bars, the results between clouds are statistically significant. Two clouds (SDG 15 and SDG 298) have steep spectra, with indices that saturate around –3.5, consistent with the picture of the Kolmogorov energy cascade for other clouds, and with results reported elsewhere (e.g. Dickey et al. 2001; Muller et al. 2004; Elmegreen and Scalo 2004). The other clouds show spectra that are significantly shallower, with κ_{2D} between –2.0 and –2.5 for the thick case. According to Lazarian and Pogosyan (2000a), this can be explained by a significant energy contribution to the turbulence on small scales. The particular behavior of these clouds seems not to be related with their reported physical properties (see Table 5.4), however analysis of a larger SEDIGISM sample is needed to confirm this.

- The characterized turbulence profiles of molecular cloud structures from the W43 region are very steep compared with the theoretical expectation. This could be related to the large amount of energy injected that is not considered in the theory. Therefore, the high α_{PCA} values could be a direct influence of the stellar feedback or the large-scale motion from the Galactic bar, since all can make contributions of similar magnitude. However, these results need more statistical support.

6.2 Prospects for the future

In this thesis, we provide more observational evidence of the YSOs physical properties, as well as, the processes occurring within them, and their effects on their surrounding material. We produce large catalogues that confirm their main radio properties, e.g., sizes, fluxes, and spectral index. We also discuss their effects in their surrounding material, for example, we analyze the turbulent motions of ionized gas from the HII region of the Orion nebula, as well the turbulent in molecular clouds probably produced by stellar feedback. However, these analyses open new and interesting question for future scientific work. These future tasks are listed according to their Chapter as follows:

Chapter 3
Our analysis has provided clues on the nature for various of the detected compact radio sources, however, more observations are necessary to better establish the nature of most of them. Natural extensions of our work are multi-wavelength, multi-epoch higher angular resolution observations. Therefore, we will ask for more data through an observational proposal to the Very Large Array and the Very Long Baseline Array telescopes in coming proposal calls. These new observations will allow us to study the variability of the sources, their brightness temperature and astrometry, as well as to get better estimates of the spectral index values.

Chapter 4
Here we present the first catalog of the GLOSTAR survey. Nature and physical properties of 1575 radio sources were investigated and reported. The sources discussed here represent only a small

fraction of the total GLOSTAR coverage, which also includes spectral line and higher-resolution data obtained with the VLA in B-array. The methods and strategies developed in the course of this thesis will be fundamental for the future analysis of the GLOSTAR survey data. The new detection of HII regions opens a possibility for new observations to investigate their properties. We will analyze these new ~ 100 HII regions in various ways: We will calculate accurate spectral indices combining our data with the THOR survey data. We will also calculate the spectral energy distribution (SED) profiles combining IR data from the ATLASGAL and Herschel sub-millimeter/far infrared surveys. Finally, we will check with the CHIMPS survey data (Rigby et al. 2016) for the sources velocities and the recombination lines from GLOSTAR to calculate their kinematic distances, which are mandatory to determine their host regions physical sizes, masses and luminosities. Practically speaking, the reported position and physical properties of the presented radio sources will be fundamental for a deep analysis of compact radio sources with the B-configuration data. The GLOSTAR survey VLA data will be combined with single-dish data that we are acquiring with the Effelsberg 100 m telescope. The combined data set will probe all angular scales larger than few arc seconds.

Chapter 5

The structure of computer programs used in this chapter will be used to develop a more automatic process to analyze the structural properties of the ISM observed with SEDIGISM in the future. Since SEDIGISM covers a significant part of the Galactic plane, a global analysis of its data will address different environments in- and outside of the Solar circle. Related to the W43 region analysis, we plan to apply the strategic plan discussed in section 5.3.5, use bootstrap Monte Carlo method, other tracers of molecular gas, and further statistical tools from *TurbuStat* to confirm the results and prepare a peer-reviewed publication.

Full list of publications

A. Peer-reviewed publications.

10. **Medina S.-N. X.**; Urquhart J. S.; GLOSTAR team; et al., 2019. *GLOSTAR — Radio Source Catalogue I:* $28^\circ < \ell < 36^\circ$ *and* $|b| < 1^\circ$. Astronomy & Astrophysics Vol. 627.

9. Dzib, S. A.; Rodríguez, L. F.; Karupussamy, R.; Loinard, L.; and **Medina, S.-N. X.**, 2018. *The Enigmatic compact radio source coincident with the energetic X-ray pulsar PSR J1813-1749 and HESS J1813-178.* The Astrophysical Journal, Vol. 866.

8. Dzib, Sergio A.; Ortiz-León, Gisela N.; Loinard, L.; Mioduszewski, A. J.; Rodríguez, L. F.; **Medina, S.-N. X.**; Torres, R. M., 2018. *VLBA Determination of the Distance to Nearby Star-forming Regions. VIII. The LkHα 101 Cluster*. The Astrophysical Journal, Vol. 853.

7. **Medina, S.-N. X.**; Dzib, S. A.; Tapia, M.; et al., 2018. *The richness of compact radio sources in NGC 6334D to F.* Astronomy & Astrophysics Vol. 610A.

6. Schuller, F.; Csengeri, T.; Urquhart, J. S.; Duarte-Cabral, A.; Barnes, P. J.; Giannetti, A.; Hernandez, A. K.; Leurini, S.; Mattern, M.; **Medina, S.-N. X.**; Agurto, C.; et al., 2017.*SEDIGISM: Structure, excitation, and dynamics of the inner Galactic interstellar medium.* Astronomy & Astrophysics Vol. 601.

5. Arthur, S. J.; **Medina, S.-N. X.**; and Henney, W. J., 2016. *Turbulence in the ionized gas of the Orion nebula.* Monthly Notices of the Royal Astronomical Society, Vol. 463.

4. Dzib, S. A.; Loinard, L.; **Medina, S.-N. X.**; et al., 2016. *Deep VLA observations of nearby star forming regions I: Barnard 59 and Lupus 1.* Revista Mexicana de Astronomía y Astrofísica, Vol. 52.

3. **Medina, S.-N. X.**; Arthur, S. J.; Henney, W. J.; Mellema, G.; and Gazol, A., 2014. *Turbulence in simulated HII region.* Monthly Notices of the Royal Astronomical Society, Vol. 445..

2. Dzib, S. A.; Rodríguez, L. F.; **S.-N. X., Medina**; et al., 2014. *High angular resolution 7 mm images toward the UC HII region W3(OH).* Astronomy & Astrophysics Vol. 567.

1. Vazquez, Federico; Olivares-Robles, M. A.; **Medina, S.**, 2011. *Size Effects on the Entropy Production in Oscillatory Flow between Parallel Plates* Entropy Vol. 13.

B. Publications to be submitted.

2. Rebolledo, D.; include **Medina S.-N. X.**; et al. *Effect of feedback of massive stars in the fragmentation, distribution and kinematics of the gas in two massive clumps in the Carina region*. To be submitted in 2019 in Astronomy & Astrophysics.

1. Duarte-Cabral, A.; Colombo, D.; Urquhar, James S.; include **Medina S.-N. X.**; et al. *The SEDIGISM survey: Molecular clouds in the inner Galaxy*. To be submitted in 2019 in Astronomy & Astrophysics.

C. Publications in progress.

2. **Medina S.-N. X.**; et al.; *Turbulence study of the W43 region*. To be submitted in 2019 in Astronomy & Astrophysics.

1. Mauersberger, R.; include **Medina S.-N. X.**; et al. *The formation of molecules due to phase transitions in diffuse translucent clouds* To be submitted in 2019 in Astronomy & Astrophysics.

Publication A.1 presents the result from my bachelor thesis. Publication A.2 is the result of a collaboration during my master studies. Publication A.3 presents the result from my master thesis. Publications A.5, A.6, A.7, A.10, and C.2 are related to my doctoral thesis. Publications A.4, A.8, A.9, B.1, B2, and C.1 are result from collaboration during my doctoral studies.

Bibliography

Aguirre, J. E. et al. (Jan. 2011). "The Bolocam Galactic Plane Survey: Survey Description and Data Reduction". In: *ApJS* 192, 4, p. 4. DOI: 10.1088/0067-0049/192/1/4. arXiv: 1011.0691 [astro-ph.GA].

Ali, A., T. J. Harries and T. A. Douglas (July 2018). "Modelling massive star feedback with Monte Carlo radiation hydrodynamics: photoionization and radiation pressure in a turbulent cloud". In: *MNRAS* 477, pp. 5422–5436. DOI: 10.1093/mnras/sty1001. arXiv: 1804.07309.

Anderson, L. D. et al. (May 2014). "The WISE Catalog of Galactic H II Regions". In: *ApJS* 212, 1, p. 1. DOI: 10.1088/0067-0049/212/1/1. arXiv: 1312.6202.

Anderson, L. D. et al. (Sept. 2017). "Galactic supernova remnant candidates discovered by THOR". In: *A&A* 605, A58, A58. DOI: 10.1051/0004-6361/201731019. arXiv: 1705.10927.

Andre, P. (1996). "Radio Emission as a Probe of Large-Scale Magnetic Structures Around Young Stellar Objects". In: *Radio Emission from the Stars and the Sun*. Ed. by A. R. Taylor and J. M. Paredes. Vol. 93. Astronomical Society of the Pacific Conference Series, pp. 273–284.

Anglada, G. et al. (Dec. 1998). "Spectral Indices of Centimeter Continuum Sources in Star-forming Regions: Implications on the Nature of the Outflow Exciting Sources". In: *AJ* 116, pp. 2953–2964. DOI: 10.1086/300637.

Arthur, S. J., S.-N. X. Medina and W. J. Henney (Dec. 2016). "Turbulence in the ionized gas of the Orion nebula". In: *MNRAS* 463, pp. 2864–2884. DOI: 10.1093/mnras/stw2165. arXiv: 1608.07012.

Avison, A and S J George (Nov. 2012). "A graphical tool for demonstrating the techniques of radio interferometry". In: *European Journal of Physics* 34.1, pp. 7–17. DOI: 10.1088/0143-0807/34/1/7. URL: https://doi.org/10.1088%2F0143-0807%2F34%2F1%2F7.

Balick, B., R. H. Gammon and R. M. Hjellming (Oct. 1974). "The structure of the Orion nebula". In: *PASP* 86, pp. 616–634. DOI: 10.1086/129654.

Ballesteros-Paredes, J. et al. (2007). "Molecular Cloud Turbulence and Star Formation". In: *Protostars and Planets V*, pp. 63–80. eprint: astro-ph/0603357.

Bassani, L. et al. (Nov. 2005). "Is the INTEGRAL IBIS Source IGR J17204-3554 a Gamma-Ray-emitting Galaxy Hidden behind the Molecular Cloud NGC 6334?" In: *ApJ* 634, pp. L21–L24. DOI: 10.1086/498718. eprint: astro-ph/0510338.

Becker, R. H. et al. (Mar. 1994). "A 5 GHz VLA survey of the galactic plane". In: *ApJS* 91, pp. 347–387. DOI: 10.1086/191941.

Becker, R. H. et al. (July 2010). "Variable Radio Sources in the Galactic Plane". In: *AJ* 140, pp. 157–166. DOI: 10.1088/0004-6256/140/1/157. arXiv: 1005.1572.

Bertin, E. and S. Arnouts (June 1996). "SExtractor: Software for source extraction." In: *A&AS* 117, pp. 393–404. DOI: 10.1051/aas:1996164.

Beuther, H. et al. (Mar. 2012). "Galactic Structure Based on the ATLASGAL 870 μm Survey". In: *ApJ* 747, 43, p. 43. DOI: 10.1088/0004-637X/747/1/43. arXiv: 1112.4609 [astro-ph.SR].

Beuther, H. et al. (Oct. 2016). "The HI/OH/Recombination line survey of the inner Milky Way (THOR). Survey overview and data release 1". In: *A&A* 595, A32, A32. DOI: 10.1051/0004-6361/201629143. arXiv: 1609.03329.

Bihr, S., K.G. Johnston and H. Beuther (Apr. 2016). "Continuum sources from the THOR survey between 1 and 2 GHz". In: *A&A* 588, A97, A97. DOI: 10.1051/0004-6361/201527697. arXiv: 1601.03427.

Bihr, S. et al. (Aug. 2015). "THOR: The H i, OH, Recombination line survey of the Milky Way. The pilot study: H i observations of the giant molecular cloud W43". In: *A&A* 580, A112, A112. DOI: 10.1051/0004-6361/201425370. arXiv: 1505.05176 [astro-ph.SR].

Bik, A. et al. (2014). "Age Spread in Galactic Star Forming Region W3 Main". In: *The Labyrinth of Star Formation*. Ed. by D. Stamatellos, S. Goodwin and D. Ward-Thompson. Vol. 36. Astrophysics and Space Science Proceedings, p. 401. DOI: 10.1007/978-3-319-03041-8_78.

Blum, R. D., A. Damineli and P. S. Conti (Mar. 1999). "The Stellar Content of Obscured Galactic Giant H II Regions. I. W43". In: *AJ* 117, pp. 1392–1401. DOI: 10.1086/300791. eprint: astro-ph/9812070.

Bondi, M. et al. (June 2003). "The VLA-VIRMOS Deep Field. I. Radio observations probing the mu Jy source population". In: *A&A* 403, pp. 857–867. DOI: 10.1051/0004-6361:20030382. eprint: astro-ph/0303364.

Bontemps, S. et al. (Dec. 2010). "Fragmentation and mass segregation in the massive dense cores of Cygnus X". In: *A&A* 524, A18, A18. DOI: 10.1051/0004-6361/200913286. arXiv: 0909.2315 [astro-ph.GA].

Boyden, R. D. et al. (Dec. 2016). "An Exploration of the Statistical Signatures of Stellar Feedback". In: *ApJ* 833, 233, p. 233. DOI: 10.3847/1538-4357/833/2/233. arXiv: 1611.00781.

Brand, J. and L. Blitz (Aug. 1993). "The Velocity Field of the Outer Galaxy". In: *A&A* 275, p. 67.

Briggs, D. S. (Dec. 1995). "High Fidelity Interferometric Imaging: Robust Weighting and NNLS Deconvolution". In: *American Astronomical Society Meeting Abstracts*. Vol. 27. Bulletin of the American Astronomical Society, p. 1444.

Brisken, W. (Dec. 2005). "Pulsar Astrometry with the VLBA". In: *Future Directions in High Resolution Astronomy*. Ed. by J. Romney and M. Reid. Vol. 340. Astronomical Society of the Pacific Conference Series, p. 489. eprint: astro-ph/0309324.

Brisken, W. F. et al. (Oct. 2000). "Measurement of the Parallax of PSR B0950+08 Using the VLBA". In: *ApJ* 541, pp. 959–962. DOI: 10.1086/309492. eprint: astro-ph/0005324.

Brogan, C. L. et al. (Dec. 2016). "The Massive Protostellar Cluster NGC 6334I at 220 au Resolution: Discovery of Further Multiplicity, Diversity, and a Hot Multi-core". In: *ApJ* 832, 187, p. 187. DOI: 10.3847/0004-637X/832/2/187. arXiv: 1609.07470.

Brooks, K. J. and J. B. Whiteoak (Feb. 2001). "Ground-state OH observations towards NGC 6334". In: *MNRAS* 320, pp. 465–476. DOI: 10.1046/j.1365-8711.2001.03964.x. eprint: astro-ph/0010399.

Brunt, C. M. and M. H. Heyer (Feb. 2002a). “Interstellar Turbulence. I. Retrieval of Velocity Field Statistics”. In: *ApJ* 566, pp. 276–288. DOI: 10.1086/338031.
– (Feb. 2002b). “Interstellar Turbulence. II. Energy Spectra of Molecular Regions in the Outer Galaxy”. In: *ApJ* 566, pp. 289–301. DOI: 10.1086/338032. eprint: astro-ph/0110155.
– (Feb. 2002c). “Interstellar Turbulence. II. Energy Spectra of Molecular Regions in the Outer Galaxy”. In: *ApJ* 566, pp. 289–301. DOI: 10.1086/338032. eprint: astro-ph/0110155.
Brunt, C. M. and M.-M. Mac Low (Mar. 2004). “Modification of Projected Velocity Power Spectra by Density Inhomogeneities in Compressible Supersonic Turbulence”. In: *ApJ* 604, pp. 196–212. DOI: 10.1086/381648. eprint: astro-ph/0311461.
Burgers, J.M. (2013). *The Nonlinear Diffusion Equation: Asymptotic Solutions and Statistical Problems*. SpringerLink : Bücher. Springer Netherlands. ISBN: 9789401017459. URL: https://books.google.de/books?id=U5vnCAAAQBAJ.
Burkhart, B. et al. (July 2013). “The Turbulence Power Spectrum in Optically Thick Interstellar Clouds”. In: *ApJ* 771, 123, p. 123. DOI: 10.1088/0004-637X/771/2/123. arXiv: 1305.3619.
Carey, S. J. et al. (Jan. 2009). “MIPSGAL: A Survey of the Inner Galactic Plane at 24 and 70 μm”. In: *PASP* 121, pp. 76–97. DOI: 10.1086/596581.
Carlhoff, P. et al. (Dec. 2013). “Large scale IRAM 30 m CO-observations in the giant molecular cloud complex W43”. In: *A&A* 560, A24, A24. DOI: 10.1051/0004-6361/201321592. arXiv: 1308.6112.
Carral, P. et al. (May 2002). “Detection of the Winds from the Exciting Sources of Shell H II Regions in NGC 6334”. In: *AJ* 123, pp. 2574–2582. DOI: 10.1086/339701.
Castaneda, H. O. (May 1988). “The velocity structure and turbulence at the center of the Orion Nebula”. In: *ApJS* 67, pp. 93–133. DOI: 10.1086/191268.
Castaneda, H. O. and C. R. O’Dell (Apr. 1987). “Fine-scale motion in the central Orion nebula”. In: *ApJ* 315, pp. L55–L59. DOI: 10.1086/184860.
Cesaroni, R. et al. (Mar. 1998). “Sub-arcsecond structure of hot cores in the NH_3 (4,4) line”. In: *A&A* 331, pp. 709–725.
Chandrasekhar, S. (Nov. 1949). “Turbulence - a Physical Theory of Astrophysical Interest.” In: *ApJ* 110, p. 329. DOI: 10.1086/145210.
Churchwell (Jan. 2002). “Ultra-Compact HII Regions and Massive Star Formation”. In: *ARA&A* 40, pp. 27–62. DOI: 10.1146/annurev.astro.40.060401.093845.
Churchwell, E. et al. (Mar. 2009). “The Spitzer/GLIMPSE Surveys: A New View of the Milky Way”. In: *PASP* 121, p. 213. DOI: 10.1086/597811.
Clark, D. H. and J. H. Parkinson (Dec. 1975). “Transient X-ray sources”. In: *Nature* 258, p. 408. DOI: 10.1038/258408a0.
Condon, J. J. (Dec. 1984). “Cosmological evolution of radio sources”. In: *ApJ* 287, pp. 461–474. DOI: 10.1086/162705.
– (Feb. 1997). “Errors in Elliptical Gaussian FITS”. In: *PASP* 109, pp. 166–172. DOI: 10.1086/133871.
Contreras, Y. et al. (Jan. 2013). “ATLASGAL - compact source catalogue: $330^\circ < l < 21^\circ$”. In: *A&A* 549, A45, A45. DOI: 10.1051/0004-6361/201220155. arXiv: 1211.0741 [astro-ph.GA].

Cotton, W. D. (Apr. 2008). "Obit: A Development Environment for Astronomical Algorithms". In: *PASP* 120, p. 439. DOI: 10.1086/586754.

Cotton, W. D. et al. (Mar. 2018). "The Angular Size Distribution of μJy Radio Sources". In: *ApJ* 856, 67, p. 67. DOI: 10.3847/1538-4357/aaaec4.

Csengeri, T. et al. (May 2014). "The ATLASGAL survey: a catalog of dust condensations in the Galactic plane". In: *A&A* 565, A75, A75. DOI: 10.1051/0004-6361/201322434. arXiv: 1312.0937.

Dale, J. E. (Oct. 2015). "The modelling of feedback in star formation simulations". In: *NewAstRev* 68, pp. 1–33. DOI: 10.1016/j.newar.2015.06.001. arXiv: 1508.06054.

Dallacasa, D. et al. (Nov. 2000). "High frequency peakers. I. The bright sample". In: *A&A* 363, pp. 887–900. eprint: astro-ph/0012428.

Deller, A. T. (Feb. 2009). "Precision VLBI astrometry: Instrumentation, algorithms and pulsar parallax determination". PhD thesis. PhD Thesis, 2009.

Dickey, J. M. et al. (Nov. 2001). "Southern Galactic Plane Survey Measurements of the Spatial Power Spectrum of Interstellar H I in the Inner Galaxy". In: *ApJ* 561, pp. 264–271. DOI: 10.1086/323409. eprint: astro-ph/0107604.

Dobbs, C. L. et al. (2014). "Formation of Molecular Clouds and Global Conditions for Star Formation". In: *Protostars and Planets VI*, pp. 3–26. DOI: 10.2458/azu_uapress_9780816531240-ch001. arXiv: 1312.3223.

Doi, T., C. R. O'Dell and P. Hartigan (June 2004). "Internal Velocities in the Orion Nebula: Large Radial Velocity Features". In: *AJ* 127, pp. 3456–3478. DOI: 10.1086/386351.

Drilling, J. S. and A. U. Landolt (2000). "Normal Stars". In: *Allen's Astrophysical Quantities*. Ed. by A. N. Cox, p. 381.

Duarte-Cabral, A. et al. (Oct. 2013). "CO outflows from high-mass Class 0 protostars in Cygnus-X". In: *A&A* 558, A125, A125. DOI: 10.1051/0004-6361/201321393. arXiv: 1308.6490 [astro-ph.GA].

Dzib, S. A. et al. (Oct. 2013a). "Radio Sources Embedded in the Dense Core B59, the "Mouthpiece" of the Pipe Nebula". In: *RevMexAA* 49, pp. 345–349. arXiv: 1308.2621 [astro-ph.SR].

Dzib, S. A. et al. (Sept. 2013b). "The Gould's Belt Very Large Array Survey. I. The Ophiuchus Complex". In: *ApJ* 775, 63, p. 63. DOI: 10.1088/0004-637X/775/1/63. arXiv: 1307.5105 [astro-ph.SR].

Dzib, S. A. et al. (Oct. 2018). "The Enigmatic Compact Radio Source Coincident with the Energetic X-Ray Pulsar PSR J1813-1749 and HESS J1813-178". In: *ApJ* 866, 100, p. 100. DOI: 10.3847/1538-4357/aada07. arXiv: 1808.04132 [astro-ph.HE].

Elia, D. et al. (Oct. 2017). "The Hi-GAL compact source catalogue - I. The physical properties of the clumps in the inner Galaxy (-71.0° < l < 67.0°)". In: *MNRAS* 471, pp. 100–143. DOI: 10.1093/mnras/stx1357. arXiv: 1706.01046.

Elmegreen, B. G. and C. J. Lada (June 1977). "Sequential formation of subgroups in OB associations." In: *ApJ* 214, pp. 725–741. DOI: 10.1086/155302.

Elmegreen, B. G. and J. Scalo (Sept. 2004). "Interstellar Turbulence I: Observations and Processes". In: *ARA&A* 42, pp. 211–273. DOI: 10.1146/annurev.astro.41.011802.094859. eprint: astro-ph/0404451.

Esquivel, A. et al. (June 2003). “Velocity statistics from spectral line data: effects of density-velocity correlations, magnetic field and shear”. In: *MNRAS* 342, pp. 325–336. DOI: 10.1046/j.1365-8711.2003.06551.x. eprint: astro-ph/0210159.

Faúndez, S. et al. (Oct. 2004). “SIMBA survey of southern high-mass star forming regions. I. Physical parameters of the 1.2 mm/IRAS sources”. In: *A&A* 426, pp. 97–103. DOI: 10.1051/0004-6361:20035755.

Feigelson, E. D. et al. (July 2009). “Stellar Clusters in the NGC 6334 Star-Forming Complex”. In: *AJ* 138, pp. 227–239. DOI: 10.1088/0004-6256/138/1/227. arXiv: 0905.0716.

Fomalont, E. B. et al. (Oct. 1991). “The micro-Jansky radio source population at 5 GHz”. In: *AJ* 102, pp. 1258–1277. DOI: 10.1086/115952.

Forbrich, J. et al. (May 2016). “The Population of Compact Radio Sources in the Orion Nebula Cluster”. In: *ApJ* 822, 93, p. 93. DOI: 10.3847/0004-637X/822/2/93. arXiv: 1603.05666 [astro-ph.SR].

Garay, G., L. F. Rodriguez and J. H. van Gorkom (Oct. 1986). “Rotating and expanding ultracompact H II regions”. In: *ApJ* 309, pp. 553–563. DOI: 10.1086/164624.

Garcia-Diaz, M. T. and W. J. Henney (Mar. 2007). “Velocity Structure in the Orion Nebula. I. Spectral Mapping in Low-Ionization Lines”. In: *AJ* 133, pp. 952–964. DOI: 10.1086/510621. eprint: astro-ph/0611417.

Garcia-Diaz, M. T. et al. (Apr. 2008). “Velocity Structure in the Orion Nebula. II. Emission Line Atlas of Partially Ionized to Fully Ionized Gas”. In: *RevMexAA* 44, pp. 181–212. arXiv: 0802.0518.

Giveon, U. et al. (Jan. 2005a). “A New Catalog of Radio Compact H II Regions in the Milky Way”. In: *AJ* 129, pp. 348–354. DOI: 10.1086/426360.

– (July 2005b). “A New Catalog of Radio Compact H II Regions in the Milky Way. II. The 1.4 GHz Data”. In: *AJ* 130, pp. 156–164. DOI: 10.1086/430459.

Goicoechea, J. R., M. Gerin and E. Bron (Mar. 2019). “Stellar Feedback in the ISM Revealed by Wide-Field Far-Infrared Spectral-Imaging”. In: *arXiv e-prints*. arXiv: 1903.03959.

Green, D. A. (June 2014). “A catalogue of 294 Galactic supernova remnants”. In: *Bulletin of the Astronomical Society of India* 42, pp. 47–58. arXiv: 1409.0637 [astro-ph.HE].

Greisen, E. W. (Mar. 2003). “AIPS, the VLA, and the VLBA”. In: *Information Handling in Astronomy - Historical Vistas*. Ed. by A. Heck. Vol. 285. Astrophysics and Space Science Library, p. 109. DOI: 10.1007/0-306-48080-8_7.

Hales, C. A. et al. (Sept. 2012a). “BLOBCAT: software to catalogue flood-filled blobs in radio images of total intensity and linear polarization”. In: *MNRAS* 425, pp. 979–996. DOI: 10.1111/j.1365-2966.2012.21373.x. arXiv: 1205.5313 [astro-ph.IM].

– (Sept. 2012b). “BLOBCAT: software to catalogue flood-filled blobs in radio images of total intensity and linear polarization”. In: *MNRAS* 425, pp. 979–996. DOI: 10.1111/j.1365-2966.2012.21373.x. arXiv: 1205.5313 [astro-ph.IM].

Helfand, D. J. et al. (May 2006). “MAGPIS: A Multi-Array Galactic Plane Imaging Survey”. In: *AJ* 131, pp. 2525–2537. DOI: 10.1086/503253.

Hennebelle, P. and E. Falgarone (Nov. 2012). “Turbulent molecular clouds”. In: *A&A Rev.* 20, 55, p. 55. DOI: 10.1007/s00159-012-0055-y. arXiv: 1211.0637.

Herpin, F. et al. (June 2012). "The massive protostar W43-MM1 as seen by Herschel-HIFI water spectra: high turbulence and accretion luminosity". In: *A&A* 542, A76, A76. DOI: 10.1051/0004-6361/201118413. arXiv: 1204.0397.

Heyer, M. H. and F. P. Schloerb (Jan. 1997). "Application of Principal Component Analysis to Large-Scale Spectral Line Imaging Studies of the Interstellar Medium". In: *ApJ* 475, pp. 173–187. DOI: 10.1086/303514.

Hoare, M. G. et al. (Jan. 2007). "Ultracompact Hii Regions and the Early Lives of Massive Stars". In: *Protostars and Planets V*. Ed. by Bo Reipurth, David Jewitt and Klaus Keil, p. 181. arXiv: astro-ph/0603560 [astro-ph].

Hoare, M. G. et al. (Sept. 2012). "The Coordinated Radio and Infrared Survey for High-Mass Star Formation (The CORNISH Survey). I. Survey Design". In: *PASP* 124, pp. 939–955. DOI: 10.1086/668058. arXiv: 1208.3351 [astro-ph.GA].

Hobbs, G. et al. (Oct. 2004). "Long-term timing observations of 374 pulsars". In: *MNRAS* 353, pp. 1311–1344. DOI: 10.1111/j.1365-2966.2004.08157.x.

Holwerda, B. W. (Dec. 2005a). "Source Extractor for Dummies v5". In: *arXiv Astrophysics e-prints*. eprint: astro-ph/0512139.

– (Dec. 2005b). "Source Extractor for Dummies v5". In: *ArXiv Astrophysics e-prints*. eprint: astro-ph/0512139.

Hunter, T. R. et al. (Oct. 2006). "Millimeter Multiplicity in NGC 6334 I and I(N)". In: *ApJ* 649, pp. 888–893. DOI: 10.1086/505965. eprint: astro-ph/0605468.

Hunter, T. R. et al. (June 2014). "Subarcsecond Imaging of the NGC 6334 I(N) Protocluster: Two Dozen Compact Sources and a Massive Disk Candidate". In: *ApJ* 788, 187, p. 187. DOI: 10.1088/0004-637X/788/2/187. arXiv: 1405.0496 [astro-ph.SR].

Huynh, M. T. et al. (Oct. 2005). "Radio Observations of the Hubble Deep Field-South Region. II. The 1.4 GHz Catalog and Source Counts". In: *AJ* 130, pp. 1373–1388. DOI: 10.1086/432873. eprint: astro-ph/0506047.

Irabor, T. et al. (July 2018). "The Coordinated Radio and Infrared Survey for High-mass Star Formation. slowromancapiv@: A new radio selected sample of compact Galactic Planetary Nebulae". In: *MNRAS*. DOI: 10.1093/mnras/sty1929. arXiv: 1807.09336 [astro-ph.SR].

Jackson, J. M. et al. (Mar. 2006). "The Boston University-Five College Radio Astronomy Observatory Galactic Ring Survey". In: *ApJS* 163, pp. 145–159. DOI: 10.1086/500091. eprint: astro-ph/0602160.

Jolliffe, I. T. (1986). *Principal component analysis*.

Kainulainen, J. et al. (Apr. 2017). "Resolving the fragmentation of high line-mass filaments with ALMA: the integral shaped filament in Orion A". In: *A&A* 600, A141, A141. DOI: 10.1051/0004-6361/201628481. arXiv: 1603.05688.

Kalcheva, I. E. et al. (Mar. 2018). "The Coordinated Radio and Infrared Survey for High-Mass Star Formation III. A catalogue of northern ultra-compact H II regions". In: *ArXiv e-prints*. arXiv: 1803.09334.

Keith, M. J. et al. (May 2009). "Discovery of 28 pulsars using new techniques for sorting pulsar candidates". In: *MNRAS* 395, pp. 837–846. DOI: 10.1111/j.1365-2966.2009.14543.x. arXiv: 0901.3570 [astro-ph.SR].

Kennicutt, R. C. (2005). "The role of massive stars in astrophysics". In: *Massive Star Birth: A Crossroads of Astrophysics*. Ed. by R. Cesaroni et al. Vol. 227. IAU Symposium, pp. 3–11. DOI: 10.1017/S1743921305004308.

Kessel-Deynet, O. and A. Burkert (Jan. 2003). "Radiation-driven implosion of molecular cloud cores". In: *MNRAS* 338.3, pp. 545–554. DOI: 10.1046/j.1365-8711.2003.05737.x. arXiv: astro-ph/0203460 [astro-ph].

Keto, E. (Dec. 2003). "The Formation of Massive Stars by Accretion through Trapped Hypercompact H II Regions". In: *ApJ* 599.2, pp. 1196–1206. DOI: 10.1086/379545. arXiv: astro-ph/0309131 [astro-ph].

Kim, J.-G., W.-T. Kim and E. C. Ostriker (May 2018). "Modeling UV Radiation Feedback from Massive Stars. II. Dispersal of Star-forming Giant Molecular Clouds by Photoionization and Radiation Pressure". In: *ApJ* 859, 68, p. 68. DOI: 10.3847/1538-4357/aabe27. arXiv: 1804.04664.

Klessen, R. S. (Nov. 2011). "Star Formation in Molecular Clouds". In: *EAS Publications Series*. Ed. by C. Charbonnel and T. Montmerle. Vol. 51. EAS Publications Series, pp. 133–167. DOI: 10.1051/eas/1151009. arXiv: 1109.0467.

Koch, E. W. et al. (Apr. 2019). "TurbuStat: Turbulence Statistics in Python". In: *arXiv e-prints*. arXiv: 1904.10484 [astro-ph.IM].

Kolmogorov, A. (1941a). "The Local Structure of Turbulence in Incompressible Viscous Fluid for Very Large Reynolds' Numbers". In: *Akademiia Nauk SSSR Doklady* 30, pp. 301–305.

– (1941b). "The Local Structure of Turbulence in Incompressible Viscous Fluid for Very Large Reynolds' Numbers". In: *Akademiia Nauk SSSR Doklady* 30, pp. 301–305.

Koornneef, J. (Nov. 1983). "Near-infrared photometry. II - Intrinsic colours and the absolute calibration from one to five micron". In: *A&A* 128, pp. 84–93.

Kounkel, M. et al. (Jan. 2017). "The Gould's Belt Distances Survey (GOBELINS) II. Distances and Structure toward the Orion Molecular Clouds". In: *ApJ* 834, 142, p. 142. DOI: 10.3847/1538-4357/834/2/142. arXiv: 1609.04041 [astro-ph.SR].

Krumholz, M. R. et al. (June 2018). "A unified model for galactic discs: star formation, turbulence driving, and mass transport". In: *MNRAS* 477, pp. 2716–2740. DOI: 10.1093/mnras/sty852. arXiv: 1706.00106.

Kurtz, S. (2005). "Hypercompact HII regions". In: *Massive Star Birth: A Crossroads of Astrophysics*. Ed. by R. Cesaroni et al. Vol. 227. IAU Symposium, pp. 111–119. DOI: 10.1017/S1743921305004424.

Kurtz, S. E. et al. (Mar. 1999). "Ultracompact H II Regions with Extended Radio-Continuum Emission". In: *ApJ* 514, pp. 232–248. DOI: 10.1086/306928.

Kurtz, S., E. Churchwell and D. O. S. Wood (Apr. 1994). "Ultracompact H II Regions. II. New High-Resolution Radio Images". In: *ApJS* 91, p. 659. DOI: 10.1086/191952.

Kurtz, S. and P. Hofner (Aug. 2005). "Water Masers Toward Ultracompact H II Regions". In: *AJ* 130, pp. 711–720. DOI: 10.1086/431546. eprint: arXiv:astro-ph/0507039.

Kurtz, S. et al. (May 2000). "Hot Molecular Cores and the Earliest Phases of High-Mass Star Formation". In: *Protostars and Planets IV*. Ed. by V. Mannings, A. P. Boss and S. S. Russell, pp. 299–326.

Lazarian, A. and D. Pogosyan (July 2000a). "Velocity Modification of H I Power Spectrum". In: *ApJ* 537, pp. 720–748. DOI: 10.1086/309040. eprint: astro-ph/9901241.

Lazarian, A. and D. Pogosyan (July 2000b). "Velocity Modification of H I Power Spectrum". In: *ApJ* 537, pp. 720–748. DOI: 10.1086/309040. eprint: astro-ph/9901241.

Lequeux, J. (2005). *The Interstellar Medium*. DOI: 10.1007/b137959.

Liszt, H. S. and J. Pety (May 2012). "Imaging diffuse clouds: bright and dark gas mapped in CO". In: *A&A* 541, A58, A58. DOI: 10.1051/0004-6361/201218771. arXiv: 1202.6523.

Liu, Z. et al. (Apr. 2019). "A Catalog of OB Stars from LAMOST Spectroscopic Survey". In: *ApJS* 241, 32, p. 32. DOI: 10.3847/1538-4365/ab0a0d. arXiv: 1902.07607 [astro-ph.SR].

Lockman, F. J. (Nov. 1989). "A survey of radio H II regions in the northern sky". In: *ApJS* 71, pp. 469–479. DOI: 10.1086/191383.

López-Chico, T. and L. Salas (Apr. 2007). "Mass determination for T Tauri stars from JHK Photometry". In: *RevMexAA* 43, pp. 155–171. eprint: astro-ph/0611721.

Louvet, F. et al. (Oct. 2014). "The W43-MM1 mini-starburst ridge, a test for star formation efficiency models". In: *A&A* 570, A15, A15. DOI: 10.1051/0004-6361/201423603. arXiv: 1404.4843 [astro-ph.SR].

Louvet, F. et al. (Nov. 2016). "Tracing extended low-velocity shocks through SiO emission. Case study of the W43-MM1 ridge". In: *A&A* 595, A122, A122. DOI: 10.1051/0004-6361/201629077. arXiv: 1607.08668.

Mac Low, M.-M. and R. S. Klessen (Jan. 2004). "Control of star formation by supersonic turbulence". In: *Reviews of Modern Physics* 76, pp. 125–194. DOI: 10.1103/RevModPhys.76.125. eprint: astro-ph/0301093.

Malarecki, J. M. et al. (May 2015). "Giant radio galaxies - II. Tracers of large-scale structure". In: *MNRAS* 449, pp. 955–986. DOI: 10.1093/mnras/stv273. arXiv: 1502.03954.

Masqué, J. M. et al. (Feb. 2017). "Searching for Compact Radio Sources Associated with UCHII Regions". In: *ApJ* 836, 96, p. 96. DOI: 10.3847/1538-4357/836/1/96. arXiv: 1701.02717 [astro-ph.SR].

McKee, Christopher F. and Jonathan C. Tan (Mar. 2003). "The Formation of Massive Stars from Turbulent Cores". In: *ApJ* 585.2, pp. 850–871. DOI: 10.1086/346149. arXiv: astro-ph/0206037 [astro-ph].

Medina, S. N. X. et al. (May 2019). "GLOSTAR – Radio Source Catalog I: $28^\circ < l < 36^\circ$ and $|b| < 1^\circ$". In: *arXiv e-prints*, arXiv:1905.09281, arXiv:1905.09281. arXiv: 1905.09281 [astro-ph.GA].

Medina, S.-N X. et al. (Feb. 2018). "Richness of compact radio sources in NGC 6334D to F". In: *A&A* 610, A27, A27. DOI: 10.1051/0004-6361/201731774. arXiv: 1711.02934.

Medina, S. et al. (Dec. 2014). "Turbulence in simulated H II regions". In: *MNRAS* 445, pp. 1797–1819. DOI: 10.1093/mnras/stu1862. arXiv: 1409.5838.

Menten, K. M. et al. (Nov. 2007). "The distance to the Orion Nebula". In: *A&A* 474, pp. 515–520. DOI: 10.1051/0004-6361:20078247. arXiv: 0709.0485.

Minier, V. et al. (June 2003). "The protostellar mass limit for 6.7 GHz methanol masers. I. A low-mass YSO survey". In: *A&A* 403, pp. 1095–1100. DOI: 10.1051/0004-6361:20030465.

Molinari, S. et al. (Mar. 2000). "A search for precursors of Ultracompact Hii regions in a sample of luminous IRAS sources. III. Circumstellar dust properties". In: *A&A* 355, pp. 617–628. arXiv: astro-ph/0001231 [astro-ph].

Molinari, S. et al. (July 2010). “Clouds, filaments, and protostars: The Herschel Hi-GAL Milky Way”. In: *A&A* 518, L100, p. L100. DOI: 10.1051/0004-6361/201014659. arXiv: 1005.3317 [astro-ph.GA].

Moran, J. M. et al. (Jan. 1990). “The large scattering disk of NGC 6334B”. In: *ApJ* 348, pp. 147–152. DOI: 10.1086/168222.

Motte, F., S. Bontemps and F. Louvet (Sept. 2018). “High-Mass Star and Massive Cluster Formation in the Milky Way”. In: *ARA&A* 56, pp. 41–82. DOI: 10.1146/annurev-astro-091916-055235. arXiv: 1706.00118 [astro-ph.GA].

Motte, F., P. Schilke and D. C. Lis (Jan. 2003). “From Massive Protostars to a Giant H II Region: Submillimeter Imaging of the Galactic Ministarburst W43”. In: *ApJ* 582, pp. 277–291. DOI: 10.1086/344538. eprint: arXiv:astro-ph/0208519.

Mottram, J. C. et al. (Jan. 2011). “The Red MSX Source survey: the bolometric fluxes and luminosity distributions of young massive stars”. In: *A&A* 525, A149, A149. DOI: 10.1051/0004-6361/201014479. arXiv: 1009.1774 [astro-ph.GA].

Muller, E. et al. (Dec. 2004). “A Statistical Investigation of H I in the Magellanic Bridge”. In: *ApJ* 616, pp. 845–856. DOI: 10.1086/425154. eprint: astro-ph/0408259.

Munch, G. (July 1958). “Internal Motions in the Orion Nebula”. In: *Reviews of Modern Physics* 30, pp. 1035–1041. DOI: 10.1103/RevModPhys.30.1035.

Murphy, T. et al. (Nov. 2007). “The second epoch Molonglo Galactic Plane Survey: compact source catalogue”. In: *MNRAS* 382.1, pp. 382–392. DOI: 10.1111/j.1365-2966.2007.12379.x. arXiv: 0708.3092 [astro-ph].

Neff, S. G., J. A. Eilek and F. N. Owen (Apr. 2015). “The Complex North Transition Region of Centaurus A: Radio Structure”. In: *ApJ* 802, 87, p. 87. DOI: 10.1088/0004-637X/802/2/87. arXiv: 1502.05066.

Nguyen Luong, Q. et al. (May 2011). “W43: the closest molecular complex of the Galactic bar?” In: *A&A* 529, A41, A41. DOI: 10.1051/0004-6361/201016271. arXiv: 1102.3460 [astro-ph.SR].

O’dell, C. R., Z. Wen and X. Hu (June 1993). “Discovery of new objects in the Orion nebula on HST images - Shocks, compact sources, and protoplanetary disks”. In: *ApJ* 410, pp. 696–700. DOI: 10.1086/172786.

O’Dell, C. R. and Kwan Wong (Feb. 1996). “Hubble Space Telescope Mapping of the Orion Nebula. I. A Survey of Stars and Compact Objects”. In: *AJ* 111, p. 846. DOI: 10.1086/117832.

O′Dell, C. R. (2001). “The Orion Nebula and its Associated Population”. In: *ARA&A* 39, pp. 99–136. DOI: 10.1146/annurev.astro.39.1.99.

O′Dell, C. R. and W. J. Henney (Oct. 2008). “High Spatial Velocity Features in the Orion Nebula”. In: *AJ* 136, pp. 1566–1586. DOI: 10.1088/0004-6256/136/4/1566. arXiv: 0807.4189.

O′Dell, C. R. and Z. Wen (Mar. 1992). “Motion at the ionization front in the Orion nebula - A kinematic study of the forbidden O I line”. In: *ApJ* 387, pp. 229–240. DOI: 10.1086/171074.

O′Dell, C. R. et al. (Jan. 2009). “The Three-Dimensional Dynamic Structure of the Inner Orion Nebula”. In: *AJ* 137, pp. 367–382. DOI: 10.1088/0004-6256/137/1/367. arXiv: 0810.4375.

Offner, S. S. R. and J. Chaban (Oct. 2017). “Impact of Protostellar Outflows on Turbulence and Star Formation Efficiency in Magnetized Dense Cores”. In: *ApJ* 847, 104, p. 104. DOI: 10.3847/1538-4357/aa8996. arXiv: 1709.01086.

Ortega, M. E. et al. (Feb. 2010). "A multiwavelength study of the star forming region IRAS 18544+0112". In: *A&A* 510, A96, A96. DOI: 10.1051/0004-6361/200912722. arXiv: 0912.1837.

Panagia, Nino (Nov. 1973). "Some Physical parameters of early-type stars". In: *AJ* 78, pp. 929–934. DOI: 10.1086/111498.

Parker, Q. A., I. S. Bojičić and D. J. Frew (July 2016). "HASH: the Hong Kong/AAO/Strasbourg Hα planetary nebula database". In: *Journal of Physics Conference Series*. Vol. 728. Journal of Physics Conference Series, p. 032008. DOI: 10.1088/1742-6596/728/3/032008. arXiv: 1603.07042 [astro-ph.SR].

Perley, R. A. et al. (Sept. 2011). "The Expanded Very Large Array: A New Telescope for New Science". In: *ApJ* 739, L1, p. L1. DOI: 10.1088/2041-8205/739/1/L1. arXiv: 1106.0532 [astro-ph.IM].

Persi, P. and M. Tapia (Dec. 2008). "Star Formation in NGC 6334". In: *Handbook of Star Forming Regions, Volume II*. Ed. by B. Reipurth, p. 456.

Purcell, C. R. et al. (Mar. 2013). "The Coordinated Radio and Infrared Survey for High-mass Star Formation. II. Source Catalog". In: *ApJS* 205, 1, p. 1. DOI: 10.1088/0067-0049/205/1/1. arXiv: 1211.7116 [astro-ph.GA].

Rahman, M. and N. Murray (Aug. 2010). "A New Sample of Very Massive Star Forming Complexes in the Spitzer Glimpse Survey". In: *ApJ* 719, pp. 1104–1122. DOI: 10.1088/0004-637X/719/2/1104. arXiv: 1004.3290 [astro-ph.GA].

Rau, U. and T. J. Cornwell (Aug. 2011). "A multi-scale multi-frequency deconvolution algorithm for synthesis imaging in radio interferometry". In: *A&A* 532, A71, A71. DOI: 10.1051/0004-6361/201117104. arXiv: 1106.2745 [astro-ph.IM].

Reed, B. C. (May 2003). "Catalog of Galactic OB Stars". In: *AJ* 125, pp. 2531–2533. DOI: 10.1086/374771.

Reid, M. J. et al. (June 2016). "A Parallax-based Distance Estimator for Spiral Arm Sources". In: *ApJ* 823, 77, p. 77. DOI: 10.3847/0004-637X/823/2/77. arXiv: 1604.02433.

Reid et al. (Mar. 2014). "Trigonometric Parallaxes of High Mass Star Forming Regions: The Structure and Kinematics of the Milky Way". In: *ApJ* 783, 130, p. 130. DOI: 10.1088/0004-637X/783/2/130. arXiv: 1401.5377 [astro-ph.GA].

Rieke, G. H. and M. J. Lebofsky (Jan. 1985). "The interstellar extinction law from 1 to 13 microns". In: *ApJ* 288, pp. 618–621. DOI: 10.1086/162827.

Rigby, A. J. et al. (Mar. 2016). "CHIMPS: the ^{13}CO/C^{18}O (J = 3 $\rightarrow$ 2) Heterodyne Inner Milky Way Plane Survey". In: *MNRAS* 456.3, pp. 2885–2899. DOI: 10.1093/mnras/stv2808. arXiv: 1512.08235 [astro-ph.GA].

Rodriguez-Fernandez, N. J. and F. Combes (Oct. 2008). "Gas flow models in the Milky Way embedded bars". In: *A&A* 489, pp. 115–133. DOI: 10.1051/0004-6361:200809644. arXiv: 0806.4252.

Rodriguez, L. F., L.A. Zapata and P.T. Ho (Jan. 2007). "Compact Centimeter and Millimeter Sources in NGC 6334 I(N): OB Stars in the Making?" In: *ApJ* 654, pp. L143–L146. DOI: 10.1086/511303. eprint: astro-ph/0612057.

Rodriguez, L. F. et al. (Aug. 2012). "Compact Radio Sources in M17". In: *ApJ* 755, 152, p. 152. DOI: 10.1088/0004-637X/755/2/152. arXiv: 1206.5339 [astro-ph.SR].

Rodriguez, J. Canto and J.M. Moran (Apr. 1982). “Radio sources in NGC 6334”. In: *ApJ* 255, pp. 103–110. DOI: 10.1086/159808.

Roman-Duval, J. et al. (Oct. 2011). “The Turbulence Spectrum of Molecular Clouds in the Galactic Ring Survey: A Density-dependent Principal Component Analysis Calibration”. In: *ApJ* 740, 120, p. 120. DOI: 10.1088/0004-637X/740/2/120. arXiv: 1107.4569.

Rosolowsky, E. W. et al. (June 2008). “Structural Analysis of Molecular Clouds: Dendrograms”. In: *ApJ* 679.2, pp. 1338–1351. DOI: 10.1086/587685. arXiv: 0802.2944 [astro-ph].

Rosolowsky, E. and A. Leroy (Apr. 2006). “Bias-free Measurement of Giant Molecular Cloud Properties”. In: *PASP* 118.842, pp. 590–610. DOI: 10.1086/502982. arXiv: astro-ph/0601706 [astro-ph].

Sandell, G. (June 2000). “(Sub)mm continuum mapping of NGC 6334 I & I(N). A cobweb of filaments and protostars”. In: *A&A* 358, pp. 242–256.

Saral, G. et al. (Apr. 2017). “Young Stellar Objects in the Massive Star-forming Regions W51 and W43”. In: *ApJ* 839, 108, p. 108. DOI: 10.3847/1538-4357/aa6575. arXiv: 1703.02771.

Sault, R. J., P. J. Teuben and M. C. H. Wright (Jan. 1995). “A Retrospective View of MIRIAD”. In: *Astronomical Data Analysis Software and Systems IV*. Ed. by R. A. Shaw, H. E. Payne and J. J. E. Hayes. Vol. 77. Astronomical Society of the Pacific Conference Series, p. 433. arXiv: astro-ph/0612759 [astro-ph].

Schleicher, D. R. G. et al. (Feb. 2013). “The small-scale dynamo: breaking universality at high Mach numbers”. In: *New Journal of Physics* 15.2, 023017, p. 023017. DOI: 10.1088/1367-2630/15/2/023017. arXiv: 1301.4371.

Schuller, F. et al. (Sept. 2009). “ATLASGAL - The APEX telescope large area survey of the galaxy at 870 μm”. In: *A&A* 504, pp. 415–427. DOI: 10.1051/0004-6361/200811568.

Schuller, F. et al. (May 2017). “SEDIGISM: Structure, excitation, and dynamics of the inner Galactic interstellar medium”. In: *A&A* 601, A124, A124. DOI: 10.1051/0004-6361/201628933. arXiv: 1701.04712.

Shima, K. et al. (May 2018). “The effect of photoionizing feedback on star formation in isolated and colliding clouds”. In: *PASJ* 70, S54, S54. DOI: 10.1093/pasj/psx124. arXiv: 1710.02285.

Smith, R. J., S. Longmore and I. Bonnell (Dec. 2009). “The simultaneous formation of massive stars and stellar clusters”. In: *MNRAS* 400.4, pp. 1775–1784. DOI: 10.1111/j.1365-2966.2009.15621.x. arXiv: 0908.3910 [astro-ph.SR].

Spitzer, L. (1978). *Physical processes in the interstellar medium*. DOI: 10.1002/9783527617722.

Sridharan, T. K. et al. (Feb. 2002). “High-Mass Protostellar Candidates. I. The Sample and Initial Results”. In: *ApJ* 566.2, pp. 931–944. DOI: 10.1086/338332. arXiv: astro-ph/0110363 [astro-ph].

Straw, S. M., A. R. Hyland and P. J. McGregor (Jan. 1989). “The centers of star formation in NGC 6334 and their stellar mass distributions”. In: *ApJS* 69, pp. 99–140. DOI: 10.1086/191309.

Tanaka, K. E. I., J. C. Tan and Y. Zhang (Jan. 2017). “The Impact of Feedback During Massive Star Formation by Core Accretion”. In: *ApJ* 835, 32, p. 32. DOI: 10.3847/1538-4357/835/1/32. arXiv: 1610.08856 [astro-ph.SR].

Tapia, M. (Dec. 1981). “Near-infrared observations of trapezium-type multiple systems Catalogue of observations and a new determination of the reddening law”. In: *MNRAS* 197, pp. 949–965. DOI: 10.1093/mnras/197.4.949.

Tapia, M., P. Persi and M. Roth (Dec. 1996). "The embedded stellar population in northern NGC 6334." In: *A&A* 316, pp. 102–110.

Synthesis Imaging in Radio Astronomy II (Jan. 1999). Vol. 180. Astronomical Society of the Pacific Conference Series.

Tenorio-Tagle, G. (Jan. 1979). "The gas dynamics of H II regions. I - The champagne model". In: *A&A* 71, pp. 59–65.

Thompson, M. A. et al. (July 2006). "A SCUBA imaging survey of ultracompact HII regions. The environments of massive star formation". In: *A&A* 453, pp. 1003–1026. DOI: 10.1051/0004-6361:20054383. eprint: arXiv:astro-ph/0604208.

Tigé, J. et al. (June 2017). "The earliest phases of high-mass star formation, as seen in NGC 6334 by Herschel-HOBYS". In: *A&A* 602, A77, A77. DOI: 10.1051/0004-6361/201628989. arXiv: 1703.09839 [astro-ph.GA].

Treichel, K. et al. (Nov. 2001). "Spectral Structure in FR II Radio Galaxies and Jets". In: *ApJ* 561, pp. 691–702. DOI: 10.1086/323254. eprint: astro-ph/0108264.

Urquhart, J. S. et al. (Jan. 2007). "The RMS survey. Radio observations of candidate massive YSOs in the southern hemisphere". In: *A&A* 461, pp. 11–23. DOI: 10.1051/0004-6361:20065837. eprint: arXiv:astro-ph/0605738.

Urquhart, J. S. et al. (July 2009). "The RMS survey. 6 cm continuum VLA observations towards candidate massive YSOs in the northern hemisphere". In: *A&A* 501, pp. 539–551. DOI: 10.1051/0004-6361/200912108. arXiv: 0905.1174.

Urquhart, J. S. et al. (Dec. 2011). "The Red MSX Source survey: ammonia and water maser analysis of massive star-forming regions". In: *MNRAS* 418, pp. 1689–1706. DOI: 10.1111/j.1365-2966.2011.19594.x. arXiv: 1107.3913 [astro-ph.GA].

Urquhart, J. S. et al. (Oct. 2013). "ATLASGAL - properties of compact H II regions and their natal clumps". In: *MNRAS* 435, pp. 400–428. DOI: 10.1093/mnras/stt1310. arXiv: 1307.4105.

Urquhart, J. S. et al. (Aug. 2014a). "ATLASGAL - Complete compact source catalogue: 280° <l< 60°". In: *A&A* 568, A41, A41. DOI: 10.1051/0004-6361/201424126. arXiv: 1406.5741.

Urquhart, J. S. et al. (Sept. 2014b). "ATLASGAL - towards a complete sample of massive star forming clumps". In: *MNRAS* 443, pp. 1555–1586. DOI: 10.1093/mnras/stu1207. arXiv: 1406.5078.

Urquhart, J. S. et al. (Jan. 2018). "ATLASGAL - properties of a complete sample of Galactic clumps". In: *MNRAS* 473, pp. 1059–1102. DOI: 10.1093/mnras/stx2258. arXiv: 1709.00392.

Vázquez-Semadeni, E. et al. (Dec. 2009). "High- and Low-Mass Star-Forming Regions from Hierarchical Gravitational Fragmentation. High Local Star Formation Rates with Low Global Efficiencies". In: *ApJ* 707.2, pp. 1023–1033. DOI: 10.1088/0004-637X/707/2/1023. arXiv: 0904.4515 [astro-ph.GA].

von Hoerner, S. (1951). "Eine Methode zur Untersuchung der Turbulenz der interstellaren Materie. Mit 10 Textabbildungen". In: *ZAp* 30, p. 17.

Wang, Y. et al. (Aug. 2018). "Radio continuum emission in the northern Galactic plane: Sources and spectral indices from the THOR survey". In: *ArXiv e-prints*. arXiv: 1808.05990.

Wen, Z. and C. R. O'Dell (May 1993). "Motion in the Orion nebula - A kinematic study of forbidden S III". In: *ApJ* 409, pp. 262–268. DOI: 10.1086/172660.

Willis, S. et al. (Dec. 2013). “A Wide-field near- and Mid-infrared Census of Young Stars in NGC 6334”. In: *ApJ* 778, 96, p. 96. DOI: 10.1088/0004-637X/778/2/96. arXiv: 1310.0821 [astro-ph.SR].

Wilson, T. L., K. Rohlfs and S. Huttemeister (Dec. 2012). *Tools of Radio Astronomy, 5th edition*.

Wood, Douglas O. S. and Churchwell (May 1989). “Massive Stars Embedded in Molecular Clouds: Their Population and Distribution in the Galaxy”. In: *ApJ* 340, p. 265. DOI: 10.1086/167390.

Wright, E. L. et al. (Dec. 2010). “The Wide-field Infrared Survey Explorer (WISE): Mission Description and Initial On-orbit Performance”. In: *AJ* 140, 1868, pp. 1868–1881. DOI: 10.1088/0004-6256/140/6/1868. arXiv: 1008.0031 [astro-ph.IM].

Wynn-Williams, C. G., C. A. Beichman and D. Downes (Apr. 1981). “VLA observations of W 33, W 44, and GL 2591”. In: *AJ* 86, pp. 565–568. DOI: 10.1086/112916.

Ybarra, J. E. et al. (Oct. 2014). “Spitzer IRAC Color Diagnostics for Extended Emission in Star-forming Regions”. In: *ApJ* 794, L25, p. L25. DOI: 10.1088/2041-8205/794/2/L25. arXiv: 1409.1238 [astro-ph.SR].

Zapata, L. A. et al. (Apr. 2004). “Compact Radio Sources in Orion: New Detections, Time Variability, and Objects in OMC-1S”. In: *AJ* 127, pp. 2252–2261. DOI: 10.1086/382715. eprint: astro-ph/0403350.

Zhang, B. et al. (Feb. 2014). “The Parallax of W43: a Massive Star-forming Complex near the Galactic Bar”. In: *ApJ* 781, 89, p. 89. DOI: 10.1088/0004-637X/781/2/89. arXiv: 1312.3849.

Zhang, D. and R.A. Chevalier (Jan. 2019). “Numerical simulations of supernova remnants in turbulent molecular clouds”. In: *MNRAS* 482, pp. 1602–1617. DOI: 10.1093/mnras/sty2769. arXiv: 1807.06603 [astro-ph.HE].

Zuckerman, B. and II Evans N. J. (Sept. 1974). “Models of Massive Molecular Clouds”. In: *ApJ* 192, p. L149. DOI: 10.1086/181613.

APPENDIX A

Complete census of radio compact sources in NGC 6334D to F

Table A.1: Radio properties of compact sources in NGC 6334

ID		Other	$S_{\nu(6\,\mathrm{GHz})}$	$S_{\nu(5\,\mathrm{GHz})}$	$S_{\nu(7\,\mathrm{GHz})}$		
#	VLA Name	Name	(μJy)	(μJy)	(μJy)	α	SNR
Sources inside region D							
1	J172038.21-354846.8	...	372±24	421±27	305±26	-0.9±0.3	28.7
2	J172038.43-354838.9	...	118±14	141±17	81±19	-1.6±0.7	9.4
3	J172039.07-354912.3	...	127±15	125±17	168±23	0.9±0.6	9.6
4	J172039.61-354935.7	...	80±16	89±18	<66±22	$<-0.9\pm1.1$	5.2
5	J172039.79-354906.7	...	144±17	176±20	116±21	-1.2±0.6	9.6
6	J172040.09-354852.7	...	63±13	70±17	< 63±21	$<-0.3\pm1.2$	5.1
7	J172040.19-354845.2	...	76±15	85±19	98±11	0.4±0.7	5.7
8	J172040.40-354943.3	2M J17204040-3549438	168±17	143±18	223±26	1.3±0.5	11.8
9	J172040.89-354856.4	...	81±13	84±17	75±17	-0.3±0.9	6.3
10	J172041.26-354941.7	...	77±15	95±19	<66±22	$<-1.0\pm1.1$	5.5
11	J172042.61-354854.9	2M J17204261-3548550	210±24	185±28	239±22	0.7±0.5	9.7
12	J172043.23-354902.2	...	236±28	269±30	189±20	-1.0 ± 0.4	9.6
13	J172043.46-354917.0	2M J17204345-3549172	271±33	266±44	212±23	-0.6 ± 0.6	9.3
14	J172043.92-354915.3	...	568±43	612±50	522±34	-0.5 ± 0.3	18.4
15	J172044.66-354916.7	2M J17204466-3549168	129±12	120±13	126±13	0.1±0.4	5.1
Remaining Sources							
16	J172028.97-354702.4	...	109±22	<105±35	...	...	5.1
17	J172029.78-355055.5	...	305±60	210±42	...	...	5.7
18	J172030.69-354741.1	...	95±19	73±19	...	...	5.6

Table A.1: continued.

ID #	VLA Name	Other Name	$S_{\nu(6\,\mathrm{GHz})}$ (μJy)	$S_{\nu(5\,\mathrm{GHz})}$ (μJy)	$S_{\nu(7\,\mathrm{GHz})}$ (μJy)	α	SNR
19	J172031.18-355048.3	...	232±48	116±34	...	...	5.0
20	J172033.41-354542.5	...	85±17	72±18	...	...	5.5
21	J172034.23-355051.6	...	793±57	772±52	...	...	20.8
22	J172034.55-354645.9	...	70±14	64±17	...	...	5.0
23	J172034.75-354543.9	...	70±14	54±17	...	...	5.3
24	J172035.44-354336.9	...	114±23	91±22	...	...	5.1
25	J172039.12-354510.5	2M J17203909-3545108	63±12	71±15	75±20	0.2±1.0	5.7
26	J172039.35-354656.3	...	49±10	66±15	<51±17	$<-0.7\pm1.2$	5.0
27	J172039.67-354632.5	...	90±10	98±13	77±15	−0.7±0.7	9.7
28	J172039.77-354309.2	...	106±21	80±22	...	...	5.3
29	J172040.21-355059.3	...	131±21	103±21	...	...	6.5
30	J172040.84-354639.0	...	68±10	84±13	53±13	−1.3±0.8	7.4
31	J172040.87-355125.4	...	130±26	106±24	...	...	5.1
32	J172043.76-355039.9	...	877±50	976±56	...	...	53.8
33	J172044.36-355027.2	...	76±15	77±19	...	...	5.2
34	J172045.47-354624.7	...	41±08	38±11	41±11	0.2±1.1	5.3
35	J172046.42-354537.6	...	83±09	73±12	95±12	0.8±0.6	10.1
36	J172046.82-354426.1	...	53±10	<60±20	<48±16	...	5.2
37	J172047.65-354447.4	...	52±10	41±13	59±14	1.0±1.1	5.3
38	J172048.27-355133.6	...	126±21	109±21	...	...	6.7
39	J172048.28-354536.6	S J172048.27-354537.0	80±11	98±17	55±13	−1.7±0.8	7.8
40	J172048.64-354336.8	...	62±13	71±15	<69±23	$<-0.1\pm1.2$	5.0
41	J172049.16-354640.4	...	41±08	40±12	40±12	0.0±1.2	5.4
42	J172050.91-354605.0	2M J17205087-3546047	821±51	612±64	889±52	1.1±0.3	32.5
43	J172051.86-354704.5	CM1	85±12	72±13	104±16	1.1±0.7	7.4
44	J172052.02-354938.0	CX 172052.0-354938	878±48	834±47	978±55	0.5±0.2	87.4
45	J172053.26-354305.7	[S2000e] SM6	90±15	105±17	...	...	6.4
46	J172053.38-354655.8	CM2	256±41	266±75	233±21	−0.4±0.9	6.6
47	J172053.42-354657.7	HBM2006 I-SMA1	466±70	551±107	608±131	0.3±0.8	7.1
48	J172053.65-354548.4	...	258±16	230±17	307±19	0.8±0.3	31.2
49	J172054.06-354548.4	S J172053.96-354547.6	54±09	50±10	54±10	0.2±0.8	6.5
50	J172054.15-354513.7	HBC2014 H_2O-C4	98±10	148±13	75±11	−1.1±0.4	11.4
51	J172054.19-354554.0	...	61±09	70±12	73±10	0.1±0.6	7.5

Table A.1: continued.

ID #	VLA Name	Other Name	$S_{\nu(6\,\mathrm{GHz})}$ (μJy)	$S_{\nu(5\,\mathrm{GHz})}$ (μJy)	$S_{\nu(7\,\mathrm{GHz})}$ (μJy)	α	SNR
52	J172054.26-355106.5	...	80±16	63±18	...	...	5.3
53	J172054.34-354358.3	S J172054.33-354358.4	74±10	71±14	84±17	0.5±0.8	7.6
54	J172054.60-354516.9	...	45±08	51±12	60±11	0.4±0.8	5.7
55	J172054.62-354508.5	HBM2006 I(N)-SMA4	162±12	152±14	181±14	0.5±0.3	19.1
56	J172054.87-354536.5	HBC2014 VLA 2	86±10	98±12	64±11	−1.2±0.6	10.1
57	J172055.19-354503.8	HBM2006 I(N)-SMA1b	353±21	347±22	360±22	0.1±0.3	43.7
58	J172055.34-354758.7	...	226±17	212±21	248±18	0.5±0.4	18.7
59	J172056.41-354921.0	...	50±10	<60±20	<48±16	...	5.1
60	J172056.47-354823.0	CX J172056.4-354823	55±10	58±12	62±11	0.2±0.8	5.5
61	J172056.96-354436.8	...	46±09	43±12	66±13	1.2±1.0	5.2
62	J172057.62-354632.0	...	76±08	105±13	52±10	−2.0±0.7	10.4
63	J172057.98-354431.6	...	252±16	272±19	236±19	−0.4±0.3	27.6
64	J172058.14-354934.6	...	625±35	689±39	560±33	−0.6±0.2	62.9
65	J172059.98-354947.5	...	55±10	60±10	< 51 ± 17	< −0.5±1.1	5.6
66	J172100.08-354743.9	...	41±08	45±11	43±10	−0.1±1.0	5.4
67	J172100.80-354626.5	...	157±11	157±13	153±13	−0.1±0.3	21.2
68	J172101.31-355014.2	...	64±13	65±14	<60±20	< −0.2±1.1	5.1
69	J172101.45-354534.0	...	41±08	58±11	<60±20	< −1.9±1.1	5.1
70	J172101.62-355106.2	...	102±19	96±20	...	...	5.5
71	J172101.80-355106.4	...	232±22	221±22	...	...	12.4
72	J172103.47-354618.8	...	573±32	639±36	506±29	−0.7±0.2	73.8
73	J172104.10-354540.5	...	44±09	47±12	38±12	−0.6±1.2	5.0
74	J172104.55-355033.1	...	94±17	70±12	...	...	5.7
75	J172108.98-354714.4	...	76±11	57±13	93±16	1.4±0.8	7.4
76	J172108.98-354153.8	...	309±62	208±43	...	...	5.1
77	J172112.53-354921.4	...	92±18	83±22	...	...	5.1
78	J172115.62-354548.6	...	94±18	70±18	...	...	5.3
79	J172116.19-354554.1	...	98±19	75±18	...	...	5.3
80	J172116.20-354627.6	...	97±19	78±19	...	...	5.3
81	J172117.26-354823.5	...	120±24	85±22	...	...	5.1
82	J172118.37-355032.2	...	321±62	207±43	...	...	5.3
83	J172118.54-354959.6	...	274±55	<183±61	...	...	5.2

Table A.1: continued.

ID		Other	$S_{\nu(6\,\mathrm{GHz})}$	$S_{\nu(5\,\mathrm{GHz})}$	$S_{\nu(7\,\mathrm{GHz})}$		
#	VLA Name	Name	(μJy)	(μJy)	(μJy)	α	SNR

Note: Other names are obtained from the following catalogs: 2M = 2MASS by Cutri et al. (2003); CX = CXOU by Feigelson et al. (2009); HBM2006 = Hunter et al. (2006); CM = Brogan et al. (2016); S = SSTU by Willis et al. (2013); [S2000e] = Sandell (2000); and HBC2014 = Hunter et al. (2014). The SNRs are obtained from the 6.0 GHz map. Upper-limits to fluxes are obtained as three times the noise level in the image, that are at the same time used as the error for these upper-limits.

APPENDIX B

Full GLOSTAR survey catalog

Table B.1: Full GLOSTAR source cataloge. The source names are appended with a ‡ to indicate if a source has been split (as described in Sect. 4.3.2) and a † if the source has been recovered (as described in Sect. 4.3.2). The * indicates the values calculated using the 8 sub images are described in Sect. 4.2. References: (1) this work, (2) Kalcheva et al. 2018, (3) Anderson et al. (2014), (4) Giveon et al. (2005a), (5) SIMBAD, (6) Irabor et al. (2018), (7) Ortega et al. (2010), (8) Purcell et al. 2013.

GLOSTAR name	ℓ	b	SNR	$S_{\rm peak}$	$\Delta S_{\rm peak}$	$S_{\rm int}$	$\Delta S_{\rm int}$	Y	Radius	Spectral index				Classification	
	(°)	(°)		(mJy beam^{-1})		(mJy)			($''$)	α	$\Delta\alpha$	α*	$\Delta\alpha$*	Type	Ref.
(1)	(2)	(3)	(4)	(5)	(6)	(7)	(8)	(9)	(10)	(11)	(12)	(13)	(14)	(15)	(16)
G028.002+00.057	28.001	0.057	4.0	1.00	0.25	0.70	0.25	0.3	6	···	···	-0.30	0.46	···	···
G028.005+00.150	28.005	0.150	4.5	1.21	0.28	1.05	0.27	0.4	8	···	···	-0.50	0.63	···	···
G028.007-00.990	28.006	-0.990	23.7	3.30	0.23	3.04	0.21	0.9	16	0.45	0.10	-0.14	0.09	···	···
G028.010-00.303	28.010	-0.303	6.1	0.86	0.15	0.78	0.15	0.6	10	···	···	-0.59	0.37	···	···
G028.011+00.327	28.010	0.317	22.7	6.53	0.45	266.28	13.32	36.9	10	···	···	···	···	HII region	1
G028.016+00.940	28.014	0.940	7.8	1.11	0.15	1.75	0.17	1.2	16	···	···	-0.28	0.66	···	···
G028.022+00.174	28.019	0.174	6.3	1.62	0.27	4.35	0.34	1.7	18	···	···	-0.02	0.41	···	···
G028.024+00.514	28.024	0.514	6.3	1.12	0.19	1.17	0.19	0.7	11	···	···	-0.56	0.33	···	···
G028.031+00.669	28.031	0.669	4.1	0.66	0.17	0.55	0.17	0.4	7	···	···	-1.51	0.85	···	···
G028.043+00.532	28.038	0.530	13.1	2.00	0.19	21.05	1.06	9.1	58	···	···	···	···	Extended/Diffuse	1
G028.048-00.989	28.048	-0.989	20.9	2.12	0.15	1.60	0.13	0.7	14	···	···	-0.35	0.16	···	···
G028.049-00.869	28.048	-0.869	12.3	1.09	0.11	1.07	0.10	0.8	14	···	···	0.31	0.57	···	···
G028.058+00.027	28.058	0.028	4.4	1.24	0.29	0.76	0.28	0.3	7	···	···	-0.60	0.40	···	···
G028.063-00.610	28.063	-0.611	7.8	0.97	0.13	1.07	0.14	0.8	13	···	···	-1.17	0.31	···	···
G028.065+00.119	28.059	0.122	10.5	2.64	0.29	5.11	0.36	1.6	22	···	···	···	···	···	···
G028.067+00.924	28.066	0.924	4.0	0.47	0.12	0.65	0.12	0.6	9	···	···	0.86	0.26	···	···
G028.075-00.296	28.075	-0.295	9.1	1.22	0.15	1.13	0.15	0.7	12	-1.12	0.09	-1.92	0.37	···	···
G028.085-00.558	28.085	-0.558	12.5	1.81	0.17	1.42	0.16	0.7	12	-0.33	0.09	-0.45	0.04	···	···
G028.087+00.729	28.087	0.729	6.0	0.81	0.14	0.58	0.14	0.5	9	-0.63	0.17	-0.87	0.88	···	···
G028.091+00.613	28.091	0.613	5.6	0.79	0.15	1.03	0.15	0.8	12	···	···	-0.42	0.34	···	···
G028.091-00.092	28.091	-0.093	11.4	3.12	0.32	4.26	0.35	1.1	16	···	···	-0.07	0.25	···	···
G028.097-00.951	28.097	-0.951	6.1	0.54	0.09	0.45	0.09	0.6	10	···	···	-0.36	0.69	···	···
G028.098-00.781	28.098	-0.781	186.9	17.80	0.96	22.06	1.11	1.2	25	-0.91	0.01	-1.08	0.03	Radio star	8
G028.100+00.644	28.099	0.644	6.5	0.87	0.14	0.76	0.14	0.6	10	···	···	-0.57	0.28	···	···

Continued on next page

Table B.1 – *Continued from previous page*

GLOSTAR name	ℓ	b	SNR	$S_{\rm peak}$	$\Delta S_{\rm peak}$	$S_{\rm int}$	$\Delta S_{\rm int}$	Y	Radius	Spectral index				Classification	
	(°)	(°)		(mJy beam^{-1})		(mJy)			($''$)	α	$\Delta\alpha$	α*	$\Delta\alpha$*	Type	Ref.
(1)	(2)	(3)	(4)	(5)	(6)	(7)	(8)	(9)	(10)	(11)	(12)	(13)	(14)	(15)	(16)
G028.107-00.301	28.109	-0.300	5.6	0.81	0.15	1.89	0.17	1.3	16	···	···	-0.57	0.62	···	···
G028.109-00.490	28.108	-0.490	20.0	2.84	0.21	2.70	0.20	0.9	15	0.06	0.09	-0.18	0.10	···	···
G028.116-00.368	28.116	-0.368	44.0	5.77	0.34	5.82	0.32	1.0	18	-0.10	0.04	-0.12	0.05	···	···
G028.120+00.419	28.120	0.419	4.9	0.87	0.19	0.64	0.18	0.4	8	···	···	0.15	0.43	···	···
G028.126+00.742	28.126	0.742	33.6	4.26	0.26	3.86	0.23	0.9	17	-0.28	0.04	-0.81	0.10	···	···
G028.127+00.341‡	28.127	0.341	58.2	12.98	0.22	51.78	0.45	4.0	···	···	···	···	···	···	···
G028.137-00.194	28.138	-0.194	4.2	0.77	0.19	0.68	0.19	0.4	8	···	···	0.53	0.37	···	···
G028.137-00.567	28.137	-0.566	5.7	1.15	0.21	1.29	0.21	0.7	11	-0.58	0.15	-1.14	0.48	···	···
G028.140+00.329‡	28.140	0.329	11.0	4.50	0.43	7.30	1.00	1.6	···	0.23	0.12	-0.52	0.19	HII region	3
G028.144-00.378	28.144	-0.379	8.0	1.08	0.15	1.11	0.15	0.8	12	···	···	-0.46	0.55	···	···
G028.146+00.517	28.145	0.517	8.7	1.21	0.15	1.86	0.17	1.2	16	···	···	-0.66	0.27	···	···
G028.149-00.998	28.149	-0.997	76.9	11.93	0.66	19.71	1.00	1.6	25	···	···	-1.05	0.05	···	···
G028.151+00.164	28.148	0.149	38.6	10.38	0.62	194.53	9.73	18.0	95	···	···	···	···	HII region	1
G028.151-00.958	28.151	-0.957	16.0	2.00	0.16	2.25	0.17	1.0	17	-0.37	0.09	-0.40	0.28	···	···
G028.159-00.024	28.157	-0.020	8.0	2.91	0.40	28.85	1.49	6.6	38	···	···	···	···	Extended/Diffuse	1
G028.159-00.798	28.159	-0.798	29.1	2.97	0.19	2.67	0.17	0.9	16	-0.35	0.05	-0.36	0.23	···	···
G028.160-00.046	28.160	-0.046	4.8	1.68	0.36	1.59	0.36	0.5	9	···	···	-0.15	0.52	HII region	3
G028.163-00.163†	28.163	-0.163	7.0	0.50	0.07	2.00	0.34	4.0	···	···	···	···	···	HII region	
G028.172-00.605	28.173	-0.606	4.9	1.13	0.24	14.55	0.76	5.5	32	···	···	···	···	Ionization Front	1
G028.178+00.074	28.178	0.072	4.3	1.49	0.35	9.56	0.59	2.5	21	···	···	···	···	···	···
G028.187+00.583	28.187	0.583	22.3	3.02	0.21	2.75	0.19	0.9	15	-0.01	0.06	-0.71	0.11	···	···
G028.189-00.744	28.189	-0.744	17.0	1.74	0.14	1.36	0.12	0.7	13	-0.33	0.08	-1.09	0.20	···	···
G028.193-00.785	28.193	-0.785	8.6	0.87	0.11	1.29	0.12	1.1	16	-0.68	0.12	-0.22	0.26	Pulsar	5
G028.197-00.891	28.198	-0.892	4.6	0.48	0.11	0.96	0.11	1.0	13	···	···	-0.94	0.47	···	···
G028.200-00.050	28.191	-0.050	771.1	332.67	17.92	396.10	19.81	1.2	48	···	···	···	···	HII region	3
G028.209+00.226	28.209	0.226	5.8	1.07	0.19	0.95	0.19	0.6	10	···	···	0.22	0.40	···	···
G028.210+00.410	28.210	0.410	5.4	0.88	0.17	0.54	0.16	0.4	8	-0.78	0.16	0.13	0.36	···	···
G028.212-00.882	28.212	-0.882	18.8	1.95	0.15	1.84	0.14	0.9	15	-0.49	0.06	-0.42	0.26	···	···
G028.216-00.824	28.216	-0.824	6.1	0.62	0.11	0.50	0.10	0.5	9	-1.05	0.14	-0.58	0.12	···	···
G028.218-00.080	28.219	-0.088	8.2	2.90	0.38	56.11	2.83	12.8	56	···	···	···	···	SNR-candidate	1
G028.218-00.220	28.218	-0.220	12.8	2.29	0.22	1.96	0.20	0.7	13	-0.07	0.13	0.07	0.27	···	···
G028.226-00.929	28.226	-0.930	5.8	0.65	0.12	0.69	0.12	0.7	11	···	···	-0.55	0.38	···	···
G028.235+00.832	28.235	0.832	6.3	0.68	0.11	0.68	0.11	0.7	11	-0.45	0.17	-0.75	0.31	···	···
G028.238+00.226	28.237	0.226	4.6	0.86	0.19	0.70	0.19	0.4	8	···	···	-1.01	0.44	···	···
G028.242-00.561	28.240	-0.570	4.1	0.82	0.21	35.23	1.77	12.9	48	···	···	···	···	Extended/Diffuse	1
G028.245+00.013	28.241	0.015	180.5	106.73	5.78	188.65	9.45	1.8	41	···	···	-0.10	0.07	HII region	3
G028.251+00.404	28.250	0.404	8.6	1.38	0.18	1.16	0.17	0.7	11	···	···	-0.07	0.30	···	···
G028.254+00.942	28.254	0.942	6.5	0.59	0.10	0.68	0.10	0.8	12	-0.79	0.15	-0.37	0.64	···	···
G028.254-00.958	28.255	-0.958	7.3	0.89	0.13	0.70	0.13	0.6	10	-0.66	0.14	-1.29	0.57	···	···
G028.258-00.370‡	28.258	-0.370	31.0	14.33	0.47	15.48	0.87	1.1	···	0.87	.03	1.05	.09	···	···
G028.265-00.560	28.265	-0.560	5.8	1.04	0.19	0.83	0.18	0.5	9	-0.67	0.15	-0.94	0.27	···	···
G028.270+00.917	28.270	0.917	5.7	0.54	0.10	0.44	0.10	0.5	9	-0.85	0.16	-0.55	1.08	···	···
G028.276+00.444	28.276	0.443	6.2	0.98	0.17	1.08	0.17	0.7	11	···	···	0.19	0.46	···	···

Continued on next page

Table B.1 – *Continued from previous page*

GLOSTAR name	ℓ	b	SNR	$S_{\rm peak}$	$\Delta S_{\rm peak}$	$S_{\rm int}$	$\Delta S_{\rm int}$	Y	Radius	Spectral index				Classification	
	(°)	(°)		(mJy beam^{-1})		(mJy)			($''$)	α	$\Delta\alpha$	α*	$\Delta\alpha$*	Type	Ref.
(1)	(2)	(3)	(4)	(5)	(6)	(7)	(8)	(9)	(10)	(11)	(12)	(13)	(14)	(15)	(16)
G028.278-00.691	28.278	-0.692	10.6	1.34	0.15	1.88	0.16	1.2	16	-0.44	0.11	-0.67	0.34	···	···
G028.287-00.364‡	28.287	-0.364	328.0	660.60	2.00	699.00	3.70	1.1	···	0.52	0.00	0.16	0.02	HII region	2
G028.289+00.142	28.288	0.143	8.5	2.81	0.36	8.34	0.53	2.2	22	···	···	···	···	···	···
G028.291+00.010‡	28.291	0.010	28.0	11.42	0.43	14.86	0.89	1.3	···	-0.07	0.06	-0.31	0.13	HII region	3
G028.295+00.004‡	28.295	0.004	14.0	5.55	0.41	7.60	0.89	1.4	···	···	···	0.05	0.35	HII region	3
G028.301+00.120	28.300	0.121	6.0	2.51	0.44	8.07	0.58	1.9	19	···	···	-0.10	0.17	···	···
G028.304-00.389‡	28.304	-0.389	17.0	116.30	6.40	681.00	43.00	5.9	···	···	···	···	···	HII region	3
G028.310-00.817	28.308	-0.817	4.0	0.40	0.10	0.77	0.11	0.8	11	···	···	-0.57	0.49	···	···
G028.319+00.940	28.319	0.940	5.7	0.54	0.10	0.35	0.10	0.4	8	···	···	-0.41	0.21	···	···
G028.320-00.015	28.306	-0.034	13.5	6.81	0.62	240.31	12.03	28.2	92	···	···	···	···	HII region	1
G028.322-00.357	28.323	-0.357	4.2	0.93	0.23	1.58	0.23	0.8	11	···	···	2.06	0.49	···	···
G028.332-00.608	28.332	-0.607	4.2	0.56	0.14	0.58	0.14	0.5	8	···	···	0.54	0.61	···	···
G028.334-00.658	28.349	-0.645	5.1	0.66	0.14	23.49	1.18	14.9	54	···	···	···	···	···	···
G028.337-00.601	28.337	-0.601	13.9	1.81	0.16	1.63	0.15	0.8	14	-0.50	0.09	-0.74	0.22	···	···
G028.338+00.143	28.325	0.141	10.8	5.13	0.55	60.53	3.06	9.1	52	···	···	···	···	Ionization Front	1
G028.339+00.122	28.340	0.121	7.7	4.15	0.58	15.78	0.95	2.7	24	···	···	···	···	HII region	1
G028.342+00.101	28.340	0.100	20.1	12.05	0.88	15.96	1.00	1.2	20	0.10	0.06	-0.17	0.06	HII region	3
G028.347+00.498	28.346	0.498	4.4	1.03	0.24	8.11	0.47	3.1	24	···	···	···	···	Ionization Front	1
G028.367-00.894	28.367	-0.894	21.0	1.82	0.13	1.58	0.12	0.8	15	0.02	0.10	-0.47	0.26	···	···
G028.376+00.209†	28.376	0.209	7.0	1.65	0.24	1.80	0.44	1.1	···	···	···	0.17	0.47	HII region	3
G028.376+00.775	28.375	0.776	28.9	3.23	0.21	3.29	0.20	1.0	18	-0.61	0.03	-0.94	0.15	···	···
G028.384+00.598	28.385	0.598	57.5	11.22	0.63	12.03	0.63	1.1	21	-0.20	0.02	-0.26	0.04	···	···
G028.387+00.869	28.387	0.869	10.7	1.07	0.12	0.91	0.11	0.7	12	-0.32	0.11	-0.73	0.40	···	···
G028.388-00.727	28.386	-0.723	5.1	0.55	0.11	2.04	0.15	1.8	19	···	···	-0.66	0.33	Extended/Diffuse	1
G028.391-00.970	28.391	-0.970	5.8	0.49	0.09	0.48	0.09	0.6	10	···	···	0.23	0.69	···	···
G028.394+00.075	28.394	0.075	61.2	36.53	2.06	47.19	2.43	1.3	22	0.20	0.02	-0.05	0.04	HII region	3
G028.396+00.451	28.393	0.441	18.3	4.66	0.36	54.98	2.76	10.7	73	···	···	···	···	HII region	3
G028.396-00.799	28.396	-0.799	4.3	0.40	0.09	0.26	0.09	0.3	7	···	···	1.50	0.52	···	···
G028.398+00.498	28.400	0.497	4.8	1.29	0.28	6.22	0.41	2.2	20	···	···	···	···	Extended/Diffuse	1
G028.402+00.478	28.402	0.479	583.8	159.47	8.59	154.43	7.73	1.0	24	0.18	0.00	-0.24	0.02	···	···
G028.402-00.517	28.402	-0.516	8.0	1.12	0.15	0.90	0.15	0.6	11	-0.84	0.13	-0.62	0.49	···	···
G028.403-00.415	28.403	-0.415	5.1	0.77	0.16	0.81	0.16	0.6	10	···	···	-1.22	0.24	···	···
G028.413+00.413	28.413	0.414	7.0	1.60	0.24	1.35	0.24	0.6	10	-0.84	0.12	-0.40	0.22	···	···
G028.413-00.115	28.413	-0.114	5.1	1.27	0.26	1.04	0.25	0.5	9	···	···	-1.19	0.36	···	···
G028.414+00.034	28.415	0.033	6.0	3.33	0.59	4.75	0.61	0.9	13	-1.08	0.13	-1.91	0.20	···	···
G028.417-00.002‡	28.417	-0.002	11.5	6.56	0.57	139.26	2.63	21.2	···	···	···	···	···	···	···
G028.419+00.990	28.419	0.989	25.3	3.14	0.21	2.71	0.18	0.8	15	-0.50	0.04	-0.67	0.07	···	···
G028.423-00.808	28.422	-0.811	4.2	0.35	0.09	0.78	0.09	1.0	12	···	···	-0.75	2.17	···	···
G028.433-00.751	28.433	-0.751	9.7	0.89	0.10	0.89	0.10	0.8	13	-0.22	0.15	-0.61	0.49	···	···
G028.437+00.016‡	28.437	0.016	16.0	14.16	0.93	35.50	3.10	2.5	···	···	···	···	···	HII region	1
G028.439+00.036†	28.439	0.036	7.0	2.50	0.41	4.50	1.10	1.8	···	···	···	1.11	0.66	HII region	3
G028.451+00.003‡	28.451	0.003	22.0	60.40	3.00	99.50	7.30	1.6	···	0.14	0.04	-0.06	0.06	HII region	2
G028.452-00.880	28.452	-0.880	5.7	0.45	0.08	0.50	0.08	0.7	11	···	···	-0.19	0.86	···	···

Continued on next page

Table B.1 – *Continued from previous page*

GLOSTAR name	ℓ	b	SNR	$S_{\rm peak}$	$\Delta S_{\rm peak}$	$S_{\rm int}$	$\Delta S_{\rm int}$	Y	Radius	Spectral index				Classification	
	(°)	(°)		(mJy beam^{-1})		(mJy)			($''$)	α	$\Delta\alpha$	α*	$\Delta\alpha$*	Type	Ref.
(1)	(2)	(3)	(4)	(5)	(6)	(7)	(8)	(9)	(10)	(11)	(12)	(13)	(14)	(15)	(16)
G028.471+00.035	28.472	0.035	12.7	7.67	0.73	10.65	0.81	1.2	17	0.14	0.12	0.41	0.15	···	···
G028.477-00.441	28.477	-0.441	9.7	1.46	0.17	1.13	0.16	0.6	11	···	···	0.28	0.24	···	···
G028.494-00.801	28.494	-0.801	6.3	0.52	0.09	0.67	0.09	0.9	13	···	···	0.12	0.36	···	···
G028.495-00.249	28.496	-0.249	23.9	3.95	0.27	6.32	0.36	1.5	21	···	···	-0.38	0.16	HII region	3
G028.507-00.533	28.508	-0.533	5.1	0.67	0.14	0.47	0.13	0.4	8	···	···	-1.26	0.56	···	···
G028.508+00.308	28.515	0.292	11.8	5.89	0.59	177.40	8.88	23.4	81	···	···	···	···	Extended/Diffuse	1
G028.514-00.644	28.513	-0.645	15.4	1.67	0.14	1.58	0.13	0.8	14	-0.56	0.08	-0.88	0.17	···	···
G028.521+00.453	28.522	0.453	5.7	1.29	0.24	2.70	0.27	1.2	15	-0.48	0.16	-1.07	0.56	···	···
G028.524+00.954	28.524	0.953	11.9	1.14	0.11	0.99	0.11	0.7	13	-0.95	0.07	-1.09	0.29	···	···
G028.528+00.790	28.528	0.790	118.8	14.11	0.77	13.56	0.69	1.0	20	-1.02	0.01	-1.23	0.06	···	···
G028.529-00.452	28.529	-0.452	6.8	1.09	0.17	0.76	0.16	0.5	9	···	···	-0.23	0.30	···	···
G028.530-00.292	28.530	-0.292	5.2	1.03	0.21	0.54	0.20	0.3	7	···	···	0.00	0.54	···	···
G028.531-00.015	28.533	-0.024	8.6	5.03	0.64	25.19	1.39	3.6	27	···	···	···	···	···	···
G028.542-00.120‡	28.542	-0.120	19.0	6.37	0.35	7.91	0.70	1.2	···	···	···	1.53	.27	···	···
G028.546-00.766	28.546	-0.766	7.3	0.64	0.09	0.53	0.09	0.6	11	-1.11	0.12	-0.56	0.64	···	···
G028.553-00.451	28.555	-0.447	28.6	4.56	0.29	6.24	0.35	1.3	24	···	···	0.32	0.50	···	···
G028.562-00.485	28.562	-0.484	18.5	2.52	0.19	2.38	0.18	0.9	15	-0.38	0.08	-1.06	0.21	···	···
G028.563+00.338	28.563	0.339	23.3	8.87	0.61	9.02	0.59	1.0	16	-0.53	0.04	-0.74	0.04	···	···
G028.563-00.424	28.563	-0.423	4.0	0.71	0.18	1.64	0.19	1.0	12	···	···	-0.80	1.37	···	···
G028.567-00.471	28.567	-0.471	4.2	0.61	0.15	0.60	0.15	0.5	8	···	···	-0.87	0.38	···	···
G028.568-00.796	28.568	-0.796	79.9	7.24	0.40	7.03	0.36	1.0	20	-0.60	0.02	-1.02	0.09	Radio star	8
G028.569+00.020	28.563	0.006	61.3	47.54	2.68	598.07	29.91	12.3	79	···	···	···	···	HII region	1
G028.571-00.894	28.571	-0.894	10.4	0.99	0.11	0.78	0.10	0.7	12	-0.67	0.13	-1.09	0.17	···	···
G028.581+00.145	28.582	0.145	60.4	42.52	2.40	43.94	2.31	1.0	20	0.11	0.02	0.01	0.03	HII region	2
G028.581-00.973	28.580	-0.973	5.3	0.52	0.10	0.41	0.10	0.5	9	···	···	-0.31	0.55	···	···
G028.586+00.935	28.586	0.934	4.4	0.47	0.11	0.72	0.11	0.7	11	···	···	-0.06	0.19	···	···
G028.586-00.883	28.588	-0.886	54.7	5.24	0.30	10.56	0.54	2.0	26	···	···	···	···	···	···
G028.588+00.391	28.588	0.392	11.2	3.02	0.32	4.40	0.35	1.2	17	-0.52	0.09	-1.19	0.18	···	···
G028.588-00.794	28.588	-0.794	4.1	0.37	0.09	0.59	0.10	0.7	10	···	···	0.55	0.46	···	···
G028.594-00.359	28.596	-0.364	294.8	58.00	3.13	471.93	23.60	8.1	67	···	···	···	···	HII region	1
G028.597-00.016‡	28.597	-0.015	20.4	20.21	0.99	150.48	2.71	7.4	···	···	···	···	···	···	···
G028.604-00.653	28.604	-0.653	30.3	3.47	0.22	3.15	0.19	0.9	16	-0.44	0.05	-1.01	0.09	···	···
G028.609+00.018‡	28.609	0.018	18.0	232.00	14.00	400.00	36.00	1.7	···	···	···	0.05	0.13	HII region	
G028.615-00.585	28.614	-0.584	96.2	11.40	0.63	13.12	0.67	1.1	22	0.10	0.03	-0.35	0.06	PN	1
G028.617+00.676	28.617	0.675	5.9	1.08	0.19	0.95	0.19	0.6	10	-0.42	0.17	-1.01	0.50	···	···
G028.620-00.344	28.620	-0.343	32.5	7.33	0.45	7.26	0.43	1.0	18	-0.91	0.03	-1.41	0.11	···	···
G028.621+00.559	28.622	0.559	15.9	3.14	0.26	3.63	0.27	1.0	16	-0.49	0.07	-1.16	0.19	···	···
G028.621-00.865	28.621	-0.864	11.7	1.12	0.11	1.36	0.12	1.0	15	···	···	-0.31	0.30	···	···
G028.634-00.272	28.634	-0.273	4.7	1.37	0.30	1.56	0.30	0.6	10	···	···	0.76	0.50	···	···
G028.635+00.478	28.643	0.478	101.6	30.10	1.65	343.72	17.19	11.3	96	···	···	···	···	HII region	1
G028.638-00.893	28.639	-0.893	18.5	1.79	0.14	2.62	0.16	1.3	21	-0.36	0.08	-0.91	0.19	···	···
G028.641-00.862	28.641	-0.863	28.9	2.77	0.18	2.73	0.17	0.9	17	-0.38	0.06	-0.60	0.09	···	···
G028.642+00.187	28.638	0.203	22.9	14.45	1.00	231.63	11.60	14.9	86	···	···	···	···	SNR-candidate	1

Continued on next page

Table B.1 – *Continued from previous page*

GLOSTAR name	ℓ	b	SNR	$S_{\rm peak}$	$\Delta S_{\rm peak}$	$S_{\rm int}$	$\Delta S_{\rm int}$	Y	Radius	Spectral index				Classification	
	(°)	(°)		(mJy beam^{-1})		(mJy)			($''$)	α	$\Delta\alpha$	α*	$\Delta\alpha$*	Type	Ref.
(1)	(2)	(3)	(4)	(5)	(6)	(7)	(8)	(9)	(10)	(11)	(12)	(13)	(14)	(15)	(16)
G028.645+00.624	28.645	0.624	16.9	2.85	0.23	2.98	0.23	0.9	16	-0.89	0.05	-1.14	0.12	···	···
G028.646+00.064	28.646	0.059	6.4	4.60	0.76	21.50	1.29	2.8	24	···	···	···	···	···	···
G028.652+00.027	28.660	0.022	285.4	253.67	13.69	380.44	19.04	1.5	56	···	···	1.04	0.20	HII region	2
G028.661-00.501	28.661	-0.501	6.1	0.93	0.16	0.91	0.16	0.6	11	···	···	-0.50	0.42	···	···
G028.661-00.637	28.661	-0.637	4.5	0.53	0.12	0.37	0.12	0.3	7	···	···	-1.65	0.31	···	···
G028.672-00.783	28.672	-0.782	205.6	20.23	1.09	20.47	1.03	1.0	24	-0.63	0.01	-0.70	0.02	···	···
G028.675-00.710	28.675	-0.710	6.0	0.65	0.11	0.65	0.11	0.7	11	···	···	-0.77	0.69	···	···
G028.680-00.805	28.681	-0.805	8.1	0.79	0.11	0.68	0.10	0.7	11	-0.70	0.16	-0.55	0.57	···	···
G028.681-00.894	28.681	-0.894	5.0	0.51	0.10	0.54	0.10	0.6	10	···	···	-1.36	0.53	···	···
G028.688+00.177	28.688	0.177	216.7	133.12	7.19	143.99	7.23	1.1	24	0.16	0.01	-0.05	0.03	HII region	2
G028.690+00.254	28.690	0.255	17.4	10.04	0.79	8.48	0.72	0.8	14	-0.58	0.05	-0.67	0.06	···	···
G028.691-00.761	28.690	-0.762	22.8	2.39	0.17	2.54	0.16	1.0	18	-0.47	0.06	-0.58	0.11	···	···
G028.693-00.297	28.691	-0.298	11.2	2.65	0.28	5.97	0.38	1.9	20	···	···	0.37	0.14	HII region	3
G028.696-00.231	28.696	-0.231	15.1	4.98	0.43	5.47	0.43	1.0	16	···	···	-0.67	0.17	···	···
G028.702+00.042	28.694	0.045	60.1	43.69	2.46	552.10	27.61	12.3	76	···	···	···	···	HII region	4
G028.702-00.374	28.705	-0.373	11.1	2.40	0.25	15.33	0.80	5.2	37	···	···	···	···	HII region	3
G028.713-00.296	28.714	-0.296	4.0	0.94	0.24	4.76	0.33	1.8	17	···	···	-0.36	0.54	HII region	1
G028.729+00.857	28.729	0.857	7.6	0.83	0.12	0.58	0.11	0.5	10	-0.60	0.14	-1.44	0.17	···	···
G028.729-00.233	28.731	-0.232	15.8	5.34	0.44	13.59	0.76	2.3	24	···	···	···	···	HII region	3
G028.730+00.761	28.729	0.762	4.9	0.88	0.19	2.20	0.21	1.3	14	···	···	-1.22	0.18	···	···
G028.734+00.894	28.734	0.894	18.2	1.91	0.15	1.68	0.13	0.8	14	-0.90	0.05	-1.20	0.13	···	···
G028.745+00.706	28.743	0.707	14.6	2.74	0.24	10.41	0.55	3.3	27	···	···	···	···	···	···
G028.749+00.872	28.749	0.872	12.5	1.29	0.12	0.96	0.11	0.6	12	-0.52	0.10	-0.83	0.29	···	···
G028.751+00.937	28.755	0.943	17.2	1.77	0.14	2.68	0.17	1.4	23	···	···	···	···	···	···
G028.752+00.559	28.752	0.559	12.2	3.88	0.38	2.99	0.35	0.7	12	-0.67	0.07	-0.87	0.07	···	···
G028.757+00.277	28.761	0.281	6.9	4.59	0.71	111.68	5.62	14.2	57	···	···	···	···	Extended/Diffuse	1
G028.762-00.885	28.760	-0.886	19.7	1.98	0.15	4.10	0.23	1.9	27	-0.29	0.08	-0.62	0.20	···	···
G028.767-00.835	28.768	-0.836	118.6	11.58	0.63	11.65	0.59	1.0	22	0.25	0.03	-0.13	0.04	···	···
G028.770-00.426	28.771	-0.427	10.1	2.29	0.26	3.84	0.30	1.4	18	-0.59	0.10	-1.51	0.18	···	···
G028.777+00.153	28.781	0.153	4.9	2.88	0.61	10.74	0.80	1.8	18	···	···	0.66	0.44	···	···
G028.788+00.244‡	28.788	0.244	14.0	28.00	2.10	82.70	8.10	3.0	···	···	···	···	···	···	···
G028.789-00.337	28.790	-0.337	11.8	2.81	0.28	2.37	0.27	0.7	13	···	···	0.12	0.19	···	···
G028.796-00.789	28.796	-0.789	5.9	0.60	0.11	0.35	0.10	0.4	8	···	···	1.56	0.35	···	···
G028.798+00.232‡	28.798	0.232	20.8	15.74	0.76	120.80	2.10	7.7	···	···	···	···	···	···	···
G028.799-00.690	28.798	-0.690	37.0	4.46	0.27	6.32	0.34	1.4	22	-0.42	0.04	-0.80	0.06	···	···
G028.804-00.924	28.804	-0.924	7.3	0.73	0.11	0.52	0.10	0.5	10	···	···	-0.68	0.41	···	···
G028.806+00.175	28.799	0.176	260.7	161.70	8.73	982.84	49.15	6.1	57	···	···	···	···	HII region	4
G028.812+00.192	28.815	0.193	23.8	15.54	1.06	40.93	2.15	2.5	28	···	···	···	···	HII region	1
G028.813-00.874	28.812	-0.874	6.6	0.64	0.10	0.52	0.10	0.6	10	-0.75	0.17	-1.29	0.34	···	···
G028.815+00.919	28.815	0.919	10.5	1.13	0.12	0.95	0.12	0.7	12	···	···	-0.41	0.22	···	···
G028.821+00.028	28.821	0.027	4.6	1.75	0.39	3.71	0.42	1.0	13	···	···	-0.74	0.17	···	···
G028.821-00.228‡	28.821	-0.228	50.4	17.08	0.34	589.34	1.99	34.5	···	···	···	···	···	HII region	
G028.831-00.974	28.830	-0.975	29.4	3.31	0.21	2.94	0.18	0.8	16	-0.62	0.04	-1.42	0.16	···	···

Continued on next page

Table B.1 – *Continued from previous page*

GLOSTAR name	ℓ	b	SNR	$S_{\rm peak}$	$\Delta S_{\rm peak}$	$S_{\rm int}$	$\Delta S_{\rm int}$	Y	Radius	Spectral index				Classification	
	(°)	(°)		(mJy beam^{-1})		(mJy)			($''$)	α	$\Delta\alpha$	α*	$\Delta\alpha$*	Type	Ref.
(1)	(2)	(3)	(4)	(5)	(6)	(7)	(8)	(9)	(10)	(11)	(12)	(13)	(14)	(15)	(16)
G028.838-00.249‡	28.838	-0.249	12.0	14.10	1.20	35.20	4.10	2.5	···	···	···	···	···	HII region	
G028.840-00.931	28.840	-0.931	5.3	0.52	0.10	0.38	0.10	0.4	8	···	···	0.67	0.70	···	···
G028.845-00.683	28.846	-0.683	7.2	0.88	0.13	0.75	0.13	0.6	11	-0.55	0.16	-0.11	0.27	···	···
G028.859+00.824	28.858	0.823	14.6	1.53	0.13	1.25	0.12	0.7	13	-0.89	0.06	-1.11	0.23	···	···
G028.861+00.678	28.861	0.678	4.9	0.68	0.14	0.61	0.14	0.5	9	···	···	0.01	0.36	···	···
G028.864+00.060	28.855	0.058	18.5	6.69	0.51	108.28	5.43	14.4	72	···	···	···	···	HII region	1
G028.866-00.517	28.865	-0.517	4.7	1.13	0.25	0.98	0.24	0.5	8	···	···	-0.51	0.56	···	···
G028.870+00.870	28.871	0.870	12.2	1.34	0.13	1.31	0.13	0.8	14	-0.70	0.08	-1.43	0.22	···	···
G028.873-00.531	28.873	-0.531	8.3	1.91	0.25	1.82	0.25	0.7	12	-0.73	0.11	-1.10	0.20	···	···
G028.880-00.938	28.878	-0.939	8.8	0.90	0.11	1.35	0.12	1.2	15	-0.89	0.11	-1.39	0.21	Pulsar	5
G028.883-00.020	28.883	-0.020	5.6	1.80	0.34	1.70	0.33	0.6	10	···	···	-1.28	0.26	HII region	3
G028.887-00.940	28.887	-0.940	8.6	0.90	0.11	0.76	0.11	0.6	11	···	···	-0.26	0.35	···	···
G028.893-00.794	28.894	-0.794	4.4	0.45	0.11	1.35	0.12	1.3	14	···	···	0.54	0.50	HII region	3
G028.895+00.798	28.895	0.801	19.9	2.23	0.16	3.01	0.19	1.2	21	···	···	-1.10	0.26	···	···
G028.916+00.955	28.917	0.955	12.8	1.85	0.18	1.68	0.17	0.8	14	-0.74	0.07	-1.08	0.13	···	···
G028.923-00.658	28.922	-0.659	29.8	6.07	0.39	5.97	0.36	0.9	17	0.78	0.12	0.92	0.07	···	···
G028.927-00.900	28.926	-0.901	13.7	1.41	0.13	2.18	0.15	1.3	18	···	···	-0.78	0.36	···	···
G028.933-00.555	28.933	-0.556	13.1	2.79	0.26	2.87	0.26	0.9	15	-0.72	0.07	-0.61	0.09	···	···
G028.944-00.617	28.944	-0.617	9.4	2.24	0.27	1.85	0.26	0.7	12	-0.76	0.10	-1.03	0.15	···	···
G028.952+00.257	28.932	0.259	82.9	26.09	1.44	182.43	9.13	6.9	02	···	···	···	···	HII region	4
G028.957-00.786	28.957	-0.788	16.1	2.38	0.20	3.96	0.25	1.5	19	···	···	-0.43	0.17	···	···
G028.957-00.822	28.956	-0.821	15.1	1.82	0.16	4.16	0.24	2.0	24	···	···	···	···	···	···
G028.970+00.335	28.971	0.334	4.1	1.11	0.28	5.07	0.37	1.7	16	···	···	-1.63	0.44	Extended/Diffuse	1
G028.970-00.620	28.984	-0.602	48.1	13.55	0.78	569.21	28.46	40.7	17	···	···	···	···	HII region	1
G028.972-00.783	28.972	-0.784	10.7	1.76	0.19	1.26	0.18	0.6	11	···	···	0.48	0.30	···	···
G028.983+00.260	28.983	0.260	4.5	1.17	0.27	0.78	0.26	0.3	7	···	···	0.41	0.53	HII region	3
G028.983-00.495	28.983	-0.495	61.7	11.65	0.65	13.04	0.68	1.1	21	0.11	0.03	-0.15	0.04	PN	1
G028.984-00.294	28.984	-0.295	32.7	7.14	0.44	6.73	0.40	0.9	17	-0.50	0.03	-0.58	0.09	Radio star	8
G028.988-00.900	28.989	-0.900	13.9	1.44	0.13	3.00	0.18	1.8	23	-0.16	0.13	-1.06	0.20	···	···
G028.995+00.778	28.995	0.778	17.5	2.03	0.16	1.71	0.14	0.8	14	-0.46	0.07	-0.29	0.26	···	···
G028.998+00.190	28.998	0.190	7.0	2.73	0.42	3.40	0.42	0.9	13	-0.19	0.17	-1.12	0.22	···	···
G029.000-00.965	29.000	-0.966	8.8	0.99	0.12	1.09	0.13	0.9	13	-0.54	0.14	-0.37	0.33	···	···
G029.003+00.071	29.005	0.084	52.5	20.77	1.19	344.52	17.23	16.1	92	···	···	···	···	HII region	4
G029.005+00.503	29.016	0.503	4.2	1.05	0.25	8.83	0.51	3.1	24	···	···	···	···	Ionization Front	1
G029.010+00.290	29.010	0.290	6.5	1.51	0.24	1.86	0.25	0.8	12	···	···	-0.25	0.47	···	···
G029.016+00.174	29.019	0.167	17.8	6.82	0.53	111.01	5.56	14.7	73	···	···	···	···	HII region	1
G029.025-00.897	29.025	-0.897	6.0	0.61	0.11	0.47	0.10	0.5	9	-0.78	0.18	-1.48	0.30	···	···
G029.025-00.906	29.025	-0.906	21.7	2.16	0.15	1.80	0.13	0.8	14	-0.85	0.05	-1.22	0.14	···	···
G029.044-00.599	29.045	-0.599	76.3	17.81	0.99	15.95	0.83	0.9	18	-0.71	0.01	-0.74	0.04	···	···
G029.048+00.791	29.049	0.791	8.6	1.01	0.13	0.94	0.13	0.7	12	···	···	-0.59	0.19	···	···
G029.054+00.992	29.054	0.992	50.7	5.99	0.34	5.79	0.31	0.9	19	0.07	0.04	-0.24	0.09	PN	6
G029.055+00.826	29.055	0.827	4.1	0.48	0.12	6.02	0.32	4.3	27	···	···	···	···	···	···
G029.055+00.868	29.059	0.862	64.1	7.25	0.41	9.26	0.48	1.3	29	···	···	···	···	···	···

Continued on next page

Table B.1 – *Continued from previous page*

GLOSTAR name	ℓ	b	SNR	$S_{\rm peak}$	$\Delta S_{\rm peak}$	$S_{\rm int}$	$\Delta S_{\rm int}$	Y	Radius	Spectral index				Classification	
	(°)	(°)		(mJy beam^{-1})		(mJy)			($''$)	α	$\Delta\alpha$	α*	$\Delta\alpha$*	Type	Ref.
(1)	(2)	(3)	(4)	(5)	(6)	(7)	(8)	(9)	(10)	(11)	(12)	(13)	(14)	(15)	(16)
G029.078+00.457	29.077	0.453	57.5	36.19	2.05	157.73	7.91	4.2	38	···	···	···	···	PN	1
G029.081-00.497	29.080	-0.497	15.7	2.86	0.24	3.67	0.26	1.1	17	-0.35	0.09	-0.55	0.08	···	···
G029.090+00.512	29.090	0.511	252.3	84.85	4.58	85.13	4.27	1.0	24	-0.98	0.00	-1.14	0.02	···	···
G029.103-00.916	29.103	-0.914	9.3	0.86	0.10	1.16	0.11	1.1	16	-0.39	0.15	-0.64	0.34	···	···
G029.108-00.155	29.108	-0.155	34.4	13.91	0.85	13.51	0.79	0.9	18	0.01	0.03	-0.54	0.06	···	···
G029.114-00.949	29.115	-0.948	4.3	0.37	0.09	0.43	0.09	0.5	9	···	···	-0.50	0.87	···	···
G029.117+00.090	29.117	0.091	11.7	4.47	0.45	7.71	0.54	1.5	19	0.12	0.11	-0.42	0.07	HII region	3
G029.120-00.025	29.125	-0.027	7.8	4.18	0.58	75.39	3.81	11.9	54	···	···	···	···	Ionization Front	1
G029.120-00.260	29.118	-0.267	7.1	1.50	0.23	34.67	1.75	13.7	55	···	···	···	···	Ionization Front	1
G029.128-00.823	29.128	-0.823	11.9	1.24	0.12	1.40	0.13	1.0	15	-0.53	0.11	-1.67	0.46	···	···
G029.128-00.882	29.129	-0.882	7.6	0.76	0.11	1.01	0.11	1.0	14	···	···	-0.72	0.32	···	···
G029.130-00.446	29.128	-0.446	19.1	3.90	0.29	6.79	0.40	1.6	22	-0.88	0.04	-1.53	0.08	···	···
G029.134-00.148	29.134	-0.144	35.5	15.15	0.92	49.01	2.49	3.1	35	···	···	···	···	HII region	4
G029.138+00.833	29.138	0.833	88.5	11.55	0.64	10.74	0.55	0.9	19	0.29	0.03	-0.51	0.06	···	···
G029.146+00.554	29.149	0.547	6.9	1.34	0.21	14.35	0.74	6.5	35	···	···	···	···	···	···
G029.153+00.945	29.153	0.945	4.3	0.32	0.08	0.30	0.08	0.4	8	···	···	0.29	0.56	···	···
G029.164-00.792	29.164	-0.792	27.9	3.39	0.22	3.38	0.21	0.9	18	0.51	0.11	-0.48	0.04	···	···
G029.165+00.606	29.164	0.605	11.8	2.11	0.21	2.53	0.22	1.0	16	-0.52	0.10	0.30	0.13	···	···
G029.165-00.017	29.165	-0.017	32.9	18.02	1.11	14.33	0.90	0.8	15	0.05	0.03	0.11	0.04	PN	6
G029.177-00.431	29.176	-0.430	4.8	0.95	0.20	0.64	0.20	0.4	7	···	···	0.37	0.33	···	···
G029.195-00.288	29.195	-0.287	18.4	3.37	0.26	2.80	0.23	0.8	14	-0.86	0.05	-1.18	0.11	···	···
G029.197-00.127	29.198	-0.127	10.7	4.98	0.54	3.75	0.50	0.6	11	-0.01	0.10	0.18	0.18	···	···
G029.207+00.308	29.207	0.307	4.6	1.45	0.32	5.28	0.41	1.7	17	···	···	-1.20	0.20	···	···
G029.207+00.545	29.202	0.554	8.5	1.67	0.21	46.10	2.31	18.2	66	···	···	···	···	Extended/Diffuse	1
G029.211-00.069‡	29.211	-0.069	87.0	150.80	1.70	158.20	3.10	1.0	···	···	···	0.06	0.02	PN	6
G029.213-00.725	29.213	-0.723	8.5	1.22	0.16	1.82	0.17	1.2	16	···	···	-1.36	0.17	···	···
G029.215-00.055‡	29.215	-0.055	15.8	8.43	0.53	349.26	3.44	41.4	···	···	···	···	···	···	···
G029.216+00.024	29.216	0.024	4.3	2.22	0.53	4.82	0.57	1.0	12	···	···	-0.91	0.22	···	···
G029.221+00.865	29.220	0.865	5.3	0.55	0.11	1.96	0.14	1.8	19	···	···	-0.14	0.31	···	···
G029.222+00.540	29.222	0.540	4.4	0.83	0.20	1.19	0.20	0.7	10	···	···	0.11	0.69	PN	1
G029.227+00.517	29.228	0.517	57.9	15.47	0.88	15.07	0.80	1.0	19	-0.94	0.01	-1.07	0.05	···	···
G029.236-00.860	29.236	-0.860	156.5	15.51	0.84	18.74	0.94	1.2	26	-0.82	0.01	-1.19	0.05	···	···
G029.243+00.256	29.244	0.257	32.6	9.47	0.59	16.23	0.86	1.6	26	0.10	0.04	-0.39	0.11	HII region	3
G029.243-00.718	29.243	-0.718	4.2	0.48	0.12	0.47	0.12	0.4	8	···	···	-2.78	0.33	···	···
G029.276-00.904	29.276	-0.904	7.8	0.72	0.10	0.54	0.10	0.6	10	-0.67	0.15	-0.56	0.40	···	···
G029.280+00.954	29.280	0.954	5.0	0.41	0.08	0.46	0.08	0.6	10	···	···	-0.85	0.63	···	···
G029.287+00.829	29.288	0.829	6.5	0.76	0.12	1.61	0.14	1.4	17	···	···	-0.26	0.50	···	···
G029.291+00.701	29.290	0.702	11.6	2.28	0.23	3.86	0.28	1.4	18	···	···	-0.74	0.12	···	···
G029.291-00.338	29.291	-0.338	5.9	1.15	0.21	1.09	0.20	0.6	10	···	···	-1.10	0.33	HII region	3
G029.293-00.583	29.292	-0.583	34.7	6.33	0.39	8.28	0.45	1.3	20	-0.43	0.03	-0.98	0.07	···	···
G029.295-00.566	29.295	-0.566	17.6	3.33	0.26	2.89	0.24	0.8	14	-0.42	0.06	-0.65	0.10	···	···
G029.297-00.739	29.297	-0.739	8.2	0.79	0.11	0.67	0.10	0.6	11	-0.86	0.12	-0.69	0.64	···	···
G029.306-00.874	29.306	-0.873	5.9	0.55	0.10	0.47	0.10	0.6	10	···	···	0.09	0.50	···	···

Continued on next page

Table B.1 – *Continued from previous page*

GLOSTAR name	ℓ	b	SNR	$S_{\rm peak}$	$\Delta S_{\rm peak}$	$S_{\rm int}$	$\Delta S_{\rm int}$	Y	Radius	Spectral index				Classification	
	(°)	(°)		(mJy beam^{-1})		(mJy)			($''$)	α	$\Delta\alpha$	α*	$\Delta\alpha$*	Type	Ref.
(1)	(2)	(3)	(4)	(5)	(6)	(7)	(8)	(9)	(10)	(11)	(12)	(13)	(14)	(15)	(16)
G029.325+00.938	29.325	0.937	6.9	0.52	0.08	0.46	0.08	0.6	11	···	···	-0.75	0.46	···	···
G029.332-00.647	29.331	-0.646	11.3	1.16	0.12	1.41	0.12	1.0	16	···	···	0.08	0.17	···	···
G029.334-00.423	29.349	-0.421	11.2	2.18	0.23	86.11	4.31	30.3	90	···	···	···	···	HII region	1
G029.356-00.390	29.356	-0.390	10.0	2.16	0.25	2.77	0.26	1.0	15	···	···	-0.76	0.22	···	···
G029.364+00.601	29.364	0.601	6.5	0.84	0.14	0.58	0.13	0.5	9	···	···	1.05	0.27	···	···
G029.367-00.317	29.368	-0.317	11.0	2.26	0.24	2.37	0.24	0.9	14	···	···	0.02	0.23	HII region	1
G029.371+00.104	29.379	0.113	37.7	16.24	0.98	558.82	27.94	33.0	19	···	···	···	···	Extended/Diffuse	1
G029.372+00.906	29.372	0.907	6.3	0.50	0.08	0.40	0.08	0.5	10	···	···	-1.17	0.17	···	···
G029.392+00.685	29.392	0.685	6.0	1.40	0.24	1.00	0.24	0.5	9	-0.69	0.14	-0.25	0.28	···	···
G029.398-00.618	29.398	-0.618	111.8	14.75	0.80	14.85	0.75	1.0	21	0.05	0.02	-0.13	0.02	PN	1
G029.399-00.852	29.400	-0.852	8.9	0.78	0.10	0.95	0.10	0.9	14	-0.71	0.14	-1.24	0.64	···	···
G029.403-00.450	29.403	-0.450	5.4	1.09	0.21	1.15	0.21	0.6	10	···	···	0.29	0.18	PN	1
G029.412+00.045	29.415	0.051	8.1	3.31	0.45	62.15	3.13	12.4	55	···	···	···	···	Extended/Diffuse	1
G029.433+00.609	29.433	0.609	4.8	0.57	0.12	0.44	0.12	0.4	8	···	···	-1.46	0.47	···	···
G029.435-00.192	29.436	-0.192	6.0	1.29	0.23	0.81	0.22	0.4	8	-0.87	0.15	-0.80	0.25	···	···
G029.437+00.272	29.436	0.277	4.8	1.49	0.32	31.91	1.62	8.7	42	···	···	···	···	HII region	1
G029.447+00.890	29.447	0.890	16.8	1.35	0.11	1.36	0.11	0.9	15	···	···	-0.02	0.22	···	···
G029.455+00.499	29.455	0.499	12.2	1.63	0.16	1.84	0.16	1.0	15	-0.68	0.08	-0.74	0.11	···	···
G029.456+00.799	29.456	0.799	6.7	1.24	0.20	0.81	0.19	0.4	9	-0.58	0.14	-0.76	0.24	···	···
G029.466+00.446	29.468	0.445	7.4	1.10	0.16	15.29	0.78	8.9	46	···	···	···	···	Extended/Diffuse	1
G029.470-00.733	29.470	-0.733	4.0	0.45	0.11	0.51	0.12	0.5	8	···	···	-0.61	0.45	···	···
G029.470-00.854	29.470	-0.854	7.0	0.66	0.10	0.55	0.10	0.6	10	···	···	-0.06	0.34	···	···
G029.473+00.772	29.473	0.771	4.0	0.80	0.20	1.67	0.21	0.9	11	···	···	-1.26	0.36	···	···
G029.475+00.029†	29.475	0.029	11.0	0.88	0.07	3.33	0.35	3.8	···	···	···	···	···	···	···
G029.476-00.178	29.475	-0.178	17.7	4.34	0.34	4.96	0.35	1.0	17	0.04	0.08	-0.73	0.13	HII region	3
G029.493+00.931	29.493	0.931	18.8	1.46	0.11	1.23	0.10	0.8	14	-0.49	0.09	-0.70	0.32	PN	1
G029.496-00.300	29.496	-0.300	33.1	6.75	0.42	5.61	0.35	0.8	15	-0.16	0.05	-1.05	0.09	···	···
G029.502+00.434	29.502	0.434	142.1	22.10	1.20	22.77	1.15	1.0	21	-0.62	0.01	-0.72	0.03	···	···
G029.502+00.624	29.502	0.624	17.5	2.34	0.18	3.36	0.21	1.3	19	···	···	-0.71	0.12	···	···
G029.507+00.824	29.505	0.825	17.1	2.72	0.22	4.34	0.27	1.4	19	-1.01	0.05	-1.05	0.15	···	···
G029.507+00.851	29.507	0.850	45.2	5.20	0.30	5.26	0.29	1.0	19	-0.75	0.03	-1.17	0.06	···	···
G029.509+00.303	29.511	0.316	6.3	1.65	0.27	26.35	1.34	9.0	46	···	···	···	···	Extended/Diffuse	1
G029.510-00.444	29.510	-0.444	5.4	1.23	0.24	1.44	0.24	0.7	11	···	···	-0.57	0.39	···	···
G029.523-00.436	29.523	-0.436	5.2	1.25	0.25	1.98	0.26	0.9	12	···	···	-0.59	0.36	···	···
G029.552+00.935	29.552	0.935	4.4	0.33	0.08	0.34	0.08	0.5	9	···	···	0.17	0.25	···	···
G029.557+00.460	29.557	0.460	24.4	3.30	0.22	3.25	0.21	0.9	16	-0.53	0.05	-0.92	0.14	···	···
G029.566-00.928	29.568	-0.931	4.2	0.43	0.11	3.15	0.19	2.7	22	···	···	···	···	···	···
G029.578-00.269	29.578	-0.269	55.9	15.02	0.85	14.36	0.77	0.9	19	···	···	0.45	0.04	PN	6
G029.580+00.979	29.581	0.979	9.2	0.83	0.10	0.66	0.10	0.6	11	···	···	-0.34	0.40	···	···
G029.587-00.659	29.587	-0.659	10.2	1.15	0.13	0.86	0.12	0.6	11	···	···	0.30	0.30	HII region	3
G029.588+00.812	29.588	0.812	5.8	1.13	0.21	1.16	0.20	0.7	11	-0.25	0.17	-1.05	0.27	···	···
G029.589+00.579	29.589	0.579	15.1	2.07	0.18	2.12	0.17	0.9	15	-0.46	0.10	-1.19	0.08	···	···
G029.602+00.749	29.602	0.749	4.3	0.82	0.20	1.51	0.21	0.9	11	···	···	-1.54	0.56	···	···

Continued on next page

Table B.1 – *Continued from previous page*

GLOSTAR name	ℓ	b	SNR	$S_{\rm peak}$	$\Delta S_{\rm peak}$	$S_{\rm int}$	$\Delta S_{\rm int}$	Y	Radius	Spectral index				Classification	
	(°)	(°)		(mJy beam^{-1})		(mJy)			($''$)	α	$\Delta\alpha$	α*	$\Delta\alpha$*	Type	Ref.
(1)	(2)	(3)	(4)	(5)	(6)	(7)	(8)	(9)	(10)	(11)	(12)	(13)	(14)	(15)	(16)
G029.603-00.847	29.602	-0.847	13.0	1.45	0.14	1.25	0.13	0.7	13	···	···	-0.35	0.40	···	···
G029.605-00.859	29.605	-0.859	140.4	15.89	0.86	15.03	0.76	0.9	21	-0.70	0.01	-0.84	0.05	···	···
G029.609-00.812	29.609	-0.808	87.5	9.40	0.52	17.07	0.86	1.8	26	···	···	···	···	···	···
G029.610+00.707	29.610	0.707	4.3	0.83	0.20	0.91	0.20	0.5	9	···	···	-1.33	0.64	···	···
G029.618-00.598	29.617	-0.599	42.8	5.06	0.30	12.88	0.65	2.5	29	···	···	···	···	HII region	1
G029.619-00.813	29.619	-0.813	6.4	0.70	0.12	0.62	0.11	0.6	10	···	···	-0.14	0.31	···	···
G029.628-00.930	29.629	-0.930	82.8	8.23	0.45	16.84	0.85	2.0	31	···	···	···	···	···	···
G029.636-00.989	29.636	-0.989	31.7	4.07	0.25	3.62	0.22	0.9	16	-0.82	0.05	-1.29	0.10	···	···
G029.639-00.571	29.639	-0.571	13.4	1.91	0.18	1.52	0.16	0.7	13	-0.69	0.10	-0.83	0.11	···	···
G029.641-00.960	29.641	-0.960	4.9	0.51	0.11	0.28	0.11	0.3	7	···	···	0.26	0.45	···	···
G029.644+00.594	29.644	0.594	11.4	1.70	0.18	1.29	0.16	0.6	12	-0.80	0.08	-1.09	0.15	···	···
G029.662+00.350	29.662	0.355	4.2	0.70	0.17	34.65	1.74	15.3	55	···	···	···	···	Extended/Diffuse	1
G029.668-00.410	29.668	-0.410	5.8	1.87	0.34	1.60	0.33	0.5	10	···	···	-0.18	0.30	···	···
G029.679-00.511	29.679	-0.510	11.9	2.19	0.22	4.37	0.29	1.7	20	···	···	-0.75	0.33	···	···
G029.680-00.068	29.680	-0.068	4.7	1.12	0.25	0.93	0.24	0.4	8	···	···	-0.99	0.41	···	···
G029.680-00.431	29.680	-0.432	7.8	2.27	0.31	12.67	0.70	3.8	27	···	···	···	···	···	···
G029.681+00.599	29.681	0.599	13.9	2.34	0.21	2.17	0.20	0.8	14	···	···	0.52	0.17	···	···
G029.682-00.990	29.682	-0.990	4.5	0.56	0.13	0.35	0.13	0.3	7	···	···	-1.34	0.35	···	···
G029.683-00.399	29.683	-0.399	6.9	2.28	0.35	2.08	0.35	0.6	11	···	···	0.74	0.27	···	···
G029.686-00.926	29.686	-0.927	27.7	2.64	0.17	3.35	0.19	1.2	22	-0.64	0.07	-1.07	0.10	···	···
G029.689-00.242	29.705	-0.248	335.2	196.90	10.62	2025.92	101.30	10.3	91	···	···	···	···	SNR-candidate	1
G029.708+00.675	29.708	0.675	5.1	0.96	0.20	0.73	0.19	0.4	8	···	···	-0.05	0.47	···	···
G029.714-00.303	29.715	-0.303	4.0	1.86	0.47	5.14	0.53	1.1	13	···	···	-0.50	0.25	···	···
G029.716-00.318	29.716	-0.318	79.0	33.73	1.87	32.02	1.66	0.9	19	0.18	0.03	-0.11	0.04	Radio star	8
G029.719-00.031	29.719	-0.031	71.2	27.41	1.53	26.14	1.36	0.9	19	0.65	0.05	0.76	0.06	Radio star	8
G029.719-00.879	29.719	-0.879	270.1	24.26	1.31	23.02	1.15	1.0	23	-0.44	0.01	-0.57	0.03	···	···
G029.724+00.584	29.724	0.584	32.6	5.32	0.33	5.49	0.32	1.0	17	-0.67	0.03	-1.24	0.06	···	···
G029.726-00.763	29.726	-0.762	5.2	0.68	0.14	0.90	0.14	0.8	11	···	···	0.54	0.30	···	···
G029.727+00.878	29.727	0.878	11.0	1.23	0.13	0.92	0.12	0.6	12	···	···	0.37	0.29	···	···
G029.732-00.849	29.732	-0.849	5.6	0.53	0.10	0.40	0.10	0.5	9	···	···	0.37	0.94	···	···
G029.737-00.813	29.738	-0.811	4.7	0.53	0.12	0.83	0.12	0.8	11	···	···	0.01	0.53	···	···
G029.744-00.601	29.746	-0.601	12.1	2.02	0.20	2.60	0.21	1.1	17	···	···	-0.57	0.23	···	···
G029.752+00.983	29.751	0.983	4.7	0.46	0.10	0.44	0.10	0.5	9	···	···	1.24	0.44	···	···
G029.763+00.939	29.763	0.939	7.4	0.65	0.09	0.80	0.10	0.9	13	···	···	-0.20	0.33	···	···
G029.766+00.876	29.766	0.876	12.7	1.28	0.12	1.03	0.11	0.7	12	···	···	0.00	0.19	···	···
G029.770+00.219	29.785	0.216	339.5	68.44	3.69	93.56	4.68	1.4	45	···	···	···	···	HII region	2
G029.776-00.803	29.778	-0.802	25.1	2.92	0.20	5.56	0.30	1.8	22	-0.48	0.06	-0.54	0.11	···	···
G029.792+00.229	29.793	0.229	4.1	0.83	0.21	0.70	0.21	0.4	7	···	···	-1.91	0.54	···	···
G029.798-00.465	29.798	-0.464	4.7	1.09	0.24	0.69	0.24	0.3	7	···	···	-0.25	0.58	···	···
G029.802-00.589	29.802	-0.589	4.0	0.76	0.19	0.54	0.19	0.3	7	···	···	-0.71	0.35	···	···
G029.804+00.426	29.804	0.427	9.2	1.68	0.20	1.40	0.20	0.7	12	-0.73	0.10	-0.85	0.31	···	···
G029.812-00.840	29.812	-0.839	17.6	2.03	0.16	2.22	0.16	1.0	17	-0.17	0.13	-0.43	0.06	···	···
G029.815+00.589	29.815	0.589	13.9	2.13	0.19	2.05	0.18	0.8	14	-0.74	0.07	-1.43	0.19	···	···

Continued on next page

Table B.1 – *Continued from previous page*

GLOSTAR name	ℓ	b	SNR	$S_{\rm peak}$	$\Delta S_{\rm peak}$	$S_{\rm int}$	$\Delta S_{\rm int}$	Y	Radius	Spectral index				Classification	
	(°)	(°)		(mJy beam^{-1})		(mJy)			($''$)	α	$\Delta\alpha$	α*	$\Delta\alpha$*	Type	Ref.
(1)	(2)	(3)	(4)	(5)	(6)	(7)	(8)	(9)	(10)	(11)	(12)	(13)	(14)	(15)	(16)
G029.818-00.956	29.818	-0.957	37.2	4.19	0.25	3.78	0.22	0.9	17	-0.78	0.04	-0.82	0.11	···	···
G029.822+00.231	29.818	0.228	12.6	2.71	0.26	4.09	0.30	1.3	20	···	···	···	···	···	···
G029.827+00.399	29.826	0.398	4.3	0.80	0.19	1.84	0.21	1.0	13	···	···	0.54	0.71	···	···
G029.841+00.081	29.841	0.081	6.0	2.72	0.47	2.59	0.47	0.6	10	-0.72	0.16	0.90	0.33	···	···
G029.846+00.603	29.846	0.603	6.7	1.00	0.16	1.05	0.16	0.7	11	···	···	-1.02	0.50	···	···
G029.854+00.548	29.854	0.548	13.9	2.40	0.22	2.53	0.21	0.9	15	0.14	0.12	-0.29	0.17	HII region	3
G029.856+00.933	29.856	0.932	620.9	52.08	2.81	70.99	3.55	1.4	31	-0.51	0.00	-0.73	0.02	···	···
G029.856-00.549	29.865	-0.552	8.8	1.87	0.23	13.92	0.73	5.8	41	···	···	···	···	Extended/Diffuse	1
G029.863+00.306	29.864	0.304	4.5	0.79	0.18	10.12	0.54	4.9	30	···	···	···	···	···	···
G029.869-00.998	29.868	-0.997	4.7	0.81	0.18	0.65	0.18	0.4	8	···	···	-0.42	0.50	···	···
G029.874-00.819	29.874	-0.820	1512.0	201.58	10.86	200.94	10.05	1.0	28	0.71	0.00	0.31	0.03	PN	6
G029.878-00.840	29.877	-0.840	14.8	1.96	0.17	1.79	0.16	0.8	14	-0.57	0.10	-0.31	0.14	···	···
G029.884-00.919	29.884	-0.920	4.1	0.52	0.13	1.32	0.14	1.1	12	···	···	2.06	0.77	···	···
G029.888-00.781	29.888	-0.780	20.3	3.18	0.23	3.96	0.25	1.2	18	0.10	0.14	-0.28	0.09	HII region	3
G029.889+00.929	29.889	0.928	6.3	0.55	0.09	0.48	0.09	0.6	10	···	···	0.03	0.55	···	···
G029.928+00.999	29.929	1.000	4.2	0.52	0.13	0.51	0.13	0.4	8	···	···	1.12	0.31	···	···
G029.931+00.802	29.931	0.801	6.6	0.63	0.10	0.77	0.10	0.8	12	-0.60	0.18	-0.42	0.55	···	···
G029.947-00.801	29.949	-0.804	18.5	3.55	0.27	14.97	0.77	3.8	34	···	···	···	···	HII region	1
G029.953-00.786	29.953	-0.786	4.9	0.96	0.20	0.64	0.20	0.4	7	···	···	-0.81	0.26	HII region	3
G029.954-00.697	29.954	-0.697	6.9	1.62	0.25	1.60	0.25	0.7	11	-0.71	0.13	-1.17	0.41	···	···
G029.956+00.128	29.956	0.128	7.6	2.29	0.32	3.10	0.34	1.0	14	-0.68	0.14	-0.62	0.37	···	···
G029.956-00.349	29.959	-0.348	13.0	4.74	0.45	26.06	1.35	4.7	35	···	···	···	···	HII region	3
G029.958+00.994	29.958	0.994	8.3	0.98	0.13	0.74	0.12	0.6	11	···	···	-1.84	0.33	···	···
G029.965-00.817	29.965	-0.817	5.9	1.14	0.20	0.92	0.20	0.5	9	-1.00	0.15	-2.14	0.31	···	···
G029.975+00.649	29.970	0.654	5.2	0.79	0.16	18.30	0.93	10.3	46	···	···	···	···	Extended/Diffuse	1
G029.977+00.843	29.977	0.843	22.8	2.13	0.15	1.89	0.13	0.8	15	0.07	0.11	-0.46	0.15	PN	1
G029.980-00.924	29.979	-0.927	5.2	0.77	0.16	4.03	0.25	2.5	22	···	···	···	···	Extended/Diffuse	1
G029.982-00.708	29.983	-0.709	22.9	5.34	0.37	4.67	0.33	0.8	15	···	···	0.24	0.04	Radio star	8
G029.989+00.996	29.988	0.995	51.5	6.36	0.36	6.77	0.36	1.0	20	-0.57	0.03	-0.81	0.05	···	···
G029.993+00.779	29.993	0.780	8.1	0.86	0.12	0.67	0.11	0.6	10	···	···	-0.32	0.29	···	···
G029.997+00.655	29.999	0.652	13.9	2.12	0.19	3.47	0.23	1.4	21	···	···	-0.38	0.49	PN	1
G029.997+00.934	29.995	0.933	13.7	1.24	0.11	2.03	0.14	1.4	21	···	···	-0.83	0.27	···	···
G029.998+00.471	29.992	0.476	5.7	1.45	0.26	28.18	1.43	9.9	47	···	···	···	···	Extended/Diffuse	1
G030.004+00.897	30.005	0.896	6.2	0.59	0.10	0.95	0.11	1.0	14	···	···	-0.09	0.84	···	···
G030.005+00.851	30.005	0.851	19.1	1.87	0.14	1.52	0.12	0.7	14	-0.85	0.06	-1.13	0.24	···	···
G030.009-00.274	30.009	-0.274	15.8	5.56	0.46	5.44	0.45	0.9	15	···	···	0.67	0.06	HII region	2
G030.013+00.938	30.013	0.938	6.4	0.57	0.09	0.47	0.09	0.6	10	···	···	-0.35	0.30	···	···
G030.022-00.879	30.023	-0.884	293.2	46.38	2.50	63.60	3.18	1.4	43	···	···	-0.32	0.04	···	···
G030.023+00.108	30.024	0.110	65.7	31.92	1.79	69.64	3.52	2.1	32	···	···	···	···	HII region	1
G030.023+00.157	30.022	0.157	32.0	10.34	0.64	9.60	0.58	0.9	17	0.03	0.06	0.20	0.12	PN	6
G030.025-00.907	30.025	-0.907	4.0	0.61	0.16	0.63	0.15	0.4	8	···	···	1.43	0.52	···	···
G030.029-00.332	30.029	-0.332	40.9	15.66	0.93	14.29	0.81	0.9	17	0.24	0.05	-0.07	0.07	PN	6
G030.033-00.153	30.033	-0.153	10.1	8.17	0.92	7.83	0.90	0.8	13	-0.62	0.08	-0.90	0.12	···	···

Continued on next page

Table B.1 – *Continued from previous page*

GLOSTAR name	ℓ	b	SNR	$S_{\rm peak}$	$\Delta S_{\rm peak}$	$S_{\rm int}$	$\Delta S_{\rm int}$	Y	Radius	Spectral index				Classification	
	(°)	(°)		(mJy beam^{-1})		(mJy)			($''$)	α	$\Delta\alpha$	α*	$\Delta\alpha$*	Type	Ref.
(1)	(2)	(3)	(4)	(5)	(6)	(7)	(8)	(9)	(10)	(11)	(12)	(13)	(14)	(15)	(16)
G030.042-00.142	30.042	-0.142	6.6	5.61	0.90	4.45	0.88	0.5	10	0.09	0.17	-0.71	0.26	HII region	3
G030.046+00.162	30.045	0.166	27.8	9.01	0.58	13.65	0.76	1.4	22	···	···	···	···	···	···
G030.048+00.835	30.048	0.835	20.1	2.16	0.16	2.12	0.15	0.9	16	-0.52	0.06	-0.98	0.14	···	···
G030.054+00.441	30.052	0.441	18.6	4.03	0.31	4.02	0.30	0.9	17	0.17	0.10	-0.35	0.09	···	···
G030.057-00.342	30.054	-0.340	22.6	8.41	0.59	83.58	4.20	9.2	56	···	···	···	···	HII region	1
G030.061+00.876	30.060	0.873	40.5	4.04	0.24	5.12	0.27	1.2	24	···	···	-1.28	0.24	···	···
G030.068+00.098	30.068	0.097	5.7	2.43	0.45	2.82	0.45	0.7	11	···	···	-0.11	0.12	HII region	3
G030.069+00.655	30.069	0.655	7.7	1.01	0.14	0.98	0.14	0.7	12	-0.20	0.17	-0.34	0.32	···	···
G030.080+00.387	30.080	0.387	4.0	0.95	0.24	2.59	0.27	1.1	13	···	···	-1.88	0.30	···	···
G030.082+00.715	30.081	0.711	100.3	11.24	0.62	12.52	0.64	1.1	27	···	···	-1.15	0.08	···	···
G030.088+00.935	30.088	0.934	4.1	0.36	0.09	0.55	0.09	0.7	10	···	···	-0.07	0.28	···	···
G030.091-00.308	30.091	-0.307	6.4	2.34	0.38	2.49	0.38	0.7	11	-0.95	0.12	-0.94	0.09	···	···
G030.098+00.721	30.098	0.721	6.6	0.73	0.12	0.61	0.11	0.6	10	···	···	-1.03	0.44	···	···
G030.100-00.480	30.097	-0.483	4.9	1.35	0.28	5.95	0.40	2.1	19	···	···	···	···	Extended/Diffuse	1
G030.104+00.399	30.104	0.398	26.7	6.12	0.40	4.96	0.34	0.8	15	-0.23	0.04	-0.69	0.12	···	···
G030.104+00.672	30.104	0.671	19.1	2.19	0.16	2.12	0.16	0.9	15	-0.53	0.07	-0.85	0.23	···	···
G030.117+00.732	30.116	0.732	5.1	0.56	0.11	0.45	0.11	0.5	9	···	···	-1.30	0.55	···	···
G030.122+00.205	30.121	0.206	4.0	1.13	0.29	7.75	0.48	2.4	20	···	···	···	···	Ionization Front	1
G030.133+00.929	30.133	0.930	40.1	3.56	0.21	3.46	0.19	0.9	18	-0.53	0.04	-1.26	0.07	···	···
G030.136+00.713	30.136	0.713	12.0	1.29	0.13	1.31	0.13	0.9	14	-0.83	0.10	-1.27	0.09	···	···
G030.136+00.747	30.135	0.747	5.0	0.54	0.11	0.59	0.11	0.6	10	···	···	-1.31	0.59	···	···
G030.138+00.351	30.138	0.351	12.4	2.92	0.28	2.48	0.27	0.7	13	-0.61	0.08	-0.74	0.30	···	···
G030.141-00.755	30.141	-0.755	8.6	1.49	0.19	1.40	0.19	0.7	12	···	···	-0.54	0.30	···	···
G030.147-00.812	30.147	-0.812	13.4	2.09	0.19	1.77	0.18	0.7	13	-1.16	0.06	-1.53	0.09	···	···
G030.150+00.124	30.150	0.123	72.1	25.19	1.40	27.45	1.42	1.1	20	0.13	0.02	-0.09	0.01	HII region	4
G030.154+00.583	30.156	0.583	4.4	0.55	0.13	1.16	0.14	1.0	12	···	···	1.09	0.99	HII region	1
G030.157-00.508	30.157	-0.508	31.1	6.04	0.38	6.40	0.37	1.0	17	-0.45	0.04	-0.56	0.06	···	···
G030.168+00.556	30.169	0.566	123.6	17.46	0.95	44.60	2.23	2.5	43	···	···	···	···	···	···
G030.169+00.688	30.169	0.689	10.7	1.20	0.13	1.24	0.13	0.8	14	···	···	-0.27	0.19	···	···
G030.187+00.533	30.187	0.533	29.5	4.55	0.29	4.37	0.27	0.9	17	-0.78	0.04	-1.06	0.10	···	···
G030.196-00.168‡	30.196	-0.168	32.6	21.17	0.65	406.97	2.85	19.2	···	···	···	···	···	···	···
G030.197+00.310†	30.197	0.310	10.0	0.67	0.04	0.24	0.04	0.4	···	···	···	···	···	HII region	3
G030.205+00.328	30.205	0.329	9.4	2.28	0.27	4.61	0.33	1.6	18	···	···	-0.06	0.25	HII region	3
G030.207-00.769	30.208	-0.768	7.3	1.37	0.20	1.59	0.20	0.8	13	-0.62	0.13	-0.97	0.16	···	···
G030.207-00.922	30.207	-0.922	5.3	0.98	0.19	1.17	0.20	0.7	11	···	···	-1.70	0.45	···	···
G030.211+00.429	30.211	0.429	150.0	25.21	1.37	27.93	1.41	1.1	24	0.05	0.01	-0.08	0.02	HII region	3
G030.219-00.946	30.219	-0.946	7.1	1.34	0.20	0.99	0.20	0.5	10	-0.72	0.14	-1.26	0.26	···	···
G030.221-00.181	30.219	-0.183	29.4	17.97	1.14	31.10	1.67	1.6	23	0.20	0.06	-0.06	0.12	HII region	3
G030.225+00.542	30.225	0.542	105.5	17.78	0.97	22.26	1.13	1.2	23	0.15	0.02	-0.18	0.04	HII region	1
G030.233-00.138‡	30.233	-0.138	316.0	415.60	1.30	420.90	2.30	1.0	···	0.17	.00	0.36	.02	PN	6
G030.236+00.569	30.236	0.569	7.8	1.45	0.20	1.34	0.20	0.7	12	···	···	-0.62	0.25	HII region	3
G030.236-00.572	30.236	-0.572	28.3	4.43	0.29	3.85	0.25	0.8	16	-0.22	0.06	-0.03	0.11	Radio star	8
G030.241-00.592	30.241	-0.592	11.4	1.73	0.18	1.30	0.16	0.6	12	-0.12	0.16	0.15	0.36	HII region	1

Continued on next page

Table B.1 – *Continued from previous page*

GLOSTAR name	ℓ	b	SNR	$S_{\rm peak}$	$\Delta S_{\rm peak}$	$S_{\rm int}$	$\Delta S_{\rm int}$	Y	Radius	Spectral index				Classification	
	(°)	(°)		(mJy beam^{-1})		(mJy)			($''$)	α	$\Delta\alpha$	α*	$\Delta\alpha$*	Type	Ref.
(1)	(2)	(3)	(4)	(5)	(6)	(7)	(8)	(9)	(10)	(11)	(12)	(13)	(14)	(15)	(16)
G030.246-00.910	30.248	-0.912	15.5	2.90	0.24	8.71	0.47	2.7	30	···	···	···	···	HII region	1
G030.248+00.245	30.250	0.242	107.4	37.98	2.08	134.34	6.73	3.5	43	···	···	···	···	HII region	3
G030.251-00.019	30.259	-0.018	28.2	18.68	1.20	271.66	13.60	13.8	77	···	···	···	···	Ionization Front	1
G030.252-00.448	30.253	-0.448	8.5	2.55	0.33	1.72	0.31	0.5	10	-0.18	0.15	0.10	0.23	···	···
G030.253+00.053	30.250	0.053	228.1	119.46	6.45	160.96	8.07	1.3	30	0.15	0.01	-0.02	0.06	HII region	2
G030.277+00.486	30.277	0.486	6.8	1.47	0.23	1.47	0.23	0.7	11	···	···	-1.02	0.16	···	···
G030.284+00.510	30.283	0.510	4.3	0.88	0.21	0.67	0.21	0.4	7	···	···	-0.41	0.46	···	···
G030.296+00.056	30.296	0.056	6.8	4.24	0.67	4.08	0.66	0.7	11	0.10	0.16	-0.24	0.14	HII region	3
G030.306+00.543	30.306	0.544	7.2	1.45	0.22	1.33	0.21	0.7	11	-0.53	0.17	-1.55	0.22	···	···
G030.309-00.213	30.323	-0.207	14.8	10.42	0.90	325.95	16.31	25.4	73	···	···	···	···	HII region	3
G030.319+00.649	30.321	0.650	27.1	5.60	0.37	9.59	0.52	1.6	21	···	···	-1.47	0.08	···	···
G030.323+00.178	30.324	0.178	5.8	2.03	0.36	1.63	0.36	0.5	9	-0.93	0.14	-1.45	0.36	···	···
G030.330+00.090‡	30.330	0.090	37.0	24.52	0.68	27.90	1.30	1.1	···	0.44	.04	0.36	.04	···	···
G030.331+00.191	30.331	0.191	6.2	2.18	0.37	1.40	0.36	0.4	9	-1.13	0.13	-0.58	0.24	···	···
G030.344+00.383	30.343	0.382	5.6	1.72	0.32	5.99	0.43	1.9	18	···	···	-0.56	0.38	HII region	1
G030.350+00.096‡	30.350	0.092	8.2	4.62	0.56	50.48	1.86	10.9	···	···	···	···	···	HII region	3
G030.363+00.400	30.361	0.403	7.2	2.44	0.36	14.58	0.80	3.9	28	···	···	···	···	···	···
G030.371+00.483	30.370	0.483	12.6	3.47	0.33	3.07	0.31	0.8	13	···	···	0.89	0.16	HII region	1
G030.374-00.492	30.364	-0.487	11.8	5.09	0.51	223.54	11.19	34.4	03	···	···	···	···	HII region	1
G030.375+00.088	30.379	0.090	4.1	2.26	0.56	38.21	1.99	5.5	32	···	···	···	···	···	···
G030.377+00.022	30.374	0.027	32.5	22.53	1.40	215.62	10.80	9.1	55	···	···	···	···	HII region	1
G030.378+00.108	30.379	0.110	41.5	19.82	1.17	42.50	2.18	2.1	29	···	···	···	···	HII region	3
G030.382-00.110	30.381	-0.109	76.8	47.82	2.65	94.94	4.79	2.0	29	···	···	···	···	HII region	3
G030.382-00.655	30.382	-0.655	35.6	6.36	0.39	6.08	0.35	0.9	18	0.02	0.05	-0.33	0.05	···	···
G030.395-00.047	30.395	-0.047	11.7	7.43	0.75	9.48	0.79	1.1	16	-0.65	0.07	-0.63	0.33	···	···
G030.395-00.626	30.395	-0.626	11.8	2.33	0.23	1.98	0.22	0.7	13	-0.62	0.09	-1.20	0.27	···	···
G030.401-00.113	30.401	-0.114	5.9	3.56	0.63	15.89	1.00	2.5	22	···	···	···	···	···	···
G030.404+00.906	30.404	0.905	26.2	2.49	0.16	2.95	0.18	1.1	18	-0.79	0.06	-1.74	0.18	···	···
G030.405+00.873	30.406	0.874	22.9	2.21	0.15	3.17	0.19	1.3	21	-0.74	0.07	-1.42	0.14	···	···
G030.409+00.938	30.409	0.937	19.2	1.66	0.12	1.41	0.11	0.8	14	-0.70	0.08	-1.45	0.19	···	···
G030.415-00.794	30.415	-0.794	4.0	0.62	0.16	0.40	0.16	0.3	6	···	···	-2.40	0.57	···	···
G030.416-00.234	30.408	-0.237	22.1	24.30	1.71	394.87	19.77	15.1	80	···	···	···	···	Ionization Front	1
G030.430+00.269	30.430	0.269	9.0	2.86	0.35	2.42	0.34	0.7	12	-0.56	0.11	-0.54	0.22	···	···
G030.430-00.006	30.434	0.002	10.7	7.29	0.78	151.88	7.62	15.8	64	···	···	···	···	Ionization Front	1
G030.437-00.206	30.436	-0.206	17.5	16.21	1.27	18.50	1.31	1.0	17	0.18	0.08	-0.13	0.12	···	···
G030.446-00.215	30.446	-0.215	8.7	8.57	1.09	5.50	1.02	0.5	10	···	···	0.79	0.15	Radio star	8
G030.452-00.929	30.452	-0.929	5.2	0.83	0.17	0.75	0.16	0.5	9	···	···	-0.41	0.32	···	···
G030.458-00.206	30.456	-0.206	4.7	4.33	0.95	9.33	1.03	1.1	13	···	···	-0.28	0.31	···	···
G030.462-00.034	30.466	-0.038	7.6	6.20	0.88	247.86	12.42	24.2	72	···	···	···	···	HII region	1
G030.464+00.224	30.469	0.223	5.0	1.81	0.38	26.44	1.37	6.3	34	···	···	···	···	HII region	1
G030.464-00.706	30.464	-0.706	5.4	1.28	0.25	0.79	0.24	0.4	8	-0.92	0.16	-0.90	0.29	···	···
G030.466-00.187	30.465	-0.189	10.9	8.93	0.95	56.67	2.95	5.0	33	···	···	···	···	HII region	1
G030.471+00.334	30.471	0.334	4.9	1.53	0.32	1.32	0.32	0.5	9	···	···	-0.43	0.21	···	···

Continued on next page

Table B.1 – *Continued from previous page*

GLOSTAR name	ℓ	b	SNR	$S_{\rm peak}$	$\Delta S_{\rm peak}$	$S_{\rm int}$	$\Delta S_{\rm int}$	Y	Radius	Spectral index				Classification	
	(°)	(°)		(mJy beam^{-1})		(mJy)			($''$)	α	$\Delta\alpha$	α*	$\Delta\alpha$*	Type	Ref.
(1)	(2)	(3)	(4)	(5)	(6)	(7)	(8)	(9)	(10)	(11)	(12)	(13)	(14)	(15)	(16)
G030.485+00.708	30.485	0.709	19.8	2.58	0.19	2.42	0.18	0.9	15	-0.86	0.06	-1.55	0.15	···	···
G030.486+00.857	30.486	0.857	10.4	1.11	0.12	0.98	0.12	0.7	13	-0.64	0.12	-0.89	0.17	···	···
G030.496+00.622	30.495	0.622	5.6	0.85	0.16	1.33	0.17	0.9	13	···	···	-0.29	0.33	···	···
G030.507+00.913	30.507	0.912	16.9	2.56	0.20	2.45	0.19	0.9	15	0.07	0.15	-0.56	0.20	···	···
G030.511-00.301	30.503	-0.310	10.6	9.60	1.05	317.01	15.88	24.9	82	···	···	···	···	Ionization Front	1
G030.518-00.956	30.518	-0.957	10.9	1.83	0.19	1.61	0.19	0.7	12	-1.43	0.07	-1.99	0.12	···	···
G030.530+00.131	30.530	0.131	48.3	24.34	1.40	25.09	1.35	1.0	19	0.05	0.03	-0.03	0.07	PN	6
G030.532-00.339	30.531	-0.339	6.2	5.29	0.90	12.26	1.05	1.4	16	···	···	-0.20	0.22	···	···
G030.533-00.258	30.533	-0.258	10.0	8.40	0.96	21.05	1.35	2.0	21	···	···	···	···	HII region	1
G030.537-00.462	30.535	-0.459	12.5	9.63	0.93	167.23	8.40	14.2	66	···	···	···	···	Ionization Front	1
G030.546+00.097	30.545	0.096	4.1	2.99	0.74	10.50	0.89	1.4	15	···	···	0.26	0.77	···	···
G030.549+00.773	30.549	0.773	6.9	0.88	0.14	0.99	0.14	0.8	12	···	···	-0.92	0.39	···	···
G030.550+00.916	30.550	0.916	8.3	1.70	0.22	1.57	0.22	0.7	12	···	···	0.08	0.28	PN	1
G030.552-00.815	30.552	-0.814	11.2	2.75	0.29	3.40	0.30	1.0	16	-0.60	0.08	-0.75	0.10	···	···
G030.553+00.211	30.554	0.210	8.6	3.63	0.47	3.73	0.46	0.8	13	-0.53	0.12	-1.00	0.16	···	···
G030.563+00.199	30.563	0.199	5.7	2.74	0.50	2.68	0.50	0.6	10	-0.64	0.16	-2.13	0.32	···	···
G030.580+00.463	30.581	0.451	4.4	0.88	0.21	7.64	0.43	3.3	26	···	···	···	···	···	···
G030.581+00.990	30.581	0.990	39.7	9.81	0.58	9.42	0.53	0.9	18	-0.95	0.02	-1.18	0.06	···	···
G030.581-00.545	30.572	-0.553	5.8	3.47	0.63	166.04	8.32	22.8	71	···	···	···	···	Extended/Diffuse	1
G030.582-00.962	30.579	-0.960	4.1	0.71	0.18	2.01	0.20	1.1	14	···	···	-0.93	0.60	···	···
G030.595-00.751	30.593	-0.751	81.6	25.93	1.43	43.26	2.19	1.6	25	-0.79	0.01	-0.98	0.12	···	···
G030.596+00.911	30.600	0.909	76.5	14.44	0.80	15.81	0.81	1.1	26	···	···	0.21	0.08	···	···
G030.599-00.599	30.599	-0.599	7.6	3.00	0.43	2.59	0.42	0.6	11	···	···	0.62	0.16	···	···
G030.602+00.880	30.604	0.880	9.0	1.51	0.19	2.28	0.20	1.2	16	-0.14	0.15	-0.34	0.17	···	···
G030.641+00.696	30.641	0.696	4.9	0.86	0.18	0.90	0.18	0.6	10	···	···	-1.63	0.33	···	···
G030.652+00.983	30.652	0.983	11.6	2.50	0.25	2.28	0.24	0.8	13	···	···	0.26	0.12	···	···
G030.653+00.260	30.670	0.259	7.6	4.74	0.67	52.82	2.71	7.4	40	···	···	···	···	Extended/Diffuse	1
G030.653+00.709	30.648	0.708	4.2	0.73	0.18	5.41	0.32	2.7	22	···	···	···	···	HII region	1
G030.655-00.302	30.655	-0.302	4.9	3.17	0.67	3.56	0.67	0.6	10	···	···	-0.13	0.56	···	···
G030.656+00.904	30.656	0.904	46.1	7.11	0.41	6.92	0.38	0.9	18	-0.85	0.02	-1.15	0.04	···	···
G030.667-00.332	30.667	-0.332	301.8	172.53	9.31	170.38	8.54	1.0	23	0.93	0.01	0.63	0.03	PN	6
G030.672-00.635	30.672	-0.636	5.7	2.10	0.38	3.99	0.42	1.1	14	···	···	-1.50	0.17	···	···
G030.673+00.964	30.672	0.964	184.9	32.05	1.73	30.96	1.56	1.0	21	-0.66	0.01	-0.82	0.01	···	···
G030.678+00.767	30.678	0.766	25.9	3.95	0.26	4.35	0.27	1.0	18	0.07	0.08	-0.46	0.04	HII region	1
G030.679-00.572	30.678	-0.571	4.1	1.80	0.45	18.82	1.04	3.6	24	···	···	···	···	Extended/Diffuse	1
G030.685-00.259	30.694	-0.260	90.3	128.35	7.06	621.41	31.10	4.8	60	···	···	···	···	HII region	4
G030.694+00.842	30.694	0.841	20.0	3.18	0.23	3.31	0.23	1.0	16	-0.65	0.06	-1.06	0.11	···	···
G030.694-00.366	30.694	-0.366	8.5	5.16	0.66	4.82	0.65	0.7	12	0.06	0.14	-0.14	0.14	HII region	3
G030.694-00.736	30.694	-0.736	5.3	1.37	0.27	3.48	0.31	1.4	15	···	···	-0.18	0.37	···	···
G030.699-00.629	30.694	-0.629	228.9	84.55	4.57	123.83	6.20	1.5	34	···	···	-1.20	0.12	Radio star	8
G030.707+00.613	30.707	0.613	11.9	2.21	0.22	1.81	0.21	0.7	12	-0.27	0.12	0.54	0.18	···	···
G030.712-00.284	30.722	-0.288	8.4	11.11	1.45	119.61	6.12	7.4	40	···	···	···	···	Extended/Diffuse	1
G030.726-00.486	30.723	-0.486	4.3	2.00	0.47	18.07	1.01	3.4	24	···	···	···	···	Ionization Front	1

Continued on next page

Table B.1 – *Continued from previous page*

GLOSTAR name	ℓ	b	SNR	$S_{\rm peak}$	$\Delta S_{\rm peak}$	$S_{\rm int}$	$\Delta S_{\rm int}$	Y	Radius	Spectral index				Classification	
	(°)	(°)		(mJy beam^{-1})		(mJy)			($''$)	α	$\Delta\alpha$	α*	$\Delta\alpha$*	Type	Ref.
(1)	(2)	(3)	(4)	(5)	(6)	(7)	(8)	(9)	(10)	(11)	(12)	(13)	(14)	(15)	(16)
G030.741+00.388	30.736	0.388	5.9	2.27	0.40	53.84	2.72	11.9	48	···	···	···	···	···	···
G030.750-00.326	30.747	-0.329	8.0	7.64	1.04	71.29	3.69	6.3	38	···	···	···	···	Ionization Front	1
G030.752-00.753	30.746	-0.754	4.4	1.03	0.24	19.02	0.98	6.6	35	···	···	···	···	Extended/Diffuse	1
G030.758+00.205	30.759	0.205	50.8	42.49	2.44	45.04	2.40	1.0	19	0.14	0.02	0.10	0.03	HII region	2
G030.758+00.367	30.759	0.367	10.3	4.09	0.46	5.12	0.47	1.0	15	-0.62	0.09	-1.10	0.10	···	···
G030.765+00.432	30.765	0.432	5.4	2.11	0.41	2.23	0.40	0.6	10	-0.47	0.17	-1.44	0.29	···	···
G030.778+00.231	30.778	0.230	4.3	3.08	0.73	5.01	0.76	0.8	11	···	···	0.89	0.21	HII region	3
G030.780-00.335	30.786	-0.333	7.0	5.39	0.82	64.24	3.30	7.3	41	···	···	···	···	Ionization Front	1
G030.782+00.732	30.782	0.732	6.9	0.97	0.15	0.97	0.15	0.7	11	···	···	-0.28	0.17	···	···
G030.783+00.447	30.782	0.449	4.9	1.80	0.38	28.89	1.49	6.7	35	···	···	···	···	Ionization Front	1
G030.783-00.027	30.781	-0.037	64.2	812.41	45.54	9979.49	499.13	12.0	89	···	···	···	···	HII region	1
G030.794+00.826	30.794	0.826	7.3	1.00	0.15	1.21	0.15	0.9	13	···	···	-0.98	0.39	···	···
G030.794-00.314	30.794	-0.312	5.3	4.71	0.92	18.71	1.28	2.0	20	···	···	···	···	Extended/Diffuse	1
G030.796+00.168	30.796	0.165	44.5	47.33	2.76	155.65	7.85	3.2	34	···	···	···	···	HII region	3
G030.797-00.680	30.797	-0.680	87.3	22.10	1.22	21.00	1.08	0.9	20	-0.09	0.02	0.05	0.05	···	···
G030.805+00.817	30.804	0.817	40.4	5.55	0.33	5.65	0.31	1.0	18	-0.81	0.03	-1.28	0.07	···	···
G030.828+00.294	30.828	0.283	5.1	2.14	0.43	48.25	2.45	10.0	45	···	···	···	···	···	···
G030.832-00.324	30.834	-0.324	4.2	2.60	0.63	12.81	0.89	1.9	18	···	···	-0.09	0.26	Ionization Front	1
G030.839+00.116	30.841	0.114	14.1	24.67	2.20	104.02	5.49	3.7	32	···	···	···	···	HII region	3
G030.839+00.895	30.840	0.895	5.6	0.65	0.12	0.66	0.12	0.6	10	···	···	0.84	0.51	···	···
G030.854+00.151	30.851	0.143	88.7	97.97	5.39	558.45	27.94	5.6	58	···	···	···	···	···	···
G030.856+00.383	30.856	0.383	187.4	53.18	2.88	51.18	2.57	1.0	21	0.23	0.01	0.01	0.02	PN	6
G030.857+00.867	30.863	0.868	76.2	8.84	0.49	21.70	1.09	2.4	30	···	···	···	···	···	···
G030.860-00.703	30.874	-0.705	4.1	0.96	0.24	42.02	2.11	13.2	48	···	···	···	···	Extended/Diffuse	1
G030.866+00.115	30.866	0.115	272.4	383.49	20.70	376.38	18.87	1.0	22	0.81	0.01	0.80	0.02	HII region	2
G030.877+00.591	30.877	0.591	12.5	2.58	0.25	2.26	0.24	0.7	13	-0.80	0.08	-0.52	0.10	···	···
G030.878+00.699	30.878	0.699	9.0	1.37	0.17	1.49	0.17	0.9	13	···	···	-0.64	0.37	···	···
G030.881-00.872	30.881	-0.871	4.8	1.35	0.29	1.56	0.29	0.6	10	···	···	-1.61	0.21	···	···
G030.887+00.754	30.887	0.754	10.9	1.70	0.18	1.37	0.17	0.7	12	-0.42	0.12	-0.86	0.04	···	···
G030.887+00.904	30.887	0.904	14.8	1.65	0.14	1.46	0.13	0.8	14	···	···	-0.20	0.14	···	···
G030.895+00.175	30.893	0.173	4.1	3.38	0.85	29.73	1.70	3.1	23	···	···	···	···	···	···
G030.906+00.160	30.907	0.160	15.6	13.61	1.14	33.32	1.88	2.2	23	···	···	···	···	HII region	3
G030.914-00.556	30.910	-0.554	4.2	1.66	0.41	77.81	3.91	14.5	53	···	···	···	···	Extended/Diffuse	1
G030.927-00.034†	30.927	-0.034	12.0	4.86	0.41	17.00	1.80	3.5	···	···	···	···	···	HII region	3
G030.930+00.784	30.941	0.821	6.5	1.00	0.16	41.93	2.10	22.3	73	···	···	···	···	···	···
G030.930-00.531	30.932	-0.531	4.2	1.59	0.39	29.19	1.51	6.1	33	···	···	···	···	Extended/Diffuse	1
G030.951+00.593	30.965	0.596	76.6	18.07	1.00	491.33	24.57	26.7	03	···	···	···	···	HII region	1
G030.952+00.540	30.950	0.543	90.8	31.55	1.73	215.48	10.78	6.7	56	···	···	···	···	HII region	3
G030.953+00.906	30.953	0.906	5.3	0.55	0.11	2.58	0.17	2.4	21	···	···	···	···	···	···
G030.955+00.081	30.957	0.082	58.8	56.19	3.17	181.01	9.10	3.1	33	···	···	···	···	HII region	3
G030.955-00.308	30.956	-0.309	4.6	2.48	0.56	32.64	1.72	5.2	31	···	···	···	···	Extended/Diffuse	1
G030.956-00.231	30.956	-0.231	11.9	7.00	0.70	6.58	0.68	0.8	13	-0.50	0.08	-0.49	0.13	···	···
G030.958-00.331	30.957	-0.330	16.8	8.15	0.65	9.13	0.67	1.0	16	-1.31	0.05	-1.70	0.06	···	···

Continued on next page

Table B.1 – *Continued from previous page*

GLOSTAR name	ℓ	b	SNR	$S_{\rm peak}$	$\Delta S_{\rm peak}$	$S_{\rm int}$	$\Delta S_{\rm int}$	Y	Radius	Spectral index				Classification	
	(°)	(°)		(mJy beam^{-1})		(mJy)			($''$)	α	$\Delta\alpha$	α*	$\Delta\alpha$*	Type	Ref.
(1)	(2)	(3)	(4)	(5)	(6)	(7)	(8)	(9)	(10)	(11)	(12)	(13)	(14)	(15)	(16)
G030.958-00.446	30.958	-0.446	11.7	3.86	0.39	3.21	0.37	0.7	13	-0.59	0.08	-1.12	0.11	···	···
G030.960-00.360	30.959	-0.359	5.8	2.29	0.41	1.64	0.40	0.5	9	-0.84	0.15	-0.22	0.22	···	···
G030.968-00.635	30.968	-0.636	23.9	9.06	0.62	7.61	0.54	0.8	15	0.33	0.06	-0.18	0.08	···	···
G030.971-00.317	30.971	-0.317	9.2	4.65	0.56	4.31	0.55	0.7	12	···	···	-0.43	0.17	···	···
G030.975-00.517	30.969	-0.523	8.2	3.09	0.41	26.85	1.39	6.1	38	···	···	···	···	Ionization Front	1
G030.976-00.031	30.981	-0.031	6.0	6.54	1.15	120.69	6.13	9.7	45	···	···	···	···	Extended/Diffuse	1
G030.978-00.669	30.969	-0.674	4.4	1.25	0.29	45.17	2.28	12.2	48	···	···	···	···	Extended/Diffuse	1
G030.984+00.212	30.985	0.207	11.4	6.20	0.64	37.91	1.97	5.1	38	···	···	···	···	Ionization Front	1
G030.987+00.074	30.987	0.075	4.7	4.33	0.94	4.56	0.94	0.6	9	···	···	-0.92	0.67	···	···
G030.987+00.374	30.988	0.373	7.4	2.41	0.35	88.84	4.45	22.1	70	···	···	···	···	Ionization Front	1
G030.996-00.299	30.998	-0.297	130.7	64.73	3.52	93.15	4.68	1.4	30	···	···	-0.48	0.03	···	···
G031.001-00.533	31.001	-0.532	4.6	1.74	0.39	17.66	0.96	4.1	27	···	···	···	···	Extended/Diffuse	1
G031.002-00.633	31.002	-0.633	12.7	4.15	0.40	4.94	0.41	1.0	16	0.10	0.11	-0.25	0.13	···	···
G031.007-00.077	31.002	-0.077	6.0	6.04	1.06	35.54	2.04	3.3	25	···	···	···	···	HII region	1
G031.017+00.193	31.016	0.192	10.2	6.22	0.70	10.65	0.81	1.4	19	-0.55	0.09	-0.72	0.11	Ionization Front	1
G031.017-00.836	31.016	-0.837	12.0	1.46	0.15	1.27	0.14	0.7	13	···	···	0.39	0.23	···	···
G031.020+00.716	31.020	0.716	6.7	0.97	0.15	0.70	0.15	0.5	9	···	···	0.85	0.34	···	···
G031.025-00.064	31.024	-0.062	9.5	9.72	1.15	21.77	1.50	1.8	20	···	···	-0.03	0.13	Ionization Front	1
G031.028+00.926	31.028	0.927	9.9	0.93	0.11	0.87	0.10	0.8	13	···	···	0.79	0.26	···	···
G031.031-00.854	31.031	-0.853	7.2	0.78	0.12	0.83	0.12	0.8	12	···	···	-0.61	0.32	···	···
G031.041-00.782	31.041	-0.782	9.8	1.41	0.16	1.28	0.16	0.7	12	-0.36	0.15	-0.23	0.22	···	···
G031.048+00.356	31.048	0.355	16.8	5.36	0.43	4.62	0.39	0.8	14	-0.05	0.08	-0.07	0.20	HII region	3
G031.048+00.913	31.047	0.913	20.2	1.83	0.13	1.60	0.12	0.8	15	-0.78	0.08	-1.26	0.27	···	···
G031.051+00.624	31.051	0.624	51.8	12.23	0.70	11.08	0.60	0.9	17	-0.90	0.02	-1.15	0.08	···	···
G031.053-00.887	31.053	-0.887	19.5	1.81	0.13	1.61	0.12	0.8	14	-0.32	0.09	-1.34	0.19	···	···
G031.054+00.749	31.054	0.749	5.2	0.57	0.11	0.52	0.11	0.5	9	···	···	-0.25	0.63	···	···
G031.054-00.185	31.054	-0.185	47.3	23.24	1.34	26.60	1.42	1.1	19	-0.62	0.02	-0.71	0.04	···	···
G031.055+00.963	31.055	0.963	20.5	1.87	0.14	1.73	0.13	0.9	15	-0.73	0.09	-0.88	0.12	···	···
G031.058+00.093	31.053	0.089	44.2	42.26	2.47	645.96	32.31	14.8	85	···	···	···	···	HII region	3
G031.059-00.938	31.059	-0.937	4.4	0.39	0.09	0.41	0.09	0.5	9	···	···	-0.06	0.28	···	···
G031.068-00.421	31.069	-0.420	16.1	5.27	0.43	6.64	0.47	1.1	17	-0.49	0.06	-0.96	0.11	···	···
G031.069+00.050	31.065	0.046	217.0	237.50	12.84	433.82	21.72	1.8	37	···	···	···	···	HII region	3
G031.074-00.047	31.074	-0.048	5.2	5.22	1.05	15.60	1.27	1.5	17	···	···	0.16	0.29	···	···
G031.075-00.682	31.074	-0.682	12.8	1.79	0.17	1.43	0.16	0.7	12	-0.88	0.08	-1.24	0.18	···	···
G031.077+00.958	31.077	0.958	14.7	1.24	0.11	0.97	0.10	0.7	13	-0.98	0.11	-1.12	0.28	···	···
G031.078+00.170	31.077	0.170	26.2	15.68	1.03	14.94	0.96	0.9	16	···	···	1.08	0.10	···	···
G031.082-00.072	31.081	-0.074	36.7	31.53	1.90	35.37	1.97	1.1	21	-0.63	0.02	-0.82	0.07	···	···
G031.083+00.538	31.083	0.538	38.1	16.01	0.96	13.64	0.80	0.8	16	-0.53	0.02	-0.52	0.07	···	···
G031.087+00.201	31.086	0.202	4.4	2.44	0.57	10.95	0.78	1.9	18	···	···	0.10	0.44	HII region	1
G031.101+00.133	31.103	0.133	11.6	7.80	0.79	23.73	1.36	2.6	24	···	···	···	···	HII region	1
G031.102-00.642	31.103	-0.643	5.7	0.89	0.16	1.15	0.17	0.8	12	···	···	-1.79	0.72	···	···
G031.118-00.282	31.119	-0.282	7.6	2.52	0.36	10.43	0.62	2.8	24	···	···	···	···	HII region	1
G031.121+00.063	31.122	0.063	6.0	5.27	0.92	5.22	0.91	0.6	11	-0.03	0.17	-0.56	0.23	HII region	3

Continued on next page

Table B.1 – *Continued from previous page*

GLOSTAR name	ℓ	b	SNR	$S_{\rm peak}$	$\Delta S_{\rm peak}$	$S_{\rm int}$	$\Delta S_{\rm int}$	Y	Radius	Spectral index				Classification	
	(°)	(°)		(mJy beam^{-1})		(mJy)			($''$)	α	$\Delta\alpha$	α*	$\Delta\alpha$*	Type	Ref.
(1)	(2)	(3)	(4)	(5)	(6)	(7)	(8)	(9)	(10)	(11)	(12)	(13)	(14)	(15)	(16)
G031.122+00.762	31.120	0.761	18.5	1.84	0.14	3.13	0.19	1.6	21	-0.37	0.10	-1.25	0.49	···	···
G031.124-00.576	31.123	-0.576	9.0	1.84	0.23	1.41	0.22	0.6	11	-0.44	0.16	-0.83	0.16	···	···
G031.130-00.701	31.130	-0.702	4.1	0.55	0.14	0.44	0.14	0.4	7	···	···	0.00	0.33	···	···
G031.133+00.269	31.134	0.286	90.6	35.27	1.94	684.84	34.24	19.1	08	···	···	···	···	HII region	1
G031.136-00.792	31.136	-0.792	11.2	1.35	0.14	1.25	0.14	0.8	13	···	···	-0.56	0.07	···	···
G031.140+00.119	31.139	0.120	17.5	10.99	0.86	43.48	2.26	3.6	30	···	···	···	···	HII region	1
G031.140+00.196	31.140	0.196	6.9	3.10	0.48	2.47	0.47	0.6	10	-0.53	0.13	-0.43	0.26	···	···
G031.148+00.774	31.148	0.774	28.3	2.84	0.18	2.97	0.18	1.0	18	-0.07	0.09	-0.38	0.17	···	···
G031.148+00.899	31.149	0.899	4.2	0.35	0.09	0.29	0.08	0.4	7	···	···	-0.95	0.68	···	···
G031.149-00.173	31.149	-0.173	8.6	5.30	0.68	3.98	0.65	0.6	11	0.16	0.16	1.11	0.18	···	···
G031.151-00.190	31.151	-0.189	30.8	15.97	1.00	15.18	0.92	0.9	17	-0.19	0.03	-0.15	0.02	···	···
G031.154-00.506	31.144	-0.511	7.8	2.21	0.31	9.60	0.56	3.2	29	···	···	···	···	···	···
G031.155+00.733	31.155	0.732	8.9	0.94	0.12	0.90	0.11	0.8	12	···	···	-0.83	0.19	···	···
G031.156+00.231	31.156	0.231	4.0	1.53	0.39	4.47	0.44	1.2	13	···	···	0.68	0.29	···	···
G031.158+00.550	31.158	0.550	215.8	58.32	3.15	57.45	2.89	1.0	22	-0.74	0.00	-0.83	0.02	···	···
G031.160+00.045	31.163	0.044	46.2	32.41	1.88	64.59	3.30	1.9	40	···	···	0.08	0.14	HII region	2
G031.163+00.715	31.163	0.714	30.2	3.29	0.21	3.30	0.20	1.0	18	-0.43	0.06	-1.32	0.07	Radio star	8
G031.169+00.810	31.169	0.810	8.1	0.78	0.10	0.73	0.10	0.7	12	···	···	-0.25	0.35	···	···
G031.170+00.756	31.170	0.757	8.4	0.84	0.11	0.75	0.11	0.7	12	···	···	-0.84	0.38	···	···
G031.171+00.583	31.170	0.581	6.9	1.50	0.23	34.92	1.76	13.6	55	···	···	···	···	Extended/Diffuse	1
G031.190-00.610	31.190	-0.610	5.3	0.88	0.17	0.58	0.17	0.4	8	···	···	-0.64	0.37	Extended/Diffuse	1
G031.207+00.099	31.207	0.099	14.9	8.35	0.72	15.76	0.97	1.7	21	0.35	0.11	-0.02	0.09	HII region	3
G031.208+00.685	31.208	0.685	4.3	0.47	0.11	0.59	0.11	0.6	10	···	···	-0.69	0.75	···	···
G031.213-00.181	31.213	-0.181	10.7	5.69	0.61	5.92	0.61	0.9	14	···	···	0.80	0.08	PN	6
G031.217-00.303	31.217	-0.303	9.8	2.69	0.31	2.66	0.30	0.8	13	···	···	-0.58	0.40	···	···
G031.219+00.950	31.219	0.950	12.8	0.99	0.09	1.04	0.09	0.9	15	-0.70	0.12	-1.39	0.26	···	···
G031.225-00.379	31.224	-0.379	10.3	2.59	0.29	2.73	0.29	0.9	14	···	···	-0.90	0.38	···	···
G031.238-00.643	31.238	-0.643	4.2	0.74	0.18	0.54	0.18	0.3	7	···	···	-0.33	0.38	···	···
G031.242+00.844	31.242	0.844	5.9	0.55	0.10	0.38	0.10	0.4	9	-0.76	0.19	-0.40	0.93	···	···
G031.243-00.110	31.240	-0.110	1035.0	683.46	36.81	848.12	42.41	1.2	35	0.51	0.00	0.11	0.03	HII region	2
G031.250+00.092	31.250	0.096	4.7	2.19	0.49	28.19	1.49	5.1	32	···	···	···	···	···	···
G031.252+00.929	31.252	0.929	10.5	0.83	0.09	0.77	0.09	0.8	13	···	···	-1.09	0.20	···	···
G031.252-00.747	31.252	-0.747	12.6	1.55	0.15	1.60	0.15	0.9	14	···	···	-0.73	0.12	···	···
G031.257-00.343	31.257	-0.342	6.3	1.55	0.26	2.28	0.27	1.0	13	···	···	-0.87	0.44	···	···
G031.260-00.022	31.262	-0.028	10.0	7.54	0.86	95.52	4.84	10.0	53	···	···	···	···	Extended/Diffuse	1
G031.260-00.965	31.261	-0.965	10.6	1.55	0.17	1.38	0.16	0.7	13	-1.15	0.09	-1.74	0.27	···	···
G031.262+00.957	31.261	0.957	12.5	0.97	0.09	0.85	0.09	0.8	13	-0.73	0.13	-0.92	0.59	···	···
G031.270-00.643	31.270	-0.643	7.4	1.36	0.20	1.33	0.20	0.7	12	···	···	-0.49	0.22	···	···
G031.273+00.922	31.268	0.927	21.0	1.69	0.12	3.76	0.20	2.1	25	···	···	···	···	···	···
G031.274+00.490	31.277	0.479	15.0	3.17	0.27	91.80	4.59	23.7	77	···	···	···	···	HII region	1
G031.274+00.658	31.274	0.657	5.0	0.72	0.15	0.57	0.14	0.4	8	···	···	-0.14	0.83	···	···
G031.279+00.063	31.278	0.064	508.5	261.96	14.12	327.20	16.37	1.3	28	0.18	0.00	-0.18	0.02	HII region	2
G031.299+00.060	31.310	0.049	14.4	7.46	0.65	146.07	7.32	16.7	76	···	···	···	···	Ionization Front	1

Continued on next page

Table B.1 – *Continued from previous page*

GLOSTAR name	ℓ	b	SNR	$S_{\rm peak}$	$\Delta S_{\rm peak}$	$S_{\rm int}$	$\Delta S_{\rm int}$	Y	Radius	Spectral index				Classification	
	(°)	(°)		(mJy beam^{-1})		(mJy)			($''$)	α	$\Delta\alpha$	α*	$\Delta\alpha$*	Type	Ref.
(1)	(2)	(3)	(4)	(5)	(6)	(7)	(8)	(9)	(10)	(11)	(12)	(13)	(14)	(15)	(16)
G031.299-00.493	31.300	-0.493	66.0	16.67	0.93	20.93	1.08	1.2	22	-0.63	0.02	-0.84	0.04	···	···
G031.303-00.103	31.303	-0.104	5.2	2.99	0.60	7.90	0.70	1.4	16	···	···	-0.39	0.27	Ionization Front	1
G031.305+00.185	31.305	0.185	9.1	2.82	0.34	2.33	0.33	0.7	12	···	···	0.15	0.30	···	···
G031.309+00.531	31.308	0.528	10.5	1.98	0.22	14.58	0.75	5.7	37	···	···	···	···	HII region	1
G031.309-00.613	31.309	-0.612	53.4	9.82	0.56	9.22	0.50	0.9	18	-0.95	0.02	-1.27	0.03	···	···
G031.311-00.254	31.312	-0.254	5.5	1.68	0.32	3.44	0.35	1.2	14	···	···	0.11	0.38	···	···
G031.326-00.533	31.327	-0.534	21.5	5.10	0.36	7.85	0.46	1.4	20	···	···	-0.05	0.10	···	···
G031.336-00.869	31.337	-0.869	16.3	1.56	0.13	2.05	0.14	1.2	18	-0.58	0.10	-0.24	0.16	···	···
G031.340+00.383	31.340	0.384	4.3	0.95	0.22	1.68	0.23	0.8	11	···	···	-0.83	1.07	···	···
G031.340-00.883	31.340	-0.884	7.0	0.67	0.10	0.64	0.10	0.7	11	···	···	0.00	0.39	···	···
G031.342+00.823	31.342	0.823	4.1	0.40	0.10	0.35	0.10	0.4	7	···	···	-1.42	0.34	···	···
G031.348-00.951	31.349	-0.950	17.3	1.74	0.14	1.83	0.14	0.9	16	-0.40	0.12	-0.75	0.17	···	···
G031.351-00.905	31.352	-0.905	11.7	1.12	0.11	0.96	0.11	0.7	13	-0.74	0.13	-1.63	0.50	···	···
G031.356-00.888	31.356	-0.887	18.2	1.74	0.13	1.81	0.13	0.9	16	-0.38	0.12	-0.54	0.26	···	···
G031.360-00.110	31.356	-0.100	6.4	3.16	0.52	83.61	4.21	14.6	56	···	···	···	···	HII region	1
G031.360-00.840	31.360	-0.841	15.5	1.47	0.12	1.85	0.13	1.1	17	···	···	-0.84	0.25	···	···
G031.372-00.751	31.372	-0.752	222.9	25.89	1.40	25.69	1.29	1.0	23	0.17	0.02	0.03	0.02	PN	6
G031.375+00.803	31.375	0.803	5.4	0.64	0.12	0.62	0.12	0.6	10	···	···	0.27	0.33	···	···
G031.377-00.802	31.377	-0.802	6.6	0.63	0.10	0.76	0.10	0.8	12	···	···	0.04	0.63	···	···
G031.378+00.306	31.368	0.306	5.7	1.77	0.32	12.60	0.70	3.8	29	···	···	···	···	···	···
G031.378-00.947	31.378	-0.947	16.0	1.57	0.13	1.68	0.13	1.0	16	-0.74	0.09	-1.35	0.11	···	···
G031.382-00.042	31.374	-0.035	9.4	5.19	0.62	124.53	6.25	17.0	65	···	···	···	···	Ionization Front	1
G031.386+00.807	31.386	0.807	10.8	1.29	0.14	1.13	0.13	0.7	13	-0.69	0.10	-0.48	0.34	···	···
G031.388-00.383	31.388	-0.383	1231.0	395.53	21.30	414.05	20.71	1.0	27	-0.79	0.00	-1.02	0.04	···	···
G031.399+00.738	31.398	0.735	84.8	11.67	0.64	24.15	1.22	2.0	28	···	···	···	···	···	···
G031.399-00.081	31.399	-0.081	15.4	7.52	0.63	8.36	0.64	1.0	16	···	···	1.03	0.15	···	···
G031.412+00.307	31.422	0.311	2508.0	824.66	44.41	1080.17	54.01	1.3	53	···	···	···	···	HII region	2
G031.417+00.710	31.416	0.710	6.2	0.90	0.15	1.56	0.17	1.1	14	-0.67	0.18	-0.53	0.45	···	···
G031.425+00.333	31.429	0.335	4.2	1.57	0.38	5.78	0.47	1.5	15	···	···	8.23	2.32	···	···
G031.426-00.140	31.420	-0.148	30.9	14.15	0.89	67.30	3.40	4.5	49	···	···	···	···	HII region	3
G031.433+00.290	31.430	0.288	7.5	2.36	0.34	17.59	0.93	4.9	31	···	···	···	···	HII region	3
G031.439+00.605	31.439	0.605	11.2	1.36	0.14	1.35	0.14	0.8	14	-1.26	0.08	-1.27	0.36	···	···
G031.440+00.509	31.440	0.509	145.9	21.43	1.16	21.27	1.07	1.0	22	-0.35	0.01	-0.33	0.03	···	···
G031.448-00.088	31.443	-0.090	4.8	2.25	0.48	33.49	1.74	6.2	33	···	···	···	···	···	···
G031.458+00.685	31.458	0.685	8.9	1.13	0.14	1.01	0.14	0.7	12	···	···	-1.36	0.25	···	···
G031.471+00.381	31.470	0.390	10.1	2.82	0.32	12.56	0.69	3.6	34	···	···	···	···	···	···
G031.471+00.994	31.472	0.994	16.8	1.61	0.13	1.39	0.12	0.8	14	-0.50	0.08	-1.20	0.11	···	···
G031.476-00.344	31.469	-0.345	77.7	36.05	2.00	321.71	16.09	8.8	66	···	···	···	···	HII region	4
G031.482-00.408	31.482	-0.408	12.7	3.65	0.35	4.00	0.35	0.9	15	-0.85	0.10	-0.84	0.12	···	···
G031.490+00.864	31.489	0.864	20.1	1.75	0.13	2.42	0.15	1.3	20	···	···	-0.32	0.11	···	···
G031.491+00.369	31.489	0.374	32.1	9.03	0.56	53.91	2.71	5.7	56	···	···	···	···	HII region	1
G031.498-00.413	31.499	-0.413	14.1	3.74	0.33	6.12	0.41	1.4	20	-0.78	0.09	-0.88	0.14	···	···
G031.503-00.833	31.503	-0.833	4.0	0.65	0.17	0.55	0.16	0.4	7	···	···	-0.04	0.43	···	···

Continued on next page

Table B.1 – *Continued from previous page*

GLOSTAR name	ℓ	b	SNR	$S_{\rm peak}$	$\Delta S_{\rm peak}$	$S_{\rm int}$	$\Delta S_{\rm int}$	Y	Radius	Spectral index				Classification	
	(°)	(°)		(mJy beam^{-1})		(mJy)			($''$)	α	$\Delta\alpha$	α*	$\Delta\alpha$*	Type	Ref.
(1)	(2)	(3)	(4)	(5)	(6)	(7)	(8)	(9)	(10)	(11)	(12)	(13)	(14)	(15)	(16)
G031.512+00.711	31.512	0.711	7.8	0.82	0.11	0.79	0.11	0.7	12	···	···	-0.66	0.25	···	···
G031.524-00.857	31.524	-0.857	25.4	3.43	0.23	3.29	0.21	0.9	16	-0.47	0.05	-0.95	0.08	···	···
G031.541-00.106	31.547	-0.118	14.8	6.13	0.53	105.05	5.27	14.7	74	···	···	···	···	Ionization Front	1
G031.546-00.980	31.546	-0.980	4.9	0.47	0.10	0.45	0.10	0.5	9	···	···	-0.97	0.28	···	···
G031.551+00.876	31.551	0.876	7.6	0.61	0.09	0.69	0.09	0.8	13	···	···	-0.68	0.34	···	···
G031.560+00.376	31.561	0.376	49.5	13.30	0.76	12.32	0.67	0.9	18	0.03	0.03	0.03	0.04	HII region	3
G031.569+00.687	31.570	0.687	381.8	37.59	2.03	36.95	1.85	1.0	24	0.72	0.02	-0.01	0.03	···	···
G031.571+00.637	31.571	0.637	192.4	18.91	1.02	18.66	0.94	1.0	23	-0.74	0.01	-0.81	0.04	···	···
G031.575+00.974	31.575	0.975	21.3	2.07	0.15	1.97	0.14	0.9	16	-0.74	0.05	-0.93	0.26	···	···
G031.575-00.996	31.575	-0.996	4.3	0.47	0.11	0.39	0.11	0.4	7	···	···	-1.15	0.53	···	···
G031.579-00.074	31.579	-0.074	4.7	1.47	0.32	1.02	0.31	0.4	7	···	···	-0.14	0.44	···	···
G031.581+00.075	31.576	0.098	50.4	21.69	1.24	217.03	10.86	9.7	03	···	···	···	···	HII region	2
G031.581-00.347	31.580	-0.347	9.7	2.77	0.32	2.42	0.31	0.7	12	-0.66	0.11	-1.43	0.18	···	···
G031.585-00.063	31.586	-0.064	8.3	2.50	0.33	2.00	0.32	0.6	11	-0.12	0.16	-0.41	0.31	···	···
G031.590-00.433	31.592	-0.433	5.2	0.95	0.19	1.87	0.20	1.1	14	···	···	-0.23	0.74	···	···
G031.596-00.910	31.595	-0.911	23.9	2.27	0.15	2.38	0.15	1.0	17	-0.72	0.06	-1.02	0.10	···	···
G031.600-00.322	31.600	-0.321	5.0	1.70	0.35	7.52	0.51	2.1	20	···	···	···	···	···	···
G031.605-00.230	31.615	-0.239	7.0	3.71	0.56	151.85	7.61	23.4	75	···	···	···	···	Extended/Diffuse	1
G031.614-00.039	31.614	-0.039	9.2	2.74	0.33	2.87	0.33	0.8	14	-0.38	0.12	-1.20	0.15	···	···
G031.621+00.674	31.621	0.674	11.7	1.19	0.12	1.23	0.12	0.9	14	-0.33	0.15	-0.30	0.15	···	···
G031.622+00.330	31.612	0.341	50.8	14.50	0.83	611.98	30.60	40.7	13	···	···	···	···	HII region	1
G031.624-00.142	31.624	-0.143	4.5	1.46	0.33	1.36	0.33	0.5	8	···	···	-1.55	0.37	···	···
G031.626+00.705	31.626	0.705	6.5	0.64	0.10	0.71	0.10	0.8	12	-1.01	0.14	-0.44	0.35	···	···
G031.626+00.747	31.626	0.747	6.2	0.53	0.09	0.42	0.09	0.5	10	···	···	-1.49	0.36	···	···
G031.628+00.629	31.626	0.630	15.9	1.61	0.13	3.46	0.20	1.9	24	···	···	-0.44	0.34	···	···
G031.634+00.949	31.634	0.949	7.9	0.63	0.09	0.48	0.08	0.6	10	···	···	1.55	0.55	···	···
G031.636-00.717	31.636	-0.717	5.7	1.02	0.19	0.95	0.19	0.6	10	···	···	-1.70	0.28	···	···
G031.639+00.995	31.638	0.995	9.6	1.02	0.12	0.85	0.11	0.7	12	···	···	-0.87	0.19	···	···
G031.657-00.816	31.675	-0.807	4.8	0.82	0.18	16.08	0.82	7.9	43	···	···	···	···	···	···
G031.661+00.366	31.661	0.366	4.2	0.87	0.21	1.28	0.22	0.7	10	···	···	0.89	0.54	HII region	3
G031.674+00.238	31.677	0.240	8.9	3.40	0.42	16.84	0.92	3.7	30	···	···	···	···	HII region	1
G031.676+00.194	31.675	0.182	4.3	1.69	0.41	60.60	3.06	11.7	45	···	···	···	···	···	···
G031.682-00.152	31.681	-0.152	5.4	1.83	0.35	2.43	0.36	0.8	12	···	···	-0.39	0.35	PN	1
G031.684+00.678	31.684	0.679	13.2	1.48	0.14	1.13	0.13	0.7	12	-0.85	0.08	-1.52	0.22	···	···
G031.685-00.940	31.685	-0.940	7.0	0.60	0.09	0.61	0.09	0.7	12	···	···	-0.70	0.45	···	···
G031.694+00.612	31.694	0.612	20.9	2.25	0.16	2.63	0.17	1.1	17	-0.42	0.06	-0.79	0.06	···	···
G031.695-00.534	31.695	-0.534	11.7	1.77	0.18	1.62	0.17	0.8	13	···	···	-0.37	0.14	···	···
G031.701-00.972	31.701	-0.972	19.0	1.71	0.13	1.42	0.11	0.8	14	···	···	0.13	0.19	···	···
G031.704+00.274	31.704	0.274	5.1	1.62	0.33	1.56	0.33	0.5	9	-0.30	0.19	-0.54	0.29	···	···
G031.707+00.550	31.707	0.550	38.6	3.86	0.23	3.55	0.20	0.9	17	0.20	0.07	-0.17	0.12	···	···
G031.712-00.831	31.712	-0.831	5.0	0.67	0.14	0.75	0.14	0.6	10	···	···	-1.37	0.57	···	···
G031.719-00.117	31.723	-0.120	4.1	1.61	0.41	11.32	0.69	2.5	20	···	···	···	···	Extended/Diffuse	1
G031.727+00.699	31.728	0.699	57.0	6.19	0.35	14.52	0.73	2.3	29	···	···	···	···	HII region	3

Continued on next page

Table B.1 – *Continued from previous page*

GLOSTAR name	ℓ	b	SNR	$S_{\rm peak}$	$\Delta S_{\rm peak}$	$S_{\rm int}$	$\Delta S_{\rm int}$	Y	Radius	Spectral index				Classification	
	(°)	(°)		(mJy beam^{-1})		(mJy)			($''$)	α	$\Delta\alpha$	α*	$\Delta\alpha$*	Type	Ref.
(1)	(2)	(3)	(4)	(5)	(6)	(7)	(8)	(9)	(10)	(11)	(12)	(13)	(14)	(15)	(16)
G031.733-00.549	31.733	-0.547	5.3	0.76	0.15	1.15	0.15	0.9	13	···	···	-0.37	0.39	···	···
G031.734+00.748	31.734	0.748	5.5	0.52	0.10	0.44	0.10	0.5	9	···	···	0.67	0.66	···	···
G031.737-00.183	31.756	-0.207	5.7	1.97	0.36	47.56	2.40	12.1	58	···	···	···	···	HII region	1
G031.739+00.256	31.739	0.256	38.9	10.93	0.65	9.31	0.54	0.8	16	-0.78	0.02	-1.16	0.08	···	···
G031.744+00.817	31.745	0.817	4.3	0.32	0.08	0.31	0.08	0.5	8	···	···	0.93	0.73	···	···
G031.754-00.719	31.747	-0.720	25.8	3.29	0.22	8.66	0.45	2.5	30	···	···	···	···	···	···
G031.758+00.261	31.760	0.263	4.1	0.98	0.25	10.95	0.60	3.8	25	···	···	···	···	Extended/Diffuse	1
G031.772-00.440	31.772	-0.440	6.8	0.90	0.14	1.13	0.14	0.9	13	···	···	-1.94	0.43	···	···
G031.774+00.655	31.774	0.655	23.6	2.47	0.17	2.50	0.16	0.9	17	0.25	0.11	-0.17	0.10	···	···
G031.775+00.422	31.775	0.422	8.3	1.24	0.16	1.62	0.17	1.0	14	···	···	-0.41	0.19	···	···
G031.780-00.038	31.780	-0.039	7.9	3.26	0.45	4.01	0.46	0.9	14	···	···	1.14	0.37	···	···
G031.792+00.537	31.792	0.537	4.8	0.51	0.11	0.38	0.11	0.4	8	···	···	-0.60	0.44	···	···
G031.806-00.403	31.806	-0.403	4.7	0.78	0.17	0.55	0.17	0.4	7	···	···	-1.92	0.85	···	···
G031.813+00.874	31.813	0.874	28.0	2.16	0.14	2.10	0.13	0.9	16	-0.52	0.05	-0.85	0.15	···	···
G031.821+00.525	31.820	0.525	4.6	0.48	0.11	0.91	0.11	0.9	12	···	···	-0.49	0.74	PN	1
G031.824+00.675	31.823	0.675	6.8	0.65	0.10	0.58	0.10	0.6	11	···	···	0.76	0.32	···	···
G031.825-00.119	31.817	-0.118	26.3	11.43	0.75	176.50	8.84	14.3	72	···	···	···	···	HII region	1
G031.831-00.596	31.830	-0.596	11.4	1.34	0.14	1.23	0.13	0.8	13	-0.27	0.14	-0.38	0.33	···	···
G031.833+00.979	31.834	0.978	21.6	1.85	0.13	3.22	0.18	1.6	21	-0.80	0.05	-0.91	0.24	···	···
G031.842-00.962	31.843	-0.962	7.5	0.63	0.09	0.73	0.09	0.9	13	···	···	-1.19	0.65	···	···
G031.845+00.880	31.845	0.880	7.3	0.56	0.08	0.55	0.08	0.7	12	···	···	-0.88	0.35	···	···
G031.847+00.408	31.847	0.408	12.3	1.96	0.19	1.88	0.19	0.8	14	-0.42	0.10	-0.77	0.12	···	···
G031.865-00.305	31.855	-0.310	6.3	2.93	0.49	52.79	2.68	9.8	46	···	···	···	···	HII region	1
G031.881-00.258	31.882	-0.259	4.7	1.64	0.36	11.64	0.68	3.0	23	···	···	···	···	Extended/Diffuse	1
G031.886-00.205	31.887	-0.205	4.0	1.19	0.30	2.12	0.31	0.8	11	···	···	-2.26	0.39	···	···
G031.890-00.820	31.890	-0.820	4.6	0.42	0.09	0.88	0.10	1.0	13	···	···	-0.03	1.03	···	···
G031.892+00.868	31.892	0.868	11.5	1.00	0.10	0.78	0.09	0.7	12	-0.93	0.08	-1.11	0.14	···	···
G031.897+00.317	31.903	0.326	49.3	8.23	0.47	20.52	1.04	2.4	52	···	···	···	···	HII region	1
G031.907-00.309	31.908	-0.309	26.4	11.57	0.76	25.84	1.36	2.1	24	···	···	···	···	PN	1
G031.912+00.195	31.914	0.196	21.1	5.31	0.38	15.52	0.82	2.7	28	···	···	···	···	HII region	1
G031.917-00.289	31.918	-0.288	9.2	3.58	0.43	4.19	0.44	0.9	14	-0.64	0.09	-0.47	0.14	Ionization Front	1
G031.927-00.508	31.927	-0.508	4.6	0.63	0.14	0.81	0.14	0.7	10	···	···	-0.47	0.52	···	···
G031.933-00.816	31.934	-0.816	5.5	0.45	0.08	0.43	0.08	0.6	10	-1.26	0.16	-0.01	0.40	···	···
G031.944-00.513	31.944	-0.513	6.6	0.94	0.15	0.74	0.15	0.5	10	-0.96	0.13	-0.60	0.39	···	···
G031.945+00.600	31.945	0.600	7.4	0.70	0.10	0.80	0.10	0.8	13	···	···	-0.76	0.51	···	···
G031.947+00.476	31.947	0.476	64.8	6.98	0.39	6.03	0.32	0.8	18	-0.67	0.02	-1.24	0.06	···	···
G031.947-00.815	31.947	-0.815	66.4	5.29	0.30	4.81	0.25	0.9	19	-0.28	0.03	-0.91	0.09	···	···
G031.948+00.772	31.948	0.772	38.7	4.40	0.26	3.84	0.22	0.8	17	0.27	0.05	-0.33	0.05	···	···
G031.950+00.169	31.945	0.166	8.3	2.49	0.33	16.28	0.87	4.6	30	···	···	···	···	Extended/Diffuse	1
G031.954+00.306	31.955	0.306	8.5	1.41	0.18	0.96	0.17	0.5	10	-0.72	0.12	-1.12	0.29	···	···
G031.958+00.434	31.957	0.434	38.8	4.37	0.26	4.84	0.27	1.1	19	-0.54	0.04	-1.18	0.11	···	···
G031.963-00.622	31.963	-0.621	9.4	0.94	0.11	0.80	0.11	0.7	12	···	···	-0.15	0.61	···	···
G031.969-00.036	31.967	-0.035	6.4	2.03	0.34	6.56	0.46	2.0	20	···	···	···	···	···	···

Continued on next page

Table B.1 – *Continued from previous page*

GLOSTAR name	ℓ	b	SNR	$S_{\rm peak}$	$\Delta S_{\rm peak}$	$S_{\rm int}$	$\Delta S_{\rm int}$	Y	Radius	Spectral index				Classification	
	(°)	(°)		(mJy beam^{-1})		(mJy)			($''$)	α	$\Delta\alpha$	α*	$\Delta\alpha$*	Type	Ref.
(1)	(2)	(3)	(4)	(5)	(6)	(7)	(8)	(9)	(10)	(11)	(12)	(13)	(14)	(15)	(16)
G031.974-00.789	31.974	-0.789	4.2	0.35	0.09	0.34	0.09	0.4	8	···	···	-0.97	0.28	···	···
G031.976-00.117	31.976	-0.117	13.0	2.45	0.23	2.09	0.22	0.7	13	-0.11	0.14	-0.27	0.34	···	···
G031.976-00.864	31.976	-0.864	5.4	0.43	0.08	0.27	0.08	0.4	8	···	···	-0.40	0.37	···	···
G031.978+00.073	31.984	0.073	4.4	1.72	0.40	13.97	0.80	3.1	24	···	···	···	···	HII region	1
G031.985-00.878	31.984	-0.877	28.2	2.25	0.14	1.89	0.12	0.8	16	0.04	0.09	-0.21	0.20	···	···
G031.994+00.516	31.994	0.515	45.2	4.77	0.28	4.02	0.23	0.8	17	-0.15	0.04	-0.32	0.06	···	···
G032.001-00.072	32.001	-0.072	11.3	2.34	0.24	2.50	0.24	0.9	14	···	···	-0.95	0.24	···	···
G032.003+00.560	32.003	0.559	36.2	3.71	0.22	3.80	0.22	1.0	18	-0.42	0.04	-0.82	0.06	···	···
G032.008+00.354	32.008	0.354	10.0	1.31	0.15	1.30	0.15	0.8	13	···	···	-0.44	0.29	···	···
G032.010+00.000	32.010	0.000	6.5	2.12	0.35	2.09	0.34	0.7	11	···	···	-1.20	0.31	···	···
G032.014-00.653	32.014	-0.653	23.7	2.58	0.18	2.08	0.15	0.8	15	-0.54	0.05	-1.07	0.13	···	···
G032.015-00.731	32.015	-0.731	4.8	0.47	0.10	0.32	0.10	0.4	7	···	···	-1.00	0.49	···	···
G032.018+00.824	32.020	0.823	4.3	0.42	0.10	2.31	0.15	2.2	19	···	···	···	···	Extended/Diffuse	1
G032.030+00.049	32.029	0.050	80.4	30.75	1.70	29.10	1.50	0.9	20	0.20	0.03	0.00	0.05	HII region	2
G032.034+00.938	32.034	0.938	15.2	1.38	0.12	1.06	0.11	0.7	13	-0.21	0.11	-0.13	0.08	···	···
G032.038-00.494	32.036	-0.499	15.9	3.11	0.26	6.13	0.36	1.8	23	···	···	···	···	···	···
G032.040-00.638	32.039	-0.638	9.5	1.02	0.12	0.82	0.12	0.6	12	···	···	-0.45	0.43	···	···
G032.042-00.324	32.042	-0.325	5.9	1.72	0.31	1.08	0.30	0.4	8	-0.40	0.16	0.37	0.29	···	···
G032.044+00.059†	32.044	0.059	26.0	1.33	0.05	1.21	0.08	0.9	···	···	···	···	···	···	···
G032.051+00.808	32.051	0.808	22.3	2.25	0.16	2.11	0.15	0.9	16	-0.54	0.05	-0.83	0.20	···	···
G032.051-00.091	32.051	-0.091	9.8	2.12	0.24	2.27	0.24	0.9	14	-0.34	0.15	-0.70	0.23	HII region	1
G032.057-00.342	32.057	-0.342	6.5	1.77	0.29	1.43	0.28	0.6	10	-0.58	0.13	-2.06	0.38	···	···
G032.060+00.444	32.060	0.444	4.0	0.41	0.11	0.82	0.11	0.8	11	···	···	-1.20	0.80	···	···
G032.060+00.510	32.061	0.510	11.8	1.22	0.12	0.88	0.11	0.6	12	-0.61	0.10	-1.12	0.36	···	···
G032.063+00.078	32.055	0.078	39.4	13.80	0.82	181.14	9.06	12.5	55	···	···	···	···	HII region	1
G032.067+00.362	32.067	0.362	98.6	13.12	0.72	11.10	0.57	0.8	19	-0.52	0.01	-0.78	0.05	···	···
G032.069-00.090	32.069	-0.090	13.6	2.97	0.27	2.93	0.26	0.9	14	···	···	-0.41	0.11	HII region	3
G032.074+00.661	32.074	0.661	46.5	5.01	0.29	4.55	0.25	0.9	18	-0.18	0.04	-0.44	0.07	···	···
G032.074+00.771	32.073	0.771	6.9	0.77	0.12	0.50	0.11	0.5	9	-0.53	0.15	-0.43	0.31	···	···
G032.074-00.818	32.071	-0.819	5.9	0.48	0.08	0.63	0.09	0.8	13	···	···	-0.32	0.33	···	···
G032.076+00.683	32.076	0.683	12.7	1.47	0.14	1.17	0.13	0.7	13	0.01	0.15	-0.23	0.28	···	···
G032.081-00.659	32.081	-0.659	26.1	2.61	0.17	1.93	0.14	0.7	14	-0.02	0.07	0.15	0.08	···	···
G032.084-00.727	32.084	-0.727	7.3	0.68	0.10	0.70	0.10	0.7	12	···	···	0.12	0.40	···	···
G032.103+00.967	32.103	0.967	21.7	2.69	0.19	2.36	0.17	0.8	15	-0.46	0.05	-0.70	0.14	···	···
G032.108-00.870	32.109	-0.868	5.2	0.41	0.08	1.08	0.10	1.4	16	···	···	-0.12	1.63	···	···
G032.113-00.641	32.113	-0.640	13.4	1.52	0.14	1.53	0.14	0.9	15	-0.17	0.11	-0.70	0.22	···	···
G032.113-00.942	32.112	-0.942	21.9	1.64	0.12	1.30	0.10	0.7	14	-0.46	0.07	-0.79	0.27	···	···
G032.116-00.723	32.116	-0.723	5.0	0.45	0.09	0.42	0.09	0.5	9	···	···	-2.30	0.32	···	···
G032.117+00.090	32.105	0.071	19.7	6.99	0.52	139.07	6.96	18.0	85	···	···	···	···	HII region	3
G032.124-00.898	32.124	-0.898	14.7	1.19	0.10	0.83	0.09	0.6	12	···	···	-0.54	0.26	···	···
G032.128-00.623	32.128	-0.623	7.2	0.88	0.13	0.96	0.13	0.8	12	···	···	-0.36	0.13	···	···
G032.130-00.094†	32.130	-0.094	5.0	0.70	0.13	2.20	0.52	3.1	···	···	···	···	···	···	···
G032.134+00.704	32.134	0.704	6.1	0.65	0.11	0.50	0.11	0.5	9	···	···	0.66	0.23	···	···

Continued on next page

Table B.1 – *Continued from previous page*

GLOSTAR name	ℓ	b	SNR	$S_{\rm peak}$	$\Delta S_{\rm peak}$	$S_{\rm int}$	$\Delta S_{\rm int}$	Y	Radius	Spectral index				Classification	
	(°)	(°)		(mJy beam^{-1})		(mJy)			($''$)	α	$\Delta\alpha$	α*	$\Delta\alpha$*	Type	Ref.
(1)	(2)	(3)	(4)	(5)	(6)	(7)	(8)	(9)	(10)	(11)	(12)	(13)	(14)	(15)	(16)
G032.138-00.930	32.135	-0.930	28.2	2.19	0.14	3.31	0.18	1.4	21	···	···	-1.00	0.16	···	···
G032.143+00.669	32.143	0.668	14.9	1.42	0.12	1.43	0.12	0.9	15	-0.73	0.08	-1.53	0.22	···	···
G032.144-00.833	32.144	-0.833	7.2	0.57	0.08	0.45	0.08	0.6	10	-0.80	0.13	-0.67	0.51	···	···
G032.144-00.915	32.144	-0.915	8.3	0.66	0.09	0.50	0.08	0.6	11	-0.52	0.15	-0.88	0.44	···	···
G032.145-00.352	32.143	-0.353	7.9	1.93	0.26	2.80	0.28	1.1	15	-0.72	0.12	-1.01	0.26	···	···
G032.147+00.024	32.147	0.024	9.6	3.44	0.40	2.51	0.38	0.6	11	···	···	-0.07	0.17	···	···
G032.149+00.645	32.149	0.646	10.7	1.00	0.11	1.42	0.12	1.2	17	···	···	0.02	0.39	···	···
G032.151+00.133	32.158	0.135	1346.0	495.83	26.70	739.33	36.97	1.5	54	···	···	···	···	HII region	2
G032.154+00.417	32.154	0.418	12.3	1.69	0.16	1.25	0.15	0.6	12	-0.04	0.14	-0.30	0.25	···	···
G032.160+00.662	32.159	0.661	6.8	0.64	0.10	0.62	0.10	0.7	12	···	···	-1.62	0.26	···	···
G032.175+00.629	32.175	0.627	17.4	1.69	0.13	1.91	0.14	1.0	19	-0.43	0.09	-1.12	0.14	···	···
G032.181+00.197	32.180	0.197	5.2	1.41	0.28	1.94	0.29	0.8	11	-0.72	0.18	0.52	0.24	···	···
G032.191+00.100	32.191	0.100	5.6	1.97	0.37	2.56	0.38	0.8	12	···	···	0.30	0.63	···	···
G032.192+00.605	32.193	0.605	7.9	0.84	0.12	0.66	0.11	0.6	11	···	···	-1.23	0.26	···	···
G032.204-00.395	32.204	-0.395	25.5	4.50	0.30	3.71	0.26	0.8	15	0.15	0.10	-0.08	0.08	PN	1
G032.228-00.035	32.229	-0.035	4.1	1.28	0.32	1.91	0.33	0.6	10	···	···	0.07	0.52	···	···
G032.228-00.172	32.220	-0.204	13.5	3.82	0.35	148.39	7.42	32.2	10	···	···	···	···	Extended/Diffuse	1
G032.232+00.540	32.231	0.540	43.9	5.81	0.34	4.90	0.28	0.8	17	-0.23	0.04	-0.40	0.05	···	···
G032.235+00.945	32.235	0.945	7.6	0.83	0.12	0.60	0.11	0.5	10	-1.06	0.12	-1.26	0.33	···	···
G032.240-00.959	32.240	-0.959	10.2	0.79	0.09	0.53	0.08	0.5	11	···	···	-0.56	0.46	···	···
G032.272-00.226	32.268	-0.226	1194.0	305.87	16.47	363.91	18.20	1.2	36	···	···	0.00	0.02	HII region	2
G032.274-00.035	32.274	-0.036	21.1	6.62	0.47	5.24	0.41	0.7	14	-0.77	0.04	-0.29	0.07	···	···
G032.278+00.342	32.279	0.342	4.5	0.68	0.16	0.55	0.16	0.4	8	···	···	-0.79	0.64	···	···
G032.281-00.475	32.280	-0.475	5.1	0.79	0.16	1.26	0.17	0.9	12	···	···	-1.05	0.28	···	···
G032.284-00.743	32.284	-0.743	9.4	0.96	0.11	0.98	0.11	0.8	13	···	···	0.49	0.27	···	···
G032.285-00.278	32.285	-0.278	10.7	2.30	0.25	1.91	0.24	0.7	12	···	···	0.57	0.32	···	···
G032.290+00.668	32.289	0.668	9.6	1.03	0.12	0.96	0.12	0.7	13	-0.57	0.13	-0.80	0.42	···	···
G032.290+00.722	32.290	0.722	4.8	0.47	0.10	0.43	0.10	0.5	9	···	···	-0.11	0.82	···	···
G032.294-00.042	32.294	-0.043	5.8	1.77	0.32	1.67	0.31	0.6	10	-0.92	0.14	-1.66	0.48	···	···
G032.303+00.557	32.304	0.557	17.1	2.22	0.18	1.66	0.15	0.7	13	-0.37	0.08	-0.57	0.11	···	···
G032.305+00.602	32.311	0.603	82.7	10.25	0.57	16.08	0.81	1.6	26	···	···	···	···	···	···
G032.308+00.153	32.307	0.154	144.2	35.83	1.95	32.01	1.62	0.9	22	0.59	0.02	0.19	0.02	PN	6
G032.310-00.906	32.310	-0.906	9.1	0.70	0.09	0.71	0.08	0.8	13	-0.37	0.15	-0.74	0.42	···	···
G032.311+00.991	32.311	0.991	6.1	1.02	0.18	0.90	0.17	0.6	10	···	···	0.21	0.46	···	···
G032.330-00.464	32.330	-0.464	4.3	0.64	0.16	0.48	0.15	0.3	7	···	···	-0.87	0.35	···	···
G032.331+00.901	32.332	0.901	5.7	0.65	0.12	0.44	0.12	0.4	8	···	···	-0.03	0.15	···	···
G032.345-00.926	32.346	-0.926	31.0	2.39	0.15	2.33	0.14	0.9	18	-0.60	0.04	-1.02	0.14	···	···
G032.353-00.950	32.352	-0.950	10.4	0.82	0.09	0.68	0.09	0.7	12	-0.76	0.10	-0.74	0.37	···	···
G032.354+00.272	32.360	0.278	8.7	1.52	0.19	10.16	0.54	5.0	35	···	···	···	···	···	···
G032.360-00.083	32.360	-0.083	5.2	1.06	0.21	0.72	0.21	0.4	8	···	···	0.18	0.26	···	···
G032.364+00.933	32.365	0.932	1335.0	146.85	7.91	237.63	11.88	1.6	40	···	···	-0.19	0.04	···	···
G032.367-00.839	32.367	-0.839	4.2	0.31	0.08	0.36	0.08	0.5	9	···	···	1.07	1.27	···	···
G032.373-00.788	32.373	-0.787	30.6	2.41	0.15	2.10	0.13	0.8	16	-0.33	0.06	-0.51	0.14	···	···

Continued on next page

Table B.1 – *Continued from previous page*

GLOSTAR name	ℓ	b	SNR	$S_{\rm peak}$	$\Delta S_{\rm peak}$	$S_{\rm int}$	$\Delta S_{\rm int}$	Y	Radius	Spectral index				Classification	
	(°)	(°)		(mJy beam^{-1})		(mJy)			($''$)	α	$\Delta\alpha$	α*	$\Delta\alpha$*	Type	Ref.
(1)	(2)	(3)	(4)	(5)	(6)	(7)	(8)	(9)	(10)	(11)	(12)	(13)	(14)	(15)	(16)
G032.378-00.555	32.378	-0.555	29.9	3.22	0.20	2.64	0.17	0.8	15	···	···	-0.10	0.10	···	···
G032.379+00.610	32.379	0.610	4.2	0.55	0.13	3.18	0.21	2.2	19	···	···	···	···	Extended/Diffuse	1
G032.382-00.631	32.382	-0.632	22.4	2.32	0.16	2.03	0.15	0.8	15	-0.29	0.11	-0.83	0.11	···	···
G032.383-00.487	32.382	-0.487	181.7	20.90	1.13	18.35	0.92	0.9	21	···	···	0.59	0.05	···	···
G032.384-00.340	32.386	-0.339	24.4	5.23	0.35	6.80	0.40	1.2	22	···	···	0.08	0.09	···	···
G032.388+00.574	32.388	0.574	10.0	1.35	0.15	1.37	0.15	0.8	14	-0.74	0.10	-1.47	0.39	···	···
G032.388-00.374	32.362	-0.362	6.4	1.44	0.24	30.50	1.54	11.7	53	···	···	···	···	···	···
G032.389-00.403	32.389	-0.403	433.9	98.67	5.32	90.08	4.51	0.9	23	-0.92	0.00	-1.15	0.02	···	···
G032.390-00.542	32.389	-0.543	12.1	1.28	0.13	1.30	0.12	0.9	14	···	···	-0.43	0.33	PN	1
G032.402-00.226	32.402	-0.226	27.2	4.67	0.30	4.20	0.27	0.8	16	-0.35	0.06	-0.44	0.16	···	···
G032.403-00.326	32.405	-0.327	4.9	1.06	0.22	9.04	0.50	3.8	25	···	···	···	···	Extended/Diffuse	1
G032.408+00.890	32.409	0.890	4.6	0.47	0.11	1.29	0.12	1.3	14	···	···	0.16	0.55	···	···
G032.410+00.383	32.410	0.383	4.8	0.77	0.17	0.57	0.16	0.4	8	···	···	-1.45	0.92	···	···
G032.435-00.834	32.435	-0.834	4.6	0.35	0.08	0.49	0.08	0.7	11	···	···	-0.22	0.45	···	···
G032.437-00.956	32.436	-0.957	4.3	0.34	0.08	0.33	0.08	0.5	8	···	···	0.37	0.99	···	···
G032.443+00.544	32.443	0.545	36.3	5.01	0.30	4.61	0.27	0.9	17	-0.74	0.03	-1.29	0.11	···	···
G032.447+00.166	32.447	0.166	13.8	4.48	0.40	3.89	0.38	0.8	14	-0.03	0.10	-0.41	0.08	···	···
G032.451-00.092	32.451	-0.092	6.1	1.52	0.26	3.73	0.31	1.5	17	···	···	-0.93	0.65	HII region	1
G032.453+00.368	32.454	0.368	8.9	1.36	0.17	0.96	0.16	0.6	11	-0.57	0.12	-1.28	0.33	···	···
G032.460+00.158	32.460	0.158	4.9	1.55	0.33	3.03	0.35	1.0	13	···	···	-0.86	0.40	···	···
G032.460+00.386	32.460	0.386	4.3	0.67	0.16	0.73	0.16	0.5	9	···	···	0.15	0.84	HII region	1
G032.461-00.696	32.461	-0.696	9.6	0.86	0.10	0.88	0.10	0.8	13	···	···	-0.86	0.21	···	···
G032.464+00.182	32.464	0.182	5.6	1.58	0.29	2.27	0.30	0.9	12	···	···	-0.89	0.25	···	···
G032.464-00.875	32.464	-0.875	1011.0	76.50	4.12	71.34	3.57	0.9	26	-0.04	0.00	-0.14	0.02	···	···
G032.468+00.281	32.468	0.281	11.8	1.78	0.18	1.36	0.17	0.6	12	0.02	0.16	-0.10	0.22	···	···
G032.472+00.203	32.469	0.199	545.8	132.84	7.16	155.88	7.80	1.2	39	···	···	-0.23	0.44	HII region	3
G032.479-00.631	32.479	-0.631	8.1	0.80	0.11	0.66	0.10	0.6	11	···	···	-0.47	0.64	···	···
G032.482+00.783	32.484	0.786	43.3	4.23	0.25	4.46	0.24	1.0	22	···	···	-0.37	0.50	···	···
G032.483-00.124	32.481	-0.123	111.5	29.99	1.64	31.59	1.60	1.0	26	0.24	0.02	-0.19	0.03	···	···
G032.494-00.348	32.491	-0.349	4.0	0.96	0.24	9.91	0.55	3.5	24	···	···	···	···	Extended/Diffuse	1
G032.498+00.161	32.498	0.161	29.6	7.49	0.48	6.41	0.41	0.8	16	0.21	0.07	0.21	0.19	PN	1
G032.503+00.430	32.503	0.430	8.3	1.28	0.17	0.88	0.16	0.5	10	···	···	-1.32	0.38	···	···
G032.504-00.701	32.504	-0.701	60.9	5.39	0.30	5.25	0.28	1.0	19	-0.37	0.03	-0.25	0.08	···	···
G032.506-00.055	32.507	-0.054	4.9	1.49	0.31	5.10	0.40	1.7	17	···	···	-0.22	0.20	···	···
G032.508+00.086	32.488	0.094	6.4	1.36	0.22	24.37	1.24	10.2	46	···	···	···	···	Extended/Diffuse	1
G032.510+00.242	32.511	0.242	9.7	1.68	0.19	1.23	0.18	0.6	11	···	···	0.34	0.30	···	···
G032.510-00.726	32.510	-0.726	6.1	0.52	0.09	0.55	0.09	0.7	11	···	···	0.47	0.75	···	···
G032.528-00.043	32.527	-0.043	11.2	3.76	0.39	7.06	0.49	1.6	21	-0.24	0.09	-0.87	0.22	···	···
G032.529-00.592	32.530	-0.592	17.2	1.75	0.14	2.10	0.15	1.1	18	···	···	-0.62	0.10	···	···
G032.545+00.930	32.545	0.930	16.1	1.57	0.13	1.42	0.12	0.8	14	-0.26	0.11	-0.19	0.28	···	···
G032.546-00.033	32.546	-0.034	7.6	2.65	0.38	2.68	0.37	0.7	12	···	···	-0.12	0.11	···	···
G032.549-00.295	32.549	-0.295	14.6	4.52	0.39	4.18	0.37	0.8	14	0.11	0.10	-0.11	0.09	···	···
G032.549-00.474	32.548	-0.474	589.4	67.81	3.65	60.80	3.04	0.9	23	0.40	0.01	0.04	0.02	PN	6

Continued on next page

Table B.1 – *Continued from previous page*

GLOSTAR name	ℓ	b	SNR	$S_{\rm peak}$	$\Delta S_{\rm peak}$	$S_{\rm int}$	$\Delta S_{\rm int}$	Y	Radius	Spectral index				Classification	
	(°)	(°)		(mJy beam^{-1})		(mJy)			($''$)	α	$\Delta\alpha$	α*	$\Delta\alpha$*	Type	Ref.
(1)	(2)	(3)	(4)	(5)	(6)	(7)	(8)	(9)	(10)	(11)	(12)	(13)	(14)	(15)	(16)
G032.552+00.821	32.552	0.821	20.4	1.98	0.14	2.10	0.14	1.0	16	-0.37	0.09	-0.65	0.20	···	···
G032.553+00.990	32.553	0.989	4.8	0.56	0.12	0.37	0.12	0.4	7	···	···	0.13	0.57	···	···
G032.557-00.124	32.557	-0.124	25.2	7.45	0.50	6.13	0.43	0.8	15	-0.28	0.05	-0.83	0.09	···	···
G032.569+00.856	32.570	0.858	11.5	1.14	0.12	1.27	0.12	0.9	16	-0.60	0.12	-0.97	0.36	···	···
G032.576+00.965	32.577	0.965	9.7	0.97	0.11	0.72	0.11	0.6	11	-0.55	0.12	-0.64	0.51	···	···
G032.581-00.347	32.591	-0.335	24.0	5.72	0.39	196.13	9.81	31.3	98	···	···	···	···	HII region	1
G032.590+00.010	32.588	0.002	53.7	13.14	0.75	227.63	11.38	16.9	80	···	···	···	···	HII region	1
G032.590-00.447	32.590	-0.447	34.7	4.04	0.25	3.53	0.21	0.8	17	···	···	-0.12	0.13	···	···
G032.591+00.876	32.591	0.877	24.9	2.48	0.17	2.30	0.15	0.9	16	-0.27	0.08	-0.85	0.17	···	···
G032.592-00.417	32.592	-0.417	29.7	3.90	0.25	3.47	0.22	0.8	17	-0.42	0.05	-0.53	0.07	···	···
G032.594+00.455	32.593	0.455	31.5	3.47	0.22	2.90	0.18	0.8	16	-0.39	0.05	-1.10	0.19	···	···
G032.599+00.826	32.600	0.827	29.7	3.18	0.20	2.62	0.17	0.8	15	-0.12	0.08	-0.24	0.05	···	···
G032.607+00.043	32.607	0.044	4.2	0.94	0.23	1.51	0.23	0.7	11	···	···	-1.14	0.25	···	···
G032.613+00.797	32.613	0.797	43.9	4.85	0.28	4.45	0.25	0.9	18	0.13	0.08	-0.23	0.07	PN	6
G032.623+00.535	32.623	0.534	5.1	0.60	0.12	0.47	0.12	0.4	8	···	···	0.54	0.47	···	···
G032.636-00.970	32.636	-0.970	4.3	0.33	0.08	0.23	0.08	0.3	7	···	···	0.91	0.67	···	···
G032.644+00.263	32.644	0.262	8.5	1.79	0.23	1.18	0.22	0.5	10	···	···	-0.33	0.71	···	···
G032.654-00.660	32.654	-0.660	6.4	0.54	0.09	0.59	0.09	0.7	11	···	···	-0.80	1.07	···	···
G032.661-00.417	32.662	-0.418	8.4	1.00	0.13	1.08	0.13	0.8	13	-0.97	0.12	-1.43	0.53	···	···
G032.663-00.778	32.662	-0.777	5.3	0.38	0.07	0.36	0.07	0.6	10	···	···	-1.36	0.23	···	···
G032.664-00.749	32.664	-0.750	38.8	2.90	0.17	2.81	0.16	0.9	18	-0.07	0.06	-0.78	0.16	···	···
G032.667+00.236	32.667	0.236	53.8	13.47	0.77	13.20	0.71	1.0	20	0.34	0.06	0.09	0.06	···	···
G032.674-00.569	32.675	-0.569	6.7	0.62	0.10	0.60	0.10	0.7	11	···	···	-0.96	0.34	···	···
G032.680+00.949	32.692	0.951	9.1	0.79	0.10	2.93	0.17	2.9	29	···	···	···	···	···	···
G032.680-00.954	32.680	-0.954	31.0	2.27	0.14	1.91	0.12	0.8	16	-0.53	0.04	-1.07	0.10	···	···
G032.687+00.083	32.686	0.083	15.7	4.24	0.35	3.22	0.31	0.7	13	-0.55	0.07	-0.66	0.29	···	···
G032.692+00.215	32.691	0.214	4.3	1.19	0.29	2.96	0.32	1.1	13	···	···	0.23	0.46	···	···
G032.692+00.831	32.692	0.831	6.1	0.53	0.09	0.54	0.09	0.7	11	···	···	···	···	···	···
G032.701+00.184	32.701	0.184	33.2	9.89	0.61	9.86	0.58	1.0	18	-0.10	0.05	0.21	0.17	···	···
G032.701-00.785	32.702	-0.785	7.3	0.51	0.08	0.62	0.08	0.9	13	···	···	-0.28	0.29	···	···
G032.711-00.994	32.711	-0.994	7.0	0.75	0.11	0.52	0.11	0.5	9	-0.72	0.13	-0.37	0.27	···	···
G032.716-00.313	32.715	-0.313	15.5	2.81	0.24	3.18	0.24	1.0	17	-0.71	0.07	-1.24	0.09	···	···
G032.720+00.813	32.720	0.813	5.5	0.47	0.09	0.33	0.09	0.4	8	···	···	-0.42	0.61	···	···
G032.720-00.648	32.720	-0.648	46.4	3.71	0.21	3.57	0.20	0.9	18	-0.54	0.03	-0.65	0.11	···	···
G032.733+00.208	32.732	0.210	38.8	15.86	0.95	53.66	2.71	3.3	32	···	···	···	···	HII region	3
G032.738+00.803	32.739	0.803	6.3	0.54	0.09	0.54	0.09	0.7	11	···	···	-0.68	0.78	···	···
G032.740+00.184	32.743	0.184	4.2	1.89	0.46	6.77	0.56	1.5	15	···	···	1.28	0.78	···	···
G032.740+00.194	32.740	0.195	16.3	7.16	0.58	6.44	0.54	0.8	15	0.28	0.14	0.48	0.16	HII region	2
G032.740+00.835	32.740	0.835	45.6	3.90	0.23	3.39	0.19	0.8	17	-0.68	0.03	-0.61	0.11	···	···
G032.742-00.865	32.743	-0.864	7.8	0.55	0.08	0.45	0.07	0.6	11	···	···	-0.10	0.63	···	···
G032.745+00.770	32.758	0.765	531.3	47.43	2.56	123.81	6.19	2.6	51	···	···	···	···	···	···
G032.755-00.930	32.755	-0.930	10.1	0.78	0.09	0.69	0.08	0.7	13	···	···	-0.95	0.32	···	···
G032.756-00.590	32.756	-0.589	11.4	0.90	0.09	1.52	0.11	1.4	18	···	···	-0.24	0.31	···	···

Continued on next page

Table B.1 – *Continued from previous page*

GLOSTAR name	ℓ	b	SNR	$S_{\rm peak}$	$\Delta S_{\rm peak}$	$S_{\rm int}$	$\Delta S_{\rm int}$	Y	Radius	Spectral index				Classification	
	(°)	(°)		(mJy beam^{-1})		(mJy)			($''$)	α	$\Delta\alpha$	α*	$\Delta\alpha$*	Type	Ref.
(1)	(2)	(3)	(4)	(5)	(6)	(7)	(8)	(9)	(10)	(11)	(12)	(13)	(14)	(15)	(16)
G032.760-00.731	32.760	-0.731	12.4	0.89	0.09	0.64	0.08	0.6	12	-0.68	0.10	-1.47	0.41	···	···
G032.763+00.092	32.763	0.092	88.3	30.86	1.70	26.60	1.38	0.9	19	0.64	0.04	0.72	0.07	Pulsar	5
G032.763-00.782	32.764	-0.782	9.7	0.68	0.08	0.74	0.08	0.9	14	···	···	0.37	0.40	···	···
G032.767+00.144	32.764	0.140	4.5	2.35	0.54	23.83	1.30	4.0	26	···	···	···	···	···	···
G032.775-00.689	32.775	-0.689	36.2	2.68	0.16	2.63	0.15	0.9	18	-1.43	0.02	-1.63	0.07	···	···
G032.783+00.731	32.784	0.731	13.3	1.36	0.13	1.30	0.12	0.8	15	···	···	0.47	0.38	···	···
G032.794+00.206	32.795	0.209	44.9	22.93	1.34	35.93	1.87	1.5	26	···	···	0.24	0.21	HII region	3
G032.798+00.191	32.803	0.186	5705.0	2960.80	159.44	3714.59	185.73	1.3	74	···	···	0.49	0.08	HII region	2
G032.802-00.842	32.803	-0.843	39.5	2.76	0.16	2.63	0.15	0.9	19	0.05	0.06	-0.05	0.09	···	···
G032.804+00.947	32.804	0.947	4.2	0.36	0.09	0.22	0.09	0.3	6	···	···	1.56	0.31	···	···
G032.808-00.316	32.808	-0.316	90.6	18.12	1.00	17.31	0.89	0.9	20	0.06	0.02	-0.11	0.05	PN	6
G032.810-00.286	32.810	-0.286	16.5	3.52	0.29	2.77	0.25	0.7	13	-0.48	0.07	-0.27	0.14	···	···
G032.812+00.639	32.812	0.639	20.2	2.63	0.19	2.38	0.18	0.8	16	···	···	0.03	0.20	···	···
G032.815-00.999	32.815	-0.998	5.0	0.55	0.12	1.17	0.13	1.1	14	···	···	-0.19	0.64	···	···
G032.820+00.703	32.819	0.704	5.8	0.65	0.12	0.63	0.12	0.6	10	···	···	0.10	0.42	···	···
G032.820-00.832	32.821	-0.832	5.7	0.40	0.07	0.45	0.07	0.7	11	-0.87	0.18	-1.08	0.53	···	···
G032.824+00.392	32.824	0.391	4.0	0.87	0.22	1.30	0.23	0.6	9	···	···	0.99	0.67	···	···
G032.834-00.599	32.834	-0.599	140.3	11.37	0.62	10.83	0.55	0.9	21	-0.64	0.01	-0.77	0.04	···	···
G032.835-00.730	32.836	-0.732	628.8	47.47	2.56	64.55	3.23	1.4	29	-0.65	0.00	-0.74	0.14	···	···
G032.836+00.669	32.836	0.669	16.4	1.96	0.16	1.53	0.14	0.7	13	-0.25	0.13	-0.62	0.31	···	···
G032.838-00.035	32.838	-0.035	11.6	5.40	0.55	3.55	0.50	0.6	11	-0.24	0.09	-0.13	0.07	···	···
G032.840-00.654	32.840	-0.653	4.0	0.31	0.08	0.43	0.08	0.6	9	···	···	···	···	···	···
G032.849+00.526	32.849	0.527	13.6	1.76	0.16	1.61	0.15	0.8	14	-0.34	0.15	-0.50	0.27	···	···
G032.858+00.624	32.858	0.624	7.2	0.94	0.14	0.88	0.14	0.7	11	···	···	-0.85	0.34	···	···
G032.858-00.940	32.857	-0.940	4.2	0.31	0.08	0.41	0.08	0.6	9	···	···	-0.42	0.50	···	···
G032.859+00.281	32.860	0.281	22.9	6.93	0.48	8.83	0.54	1.2	19	0.05	0.09	0.41	0.20	···	···
G032.859-00.599	32.859	-0.598	5.4	0.47	0.09	0.48	0.09	0.6	10	···	···	-0.17	0.38	···	···
G032.878+00.404	32.878	0.404	99.1	16.66	0.91	14.19	0.73	0.8	20	-0.40	0.02	-0.65	0.01	···	···
G032.883+00.938	32.884	0.939	63.8	5.52	0.31	5.03	0.27	0.9	18	-0.50	0.02	-1.00	0.10	···	···
G032.885-00.431	32.876	-0.421	36.2	6.74	0.41	174.96	8.75	24.9	97	···	···	···	···	HII region	1
G032.887+00.447	32.887	0.447	11.4	1.46	0.15	1.16	0.14	0.7	12	···	···	0.29	0.37	···	···
G032.894-00.703	32.896	-0.704	4.4	0.35	0.08	0.80	0.09	1.0	13	···	···	6.92	2.63	···	···
G032.904-00.962	32.904	-0.962	16.2	1.25	0.10	1.21	0.10	0.9	15	-0.80	0.07	-1.28	0.21	···	···
G032.906-00.912	32.903	-0.914	64.6	5.13	0.29	6.36	0.33	1.2	25	···	···	-0.91	0.05	···	···
G032.913+00.211	32.914	0.209	5.2	1.86	0.37	8.45	0.56	2.3	19	···	···	···	···	HII region	1
G032.927-00.645	32.927	-0.646	4.5	0.41	0.10	0.91	0.10	1.0	13	···	···	-1.09	0.88	···	···
G032.928+00.606	32.928	0.612	2078.0	308.50	16.61	381.42	19.07	1.2	61	···	···	0.03	0.02	HII region	2
G032.931-00.927	32.930	-0.927	16.6	1.30	0.11	1.10	0.10	0.8	14	-0.48	0.09	-0.57	0.29	···	···
G032.939-00.441	32.942	-0.439	7.4	1.84	0.27	3.86	0.31	1.5	19	···	···	···	···	···	···
G032.940-00.747	32.939	-0.748	71.2	5.55	0.31	4.86	0.26	0.9	18	0.02	0.04	-0.14	0.08	···	···
G032.947-00.376†	32.947	-0.376	7.0	0.71	0.10	0.79	0.18	1.1	···	···	···	0.23	.84	HII region	3
G032.951-00.501	32.947	-0.508	4.1	0.88	0.22	35.14	1.77	11.8	48	···	···	···	···	Extended/Diffuse	1
G032.965-00.328	32.981	-0.338	22.5	6.10	0.43	231.05	11.56	34.6	03	···	···	···	···	HII region	1

Continued on next page

Table B.1 – *Continued from previous page*

GLOSTAR name	ℓ	b	SNR	$S_{\rm peak}$	$\Delta S_{\rm peak}$	$S_{\rm int}$	$\Delta S_{\rm int}$	Y	Radius	Spectral index				Classification	
	(°)	(°)		(mJy beam^{-1})		(mJy)			($''$)	α	$\Delta\alpha$	α*	$\Delta\alpha$*	Type	Ref.
(1)	(2)	(3)	(4)	(5)	(6)	(7)	(8)	(9)	(10)	(11)	(12)	(13)	(14)	(15)	(16)
G032.969-00.468	32.972	-0.465	372.5	87.03	4.69	87.17	4.36	1.0	31	···	···	-0.25	0.03	···	···
G032.975+00.238	32.975	0.237	18.5	4.21	0.32	3.55	0.29	0.8	14	···	···	-0.44	0.23	···	···
G032.975-00.264	32.975	-0.264	4.5	1.24	0.29	0.67	0.28	0.3	6	···	···	-0.09	1.10	···	···
G032.986-00.868	32.986	-0.868	4.1	0.29	0.07	0.43	0.07	0.7	10	···	···	···	···	···	···
G032.990-00.548	32.983	-0.547	40.0	9.25	0.55	83.74	4.19	8.7	70	···	···	···	···	HII region	1
G032.991+00.039	32.991	0.040	259.6	116.64	6.30	202.62	10.14	1.7	31	···	···	-0.09	0.03	HII region	3
G033.003-00.007	33.002	-0.014	9.7	4.47	0.52	30.39	1.59	5.3	37	···	···	···	···	Ionization Front	1
G033.009-00.592	33.009	-0.592	22.7	4.32	0.30	3.85	0.27	0.8	15	-0.43	0.05	-0.56	0.08	···	···
G033.014+00.447	33.014	0.447	5.0	0.58	0.12	0.98	0.12	0.9	12	···	···	0.47	0.46	···	···
G033.015+00.292	33.005	0.290	13.6	2.44	0.22	5.65	0.33	2.0	28	···	···	···	···	···	···
G033.022+00.278	33.023	0.279	9.9	1.79	0.21	1.43	0.19	0.7	12	···	···	-0.09	0.34	PN	1
G033.024-00.367	33.022	-0.370	32.5	8.54	0.53	13.91	0.74	1.6	29	···	···	-0.30	0.18	HII region	3
G033.029+00.800	33.027	0.797	4.0	0.37	0.09	1.57	0.12	1.6	16	···	···	0.27	0.58	···	···
G033.034-00.908	33.034	-0.909	4.0	0.28	0.07	0.52	0.08	0.8	11	···	···	1.48	1.33	···	···
G033.036-00.164	33.036	-0.164	6.7	2.97	0.47	35.67	1.84	7.0	37	···	···	···	···	Extended/Diffuse	1
G033.052+00.883	33.053	0.883	13.9	1.11	0.10	0.97	0.09	0.8	13	-0.48	0.10	-0.87	0.26	···	···
G033.054+00.352	33.055	0.353	5.1	0.78	0.16	1.38	0.17	1.0	13	···	···	-1.19	0.72	···	···
G033.057-00.224	33.057	-0.224	6.7	2.23	0.36	2.36	0.36	0.7	11	-0.44	0.15	-0.91	0.22	···	···
G033.063-00.362	33.062	-0.361	15.9	4.24	0.35	3.38	0.32	0.7	13	-0.36	0.06	-0.88	0.10	···	···
G033.065-00.317	33.066	-0.317	6.8	1.75	0.27	1.97	0.28	0.8	12	···	···	0.71	0.25	···	···
G033.083+00.321	33.083	0.321	5.3	0.77	0.15	0.77	0.15	0.6	10	-0.74	0.20	-1.00	0.68	···	···
G033.086+00.433	33.086	0.434	109.6	13.26	0.72	12.94	0.66	1.0	21	-0.88	0.01	-1.12	0.04	···	···
G033.090+00.834	33.090	0.834	5.0	0.43	0.09	0.44	0.09	0.6	10	···	···	0.67	0.63	···	···
G033.093+00.074	33.092	0.069	18.8	6.36	0.48	78.77	3.95	11.0	64	···	···	···	···	Ionization Front	1
G033.095-00.815	33.095	-0.816	24.5	1.79	0.12	1.86	0.12	1.0	17	-0.58	0.05	-0.56	0.15	···	···
G033.104+00.619	33.105	0.619	10.6	1.29	0.14	1.22	0.14	0.8	13	-0.34	0.16	-1.21	0.16	···	···
G033.110-00.094	33.110	-0.094	9.2	8.60	1.04	11.89	1.11	1.1	16	-0.01	0.11	-0.21	0.07	HII region	3
G033.111+00.423	33.110	0.422	9.5	1.17	0.14	1.60	0.15	1.1	16	···	···	-0.55	0.13	···	···
G033.115-00.125	33.109	-0.123	6.3	4.52	0.76	128.02	6.44	15.4	58	···	···	···	···	···	···
G033.120-00.894	33.119	-0.895	237.0	17.07	0.92	16.86	0.85	1.0	23	-0.23	0.01	-0.62	0.04	PN	6
G033.124+00.199	33.124	0.199	9.9	1.76	0.20	2.00	0.20	0.9	14	···	···	-0.34	0.39	···	···
G033.128+00.364	33.128	0.364	40.1	5.48	0.33	4.95	0.28	0.9	17	-0.31	0.04	-0.68	0.12	···	···
G033.133-00.092	33.137	-0.090	436.1	412.55	22.24	504.15	25.23	1.2	33	···	···	-0.04	0.12	HII region	2
G033.138-00.307	33.138	-0.306	7.2	1.50	0.22	2.06	0.23	1.0	14	···	···	0.65	0.31	···	···
G033.140+00.843	33.140	0.844	4.1	0.33	0.08	0.64	0.09	0.8	11	···	···	-0.27	0.39	···	···
G033.141-00.673	33.141	-0.673	6.8	0.84	0.13	0.98	0.13	0.8	12	-0.79	0.12	-1.24	0.55	···	···
G033.150-00.557	33.150	-0.557	8.0	1.69	0.23	1.55	0.23	0.7	11	0.04	0.17	-0.56	0.24	···	···
G033.161+00.630	33.161	0.630	4.5	0.48	0.11	0.58	0.11	0.6	10	···	···	-1.44	0.48	···	···
G033.165+00.492	33.165	0.491	12.9	1.58	0.15	1.70	0.15	0.9	15	···	···	-0.53	0.48	···	···
G033.176-00.197	33.176	-0.196	8.5	3.11	0.40	3.63	0.41	0.9	14	-0.55	0.11	-0.89	0.30	···	···
G033.177+00.424	33.177	0.424	9.3	1.17	0.14	1.65	0.15	1.1	15	···	···	-0.46	0.26	···	···
G033.180+00.873	33.180	0.873	5.3	0.38	0.08	0.30	0.07	0.5	9	···	···	0.40	0.63	···	···
G033.186+00.953	33.186	0.953	45.0	3.16	0.18	3.26	0.18	1.0	19	-0.54	0.03	-1.01	0.07	···	···

Continued on next page

Table B.1 – *Continued from previous page*

GLOSTAR name	ℓ	b	SNR	$S_{\rm peak}$	$\Delta S_{\rm peak}$	$S_{\rm int}$	$\Delta S_{\rm int}$	Y	Radius	Spectral index				Classification	
	(°)	(°)		(mJy beam^{-1})		(mJy)			($''$)	α	$\Delta\alpha$	α*	$\Delta\alpha$*	Type	Ref.
(1)	(2)	(3)	(4)	(5)	(6)	(7)	(8)	(9)	(10)	(11)	(12)	(13)	(14)	(15)	(16)
G033.200-00.254	33.218	-0.263	11.7	2.68	0.27	169.70	8.49	49.7	23	···	···	···	···	···	···
G033.201+00.216	33.201	0.216	5.6	0.94	0.18	0.89	0.17	0.6	10	···	···	-0.50	0.83	···	···
G033.206-00.747	33.206	-0.747	22.6	1.92	0.13	1.80	0.12	0.9	16	-0.30	0.06	-0.81	0.09	···	···
G033.218-00.613	33.218	-0.613	5.3	0.63	0.13	0.47	0.12	0.4	8	···	···	-0.85	0.76	···	···
G033.232-00.882	33.233	-0.892	32.1	2.62	0.16	7.51	0.38	2.7	39	···	···	···	···	Ionization Front	1
G033.236+00.653	33.237	0.653	13.4	1.23	0.11	1.30	0.11	0.9	15	-0.41	0.11	-1.06	0.25	···	···
G033.252-00.154	33.253	-0.154	21.2	6.14	0.44	5.87	0.41	0.9	16	-0.44	0.05	-0.24	0.10	···	···
G033.265+00.066	33.264	0.065	79.5	24.18	1.34	34.05	1.73	1.4	25	0.12	0.03	-0.10	0.03	HII region	3
G033.265-00.972	33.265	-0.972	7.1	0.79	0.12	0.98	0.12	0.9	13	···	···	0.32	0.33	···	···
G033.268-00.588	33.267	-0.588	13.2	1.79	0.17	1.47	0.15	0.7	13	-0.43	0.08	-0.26	0.21	···	···
G033.270+00.629	33.271	0.630	13.6	1.23	0.11	3.06	0.18	2.2	23	···	···	···	···	···	···
G033.278+00.958	33.279	0.959	11.4	0.80	0.08	1.78	0.11	1.9	21	-0.42	0.12	-1.40	0.51	···	···
G033.279-00.954	33.280	-0.953	6.7	0.63	0.10	0.51	0.10	0.6	10	-0.60	0.14	0.42	0.40	···	···
G033.288+00.642	33.288	0.642	10.1	0.87	0.10	0.88	0.10	0.8	13	···	···	0.02	0.38	···	···
G033.289-00.019	33.289	-0.019	5.0	1.97	0.41	2.48	0.41	0.7	11	···	···	-0.22	0.57	HII region	3
G033.299+00.865	33.299	0.866	5.9	0.40	0.07	0.33	0.07	0.5	9	···	···	0.05	0.71	···	···
G033.310-00.897	33.310	-0.897	8.9	0.73	0.09	0.78	0.09	0.9	13	-0.50	0.12	-0.49	0.39	···	···
G033.311-00.440	33.311	-0.440	4.7	1.13	0.25	5.18	0.35	2.1	19	···	···	···	···	···	···
G033.312+00.658	33.312	0.658	13.6	1.11	0.10	1.47	0.11	1.2	17	-0.49	0.11	-1.09	0.22	···	···
G033.315+00.532	33.315	0.532	16.3	1.52	0.12	1.46	0.12	0.9	15	-0.82	0.08	-1.73	0.23	···	···
G033.317+00.259	33.319	0.258	29.1	4.12	0.26	6.31	0.35	1.5	22	-0.76	0.05	-0.85	0.17	···	···
G033.319-00.850	33.319	-0.851	14.6	1.09	0.10	0.87	0.09	0.7	13	0.11	0.12	0.14	0.26	···	···
G033.320+00.899	33.320	0.899	4.4	0.30	0.07	0.48	0.07	0.8	11	···	···	0.01	0.64	···	···
G033.321+00.703	33.321	0.703	9.2	0.71	0.09	0.82	0.09	0.9	14	···	···	0.00	0.62	···	···
G033.321+00.981	33.321	0.981	8.7	0.70	0.09	0.68	0.09	0.8	12	···	···	-0.37	0.38	···	···
G033.323-00.374	33.323	-0.374	7.3	1.98	0.29	1.60	0.28	0.6	10	-1.00	0.11	-1.04	0.18	···	···
G033.325-00.642	33.325	-0.642	8.3	0.87	0.12	0.86	0.11	0.7	12	-0.56	0.12	-0.67	0.80	···	···
G033.328+00.825	33.326	0.825	4.3	0.30	0.07	1.21	0.09	1.7	17	···	···	0.47	0.48	···	···
G033.332+00.967	33.332	0.967	7.1	0.52	0.08	0.75	0.08	1.0	14	-0.64	0.15	-0.68	0.36	···	···
G033.342+00.640	33.342	0.640	4.1	0.33	0.08	0.38	0.08	0.5	8	···	···	0.22	0.64	···	···
G033.347-00.564	33.347	-0.564	4.6	0.58	0.13	0.43	0.13	0.4	8	···	···	-1.70	0.46	···	···
G033.352+00.404	33.353	0.404	175.5	17.86	0.97	17.35	0.87	1.0	22	0.61	0.06	0.15	0.03	PN	6
G033.375-00.960	33.377	-0.959	27.8	1.94	0.13	3.54	0.19	1.7	24	···	···	-1.11	0.12	···	···
G033.385+00.617	33.386	0.616	14.4	1.14	0.10	1.20	0.10	0.9	15	···	···	-0.36	0.38	···	···
G033.400-00.883	33.400	-0.883	8.9	0.64	0.08	0.48	0.08	0.6	11	-0.49	0.13	-0.96	0.44	···	···
G033.403+00.008‡	33.403	0.008	20.4	21.00	2.10	157.83	17.77	7.5	···	···	···	···	···	HII region	1
G033.410-00.477	33.407	-0.480	27.2	3.75	0.24	7.27	0.39	1.8	32	···	···	-0.57	0.26	···	···
G033.413+00.374	33.412	0.373	4.4	0.56	0.13	0.59	0.13	0.5	9	···	···	0.23	0.66	···	···
G033.413+00.943	33.414	0.942	9.8	0.65	0.07	0.64	0.07	0.8	13	-0.38	0.13	-0.69	0.44	···	···
G033.414+00.299	33.418	0.303	4.8	0.89	0.19	12.09	0.63	5.6	33	···	···	···	···	Extended/Diffuse	1
G033.418-00.004‡	33.418	-0.004	82.4	84.96	2.63	239.10	9.68	2.8	···	···	···	···	···	HII region	2
G033.419+00.030†	33.419	0.030	5.0	0.81	0.14	0.53	0.18	0.7	···	···	···	···	···	···	···
G033.431-00.933	33.431	-0.933	15.6	1.04	0.09	1.06	0.09	0.9	15	-0.68	0.07	-1.02	0.31	···	···

Continued on next page

Table B.1 – *Continued from previous page*

GLOSTAR name	ℓ	b	SNR	$S_{\rm peak}$	$\Delta S_{\rm peak}$	$S_{\rm int}$	$\Delta S_{\rm int}$	Y	Radius	Spectral index				Classification	
	(°)	(°)		(mJy beam^{-1})		(mJy)			($''$)	α	$\Delta\alpha$	α*	$\Delta\alpha$*	Type	Ref.
(1)	(2)	(3)	(4)	(5)	(6)	(7)	(8)	(9)	(10)	(11)	(12)	(13)	(14)	(15)	(16)
G033.432+00.376	33.430	0.375	4.4	0.57	0.13	5.22	0.29	3.5	25	···	···	···	···	Extended/Diffuse	1
G033.448+00.318	33.448	0.319	18.3	3.28	0.25	2.77	0.23	0.8	14	···	···	-0.45	0.12	Radio star	8
G033.453-00.031‡	33.453	-0.031	37.7	10.34	0.27	261.55	1.38	25.3	···	···	···	···	···	···	···
G033.454-00.615	33.454	-0.615	937.4	93.09	5.01	91.67	4.58	1.0	26	1.09	0.01	0.74	0.02	PN	6
G033.457+00.303	33.457	0.303	4.9	0.97	0.20	0.97	0.20	0.6	9	···	···	-1.63	0.45	···	···
G033.458+00.017	33.458	0.017	8.8	5.16	0.65	5.46	0.64	0.8	13	-0.56	0.11	-0.79	0.16	···	···
G033.472+00.388	33.472	0.387	11.5	1.37	0.14	1.35	0.14	0.8	14	···	···	0.05	0.39	···	···
G033.474-00.360	33.474	-0.360	19.9	4.12	0.30	3.52	0.27	0.8	14	0.03	0.09	0.15	0.04	···	···
G033.489-00.358	33.489	-0.358	118.2	24.04	1.31	23.29	1.18	1.0	21	-0.59	0.01	-0.67	0.02	···	···
G033.492+00.919	33.492	0.918	9.5	0.67	0.08	0.57	0.08	0.7	12	···	···	-0.54	0.45	···	···
G033.494+00.158	33.490	0.155	9.6	2.60	0.30	13.71	0.74	4.1	34	···	···	···	···	HII region	1
G033.498+00.194	33.498	0.195	3733.0	914.70	49.26	914.82	45.74	1.0	29	0.08	0.00	0.21	0.02	···	···
G033.509-00.117	33.507	-0.117	7.6	3.14	0.45	17.17	0.95	3.7	27	···	···	···	···	Ionization Front	1
G033.509-00.419	33.509	-0.419	14.7	1.89	0.16	1.98	0.16	0.9	15	···	···	-1.43	0.13	···	···
G033.510-00.541	33.509	-0.543	5.1	0.46	0.09	0.85	0.10	1.0	13	···	···	-1.47	0.57	···	···
G033.520-00.815	33.520	-0.815	9.5	0.68	0.08	0.66	0.08	0.8	13	-0.60	0.11	-1.74	0.30	···	···
G033.523+00.969	33.523	0.969	4.4	0.31	0.07	0.38	0.07	0.6	10	···	···	-1.01	1.39	···	···
G033.525+00.848	33.525	0.848	48.6	3.45	0.20	3.22	0.18	0.9	18	0.54	0.08	-0.07	0.14	···	···
G033.528+00.424	33.528	0.424	14.0	1.55	0.14	1.21	0.13	0.7	13	···	···	0.18	0.30	···	···
G033.528-00.632	33.528	-0.632	7.1	0.60	0.09	0.48	0.09	0.6	10	···	···	0.58	0.30	···	···
G033.528-00.908	33.526	-0.911	5.8	0.42	0.08	1.13	0.09	1.5	17	···	···	···	···	···	···
G033.534-00.108	33.531	-0.110	12.0	4.82	0.48	14.35	0.82	2.5	27	···	···	···	···	HII region	3
G033.537+00.619	33.537	0.619	499.8	38.03	2.05	37.11	1.86	1.0	24	-0.55	0.00	-0.98	0.03	···	···
G033.549+00.414	33.549	0.414	4.5	0.56	0.13	1.72	0.15	1.4	15	···	···	0.80	0.66	···	···
G033.553-00.381	33.553	-0.380	6.5	1.19	0.19	0.88	0.19	0.5	9	···	···	0.27	0.12	···	···
G033.554+00.288	33.555	0.288	27.5	4.43	0.29	5.79	0.33	1.2	19	-0.49	0.10	-0.56	0.11	···	···
G033.556+00.817	33.556	0.817	8.2	0.57	0.08	0.50	0.07	0.7	11	···	···	0.47	0.46	···	···
G033.563-00.094	33.563	-0.095	4.4	1.60	0.37	1.02	0.37	0.3	7	···	···	-0.78	0.24	···	···
G033.572-00.533	33.573	-0.533	19.9	1.74	0.13	2.48	0.15	1.3	18	-0.75	0.05	-1.29	0.15	···	···
G033.582+00.618	33.581	0.618	35.6	2.80	0.17	2.98	0.17	1.0	19	-0.58	0.04	-0.42	0.09	···	···
G033.583-00.714	33.583	-0.715	4.1	0.30	0.08	0.59	0.08	0.9	11	···	···	-0.49	0.78	···	···
G033.586-00.344	33.586	-0.342	8.4	1.80	0.24	3.70	0.28	1.6	19	···	···	-0.24	0.27	···	···
G033.595+00.185	33.595	0.185	10.3	2.41	0.27	1.91	0.25	0.6	12	-0.55	0.16	0.08	0.30	···	···
G033.600+00.794	33.599	0.795	5.6	0.37	0.07	0.37	0.07	0.6	10	···	···	0.30	0.23	···	···
G033.600-00.537	33.600	-0.537	6.2	0.53	0.09	0.39	0.09	0.5	9	···	···	···	···	···	···
G033.605-00.981	33.605	-0.981	6.6	0.60	0.10	0.58	0.10	0.7	11	···	···	-0.03	0.24	···	···
G033.606-00.347	33.605	-0.348	4.1	0.88	0.22	5.53	0.35	2.3	20	···	···	···	···	···	···
G033.608+00.941	33.611	0.941	45.8	2.98	0.17	4.10	0.21	1.3	24	0.08	0.07	-0.54	0.09	···	···
G033.612-00.198	33.612	-0.198	12.8	2.63	0.25	2.93	0.25	1.0	15	-0.64	0.08	-1.07	0.24	···	···
G033.613-00.369	33.612	-0.368	8.9	1.78	0.22	10.70	0.57	4.5	33	···	···	···	···	···	···
G033.621+00.141	33.624	0.139	7.6	3.15	0.45	21.34	1.15	4.6	32	···	···	···	···	HII region	1
G033.633-00.962	33.633	-0.962	167.9	14.78	0.80	15.92	0.80	1.1	23	-0.56	0.01	-0.73	0.03	···	···
G033.635+00.712	33.635	0.712	5.3	0.38	0.07	0.44	0.07	0.7	11	···	···	1.16	1.12	···	···

Continued on next page

Table B.1 – *Continued from previous page*

GLOSTAR name	ℓ	b	SNR	$S_{\rm peak}$	$\Delta S_{\rm peak}$	$S_{\rm int}$	$\Delta S_{\rm int}$	Y	Radius	Spectral index				Classification	
	(°)	(°)		(mJy beam^{-1})		(mJy)			($''$)	α	$\Delta\alpha$	α*	$\Delta\alpha$*	Type	Ref.
(1)	(2)	(3)	(4)	(5)	(6)	(7)	(8)	(9)	(10)	(11)	(12)	(13)	(14)	(15)	(16)
G033.638+00.169	33.637	0.169	15.4	4.12	0.35	47.23	2.38	9.9	55	···	···	···	···	HII region	1
G033.639-00.579	33.638	-0.579	7.1	0.58	0.09	0.45	0.08	0.6	10	···	···	-0.44	0.39	···	···
G033.643+00.844	33.643	0.845	9.3	0.63	0.08	0.46	0.07	0.6	11	···	···	-0.07	0.34	···	···
G033.645-00.228	33.644	-0.228	35.6	6.94	0.42	14.00	0.73	1.9	27	···	···	-0.14	0.11	HII region	3
G033.648+00.576	33.648	0.576	4.4	0.41	0.09	0.36	0.09	0.4	8	···	···	0.16	0.63	···	···
G033.650-00.657	33.650	-0.657	9.9	0.79	0.09	0.77	0.09	0.8	13	-0.84	0.10	-1.56	0.41	···	···
G033.650-00.799	33.651	-0.799	7.0	0.51	0.08	0.42	0.08	0.6	10	-0.80	0.15	-0.36	0.57	···	···
G033.655-00.756	33.655	-0.755	8.2	0.61	0.08	0.59	0.08	0.7	12	···	···	-0.79	0.29	···	···
G033.655-00.812	33.654	-0.812	8.9	0.65	0.08	0.56	0.08	0.7	11	-0.85	0.11	-0.81	0.14	···	···
G033.659-00.458	33.660	-0.458	13.9	1.45	0.13	2.58	0.17	1.5	19	···	···	-0.73	0.24	···	···
G033.697+00.731	33.696	0.728	14.3	1.06	0.09	3.92	0.21	3.3	32	···	···	···	···	···	···
G033.700-00.906	33.700	-0.907	19.4	1.60	0.12	1.42	0.11	0.8	15	···	···	-0.03	0.31	···	···
G033.703-00.838	33.702	-0.838	8.7	0.64	0.08	0.63	0.08	0.8	12	···	···	-0.33	0.46	···	···
G033.704-00.414	33.717	-0.408	34.9	6.01	0.37	115.90	5.80	18.5	90	···	···	···	···	HII region	1
G033.704-00.963	33.704	-0.963	32.2	2.90	0.18	3.11	0.18	1.0	18	-0.55	0.04	-0.44	0.06	···	···
G033.714+00.256	33.715	0.255	7.4	1.50	0.22	1.54	0.22	0.7	12	···	···	-0.06	0.29	HII region	1
G033.721-00.705	33.721	-0.705	4.4	0.34	0.08	0.40	0.08	0.6	9	···	···	0.99	0.41	···	···
G033.723+00.302	33.724	0.302	9.1	1.66	0.20	2.98	0.24	1.4	17	···	···	-0.75	0.26	···	···
G033.725-00.889	33.724	-0.891	111.7	8.81	0.48	9.27	0.47	1.0	25	···	···	-0.79	0.06	···	···
G033.736-00.739	33.736	-0.739	10.8	0.82	0.09	0.76	0.08	0.8	13	-0.44	0.12	-0.29	0.36	···	···
G033.739+00.596	33.740	0.596	6.3	0.63	0.11	0.57	0.10	0.6	10	···	···	-0.81	0.54	···	···
G033.742+00.353	33.742	0.353	30.6	4.78	0.30	4.35	0.27	0.9	16	-0.45	0.06	-1.07	0.09	···	···
G033.754-00.067	33.750	-0.065	15.2	4.73	0.40	44.84	2.26	8.2	49	···	···	···	···	HII region	1
G033.755+00.297	33.756	0.293	5.8	1.07	0.19	8.51	0.46	4.3	31	···	···	···	···	HII region	1
G033.761-00.050	33.761	-0.050	4.5	1.35	0.31	9.34	0.55	2.8	22	···	···	···	···	Extended/Diffuse	1
G033.766+00.428	33.765	0.428	8.0	1.14	0.15	0.81	0.15	0.5	10	-0.80	0.14	0.25	0.23	···	···
G033.766-00.199	33.766	-0.195	21.3	4.53	0.32	7.33	0.42	1.5	25	···	···	-0.74	0.17	···	···
G033.769+00.752	33.769	0.752	5.3	0.39	0.08	0.32	0.07	0.5	9	···	···	0.24	0.47	···	···
G033.772-00.395	33.772	-0.396	12.6	1.95	0.19	1.63	0.17	0.7	13	-0.06	0.14	0.07	0.29	···	···
G033.784+00.798	33.784	0.798	30.2	2.15	0.14	1.85	0.12	0.8	16	-0.67	0.05	-0.82	0.11	···	···
G033.784+00.944	33.784	0.943	4.1	0.30	0.07	0.25	0.07	0.4	7	···	···	0.09	0.92	···	···
G033.795+00.431	33.795	0.431	92.0	13.19	0.72	13.16	0.67	1.0	21	0.33	0.04	0.16	0.03	PN	6
G033.796-00.803	33.795	-0.805	7.4	0.54	0.08	0.68	0.08	0.9	14	···	···	-1.02	0.89	···	···
G033.800-00.588	33.800	-0.589	10.4	0.78	0.09	0.56	0.08	0.6	11	-0.77	0.13	-0.94	0.41	···	···
G033.801+00.239	33.800	0.239	9.3	1.73	0.21	2.25	0.22	1.0	15	···	···	-0.79	0.51	···	···
G033.801-00.781	33.801	-0.780	5.6	0.41	0.08	0.44	0.08	0.7	11	-0.86	0.19	-1.46	0.59	···	···
G033.809-00.154	33.815	-0.149	97.5	24.76	1.36	93.11	4.66	3.7	47	···	···	···	···	HII region	1
G033.810-00.188	33.812	-0.190	877.3	190.45	10.26	349.91	17.50	1.8	36	···	···	0.11	0.06	HII region	2
G033.812-00.760	33.811	-0.761	7.8	0.56	0.08	0.42	0.07	0.6	10	···	···	-0.53	0.64	···	···
G033.814+00.906	33.814	0.906	8.8	0.64	0.08	0.50	0.08	0.6	11	···	···	-0.09	0.42	···	···
G033.819+00.913	33.819	0.913	19.0	1.40	0.10	1.39	0.10	0.9	16	···	···	-0.34	0.06	···	···
G033.821+00.505	33.821	0.505	5.7	0.87	0.16	0.56	0.16	0.4	8	···	···	0.11	0.50	···	···
G033.824+00.855	33.824	0.855	13.5	0.96	0.09	1.18	0.09	1.1	16	-0.75	0.08	-1.29	0.34	···	···

Continued on next page

Table B.1 – *Continued from previous page*

GLOSTAR name	ℓ	b	SNR	$S_{\rm peak}$	$\Delta S_{\rm peak}$	$S_{\rm int}$	$\Delta S_{\rm int}$	Y	Radius	Spectral index				Classification	
	(°)	(°)		(mJy beam^{-1})		(mJy)			($''$)	α	$\Delta\alpha$	α*	$\Delta\alpha$*	Type	Ref.
(1)	(2)	(3)	(4)	(5)	(6)	(7)	(8)	(9)	(10)	(11)	(12)	(13)	(14)	(15)	(16)
G033.828-00.163	33.828	-0.163	14.8	3.46	0.30	4.12	0.31	1.0	16	···	···	-0.25	0.16	HII region	3
G033.840-00.888	33.840	-0.888	13.7	0.96	0.09	0.86	0.08	0.8	13	···	···	0.39	0.23	···	···
G033.850+00.060	33.848	0.062	12.6	3.09	0.30	8.18	0.48	2.3	23	···	···	···	···	···	···
G033.854-00.526	33.854	-0.526	4.5	0.34	0.08	0.24	0.08	0.3	7	···	···	0.10	0.48	···	···
G033.868-00.398	33.869	-0.399	4.8	0.53	0.12	3.89	0.22	3.2	24	···	···	···	···	HII region	1
G033.871-00.363	33.871	-0.364	5.5	0.64	0.12	0.68	0.12	0.7	10	···	···	-0.74	0.66	···	···
G033.878-00.880	33.879	-0.880	29.6	2.03	0.13	2.44	0.14	1.1	19	-0.42	0.06	-0.71	0.18	···	···
G033.882+00.401	33.883	0.401	8.1	1.48	0.20	1.23	0.19	0.6	11	-0.99	0.11	-1.43	0.22	···	···
G033.883+00.058	33.877	0.053	44.5	11.97	0.70	56.67	2.85	4.6	59	···	···	···	···	HII region	3
G033.887+00.328	33.887	0.328	5.2	0.90	0.18	0.97	0.18	0.6	10	···	···	-1.85	0.39	···	···
G033.893-00.985	33.893	-0.985	17.8	1.47	0.11	1.38	0.11	0.9	15	-0.90	0.06	-1.04	0.30	···	···
G033.895+00.400	33.895	0.400	8.4	1.53	0.20	1.14	0.19	0.6	10	-0.98	0.11	-0.91	0.21	···	···
G033.895+00.522	33.895	0.522	47.8	6.41	0.37	6.53	0.35	1.0	19	-0.49	0.03	-0.91	0.07	···	···
G033.896+00.325	33.896	0.325	16.8	2.94	0.24	2.49	0.21	0.8	14	-0.04	0.14	-0.65	0.17	···	···
G033.896-00.846	33.895	-0.846	5.4	0.36	0.07	0.28	0.07	0.5	9	···	···	-0.91	0.59	···	···
G033.906-00.044‡	33.906	-0.044	62.0	22.85	0.38	24.53	0.69	1.1	···	···	···	1.15	.04	PN	6
G033.907-00.247	33.907	-0.247	14.2	2.07	0.18	2.43	0.19	1.0	16	···	···	0.13	0.23	···	···
G033.907-00.594	33.907	-0.593	42.9	3.46	0.20	3.39	0.19	1.0	18	-0.66	0.05	-0.84	0.07	···	···
G033.911-00.789	33.912	-0.788	5.1	0.35	0.07	1.27	0.09	1.8	18	···	···	0.22	0.68	···	···
G033.914+00.110	33.924	0.113	2894.0	795.39	42.83	1112.26	55.61	1.4	56	···	···	···	···	HII region	2
G033.916+00.264	33.915	0.264	26.7	4.48	0.29	4.38	0.28	0.9	17	···	···	0.61	0.10	PN	1
G033.918-00.869	33.918	-0.869	10.9	0.72	0.08	0.78	0.08	0.9	14	-1.24	0.08	-1.61	0.21	···	···
G033.921-00.422	33.920	-0.422	7.0	0.68	0.10	0.41	0.10	0.4	9	···	···	-1.15	0.43	···	···
G033.925-00.442	33.927	-0.444	7.8	0.73	0.10	1.50	0.12	1.5	18	···	···	-0.44	0.90	···	···
G033.932+00.428	33.932	0.428	53.3	9.34	0.53	9.59	0.51	1.0	20	0.11	0.05	-0.17	0.12	···	···
G033.934-00.905	33.934	-0.905	6.6	0.45	0.07	0.35	0.07	0.5	10	···	···	-0.10	0.60	···	···
G033.941-00.141	33.941	-0.141	7.0	1.48	0.23	2.03	0.23	1.0	13	-0.65	0.14	-1.61	0.35	···	···
G033.956-00.141	33.956	-0.141	5.1	1.11	0.23	0.99	0.23	0.5	9	-0.76	0.18	-1.63	0.24	···	···
G033.969+00.769	33.969	0.769	30.7	2.81	0.18	2.85	0.17	1.0	18	-0.64	0.06	-0.48	0.07	···	···
G033.978-00.613	33.979	-0.613	10.6	0.91	0.10	0.87	0.10	0.8	13	-0.74	0.12	-1.04	0.29	···	···
G033.978-00.985	33.978	-0.985	48.8	4.68	0.27	5.07	0.27	1.1	20	0.15	0.06	0.02	0.04	···	···
G033.989-00.009‡	33.989	-0.009	19.0	7.78	0.44	16.40	1.30	2.1	···	···	···	···	···	HII region	3
G033.990-00.949	33.989	-0.949	39.7	3.09	0.18	3.14	0.18	1.0	18	-0.83	0.03	-0.81	0.07	···	···
G033.991-00.005‡	33.991	-0.005	45.0	14.75	0.34	17.30	0.66	1.2	···	···	···	0.12	.16	HII region	3
G033.996-00.562	33.995	-0.562	6.6	0.59	0.10	0.63	0.10	0.7	12	···	···	-1.07	0.50	···	···
G033.996-00.978	33.996	-0.978	6.8	0.63	0.10	0.72	0.10	0.8	12	···	···	-0.64	0.45	···	···
G034.001+00.469	34.001	0.469	11.1	1.85	0.19	1.86	0.19	0.8	14	-0.74	0.09	-0.67	0.19	···	···
G034.008+00.704	34.008	0.703	4.2	0.42	0.10	0.76	0.11	0.8	11	···	···	-0.63	1.51	···	···
G034.014+00.625	34.014	0.625	11.5	1.67	0.17	1.47	0.16	0.7	13	-0.89	0.09	-0.92	0.12	···	···
G034.022-00.925	34.022	-0.925	261.2	18.94	1.02	18.89	0.95	1.0	23	-0.91	0.00	-0.89	0.03	···	···
G034.028-00.605	34.024	-0.609	11.5	1.00	0.10	2.40	0.15	2.0	26	···	···	···	···	···	···
G034.037-00.176	34.037	-0.175	6.2	1.34	0.23	1.18	0.22	0.6	10	···	···	-0.26	0.50	···	···
G034.043+00.054	34.041	0.055	74.6	24.55	1.36	114.38	5.73	4.6	53	···	···	···	···	HII region	3

Continued on next page

Table B.1 – *Continued from previous page*

GLOSTAR name	ℓ	b	SNR	$S_{\rm peak}$	$\Delta S_{\rm peak}$	$S_{\rm int}$	$\Delta S_{\rm int}$	Y	Radius	Spectral index				Classification	
	(°)	(°)		(mJy beam^{-1})		(mJy)			($''$)	α	$\Delta\alpha$	α*	$\Delta\alpha$*	Type	Ref.
(1)	(2)	(3)	(4)	(5)	(6)	(7)	(8)	(9)	(10)	(11)	(12)	(13)	(14)	(15)	(16)
G034.046+00.140	34.047	0.140	20.5	5.47	0.40	14.83	0.79	2.5	26	···	···	···	···	HII region	3
G034.049-00.299†	34.049	-0.299	11.0	0.64	0.06	2.41	0.26	3.8	···	···	···	···	···	HII region	3
G034.049-00.426	34.051	-0.424	4.8	0.53	0.11	3.30	0.20	2.8	22	···	···	···	···	HII region	1
G034.056-00.056	34.032	-0.067	8.9	3.18	0.40	65.38	3.29	16.1	69	···	···	···	···	Ionization Front	1
G034.060-00.326	34.061	-0.329	4.5	0.72	0.16	2.19	0.19	1.4	15	···	···	-0.27	0.74	···	···
G034.073-00.051	34.073	-0.051	4.3	1.60	0.38	0.92	0.38	0.3	6	···	···	0.90	0.19	···	···
G034.074+00.813	34.074	0.813	12.9	1.15	0.11	1.18	0.11	0.9	15	···	···	-0.24	0.61	···	···
G034.079-00.691	34.079	-0.691	41.8	3.42	0.20	3.91	0.21	1.1	21	-0.62	0.04	-0.53	0.10	···	···
G034.082-00.344	34.082	-0.345	15.2	2.16	0.18	2.53	0.19	1.0	16	···	···	-0.32	0.12	···	···
G034.084-00.644	34.084	-0.644	24.8	2.05	0.14	1.89	0.13	0.9	16	···	···	-0.19	0.07	···	···
G034.089+00.436	34.083	0.441	402.2	78.27	4.22	266.34	13.32	3.4	58	···	···	···	···	HII region	2
G034.092-00.752	34.092	-0.750	38.6	2.98	0.18	4.39	0.23	1.4	23	-0.59	0.04	-0.55	0.16	···	···
G034.101-00.521	34.101	-0.521	8.4	0.82	0.11	0.67	0.10	0.6	11	···	···	0.07	0.58	···	···
G034.103-00.027	34.099	-0.015	9.7	3.93	0.46	28.08	1.46	5.7	43	···	···	···	···	HII region	3
G034.121+00.485	34.116	0.485	11.1	2.15	0.22	5.19	0.32	2.0	23	···	···	···	···	···	···
G034.133+00.471	34.133	0.471	2085.0	407.23	21.93	575.03	28.75	1.4	52	0.17	0.00	-0.03	0.02	HII region	3
G034.134-00.279	34.135	-0.279	6.3	1.18	0.20	2.73	0.23	1.5	17	···	···	0.56	0.28	···	···
G034.139+00.092	34.139	0.092	4.8	2.79	0.60	4.33	0.62	0.8	11	···	···	-0.18	0.44	Extended/Diffuse	1
G034.140-00.715	34.140	-0.715	47.8	4.06	0.23	4.29	0.23	1.0	19	-0.00	0.06	0.19	0.07	···	···
G034.142+00.904	34.143	0.904	28.6	2.28	0.15	2.14	0.13	0.9	16	-0.52	0.06	-0.25	0.14	···	···
G034.143-00.502	34.143	-0.497	5.6	0.57	0.11	16.78	0.84	14.1	54	···	···	···	···	Extended/Diffuse	1
G034.149+00.751	34.149	0.751	6.3	0.70	0.12	0.50	0.11	0.5	9	···	···	0.61	0.93	···	···
G034.151-00.351‡	34.151	-0.351	22.0	2.07	0.09	2.16	0.17	1.0	···	0.67	0.06	0.99	0.41	···	···
G034.151-00.362‡	34.151	-0.362	18.0	1.82	0.11	6.11	0.45	3.4	···	···	···	···	···	···	···
G034.156-00.372‡	34.156	-0.372	15.0	0.92	0.06	1.32	0.14	1.4	···	0.62	0.13	0.43	0.31	···	···
G034.163-00.867	34.163	-0.867	21.3	1.56	0.11	1.55	0.11	0.9	16	-0.06	0.12	0.12	0.19	···	···
G034.166+00.979	34.164	0.977	6.2	0.52	0.09	0.70	0.09	0.9	13	···	···	1.13	0.31	···	···
G034.169-00.717	34.170	-0.718	4.4	0.38	0.09	0.77	0.10	1.0	12	···	···	···	···	···	···
G034.173-00.294	34.173	-0.295	41.6	6.43	0.38	10.99	0.57	1.7	22	-0.72	0.03	-0.96	0.12	···	···
G034.173-00.894	34.173	-0.894	6.1	0.45	0.08	0.36	0.08	0.5	9	-1.08	0.16	0.32	0.63	···	···
G034.178+00.257	34.179	0.257	13.3	5.30	0.49	4.62	0.46	0.8	13	···	···	0.64	0.29	···	···
G034.178-00.711	34.177	-0.711	156.8	13.89	0.75	14.50	0.73	1.0	23	0.04	0.02	-0.25	0.03	···	···
G034.179-00.178	34.179	-0.177	56.8	13.24	0.75	13.27	0.70	1.0	19	0.09	0.03	0.08	0.06	PN	6
G034.185-00.687	34.185	-0.686	26.9	2.52	0.16	3.10	0.18	1.2	18	···	···	-0.79	0.10	···	···
G034.187-00.706	34.187	-0.706	4.4	0.40	0.09	0.45	0.09	0.6	9	···	···	-1.96	0.49	···	···
G034.197-00.592	34.200	-0.589	148.7	15.79	0.86	20.00	1.01	1.3	30	···	···	-0.04	0.06	HII region	2
G034.210-00.803	34.210	-0.803	6.0	0.49	0.09	0.34	0.08	0.5	9	···	···	-1.09	0.39	···	···
G034.210-00.934	34.209	-0.935	10.6	0.79	0.09	1.31	0.10	1.4	18	-0.66	0.13	-0.53	0.20	···	···
G034.215+00.513	34.215	0.513	29.0	4.83	0.31	5.06	0.30	1.0	18	-0.23	0.07	-0.18	0.14	···	···
G034.217-00.827	34.218	-0.827	36.4	2.91	0.18	3.70	0.20	1.2	20	-0.54	0.05	-0.67	0.06	···	···
G034.221+00.546	34.221	0.546	9.1	1.44	0.18	0.99	0.17	0.5	10	···	···	0.28	0.31	···	···
G034.224+00.876	34.223	0.876	10.6	0.85	0.09	0.72	0.09	0.7	12	-0.42	0.13	0.31	0.34	···	···
G034.224-00.698	34.224	-0.698	10.3	1.02	0.11	0.81	0.11	0.7	12	···	···	0.02	0.43	···	···

Continued on next page

Table B.1 – *Continued from previous page*

GLOSTAR name	ℓ	b	SNR	$S_{\rm peak}$	$\Delta S_{\rm peak}$	$S_{\rm int}$	$\Delta S_{\rm int}$	Y	Radius	Spectral index				Classification	
	(°)	(°)		(mJy beam^{-1})		(mJy)			($''$)	α	$\Delta\alpha$	α*	$\Delta\alpha$*	Type	Ref.
(1)	(2)	(3)	(4)	(5)	(6)	(7)	(8)	(9)	(10)	(11)	(12)	(13)	(14)	(15)	(16)
G034.231-00.942	34.226	-0.940	9.2	0.71	0.09	1.21	0.10	1.4	18	···	···	···	···	···	···
G034.248+00.408	34.248	0.408	4.1	0.78	0.19	0.91	0.19	0.5	9	···	···	-1.08	0.34	···	···
G034.254+00.399	34.254	0.398	36.2	7.01	0.42	6.51	0.38	0.9	17	-0.00	0.06	-0.21	0.11	···	···
G034.258+00.765	34.256	0.764	5.0	0.52	0.11	1.20	0.12	1.2	15	···	···	-0.94	0.41	HII region	1
G034.264-00.876	34.265	-0.874	23.8	1.94	0.13	2.89	0.17	1.4	21	···	···	-0.56	0.20	···	···
G034.265+00.719	34.265	0.720	17.6	2.28	0.18	1.86	0.16	0.7	14	-0.14	0.10	0.59	0.20	···	···
G034.268-00.394	34.268	-0.395	28.9	3.78	0.24	3.58	0.22	0.9	16	-0.82	0.04	-0.62	0.14	···	···
G034.270-00.851	34.270	-0.851	7.0	0.56	0.09	0.71	0.09	0.9	13	···	···	-0.97	0.41	···	···
G034.272-00.458	34.272	-0.458	6.3	0.87	0.15	0.79	0.14	0.6	10	···	···	-0.66	0.54	···	···
G034.272-00.619	34.271	-0.618	13.3	1.46	0.13	1.99	0.15	1.2	18	···	···	-0.30	0.24	···	···
G034.273+00.608	34.273	0.610	10.9	1.69	0.18	2.31	0.19	1.1	17	-0.40	0.13	-0.50	0.30	···	···
G034.274-00.151	34.274	-0.151	6.9	1.01	0.16	1.03	0.16	0.7	11	···	···	-0.75	0.90	HII region	1
G034.281+00.536	34.278	0.532	176.8	26.46	1.43	65.46	3.28	2.5	33	···	···	···	···	···	···
G034.281-00.970	34.281	-0.970	47.1	4.09	0.24	3.90	0.21	0.9	18	-1.29	0.02	-1.28	0.10	···	···
G034.282-00.271	34.282	-0.271	9.2	1.43	0.17	2.07	0.19	1.1	15	···	···	-0.96	0.29	···	···
G034.291-00.865	34.291	-0.866	10.0	0.81	0.09	0.90	0.09	0.9	14	-0.66	0.15	-1.01	0.36	···	···
G034.294-00.190	34.294	-0.190	4.4	0.74	0.17	0.60	0.17	0.4	8	···	···	0.24	0.43	···	···
G034.299-00.745	34.299	-0.745	43.3	4.22	0.25	4.64	0.25	1.1	19	-0.78	0.03	-0.66	0.12	···	···
G034.301-00.622	34.301	-0.622	10.8	1.26	0.13	1.01	0.13	0.7	12	···	···	-0.70	0.33	···	···
G034.311+00.843	34.311	0.843	54.9	4.42	0.25	4.43	0.24	1.0	19	0.09	0.05	-0.23	0.06	···	···
G034.324+00.855	34.324	0.856	7.1	0.53	0.08	0.57	0.08	0.8	12	···	···	0.44	0.22	···	···
G034.326-00.542	34.326	-0.542	32.0	4.76	0.30	5.04	0.29	1.0	18	-0.70	0.04	-0.77	0.10	···	···
G034.334+00.889	34.334	0.889	4.7	0.33	0.07	0.50	0.07	0.8	11	···	···	-0.15	1.27	···	···
G034.335+00.463	34.336	0.463	13.8	2.24	0.20	2.42	0.20	1.0	15	-0.83	0.07	-1.20	0.30	···	···
G034.338-00.694	34.337	-0.694	4.3	0.49	0.12	0.98	0.12	0.9	12	···	···	-0.65	0.51	HII region	1
G034.340+00.633	34.339	0.633	6.7	1.01	0.16	1.18	0.16	0.8	12	···	···	-1.82	0.66	···	···
G034.357-00.981	34.357	-0.981	4.0	0.48	0.12	0.35	0.12	0.3	7	···	···	-1.68	0.83	···	···
G034.361+00.660	34.361	0.660	39.9	5.46	0.32	5.09	0.29	0.9	17	-0.80	0.02	-0.74	0.13	···	···
G034.361-00.765	34.362	-0.765	11.6	1.33	0.14	1.39	0.13	0.9	14	-0.64	0.12	-0.98	0.42	···	···
G034.376+00.410	34.376	0.411	5.9	0.91	0.16	1.53	0.17	1.0	14	···	···	-1.16	0.49	···	···
G034.385+00.926	34.386	0.927	11.1	0.72	0.08	0.86	0.08	1.0	16	-0.45	0.14	-0.10	0.69	···	···
G034.387+00.985	34.387	0.985	9.7	0.73	0.09	0.83	0.09	0.9	14	···	···	0.14	0.57	···	···
G034.390+00.710	34.391	0.711	9.6	0.95	0.11	1.12	0.11	1.0	15	···	···	0.25	0.63	···	···
G034.390-00.416	34.389	-0.416	14.1	6.08	0.54	5.08	0.50	0.7	13	0.27	0.14	-0.04	0.08	···	···
G034.403+00.228	34.403	0.228	32.4	9.52	0.59	9.54	0.56	1.0	18	0.38	0.08	-0.10	0.12	HII region	2
G034.403-00.277	34.403	-0.277	6.9	2.01	0.31	2.36	0.32	0.8	13	···	···	-1.15	0.29	···	···
G034.404+00.540	34.404	0.539	7.2	0.94	0.14	1.06	0.14	0.8	12	···	···	-0.40	0.50	···	···
G034.410+00.816	34.410	0.816	8.8	0.72	0.09	0.56	0.09	0.6	11	···	···	-0.04	0.60	···	···
G034.411+00.237†	34.411	0.237	17.0	0.77	0.05	1.39	0.13	1.8	···	···	···	···	···	···	···
G034.420-00.318	34.420	-0.318	23.3	12.46	0.86	11.45	0.78	0.9	15	0.54	0.09	0.39	0.09	PN	6
G034.427-00.020	34.427	-0.020	101.3	26.21	1.44	30.12	1.53	1.1	22	-0.87	0.01	-1.06	0.11	···	···
G034.433-00.071	34.434	-0.072	9.0	2.09	0.26	6.67	0.41	2.4	22	···	···	···	···	···	···
G034.435-00.090	34.435	-0.089	13.4	3.13	0.29	3.34	0.29	0.9	15	-0.53	0.08	-0.71	0.11	···	···

Continued on next page

Table B.1 – *Continued from previous page*

GLOSTAR name	ℓ	b	SNR	$S_{\rm peak}$	$\Delta S_{\rm peak}$	$S_{\rm int}$	$\Delta S_{\rm int}$	Y	Radius	Spectral index				Classification	
	(°)	(°)		(mJy beam^{-1})		(mJy)			($''$)	α	$\Delta\alpha$	α*	$\Delta\alpha$*	Type	Ref.
(1)	(2)	(3)	(4)	(5)	(6)	(7)	(8)	(9)	(10)	(11)	(12)	(13)	(14)	(15)	(16)
G034.440+00.060	34.440	0.060	4.5	1.53	0.35	2.33	0.36	0.8	11	···	···	-0.85	0.34	HII region	1
G034.454+00.302	34.454	0.302	6.6	1.14	0.18	0.80	0.18	0.5	9	···	···	0.91	0.36	···	···
G034.458-00.015	34.473	-0.017	4.1	1.06	0.27	57.93	2.91	16.1	56	···	···	···	···	HII region	1
G034.462+00.897	34.461	0.897	12.2	0.86	0.08	0.88	0.08	0.9	14	-0.64	0.12	-0.92	0.26	···	···
G034.467-00.742	34.467	-0.741	9.3	2.57	0.31	2.80	0.31	0.9	14	-0.77	0.11	-1.29	0.16	···	···
G034.479-00.168	34.479	-0.168	11.0	3.03	0.32	2.85	0.31	0.8	13	-0.01	0.14	-1.18	0.20	···	···
G034.483-00.105	34.476	-0.102	5.1	1.31	0.27	23.12	1.18	7.8	38	···	···	···	···	Extended/Diffuse	1
G034.502-00.947	34.502	-0.947	10.9	1.63	0.17	1.75	0.17	0.9	14	···	···	0.11	0.26	···	···
G034.504+00.935	34.504	0.936	5.9	0.37	0.07	0.53	0.07	0.9	13	···	···	-0.06	1.09	···	···
G034.512+00.831	34.512	0.831	9.3	0.80	0.10	0.61	0.09	0.6	11	···	···	1.09	0.30	···	···
G034.522+00.964	34.522	0.964	13.4	0.85	0.08	0.93	0.08	1.0	16	-0.61	0.11	-0.63	0.42	···	···
G034.527+00.656	34.519	0.656	5.2	0.53	0.11	2.88	0.18	2.7	24	···	···	···	···	Extended/Diffuse	1
G034.540+00.073	34.544	0.070	16.9	5.14	0.41	78.78	3.95	13.6	67	···	···	···	···	Ionization Front	1
G034.547+00.391	34.547	0.391	35.8	5.04	0.31	4.96	0.29	0.9	17	-0.04	0.05	0.09	0.06	···	···
G034.547-00.029	34.547	-0.029	4.9	1.67	0.36	1.45	0.35	0.5	9	···	···	-0.05	0.22	···	···
G034.561+00.338	34.563	0.340	4.4	0.60	0.14	2.06	0.17	1.5	16	···	···	-1.60	0.41	···	···
G034.566+00.492	34.566	0.492	6.3	0.92	0.15	0.70	0.15	0.5	9	-0.85	0.13	-0.29	0.37	···	···
G034.592+00.244	34.612	0.236	99.8	22.79	1.25	108.40	5.42	4.7	93	···	···	···	···	HII region	2
G034.602+00.600	34.603	0.600	9.2	1.13	0.14	1.02	0.13	0.7	12	-0.72	0.09	-0.90	0.39	···	···
G034.604+00.696	34.604	0.696	5.8	0.59	0.11	0.48	0.10	0.5	9	-0.78	0.19	-0.40	0.54	···	···
G034.611+00.972	34.611	0.971	5.7	0.41	0.08	0.40	0.08	0.6	10	-0.63	0.19	0.00	0.84	···	···
G034.612+00.472	34.612	0.472	81.4	11.02	0.61	11.30	0.58	1.0	20	0.16	0.02	0.18	0.04	···	···
G034.624-00.130	34.624	-0.129	38.4	11.34	0.68	12.84	0.71	1.1	21	0.23	0.06	0.26	0.05	HII region	3
G034.644-00.919	34.643	-0.920	28.1	4.93	0.32	4.64	0.29	0.9	16	-0.57	0.04	-0.45	0.08	···	···
G034.656-00.846	34.656	-0.846	13.8	2.21	0.20	1.78	0.18	0.7	13	-0.65	0.09	-0.52	0.22	···	···
G034.660+00.807	34.660	0.806	6.0	0.56	0.10	0.87	0.10	1.0	13	···	···	-0.51	0.42	···	···
G034.662+00.731	34.661	0.730	14.4	1.32	0.12	1.32	0.11	0.9	15	-0.75	0.08	-0.38	0.29	···	···
G034.662+00.992	34.661	0.992	28.7	2.72	0.17	2.75	0.17	1.0	17	0.03	0.06	0.29	0.09	···	···
G034.665+00.706	34.665	0.707	4.0	0.36	0.09	0.35	0.09	0.4	8	···	···	-0.53	0.36	···	···
G034.669-00.004	34.670	-0.004	20.9	8.37	0.60	8.20	0.57	0.9	16	-0.18	0.05	-0.24	0.03	···	···
G034.682+00.740	34.681	0.740	9.7	0.89	0.10	0.80	0.10	0.7	12	···	···	-0.83	0.26	···	···
G034.683+00.886	34.683	0.887	5.5	0.43	0.08	0.78	0.09	1.0	14	···	···	-0.70	0.27	···	···
G034.685+00.069	34.685	0.067	145.4	63.38	3.44	143.87	7.21	2.2	34	···	···	···	···	HII region	3
G034.688-00.027	34.690	-0.025	32.3	12.17	0.76	17.51	0.95	1.4	24	···	···	0.21	0.18	HII region	3
G034.691-00.074	34.691	-0.074	8.7	2.88	0.37	4.28	0.40	1.2	15	-0.52	0.11	-0.50	0.18	···	···
G034.703+00.389	34.702	0.389	7.1	0.84	0.13	1.18	0.13	1.0	14	···	···	-1.10	0.61	···	···
G034.712+00.008	34.720	0.009	5.5	2.40	0.46	19.62	1.07	4.1	29	···	···	···	···	Extended/Diffuse	1
G034.712+00.450	34.712	0.450	8.4	0.98	0.13	1.05	0.13	0.8	13	···	···	-0.60	0.39	···	···
G034.715+00.334	34.715	0.334	5.2	0.95	0.19	1.13	0.19	0.7	11	-0.57	0.17	-1.28	1.10	···	···
G034.715-00.758	34.715	-0.758	11.7	4.65	0.47	4.31	0.45	0.8	13	-0.72	0.07	-0.25	0.10	···	···
G034.724+00.666	34.725	0.668	46.5	4.07	0.24	6.98	0.36	1.7	26	-0.41	0.03	-0.52	0.09	···	···
G034.730-00.746	34.729	-0.746	10.0	4.93	0.56	4.28	0.54	0.7	12	-0.87	0.08	-0.59	0.08	···	···
G034.753+00.023	34.750	0.030	44.5	20.47	1.19	228.63	11.44	10.8	87	···	···	···	···	HII region	1

Continued on next page

Table B.1 – *Continued from previous page*

GLOSTAR name	ℓ	b	SNR	$S_{\rm peak}$	$\Delta S_{\rm peak}$	$S_{\rm int}$	$\Delta S_{\rm int}$	Y	Radius	Spectral index				Classification	
	(°)	(°)		(mJy beam^{-1})		(mJy)			($''$)	α	$\Delta\alpha$	α*	$\Delta\alpha$*	Type	Ref.
(1)	(2)	(3)	(4)	(5)	(6)	(7)	(8)	(9)	(10)	(11)	(12)	(13)	(14)	(15)	(16)
G034.764-00.945	34.764	-0.945	10.4	1.38	0.15	1.25	0.15	0.7	13	···	···	-0.78	0.34	···	···
G034.767+00.544	34.767	0.544	4.2	0.35	0.08	0.37	0.08	0.5	8	···	···	-1.11	0.34	···	···
G034.767-00.110	34.767	-0.110	16.2	7.95	0.65	7.82	0.63	0.9	15	-0.33	0.06	-0.11	0.10	···	···
G034.775+00.156	34.776	0.156	53.4	19.75	1.13	19.46	1.04	1.0	19	-0.54	0.02	-0.53	0.05	···	···
G034.784+00.335	34.784	0.334	16.0	3.44	0.28	4.23	0.30	1.1	17	0.04	0.08	-1.10	0.16	···	···
G034.793-00.711	34.783	-0.706	4.6	1.89	0.43	211.57	10.59	39.6	80	···	···	···	···	HII region	7
G034.796+00.545	34.796	0.545	4.7	0.38	0.08	0.37	0.08	0.5	9	···	···	0.18	0.17	···	···
G034.814-00.989	34.814	-0.989	26.3	3.87	0.26	4.06	0.25	1.0	17	-0.68	0.04	-0.62	0.10	···	···
G034.818+00.347†	34.818	0.347	34.0	0.72	0.02	0.85	0.04	1.2	···	···	···	0.79	0.40	···	···
G034.824+00.733	34.824	0.733	38.3	2.61	0.16	2.71	0.15	1.0	19	-0.04	0.06	0.19	0.09	···	···
G034.830+00.720	34.830	0.720	24.9	1.69	0.11	1.69	0.11	0.9	16	-0.30	0.07	-0.37	0.20	···	···
G034.832+00.685	34.832	0.685	5.7	0.40	0.07	0.46	0.07	0.7	11	···	···	0.03	0.43	···	···
G034.841+00.762	34.841	0.762	123.7	8.20	0.45	8.49	0.43	1.0	22	-0.77	0.01	-0.67	0.02	···	···
G034.842+00.503	34.841	0.503	4.3	0.41	0.10	0.53	0.10	0.6	10	···	···	-0.03	0.44	···	···
G034.842+00.912	34.845	0.907	140.2	10.65	0.58	14.36	0.72	1.3	29	···	···	-1.14	0.50	···	···
G034.845-00.849	34.844	-0.849	7.6	0.81	0.11	0.87	0.11	0.8	12	-0.75	0.14	-0.39	0.64	···	···
G034.855-00.211	34.841	-0.195	10.9	10.45	1.11	213.92	10.74	15.9	71	···	···	···	···	Extended/Diffuse	1
G034.860-00.078‡	34.860	-0.078	16.4	9.22	0.56	157.21	2.33	17.0	···	···	···	···	···	···	···
G034.862-00.063‡	34.862	-0.063	58.0	73.70	1.30	81.80	2.40	1.1	···	0.36	.02	0.10	.02	PN	6
G034.873+00.281	34.872	0.281	4.2	1.14	0.28	17.91	0.94	5.3	33	···	···	···	···	Extended/Diffuse	1
G034.877-00.996	34.877	-0.996	5.7	0.78	0.14	0.57	0.14	0.5	9	···	···	-0.27	0.66	···	···
G034.890+00.504	34.889	0.504	44.6	3.93	0.23	3.96	0.22	1.0	18	-1.05	0.02	-0.80	0.09	···	···
G034.896+00.303	34.896	0.303	19.1	5.16	0.39	12.36	0.67	2.2	24	···	···	···	···	HII region	1
G034.897-00.011	34.907	-0.010	7.7	3.66	0.52	81.08	4.08	14.5	59	···	···	···	···	···	···
G034.897-00.846	34.897	-0.846	51.2	5.54	0.32	6.01	0.32	1.1	21	-0.88	0.02	-0.93	0.07	···	···
G034.898+00.716	34.898	0.716	8.2	0.54	0.07	0.47	0.07	0.7	11	···	···	-0.58	0.37	···	···
G034.906+00.834	34.907	0.834	4.8	0.31	0.07	0.30	0.07	0.5	9	···	···	-0.22	0.74	···	···
G034.910+00.723	34.910	0.723	7.9	0.52	0.07	0.42	0.07	0.6	11	···	···	0.56	0.60	···	···
G034.920+00.856	34.919	0.857	11.4	0.75	0.08	0.66	0.07	0.7	13	-0.43	0.12	-0.66	0.30	···	···
G034.923+00.619	34.924	0.620	11.8	0.84	0.08	2.22	0.13	2.2	24	···	···	···	···	···	···
G034.924+00.483	34.925	0.484	22.8	2.44	0.17	3.30	0.20	1.3	19	···	···	0.16	0.12	···	···
G034.928-00.387	34.928	-0.387	21.7	7.78	0.55	7.83	0.53	0.9	16	-0.89	0.04	-0.83	0.15	···	···
G034.932+00.475	34.932	0.474	5.4	0.63	0.12	1.42	0.13	1.3	14	···	···	0.53	0.37	HII region	1
G034.933+00.840	34.933	0.841	9.9	0.65	0.07	0.63	0.07	0.8	13	-0.27	0.16	0.58	0.32	···	···
G034.959+00.438	34.959	0.438	7.5	1.16	0.17	1.96	0.18	1.2	16	-0.41	0.14	-0.45	0.43	···	···
G034.962-00.150	34.962	-0.150	45.4	21.35	1.24	20.33	1.12	0.9	18	0.05	0.03	-0.01	0.04	···	···
G034.969-00.837	34.969	-0.837	80.4	8.90	0.49	8.78	0.45	1.0	20	-0.97	0.01	-0.99	0.06	···	···
G034.974+00.214	34.975	0.214	6.2	1.20	0.20	0.99	0.20	0.5	10	-0.22	0.19	-0.56	0.25	···	···
G034.975+00.997	34.975	0.997	12.1	1.12	0.11	0.94	0.10	0.7	13	0.08	0.14	-0.20	0.29	···	···
G034.990+00.741	34.991	0.741	8.1	0.56	0.08	0.49	0.07	0.7	11	···	···	0.32	0.39	···	···
G034.994-00.053	34.991	-0.051	4.8	2.30	0.49	6.26	0.57	1.3	16	···	···	···	···	···	···
G035.006-00.509	35.006	-0.509	4.0	0.78	0.20	1.80	0.21	1.0	12	···	···	-0.48	0.64	···	···
G035.009+00.935	35.010	0.935	22.6	1.45	0.10	1.37	0.09	0.9	16	-0.55	0.06	-0.59	0.15	···	···

Continued on next page

Table B.1 – *Continued from previous page*

GLOSTAR name	ℓ	b	SNR	$S_{\rm peak}$	$\Delta S_{\rm peak}$	$S_{\rm int}$	$\Delta S_{\rm int}$	Y	Radius	Spectral index				Classification	
	(°)	(°)		(mJy beam^{-1})		(mJy)			($''$)	α	$\Delta\alpha$	α*	$\Delta\alpha$*	Type	Ref.
(1)	(2)	(3)	(4)	(5)	(6)	(7)	(8)	(9)	(10)	(11)	(12)	(13)	(14)	(15)	(16)
G035.010+00.399	35.007	0.397	28.7	5.01	0.32	10.42	0.55	2.0	23	···	···	···	···	···	···
G035.016-00.444	35.015	-0.444	10.0	2.43	0.28	5.92	0.38	2.0	20	···	···	···	···	···	···
G035.024+00.350‡	35.024	0.350	19.0	16.27	0.89	22.40	1.90	1.4	···	0.76	0.07	0.26	0.08	HII region	2
G035.025+00.337‡	35.025	0.337	9.8	2.54	0.26	100.89	1.63	39.7	···	···	···	···	···	HII region	2
G035.032-00.502‡	35.032	-0.502	441.8	86.60	0.20	743.39	0.57	8.6	···	···	···	···	···	HII region	1
G035.043+00.492	35.043	0.492	8.5	0.81	0.10	0.67	0.10	0.6	11	···	···	-0.57	0.28	···	···
G035.043+00.551	35.042	0.550	4.9	0.40	0.08	0.40	0.08	0.5	9	···	···	-0.02	0.39	···	···
G035.044+00.788	35.044	0.788	4.8	0.40	0.09	0.42	0.09	0.6	9	···	···	0.72	0.92	···	···
G035.052-00.518‡	35.052	-0.518	31.0	144.30	5.00	218.00	12.00	1.5	···	···	···	0.06	0.07	HII region	2
G035.053+00.174	35.048	0.183	12.6	2.45	0.24	10.38	0.55	3.6	35	···	···	···	···	···	···
G035.060+00.780	35.060	0.780	7.7	0.69	0.10	0.69	0.10	0.7	12	-0.74	0.11	-0.68	0.76	···	···
G035.068+00.778	35.068	0.778	4.3	0.40	0.09	0.26	0.09	0.3	7	···	···	0.97	0.79	···	···
G035.082-00.326	35.082	-0.326	47.4	11.69	0.68	11.87	0.64	1.0	19	-0.34	0.02	-1.12	0.07	···	···
G035.084+00.562	35.085	0.562	32.3	2.62	0.16	2.65	0.16	1.0	18	-0.73	0.03	-0.59	0.11	···	···
G035.086+00.993	35.086	0.993	5.2	0.58	0.11	0.65	0.11	0.7	10	-0.63	0.17	-0.46	0.24	···	···
G035.099-00.243	35.099	-0.243	41.6	9.34	0.55	11.53	0.62	1.2	21	0.17	0.04	-0.14	0.03	HII region	3
G035.104-00.725	35.104	-0.725	5.8	0.72	0.13	0.73	0.13	0.6	10	···	···	0.07	0.37	···	···
G035.107-00.759‡	35.107	-0.759	15.6	2.03	0.13	31.50	0.51	15.5	···	···	···	···	···	HII region	1
G035.119+00.688‡	35.119	0.688	19.0	0.52	0.03	0.88	0.07	1.7	···	···	···	0.05	0.47	···	···
G035.123+00.525	35.124	0.525	19.0	1.61	0.12	1.55	0.12	0.9	16	-0.69	0.06	-0.49	0.12	···	···
G035.126+00.691‡	35.126	0.691	22.0	0.43	0.02	1.37	0.08	3.2	···	···	···	···	···	···	···
G035.131-00.745‡	35.131	-0.745	9.0	1.01	0.12	1.53	0.27	1.5	···	···	···	0.10	0.46	HII region	1
G035.132-00.850	35.131	-0.851	21.3	2.17	0.16	3.02	0.18	1.3	20	-0.35	0.07	-0.52	0.22	···	···
G035.133+00.622	35.129	0.617	12.3	0.89	0.09	2.24	0.13	2.2	25	···	···	···	···	···	···
G035.134-00.012	35.135	-0.012	4.8	0.73	0.16	0.52	0.15	0.4	8	···	···	0.10	0.20	···	···
G035.136+00.476	35.137	0.476	11.9	1.21	0.12	0.99	0.11	0.7	12	-0.15	0.13	-0.54	0.25	···	···
G035.138-00.761‡	35.138	-0.761	94.0	129.30	1.50	263.10	4.30	2.0	···	···	···	···	···	HII region	1
G035.141+00.913	35.141	0.913	109.1	12.82	0.70	13.11	0.67	1.0	21	-0.79	0.01	-0.88	0.03	···	···
G035.141-00.688	35.141	-0.688	5.4	0.63	0.12	0.48	0.12	0.5	9	···	···	-0.03	0.69	···	···
G035.148+00.829	35.142	0.811	21.4	2.99	0.21	55.18	2.76	17.0	77	···	···	···	···	HII region	1
G035.149-00.986	35.148	-0.986	7.5	1.04	0.15	0.84	0.14	0.6	10	-0.74	0.12	-1.06	0.39	···	···
G035.152-00.038	35.151	-0.038	6.0	0.93	0.16	0.65	0.16	0.5	9	-0.58	0.16	-0.58	0.29	···	···
G035.166+00.072	35.166	0.072	21.5	3.67	0.26	4.01	0.26	1.0	17	-0.11	0.06	-0.42	0.10	···	···
G035.179+00.328	35.178	0.329	9.3	1.47	0.18	2.87	0.21	1.5	19	-0.61	0.10	-1.30	0.40	···	···
G035.197-00.743	35.197	-0.745	117.8	14.14	0.77	23.22	1.17	1.6	43	0.38	0.03	-0.08	0.15	HII region	3
G035.207-00.643	35.207	-0.643	7.8	0.92	0.13	0.97	0.13	0.8	12	···	···	-0.52	0.48	···	···
G035.208+00.174	35.208	0.174	18.6	4.00	0.30	4.17	0.30	1.0	16	-1.12	0.04	-1.48	0.07	···	···
G035.214+00.363	35.213	0.363	40.3	4.34	0.26	4.04	0.23	0.9	17	···	···	-0.14	0.05	···	···
G035.214+00.703	35.214	0.703	4.5	0.81	0.19	8.55	0.46	4.1	26	···	···	···	···	···	···
G035.216+00.428	35.217	0.428	154.7	16.06	0.87	17.41	0.88	1.1	25	0.04	0.01	-0.08	0.02	PN	6
G035.218-00.931	35.218	-0.931	9.8	1.08	0.12	0.71	0.12	0.5	10	-0.51	0.12	-0.67	0.32	···	···
G035.220-00.288	35.221	-0.283	7.1	1.03	0.16	2.01	0.18	1.4	17	···	···	···	···	···	···
G035.225+00.888	35.225	0.888	11.1	1.64	0.17	3.79	0.24	1.9	21	···	···	-0.20	0.22	···	···

Continued on next page

Table B.1 – *Continued from previous page*

GLOSTAR name	ℓ	b	SNR	$S_{\rm peak}$	$\Delta S_{\rm peak}$	$S_{\rm int}$	$\Delta S_{\rm int}$	Y	Radius	Spectral index				Classification	
	(°)	(°)		(mJy beam^{-1})		(mJy)			($''$)	α	$\Delta\alpha$	α*	$\Delta\alpha$*	Type	Ref.
(1)	(2)	(3)	(4)	(5)	(6)	(7)	(8)	(9)	(10)	(11)	(12)	(13)	(14)	(15)	(16)
G035.236+00.794	35.236	0.793	14.5	3.31	0.29	4.56	0.32	1.2	18	-0.22	0.06	-0.50	0.09	···	···
G035.246-00.485	35.246	-0.485	4.1	0.56	0.14	0.59	0.14	0.5	8	···	···	-0.58	0.50	···	···
G035.258+00.399	35.258	0.399	9.7	0.98	0.11	1.33	0.12	1.1	15	-0.38	0.14	-0.75	0.36	···	···
G035.262-00.528	35.262	-0.528	9.1	1.22	0.15	1.26	0.15	0.8	13	-0.44	0.12	-0.24	0.42	···	···
G035.265+00.120	35.261	0.119	28.8	6.96	0.45	22.83	1.17	3.1	32	···	···	···	···	HII region	1
G035.267+00.749	35.267	0.750	4.1	0.80	0.20	1.42	0.21	0.8	11	···	···	0.35	0.39	···	···
G035.268-00.765	35.268	-0.764	14.5	1.72	0.15	2.42	0.17	1.2	19	-0.22	0.12	-0.50	0.35	···	···
G035.270-00.153	35.269	-0.150	4.2	0.74	0.18	20.29	1.03	9.0	42	···	···	···	···	Extended/Diffuse	1
G035.294+00.977	35.297	0.978	4.8	1.19	0.25	7.41	0.45	2.8	22	···	···	···	···	···	···
G035.298-00.842	35.298	-0.842	23.4	2.98	0.21	2.96	0.20	0.9	17	-0.21	0.07	-0.70	0.11	···	···
G035.301-00.785	35.301	-0.786	46.3	6.00	0.35	5.87	0.32	0.9	18	0.07	0.05	0.33	0.06	···	···
G035.304-00.832	35.304	-0.832	12.9	1.70	0.16	1.80	0.16	0.9	15	-0.72	0.08	-1.06	0.15	···	···
G035.308+00.145	35.309	0.147	100.2	22.80	1.25	27.02	1.37	1.2	23	-1.06	0.01	-1.22	0.11	···	···
G035.311-00.890	35.312	-0.888	23.1	3.01	0.21	4.44	0.26	1.4	22	-0.27	0.06	-0.54	0.15	···	···
G035.318-00.823	35.318	-0.823	95.3	13.04	0.72	12.15	0.62	0.9	19	-0.72	0.01	-0.81	0.03	···	···
G035.331+00.615	35.330	0.613	295.6	27.56	1.49	44.11	2.21	1.6	30	···	···	-0.46	0.10	···	···
G035.344+00.348	35.344	0.348	4.4	0.46	0.11	0.51	0.11	0.5	9	···	···	-1.13	0.59	HII region	1
G035.344-00.381	35.351	-0.383	4.3	0.60	0.15	19.90	1.00	10.8	47	···	···	···	···	Ionization Front	1
G035.351+00.239	35.351	0.239	410.6	59.76	3.22	59.58	2.98	1.0	25	-0.20	0.00	-0.21	0.02	···	···
G035.358+00.584	35.358	0.584	4.6	0.41	0.09	0.39	0.09	0.5	8	···	···	-0.55	0.17	···	···
G035.365+00.425	35.366	0.425	4.9	0.46	0.10	1.80	0.13	1.9	18	···	···	-0.77	0.36	···	···
G035.367+00.980	35.369	0.982	4.8	1.20	0.26	9.67	0.54	3.5	25	···	···	···	···	Ionization Front	1
G035.371+00.663	35.371	0.663	20.0	1.70	0.13	1.54	0.11	0.8	15	···	···	0.46	0.18	···	···
G035.376+00.494	35.378	0.493	8.5	0.82	0.11	1.89	0.14	1.8	21	···	···	0.29	0.44	···	···
G035.402+00.342	35.402	0.342	4.0	0.44	0.11	0.60	0.12	0.6	9	···	···	0.11	0.79	···	···
G035.427-00.251	35.427	-0.261	18.2	3.33	0.26	80.52	4.03	21.2	75	···	···	···	···	HII region	1
G035.428+00.393	35.428	0.393	15.9	1.88	0.16	1.43	0.14	0.7	13	···	···	0.60	0.19	···	···
G035.429+00.831	35.429	0.831	236.0	18.01	0.97	21.99	1.10	1.2	26	-0.54	0.01	-0.70	0.03	···	···
G035.437+00.761	35.437	0.762	4.1	0.30	0.07	0.49	0.08	0.7	10	···	···	-2.04	1.06	···	···
G035.437+00.992	35.438	0.992	5.8	1.29	0.23	1.55	0.23	0.8	12	···	···	-0.58	0.18	···	···
G035.452-00.295†	35.452	-0.295	62.0	0.81	0.01	0.60	0.02	0.7	···	···	···	1.19	.50	···	···
G035.455+00.844	35.455	0.845	13.6	0.93	0.08	0.85	0.08	0.8	14	···	···	0.01	0.29	···	···
G035.457-00.179	35.457	-0.179	35.6	8.42	0.51	7.72	0.45	0.9	17	0.13	0.05	0.15	0.07	HII region	2
G035.461+00.360	35.456	0.345	14.4	1.84	0.16	61.78	3.09	28.1	89	···	···	···	···	Extended/Diffuse	1
G035.467+00.139	35.467	0.139	1121.0	312.12	16.81	324.95	16.25	1.1	26	0.22	0.00	-0.02	0.03	HII region	2
G035.472-00.436	35.472	-0.436	907.1	226.29	12.19	232.65	11.64	1.0	26	0.33	0.00	0.05	0.02	PN	6
G035.473+00.874	35.472	0.874	7.7	0.55	0.08	0.64	0.08	0.9	13	-0.56	0.17	-0.02	0.32	···	···
G035.476+00.842	35.476	0.843	4.3	0.29	0.07	0.32	0.07	0.5	9	···	···	4.05	3.82	···	···
G035.479+00.960	35.482	0.961	12.7	1.40	0.13	1.70	0.14	1.0	17	···	···	-0.95	0.40	···	···
G035.481+00.226	35.482	0.226	4.1	0.72	0.18	4.88	0.30	2.4	20	···	···	···	···	HII region	1
G035.482+00.090	35.486	0.090	12.1	5.31	0.52	8.06	0.60	1.3	19	···	···	···	···	···	···
G035.484+00.424	35.484	0.424	398.8	45.56	2.46	45.03	2.25	1.0	24	-0.56	0.00	-0.73	0.02	···	···
G035.495+00.856	35.495	0.856	5.2	0.35	0.07	0.28	0.07	0.5	9	-0.96	0.19	-1.01	0.63	···	···

Continued on next page

Table B.1 – *Continued from previous page*

GLOSTAR name	ℓ	b	SNR	$S_{\rm peak}$	$\Delta S_{\rm peak}$	$S_{\rm int}$	$\Delta S_{\rm int}$	Y	Radius	Spectral index				Classification	
	(°)	(°)		(mJy beam^{-1})		(mJy)			($''$)	α	$\Delta\alpha$	α*	$\Delta\alpha$*	Type	Ref.
(1)	(2)	(3)	(4)	(5)	(6)	(7)	(8)	(9)	(10)	(11)	(12)	(13)	(14)	(15)	(16)
G035.507+00.880	35.506	0.880	5.4	0.37	0.07	0.29	0.07	0.5	9	···	···	0.15	0.97	···	···
G035.525-00.814	35.526	-0.814	4.2	0.73	0.18	0.69	0.18	0.4	8	···	···	-0.97	0.26	···	···
G035.528-00.146	35.528	-0.146	6.0	2.15	0.38	2.69	0.38	0.8	12	···	···	-0.13	0.39	HII region	3
G035.534+00.274	35.534	0.273	12.2	1.76	0.17	1.87	0.17	0.9	15	-0.63	0.08	-0.30	0.39	···	···
G035.541+00.795	35.541	0.795	31.9	2.12	0.13	1.95	0.12	0.9	16	-1.09	0.03	-1.61	0.13	···	···
G035.542+00.485	35.543	0.485	9.8	0.94	0.11	1.17	0.11	1.0	15	-0.76	0.09	-0.89	0.45	···	···
G035.543+00.240	35.542	0.240	31.0	5.24	0.33	6.46	0.36	1.2	21	-0.34	0.04	-0.25	0.25	···	···
G035.548+00.720	35.548	0.720	77.5	5.37	0.30	5.01	0.26	0.9	19	0.17	0.04	0.53	0.03	···	···
G035.564-00.492	35.565	-0.491	194.2	80.24	4.34	93.64	4.70	1.2	25	0.09	0.01	-0.08	0.03	PN	6
G035.565+00.958	35.565	0.958	4.9	0.36	0.08	0.53	0.08	0.8	11	···	···	-0.69	0.46	···	···
G035.566+00.156	35.565	0.156	14.9	2.56	0.22	2.05	0.20	0.7	13	···	···	0.35	0.14	···	···
G035.574+00.819	35.574	0.819	15.5	1.07	0.09	0.92	0.08	0.8	14	-0.65	0.08	-0.29	0.46	···	···
G035.581-00.153	35.581	-0.154	10.1	5.96	0.67	5.42	0.65	0.7	12	-0.65	0.08	-0.49	0.04	···	···
G035.588+00.851	35.588	0.852	53.5	3.72	0.21	4.99	0.26	1.3	23	-0.34	0.04	-0.58	0.08	···	···
G035.599+00.812	35.600	0.812	7.8	0.55	0.08	0.43	0.07	0.6	11	···	···	0.50	0.53	···	···
G035.601+00.688	35.601	0.688	4.3	0.30	0.07	0.55	0.07	0.9	11	···	···	0.21	0.40	···	···
G035.623+00.613	35.622	0.613	37.8	3.02	0.18	2.58	0.15	0.8	16	-0.42	0.04	-0.50	0.09	···	···
G035.624+00.742	35.623	0.742	413.0	27.67	1.49	27.35	1.37	1.0	25	-0.40	0.00	-0.47	0.01	···	···
G035.626+00.681	35.626	0.680	10.1	0.72	0.08	0.65	0.08	0.7	13	···	···	1.87	0.27	···	···
G035.628+00.769	35.630	0.770	4.1	0.28	0.07	0.64	0.07	1.0	12	···	···	-0.81	1.00	···	···
G035.631+00.866	35.631	0.866	27.4	1.89	0.12	1.75	0.11	0.9	16	-0.07	0.08	-0.45	0.17	···	···
G035.638+00.825	35.638	0.825	7.4	0.51	0.07	0.39	0.07	0.6	10	···	···	-0.94	0.52	···	···
G035.652+00.871	35.651	0.872	4.8	0.32	0.07	1.57	0.10	2.2	20	···	···	···	···	Ionization Front	1
G035.654+00.961	35.653	0.961	44.6	3.05	0.18	3.03	0.17	1.0	18	-0.68	0.03	-0.92	0.11	···	···
G035.669+00.528	35.665	0.524	4.4	0.34	0.08	5.81	0.30	6.2	32	···	···	···	···	Extended/Diffuse	1
G035.681-00.194	35.680	-0.194	13.2	4.72	0.44	5.44	0.45	1.0	16	-0.91	0.06	-0.63	0.10	···	···
G035.684-00.966	35.684	-0.966	4.2	1.00	0.24	1.00	0.24	0.5	8	···	···	-0.47	0.20	···	···
G035.688+00.346	35.691	0.343	124.4	14.42	0.79	24.09	1.21	1.7	29	···	···	···	···	···	···
G035.704-00.753	35.705	-0.753	5.3	1.08	0.21	1.10	0.21	0.6	10	-0.53	0.18	-1.47	0.27	···	···
G035.707-00.485	35.707	-0.485	14.1	3.76	0.33	3.17	0.31	0.7	13	-0.92	0.06	-1.06	0.07	···	···
G035.717+00.241	35.716	0.240	8.7	1.34	0.17	1.91	0.18	1.1	15	···	···	-0.94	0.22	···	···
G035.727+00.758	35.724	0.758	4.9	0.30	0.06	0.88	0.08	1.5	16	···	···	0.15	0.55	···	···
G035.732+00.726	35.732	0.727	20.4	1.32	0.10	1.26	0.09	0.9	16	-0.60	0.06	-0.88	0.14	···	···
G035.732+00.962	35.732	0.961	4.2	0.29	0.07	0.30	0.07	0.5	8	···	···	0.91	1.06	···	···
G035.733+00.363	35.733	0.363	6.3	0.68	0.11	0.78	0.12	0.8	12	···	···	-0.22	0.53	···	···
G035.734-00.465	35.734	-0.465	85.7	19.38	1.07	18.51	0.95	0.9	20	-0.32	0.01	-0.46	0.03	···	···
G035.737+00.159	35.737	0.159	13.9	2.54	0.23	2.61	0.22	0.9	15	-0.46	0.09	-0.62	0.29	···	···
G035.746+00.156	35.746	0.157	16.9	3.07	0.25	3.02	0.24	0.9	15	-0.01	0.11	-0.14	0.12	HII region	3
G035.761+00.706	35.761	0.706	5.5	0.39	0.07	0.45	0.07	0.7	11	-0.85	0.18	-1.50	0.68	···	···
G035.768-00.242	35.768	-0.242	9.1	1.83	0.22	1.59	0.22	0.7	12	-0.26	0.13	-0.07	0.34	···	···
G035.784-00.667	35.784	-0.667	23.4	3.14	0.22	3.08	0.20	0.9	16	-0.67	0.05	-0.88	0.08	···	···
G035.785+00.065	35.785	0.065	5.0	0.85	0.18	0.59	0.17	0.4	8	-0.84	0.19	-1.31	0.46	···	···
G035.789+00.399	35.789	0.399	6.5	0.66	0.11	0.55	0.11	0.6	10	···	···	-1.70	0.70	···	···

Continued on next page

Table B.1 – *Continued from previous page*

GLOSTAR name	ℓ	b	SNR	$S_{\rm peak}$	$\Delta S_{\rm peak}$	$S_{\rm int}$	$\Delta S_{\rm int}$	Y	Radius	Spectral index				Classification	
	(°)	(°)		(mJy beam^{-1})		(mJy)			($''$)	α	$\Delta\alpha$	α*	$\Delta\alpha$*	Type	Ref.
(1)	(2)	(3)	(4)	(5)	(6)	(7)	(8)	(9)	(10)	(11)	(12)	(13)	(14)	(15)	(16)
G035.790+00.688	35.790	0.688	46.0	3.21	0.19	3.12	0.17	0.9	18	-0.69	0.03	-0.64	0.07	···	···
G035.796-00.172†	35.796	-0.172	4.0	0.24	0.06	0.67	0.24	2.8	···	···	···	···	···	···	···
G035.801+00.143	35.801	0.143	5.9	0.86	0.15	0.71	0.15	0.5	9	···	···	0.30	0.23	···	···
G035.809-00.665	35.809	-0.665	29.0	3.65	0.23	4.39	0.25	1.1	19	-0.51	0.04	-0.73	0.12	···	···
G035.812-00.385	35.812	-0.385	4.3	0.66	0.16	0.54	0.16	0.4	7	···	···	-0.06	0.39	···	···
G035.815-00.251	35.814	-0.252	9.7	1.55	0.18	1.92	0.19	1.0	14	-0.06	0.16	-0.47	0.34	···	···
G035.818+00.823	35.819	0.823	4.1	0.23	0.06	0.20	0.06	0.4	8	···	···	-0.53	0.67	···	···
G035.818-00.616	35.817	-0.617	10.8	1.39	0.15	2.48	0.18	1.5	19	···	···	-0.41	0.22	···	···
G035.828+00.090	35.828	0.091	13.0	1.60	0.15	1.23	0.14	0.7	12	-0.52	0.10	-0.37	0.10	···	···
G035.832-00.990	35.832	-0.990	7.5	1.23	0.18	1.03	0.17	0.6	11	-0.45	0.13	-1.21	0.42	···	···
G035.837-00.944	35.837	-0.946	19.7	2.47	0.18	2.83	0.19	1.1	18	-0.56	0.05	-0.78	0.17	···	···
G035.842-00.275	35.842	-0.275	16.4	2.37	0.19	3.05	0.21	1.2	18	-0.31	0.08	-0.66	0.13	···	···
G035.845-00.143	35.845	-0.143	10.4	1.30	0.14	1.73	0.15	1.1	15	-0.57	0.11	-0.74	0.25	Ionization Front	1
G035.849+00.328	35.849	0.328	294.0	30.34	1.64	29.38	1.47	1.0	23	-0.28	0.01	-0.53	0.02	···	···
G035.868+00.376	35.871	0.374	20.8	2.15	0.16	4.18	0.23	1.8	23	···	···	-1.13	0.26	···	···
G035.871+00.631	35.871	0.630	13.6	1.00	0.09	0.90	0.09	0.8	14	0.09	0.15	0.41	0.22	···	···
G035.878+00.648	35.878	0.648	6.1	0.44	0.08	0.34	0.07	0.5	9	···	···	-0.46	0.29	···	···
G035.878+00.660	35.878	0.660	10.8	0.76	0.08	0.78	0.08	0.8	14	-0.24	0.14	-0.37	0.33	···	···
G035.881-00.961	35.881	-0.961	5.0	0.64	0.13	0.69	0.13	0.6	10	···	···	0.40	0.34	···	···
G035.887-00.244	35.887	-0.244	4.6	0.61	0.14	0.37	0.13	0.3	7	···	···	-0.80	0.46	···	···
G035.891+00.145	35.892	0.145	12.4	1.65	0.16	1.42	0.15	0.7	13	-0.47	0.09	-0.78	0.21	···	···
G035.891+00.521	35.892	0.520	11.7	1.04	0.11	0.82	0.10	0.7	12	-0.34	0.11	-1.17	0.47	···	···
G035.892-00.538	35.892	-0.538	6.0	0.63	0.11	0.55	0.11	0.6	10	-0.97	0.15	-1.10	0.31	···	···
G035.900-00.237	35.900	-0.237	7.4	0.97	0.14	0.76	0.14	0.6	10	-0.45	0.15	-0.23	0.42	···	···
G035.904-00.481	35.904	-0.481	44.2	4.44	0.26	5.16	0.28	1.1	21	-0.73	0.02	-0.69	0.06	···	···
G035.905+00.142	35.905	0.142	6.1	0.79	0.14	1.20	0.14	1.0	13	···	···	-0.85	0.50	···	···
G035.921-00.621	35.922	-0.621	8.8	0.96	0.12	1.37	0.13	1.1	15	···	···	-1.16	0.50	···	···
G035.921-00.639	35.922	-0.639	6.5	0.72	0.12	1.21	0.13	1.1	14	···	···	-0.25	0.40	···	···
G035.923-00.049	35.922	-0.049	17.5	2.07	0.16	7.81	0.41	3.4	30	···	···	···	···	HII region	1
G035.931-00.818	35.931	-0.818	7.3	0.76	0.11	0.63	0.11	0.6	11	···	···	-0.35	0.78	···	···
G035.934+00.190	35.932	0.190	6.8	0.85	0.13	1.11	0.14	0.9	13	-0.91	0.14	-1.44	0.58	···	···
G035.939-00.617	35.939	-0.617	7.6	0.75	0.11	0.66	0.10	0.7	11	-0.82	0.12	0.36	0.59	···	···
G035.940+00.343	35.943	0.343	4.2	0.44	0.11	2.40	0.16	2.1	18	···	···	···	···	Extended/Diffuse	1
G035.941+00.592	35.941	0.593	13.2	1.06	0.10	1.00	0.09	0.8	14	-0.31	0.11	-0.72	0.61	···	···
G035.946+00.379	35.946	0.379	1703.0	178.22	9.60	177.43	8.87	1.0	27	0.05	0.00	0.10	0.02	Radio star	8
G035.947+00.152	35.946	0.153	10.9	1.33	0.14	1.99	0.16	1.2	18	-0.38	0.14	-0.85	0.16	···	···
G035.949-00.147	35.949	-0.147	254.2	24.06	1.30	28.61	1.43	1.2	26	0.11	0.01	-0.08	0.01	HII region	3
G035.955-00.636	35.956	-0.636	6.1	0.59	0.10	0.60	0.10	0.7	11	···	···	0.29	0.69	···	···
G035.962+00.859	35.962	0.859	5.2	0.34	0.07	0.28	0.07	0.5	9	···	···	-1.20	0.95	···	···
G035.968-00.856	35.967	-0.856	4.1	0.39	0.10	0.39	0.10	0.4	8	···	···	-1.33	0.34	···	···
G035.971-00.963	35.971	-0.963	4.6	0.67	0.15	0.49	0.15	0.4	8	···	···	0.10	0.57	···	···
G035.986+00.672	35.986	0.672	6.0	0.50	0.09	1.04	0.10	1.3	15	···	···	0.67	0.88	···	···
G035.987+00.205	35.987	0.205	28.0	3.96	0.26	3.54	0.23	0.8	16	-0.56	0.04	-0.69	0.09	···	···

Continued on next page

Table B.1 – *Continued from previous page*

GLOSTAR name	ℓ	b	SNR	$S_{\rm peak}$	$\Delta S_{\rm peak}$	$S_{\rm int}$	$\Delta S_{\rm int}$	Y	Radius	Spectral index				Classification	
	(°)	(°)		(mJy beam^{-1})		(mJy)			($''$)	α	$\Delta\alpha$	α*	$\Delta\alpha$*	Type	Ref.
(1)	(2)	(3)	(4)	(5)	(6)	(7)	(8)	(9)	(10)	(11)	(12)	(13)	(14)	(15)	(16)
G035.994+00.332	35.995	0.332	4.4	0.60	0.14	0.48	0.14	0.4	8	···	···	-0.64	0.39	···	···
G035.994-00.526	35.994	-0.526	7.0	0.91	0.14	0.75	0.13	0.6	10	-0.37	0.16	-0.51	0.47	···	···
G035.996-00.555	35.997	-0.555	9.5	1.30	0.15	1.27	0.15	0.8	13	-0.80	0.10	-0.80	0.20	···	···

List of Figures

List of Tables